

The Effect of Stress State and Precipitation on Stress-
Induced Martensitic Transformations in Polycrystalline
and Single Crystal Shape Memory Alloys:
Experiments and Micro-Mechanical Modeling

by

Kenneth Allen Gall

B.S., University of Illinois, 1995

M.S., University of Illinois, 1996

THESIS

Submitted in partial fulfillment of the requirements
for the degree of Doctor of Philosophy in Mechanical Engineering
in the Graduate College of the
University of Illinois at Urbana-Champaign, 1998

Urbana, Illinois

UNIVERSITY OF ILLINOIS AT URBANA-CHAMPAIGN
THE GRADUATE COLLEGE

March 19, 1998
(date)

WE HEREBY RECOMMEND THAT THE THESIS BY

Kenneth Allen Gall

ENTITLED The Effect of Stress State and Precipitation on Stress-Induced

Martensitic Transformations in Polycrystalline and Single Crystal Shape
Memory Alloys: Experiments and Micro-Mechanical Modeling

BE ACCEPTED IN PARTIAL FULFILLMENT OF THE REQUIREMENTS FOR

THE DEGREE OF Doctor of Philosophy

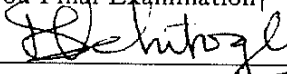


Director of Thesis Research

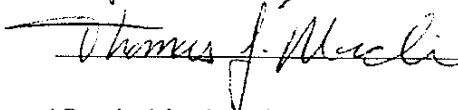
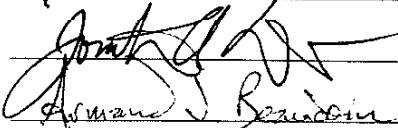
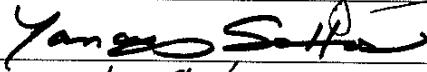


Head of Department

Committee on Final Examination†



Chairperson



† Required for doctor's degree but not for master's.

ABSTRACT

Shape memory alloys such as CuZnAl and NiTi have been a strong focus of current research efforts primarily in the fields of basic materials science and applied mechanics. Although research efforts in both fields have uncovered many of the microscopic and macroscopic features of these alloys, there still exists some unresolved issues related to the mechanical behavior of shape memory alloys. With this, the purpose of the present work is to answer several critical questions related to the mechanical behavior of shape memory alloys: 1. Why do polycrystalline NiTi and CuZnAl shape memory alloys sometimes demonstrate tension/compression asymmetry? 2. Why do peak aged NiTi single crystals demonstrate a decrease in the orientation dependence of critical transformation stress levels, σ_{cr} ? 3. What is the effect of different aging treatments on σ_{cr} and martensite start temperatures, M_s , in polycrystalline and single crystal NiTi?

To answer the first question a micro-mechanical model is used which incorporates single crystal constitutive relationships and individual grain orientations into the self-consistent formulation. With this model it is shown that tension/compression asymmetry in CuZnAl alloys is linked to the unidirectional nature of the martensitic transformation. In NiTi alloys it is shown that tension/compression asymmetry is caused by a strong crystallographic texture of the $\{110\}\langle 111\rangle$ type coupled with the unidirectional nature of the transformation. As experimentally observed, the model successfully captures the distinctly different martensite flow behavior and transformation stress-strain response in tension versus compression.

To properly understand stress-induced transformations in aged NiTi single crystals, a micro-mechanical model is used to quantify the stress fields outside perfectly coherent $Ti_{11}Ni_{14}$ precipitates in NiTi. Using the model, the decrease in the orientation dependence of σ_{cr} is linked to the unique orientation relationship that exists between the coherent precipitates in NiTi

and the martensite correspondence variant pairs. As experimentally observed the model predicts that peak aged NiTi single crystals loaded under tension along the [100] orientation will show a dramatic decrease in σ_{cr} while those loaded along [111] will show less of a decrease in σ_{cr} . The effect of different aging treatments is properly explained by extending the local stress field model to the case of semi-coherent precipitates. In addition, the depletion of Ni in the matrix surrounding the precipitates is found to contribute to changes in σ_{cr} and M_s for aged NiTi alloys.

ACKNOWLEDGMENTS

The work presented in this dissertation was funded by a grant from the Department of Energy, Basic Energy Sciences Division, Germantown, Maryland, DOE DEFG02-93ER14393. The author would first like to thank his advisor Professor Huseyin Sehitoglu. His abundance of technical skills have helped the present author to produce results that are worthy of international recognition. In addition, his incredible insight into the general philosophy of advanced research has been instrumental in teaching the author how to successfully complete future research projects. The author would also like to thank Dr. Hans Maier and Professor Yuriy Chumlyakov. Dr. Maier has helped extremely with the materials science perspectives of this work, and has taught the author how to properly understand the relationships between microstructure and mechanical properties. Professor Chumlyakov has provided the author with single crystals of NiTi which have provided a means to better understand the mechanical behavior of the polycrystalline alloys originally studied. In addition, discussions with him have always greatly furthered the authors knowledge on the subject. Professor Armand Beaudoin is also gratefully thanked for analyzing the texture in NiTi.

The author would also like to thank Kurt Jacobus for his helpful discussions throughout the authors stay at this University. In addition, Mark Balzer is thanked for helping the author conduct experiments under three dimensional stress states. Ibrahim Karaman is thanked for effectively working together with me on several joint projects. My close friends are also thanked for making my stay at the University of Illinois a memorable one. Most importantly, my parents are thanked for the unconditional support that they have always given me. Their strong motivations are the reason for my successes in every part of my life. Exactly 8 years ago they were able to provide me with the vision that college was important for me -- without them I would have never started. Finally, with the hope that he will continue to follow his dreams, I would like to dedicate this work to my brother. His

never-ending drive and ability to always be the best at what he does have never ceased to amaze me.

TABLE OF CONTENTS

	Page
CHAPTER 1: INTRODUCTION.....	1
PREVIEW.....	1
1.1 SHAPE MEMORY ALLOYS (SMA's)	1
1.1.1 HISTORY AND BACKGROUND OF SMA's	1
1.1.2 CURRENT RESEARCH NEEDS AND PROPOSAL.....	2
1.2 COMPOSITIONS OF COMMON SMA's	4
1.2.1 NiTi.....	4
1.2.2 Cu-Zn-Al.....	5
1.2.3 ALLOYING ELEMENTS	5
1.3 MARTENSITIC PHASE TRANSFORMATIONS (MT's) IN SMA's.....	7
1.4 CRYSTAL STRUCTURES OF DIFFERENT PHASES.....	10
1.4.1 NiTi.....	10
1.4.3 Cu-Zn-Al.....	11
1.5 CHARACTERIZATION OF MT's.....	12
1.5.1 DIFFERENTIAL SCANNING CALORIMETRY.....	12
1.5.2 CONSTRAINT CYCLING	13
1.5.3 RESISTIVITY.....	14
1.5.4 ACOUSTIC EMISSION	15
1.6 HEAT TREATMENT OF SMA's.....	16
1.6.1 NiTi.....	16
1.6.2 Cu-Zn-Al.....	22
1.7 THERMO-MECHANICAL BEHAVIOR OF NiTi AND Cu-Zn-Al.....	24
1.7.1 STRESS INDUCED MARTENSITE.....	24
1.7.2 PSEUDOELASTICITY.....	27
1.7.3 SHAPE MEMORY EFFECT.....	28
1.7.4 TWO-WAY SHAPE MEMORY EFFECT	30
1.7.5 MECHANICAL FATIGUE.....	31
1.7.6 THERMAL FATIGUE.....	32
1.7.7 STRESS-STATE EFFECTS	34
1.7.8 STRAIN RATE EFFECTS	36
1.7.9 SINGLE CRYSTALS AND ORIENTATION DEPENDENCE.....	38
1.7.10 PHASE BOUNDARY MOTION.....	41
REFERENCES.....	42

CHAPTER 2: EXPERIMENTAL TECHNIQUES.....	53
PREVIEW.....	53
2.1 SMALL SCALE TEST EQUIPMENT.....	53
2.2 SMALL SCALE SPECIMENS.....	58
2.3 TRIAXIAL TESTING EQUIPMENT.....	60
2.4 MICROSCOPY SAMPLE PREPARATION.....	61
2.5 Cu-Zn-Al and NiTi SPECIMEN COMPOSITIONS.....	62
2.6 HEAT TREATMENT TECHNIQUES.....	62
REFERENCES.....	64
CHAPTER 3: ANALYTICAL MODELING APPROACH.....	65
PREVIEW.....	65
3.1 CONSTITUTIVE MODELING.....	65
3.2 NOTATION AND SYMBOLS USED IN MODELING.....	67
3.2.1 STRESS-STRAIN VARIABLES.....	67
3.2.2 TRANSFORMATION VARIABLES.....	68
3.2.3 THERMODYNAMIC VARIABLES.....	69
3.3 PHENOMENOLOGICAL THEORY OF MT's.....	69
3.4 THERMODYNAMICAL CONSIDERATIONS.....	73
3.5 POLYCRYSTALLINE TRANSITION.....	80
3.6 SUMMARY OF IMPORTANT EQUATIONS.....	83
3.7 CRYSTALLOGRAPHIC DATA.....	84
REFERENCES.....	87
CHAPTER 4: STRESS STATE EFFECTS IN POLY. CuZnAl.....	88
PREVIEW.....	88
4.1 BACKGROUND.....	88
4.2 EXPERIMENTAL TECHNIQUES.....	93

4.3 EXPERIMENTAL RESULTS	96
4.4 MICROSCOPIC OBSERVATIONS.....	102
4.5 MICRO-MECHANICAL MODELING.....	103
4.6 DISCUSSION.....	107
4.7 CONCLUSIONS.....	113
REFERENCES.....	115
CHAPTER 5: STRESS STATE EFFECTS IN POLY. NiTi	119
PREVIEW.....	119
5.1 NOMENCLATURE.....	119
5.2 BACKGROUND	120
5.3 MICRO-MECHANICAL MODELING.....	124
5.4 TEXTURE ANALYSIS.....	135
5.5 DISCUSSION.....	139
5.6 CONCLUSIONS.....	149
REFERENCES.....	151
CHAPTER 6: MODELING THE EFFECTS OF AGING IN NiTi .	154
PREVIEW.....	154
6.1 BACKGROUND	154
6.2 EXPERIMENTAL TECHNIQUES.....	159
6.3 MICROSTRUCTURE IN AGED NiTi.....	160
6.4 MODELING TRANSFORMATIONS IN SOLUTIONIZED NiTi.....	162
6.5 MODELING PHILOSOPHY IN AGED NiTi.....	165
6.6 MODELING THE EFFECT OF COHERENT PRECIPITATES	168
6.7 ESTIMATING THE EFFECT OF Ni LOSS IN THE MATRIX.....	177

6.8 CONCLUSIONS.....	181
REFERENCES.....	182
CHAPTER 7: EXPERIMENTS ON AGED NiTi.....	185
PREVIEW.....	185
7.1 BACKGROUND	185
7.2 EXPERIMENTAL TECHNIQUES.....	191
7.3 THERMALLY INDUCED MARTENSITE.....	193
7.4 ROOM TEMPERATURE STRESS INDUCED MARTENSITE.....	195
7.5 TEMP. DEPENDENCE OF STRESS INDUCED MARTENSITE.....	202
7.6 DISCUSSION OF EXPERIMENTAL RESULTS.....	206
7.7 CONCLUSIONS.....	212
REFERENCES.....	215
APPENDIX A: FORTRAN PROGRAM SHAPE.F.....	219
APPENDIX B: RESOLVED SHEAR STRESS CONTOURS.....	231
APPENDIX C: PRECIPITATE STRESS FIELD PROGRAM.....	255
VITA.....	268

LIST OF TABLES

	Page
Table 1.4.1: Various parent and martensitic phases which have been observed in Cu-Zn-Al and other copper based alloys [Delaey et al. 1981].	11
Table 1.6.1: Precipitation reactions in a Ti - 51.96 % Ni shape memory alloy. The processes will be similar in less Ni rich alloys, however, the reactions may be considerably slowed [Nishida et al. 1986].	17
Table 1.6.2: Transformation temperatures of Ti - 51 at% Ni alloys as-quenched and quenched-aged. The as quenched and quenched-aged transformation temperatures of Ti - 52 at% Ni alloys are similar [Xie et al. 1989].	18
Table 1.7.1: Summary of the experimental work on NiTi single crystals. The times and temperatures cited under heat treatments are aging treatments after quenching.	39
Table 3.7.1: The habit plane normal and transformation direction for the martensitic transformation (B2 -> B19) in a NiTi shape memory alloy.	84
Table 3.7.2: The habit plane normal and transformation direction for the martensitic transformation (B2 -> 9R) in a Cu-Zn-Al shape memory alloy.	85
Table 4.2.1: Uniaxial (1 & 3) and three dimensional (2 & 4-7) stress states applied to the polycrystalline CuZnAl specimens. The tests have increasing values of applied hydrostatic pressure with respect to the applied effective stress. Note that the hydrostatic <i>stress</i> is negative while the hydrostatic <i>pressure</i> is positive.	97
Table 5.3.1: Crystallographic data for the 24 martensite variants in NiTi (Matsumoto <i>et al.</i> , 1987). The small expansion perpendicular to the habit plane has been removed (Buchheit and Wert, 1984).	126
Table 5.3.2: Compatibility (H^{mn}) matrix for NiTi. The interaction energy matrix, H^{mn} , is created by assigning compatible variants interaction energies of $C = \mu/3000$, and incompatible variants interaction energies of $I = \mu/750$. The resulting 24	

	by 24 matrix can be directly implemented into equation 5.3.13 where the summations over H^{mn} only hold for variants which are currently transforming.....	130
Table 5.4.1:	Maximum value of the orientation tensor (maximum resolved shear stress factor) for several crystallographic orientations of NiTi.....	138
Table 6.1.1:	Three different aging treatments for NiTi alloys with approximately 51 at% Ni. The heat treatments cited represent the combined results of several researchers on both polycrystalline and single crystal NiTi (Todoroki and Tamura, 1987; Nishida and Wayman, 1988; Abujudom <i>et al.</i> 1990; Chumlyakov and Starenchenko, 1995).....	157
Table 6.4.1:	Transformation parameters for the B2 -> B19' martensitic transformation in NiTi (Matsumoto <i>et al.</i> 1987). CVP stands for correspondence variant pair.....	164
Table 6.6.1:	Summary of maximum (positive) average local resolved shear stresses for all 24 martensite CVP's (correspondence variant pairs). The tabulated results are for one precipitate variant out of 4.	175
Table 6.7.1:	Experimentally measured compositions of precipitates and surrounding matrix in over-aged NiTi. The measurements were made on several different specimen areas.	178
Table 7.4.1:	Schmid factor for the most favorably oriented martensite correspondence variant pair (CVP) for several different crystallographic orientations of NiTi loaded under tension.....	198
Table 7.4.2:	Summary of experimentally determined critical transformation parameters for aged and solutionized NiTi. The [111] and [110] orientations are compared since they have drastically different Schmid factors (Table 7.4.1).....	199
Table 7.6.1:	Local resolved shear stresses on different martensite correspondence variant pairs due to lattice mismatch strains for a perfectly coherent precipitate (10 nm) and several semi-coherent precipitates (75 and 150 nm) (chapter 6).....	207

LIST OF FIGURES

	Page
Figure 1.3.1: Free energy curves and differential scanning calorimetry curves demonstrating the critical variables in a thermally induced martensitic transformation.....	9
Figure 1.5.1: Intersecting slopes method used to determine transformation temperature from a DSC curve.....	13
Figure 1.5.2: Transformation curve for a specimen under constant load and subjected to a fluctuating temperature.....	14
Figure 1.5.3: Typical schematic of resistivity as a function of temperature for a material undergoing a martensitic phase transformation.....	15
Figure 1.7.1: Stress and temperature phase diagram for materials which undergo martensitic transformations.....	25
Figure 1.7.2: Schematic diagram of pseudoelasticity.....	28
Figure 1.7.3: Schematic diagram of the shape memory effect.....	29
Figure 1.7.4: Schematic diagram of the two-way shape memory effect.....	30
Figure 2.1.1: Picture of the small scale testing machine.....	54
Figure 2.1.2: Small scale specimen grips used for tensile testing. The connecting clasp is not show.....	55
Figure 2.1.3: Small scale specimen grips used for compressive testing.....	56
Figure 2.2.1: Small scale specimens designed for tensile or compressive loading.....	58
Figure 2.2.2: Preparation of single crystal specimens of different orientations.....	59
Figure 2.3.1: Cross sectional view of the triaxial test apparatus [Balzer and Sehitoglu 1997].....	60
Figure 2.6.1: Two evacuated quartz tubes holding long cylindrical high pressure specimens wrapped in nickel wire. The tubes are broken upon quenching.....	62

Figure 3.1.1: Schematic of shape memory alloy deformation phenomenon at various length scales.....	66
Figure 3.3.1: Basic definitions in the phenomenological theory of martensitic phase transformations.....	70
Figure 4.3.1: Uniaxial stress-strain plots for a polycrystalline CuZnAl shape memory alloy specimen above the austenite finish temperature, A_f . The plot demonstrates the asymmetry between tensile and compressive loading at high and low strain rates.....	97
Figure 4.3.2: Cyclic ($R = -1$) stress-strain loops for a polycrystalline CuZnAl shape memory alloy specimen above the austenite finish temperature, A_f . The plot demonstrates the existence of the pseudoelastic effect for strains up to 3% and the asymmetry between tensile and compressive behavior during cyclic loading.....	98
Figure 4.3.3: Effective stress-strain plots for a polycrystalline CuZnAl shape memory alloy specimen above the austenite finish temperature, A_f . The plot demonstrates the effect of several different three dimensional stress states on the transformation behavior.....	99
Figure 4.3.4: Plot of the effective stress at the onset transformation versus the hydrostatic stress at the onset transformation for a polycrystalline CuZnAl shape memory alloy specimen above the austenite finish temperature, A_f . The negative sign in front of σ_h^y converts the hydrostatic pressure into hydrostatic stress.....	100
Figure 4.3.5: Response of a polycrystalline CuZnAl shape memory alloy, above the austenite finish temperature, A_f , to pure hydrostatic pressure. No stress-induced martensitic transformation is observed for pressures up to 700 MPa. The difference in the axial, ϵ_{11} , and diametral, ϵ_{22} and ϵ_{33} , strains is an artifact of texture induced during the drawing of the bars.....	101
Figure 4.4.1: Scanning electron microscope image of several partially transformed CuZnAl grains. The needle like lines are 2-D cross sections of martensite plates (variants). The raised appearance of the plates is due to the deep etching of the parent phase. The picture demonstrates that the formation	

of martensite variants between grains is highly dependent on the crystallographic orientation of the grains..... 102

Figure 4.6.1: Plot of the effective stress at the onset of transformation versus the hydrostatic stress at the onset transformation for a polycrystalline CuZnAl shape memory alloy. The plot was generated from effective stress-strain plots created using a self-consistent scheme similar to the model of Patoor et al. 1994. The numerical model predicts the general experimental trends observed in this CuZnAl alloy.... 108

Figure 4.6.2: Plot of the average volume fraction of martensite versus the applied effective stress for a polycrystalline CuZnAl shape memory alloy. The plot was generated using a self-consistent scheme similar to the model of Patoor et al. 1994. For the growth of martensite, pure tension is the most favorable stress state while pure compression is the least favorable..... 109

Figure 4.6.3: Plot of the average number of active martensite variants versus the applied effective stress for a polycrystalline CuZnAl shape memory alloy. The plot was generated using a self-consistent scheme similar to the model of Patoor et al. 1994. At a given applied stress level, pure tension activates the largest number of martensite variants followed by triaxial compression and then pure compression..... 110

Figure 5.3.1: Transformation parameters in the phenomenological theory of martensitic transformations. For this simple example the martensite is favorably oriented with respect to the coordinate system chosen in the parent phase..... 124

Figure 5.4.1: a. Normalized experimental {110} pole figure. b. Normalized experimental {100} pole figure. c. Discretized {100} pole figure derived from figures a, b, and the {111} pole figure. The experimental figures were all taken from a polycrystalline NiTi sample with the reference direction (the center of the projection) chosen parallel to the loading axis of the specimen..... 137

Figure 5.5.1: Schematic demonstrating the origin of stress state effects in a single crystal of NiTi..... 140

Figure 5.5.2: Modeling results for polycrystalline NiTi demonstrating the effect of the experimentally measured texture on the predicted stress-strain curves..... 141

Figure 5.5.3: Modeling results for polycrystalline NiTi demonstrating the effect of various interaction energy magnitudes on the predicted tensile stress-strain curves.....	142
Figure 5.5.4: Comparison of modeling results with experimental results for polycrystalline NiTi.....	143
Figure 5.5.5: Plot of average volume fraction of martensite versus the applied uniaxial stress level as predicted by the model.....	145
Figure 5.5.6: Plot of average number of active martensite variants per grain versus the applied uniaxial stress level as predicted by the model.....	146
Figure 5.5.7: Scanning electron micrograph of polycrystalline NiTi deformed under tension. The number of stress induced martensite variants per grain is between one and two.....	147
Figure 6.3.1: Microstructures in aged Ni rich NiTi: (a and b) aged 1.5 h @ 673 K, (c) aged 1 h @ 773 K, (d) aged 15 h @ 773 K. Figure c is a weak beam TEM image. The volume fraction of the precipitates in the over-aged material was determined to be approximately 0.074.	161
Figure 6.5.1: Schematic of possible stress fields and morphological changes associated with $Ti_{11}Ni_{14}$ precipitates in Ni rich NiTi...	166
Figure 6.6.1: Schematic of the proposed effect of local lattice mismatch strains (stresses) on martensitic transformations in aged NiTi.....	169
Figure 6.6.2: (a-d) Predicted resolved shear stress fields outside of perfectly coherent precipitates due to lattice mismatch strains. As the precipitates grow larger than 10 nm they become semi-coherent (Treppmann <i>et al.</i> , 1995). The plots are axis-symmetric about the [111] direction and have mirror symmetry about the (111) plane. CVP stands for correspondence variant pair.....	174
Figure 6.6.3: Plot which demonstrates the weakening of internal resolved shear stress fields due to the loss of coherency of $Ti_{11}Ni_{14}$ precipitates. The precipitate sizes for perfectly coherent precipitates (10 nm) and incoherent precipitates (300 nm) were determined by Treppmann <i>et al.</i> , (1995) for recrystallized Ti - 50.8 at% Ni.....	176

Figure 6.7.1: The martensite start temperature as a function of composition as taken from Duerig and Pelton (1994). The measured composition of the solutionized alloy and the matrix composition of the over-aged alloy (calculated from volume fraction of precipitates and known precipitate composition) are also included in the figure.....	180
Figure 7.3.1: Differential scanning calorimetry (DSC) curves for single crystal and polycrystalline NiTi given four different heat treatments. On the plot, M is the martensitic phase (B19'), R is the commensurate phase (rhombohedral), and A is the parent phase (B2).....	194
Figure 7.4.1: Room temperature tensile stress-strain curves for single crystal and polycrystalline NiTi subjected to four different aging treatments: (a) as solutionized, (b) aged 1.5 h @ 673 K, (c) aged 1 h @ 773 K, (d) aged 15 h @ 773 K.	197
Figure 7.4.2: Effect of heat treatment on the orientation dependence of the critical resolved shear stress, τ_{crss} , under tension. In the figure α_{11} is the Schmid factor and σ_{cr} is the critical stress level at the onset of the transformation for a given orientation.....	201
Figure 7.5.1: Orientation and temperature dependence of the critical stress required to induce the martensitic transformation under tension in peak-aged single crystal NiTi.....	203
Figure 7.5.2: Temperature dependence of the critical stress required to induce the martensitic transformation in polycrystalline NiTi given several different heat treatments.....	205
Figure B.1: Resolved shear stress contours due to lattice mismatch strains around a $Ti_{11}Ni_{14}$ precipitate in a NiTi matrix. The resolved shear stresses are calculated on martensite variant #1. The plot is axessymmetric around the [111] axes and posses mirror symmetry about the {111} plane.....	231
Figure B.2: Resolved shear stress contours due to lattice mismatch strains around a $Ti_{11}Ni_{14}$ precipitate in a NiTi matrix. The resolved shear stresses are calculated on martensite variant #2. The plot is axessymmetric around the [111] axes and posses mirror symmetry about the {111} plane.....	232
Figure B.3: Resolved shear stress contours due to lattice mismatch strains around a $Ti_{11}Ni_{14}$ precipitate in a NiTi matrix. The	

	resolved shear stresses are calculated on martensite variant #3. The plot is axessymmetric around the [111] axes and posses mirror symmetry about the {111} plane.....	233
Figure B.4:	Resolved shear stress contours due to lattice mismatch strains around a $Ti_{11}Ni_{14}$ precipitate in a NiTi matrix. The resolved shear stresses are calculated on martensite variant #4. The plot is axessymmetric around the [111] axes and posses mirror symmetry about the {111} plane.....	234
Figure B.5:	Resolved shear stress contours due to lattice mismatch strains around a $Ti_{11}Ni_{14}$ precipitate in a NiTi matrix. The resolved shear stresses are calculated on martensite variant #5. The plot is axessymmetric around the [111] axes and posses mirror symmetry about the {111} plane.....	235
Figure B.6:	Resolved shear stress contours due to lattice mismatch strains around a $Ti_{11}Ni_{14}$ precipitate in a NiTi matrix. The resolved shear stresses are calculated on martensite variant #6. The plot is axessymmetric around the [111] axes and posses mirror symmetry about the {111} plane.....	236
Figure B.7:	Resolved shear stress contours due to lattice mismatch strains around a $Ti_{11}Ni_{14}$ precipitate in a NiTi matrix. The resolved shear stresses are calculated on martensite variant #7. The plot is axessymmetric around the [111] axes and posses mirror symmetry about the {111} plane.....	237
Figure B.8:	Resolved shear stress contours due to lattice mismatch strains around a $Ti_{11}Ni_{14}$ precipitate in a NiTi matrix. The resolved shear stresses are calculated on martensite variant #8. The plot is axessymmetric around the [111] axes and posses mirror symmetry about the {111} plane.....	238
Figure B.9:	Resolved shear stress contours due to lattice mismatch strains around a $Ti_{11}Ni_{14}$ precipitate in a NiTi matrix. The resolved shear stresses are calculated on martensite variant #9. The plot is axessymmetric around the [111] axes and posses mirror symmetry about the {111} plane.....	239
Figure B.10:	Resolved shear stress contours due to lattice mismatch strains around a $Ti_{11}Ni_{14}$ precipitate in a NiTi matrix. The resolved shear stresses are calculated on martensite variant #10. The plot is axessymmetric around the [111] axes and posses mirror symmetry about the {111} plane.....	240

Figure B.11: Resolved shear stress contours due to lattice mismatch strains around a $Ti_{11}Ni_{14}$ precipitate in a NiTi matrix. The resolved shear stresses are calculated on martensite variant #11. The plot is axessymmetric around the [111] axes and posses mirror symmetry about the {111} plane..... 241

Figure B.12: Resolved shear stress contours due to lattice mismatch strains around a $Ti_{11}Ni_{14}$ precipitate in a NiTi matrix. The resolved shear stresses are calculated on martensite variant #12. The plot is axessymmetric around the [111] axes and posses mirror symmetry about the {111} plane..... 242

Figure B.13: Resolved shear stress contours due to lattice mismatch strains around a $Ti_{11}Ni_{14}$ precipitate in a NiTi matrix. The resolved shear stresses are calculated on martensite variant #13. The plot is axessymmetric around the [111] axes and posses mirror symmetry about the {111} plane..... 243

Figure B.14: Resolved shear stress contours due to lattice mismatch strains around a $Ti_{11}Ni_{14}$ precipitate in a NiTi matrix. The resolved shear stresses are calculated on martensite variant #14. The plot is axessymmetric around the [111] axes and posses mirror symmetry about the {111} plane..... 244

Figure B.15: Resolved shear stress contours due to lattice mismatch strains around a $Ti_{11}Ni_{14}$ precipitate in a NiTi matrix. The resolved shear stresses are calculated on martensite variant #15. The plot is axessymmetric around the [111] axes and posses mirror symmetry about the {111} plane..... 245

Figure B.16: Resolved shear stress contours due to lattice mismatch strains around a $Ti_{11}Ni_{14}$ precipitate in a NiTi matrix. The resolved shear stresses are calculated on martensite variant #16. The plot is axessymmetric around the [111] axes and posses mirror symmetry about the {111} plane..... 246

Figure B.17: Resolved shear stress contours due to lattice mismatch strains around a $Ti_{11}Ni_{14}$ precipitate in a NiTi matrix. The resolved shear stresses are calculated on martensite variant #17. The plot is axessymmetric around the [111] axes and posses mirror symmetry about the {111} plane..... 247

Figure B.18: Resolved shear stress contours due to lattice mismatch strains around a $Ti_{11}Ni_{14}$ precipitate in a NiTi matrix. The resolved shear stresses are calculated on martensite variant #18. The plot is axessymmetric around the [111] axes and posses mirror symmetry about the {111} plane..... 248

- Figure B.19:** Resolved shear stress contours due to lattice mismatch strains around a $\text{Ti}_{11}\text{Ni}_{14}$ precipitate in a NiTi matrix. The resolved shear stresses are calculated on martensite variant #19. The plot is axessymmetric around the [111] axes and posses mirror symmetry about the {111} plane..... 249
- Figure B.20:** Resolved shear stress contours due to lattice mismatch strains around a $\text{Ti}_{11}\text{Ni}_{14}$ precipitate in a NiTi matrix. The resolved shear stresses are calculated on martensite variant #20. The plot is axessymmetric around the [111] axes and posses mirror symmetry about the {111} plane..... 250
- Figure B.21:** Resolved shear stress contours due to lattice mismatch strains around a $\text{Ti}_{11}\text{Ni}_{14}$ precipitate in a NiTi matrix. The resolved shear stresses are calculated on martensite variant #21. The plot is axessymmetric around the [111] axes and posses mirror symmetry about the {111} plane..... 251
- Figure B.22:** Resolved shear stress contours due to lattice mismatch strains around a $\text{Ti}_{11}\text{Ni}_{14}$ precipitate in a NiTi matrix. The resolved shear stresses are calculated on martensite variant #22. The plot is axessymmetric around the [111] axes and posses mirror symmetry about the {111} plane..... 252
- Figure B.23:** Resolved shear stress contours due to lattice mismatch strains around a $\text{Ti}_{11}\text{Ni}_{14}$ precipitate in a NiTi matrix. The resolved shear stresses are calculated on martensite variant #23. The plot is axessymmetric around the [111] axes and posses mirror symmetry about the {111} plane..... 253
- Figure B.24:** Resolved shear stress contours due to lattice mismatch strains around a $\text{Ti}_{11}\text{Ni}_{14}$ precipitate in a NiTi matrix. The resolved shear stresses are calculated on martensite variant #24. The plot is axessymmetric around the [111] axes and posses mirror symmetry about the {111} plane..... 254

CHAPTER 1: INTRODUCTION

PREVIEW

A review of current and past research efforts on NiTi and Cu-Zn-Al shape memory alloys is presented. At the beginning of the chapter, the current research needs are discussed, and the purpose of this work is stated. In the subsequent sections, fundamental references in the field are discussed. The literature survey first considers the microscopic aspects of shape memory alloy behavior from a materials science point of view. Following this the heat treatment and macroscopic deformation (stress-strain) behavior are discussed.

1.1 SHAPE MEMORY ALLOYS (SMA's)

1.1.1 HISTORY AND BACKGROUND OF SMA's

In 1951 Chang and Read observed an unexplainable phenomenon while performing research on the bending behavior of Gold-Cadmium bars. Upon loading, the AuCd bar deformed in a manner consistent with expectations. However, after load removal and subsequent heating, the bar returned to its original undeformed shape. At the time of this bending experiment, the unique thermo-mechanical behavior of AuCd was not completely understood. However, years of research have furthered the understanding of the AuCd bending experiment. Today, the ability of a material to apparently "remember" its original shape upon heating is called the "shape memory effect", and materials which demonstrate this effect are classified as "shape memory alloys". Although AuCd demonstrated shape memory nearly forty years ago, its applicability in engineering applications was limited. Some ten years later the discovery of a technologically important shape memory alloy (NiTi) was made [Buehler et al. 1963], and in

the late 70's NiTi was used for it's first wide scale application in Orthodontics [Andreason and Morrow 1978].

Shape memory alloys owe their unique macroscopic deformation behavior to a reversible thermo-elastic martensitic transformation. The martensitic transformation is a diffusionless transformation that may be triggered by either an applied stress or temperature change. The microscopic martensitic transformation leads to recoverable macroscopic deformation modes that are similar, in some respects, to those caused by non-recoverable plastic deformation (slip). Hence, macroscopic deformation that proceeds through a microscopic martensitic transformation is sometimes called transformation-induced plasticity (TRIP). Given the proper combination of applied stress and/or temperature, the reversible martensitic transformation is thermodynamically favored over slip in shape memory alloys. In addition to the shape memory effect, several other macroscopic responses are representative of shape memory alloys such as pseudoelasticity or the two way shape memory effect. These effects will be extensively discussed throughout this review.

Although there are nearly 20 different intermetallic alloy systems that exhibit shape memory properties, NiTi and Cu-Zn-Al have been the primary focus of current research efforts [Shimizu and Tadaki 1988]. Of the two, NiTi has been more widely used in applications due to it's high recoverable strain limit (about 8%), along with its remarkable physical properties. However, Cu-Zn-Al has provoked some interest due to it's moderate recoverability (about 4%), low cost, and ease in processing [Wayman 1980].

1.1.2 CURRENT RESEARCH NEEDS AND PROPOSAL

Although the microscopic transformation behavior and the macroscopic stress-strain response are well characterized under simple loading conditions, there is a shortage of work on the effect of the applied stress state on shape memory alloy stress-strain behavior. More specifically, there has been limited research on the macroscopic response of shape

memory alloys under compression or three dimensional stress states, even less research on the microscopic transformation characteristics under these different stress states, and virtually no work linking the two. Interestingly enough, the work that has been completed to date has demonstrated that the applied stress state has a strong influence on the macroscopic deformation characteristics of shape memory alloys.

With this in mind, the purpose of the current research is to link the macroscopic and microscopic aspects of stress state effects in shape memory alloys. The research will start with an experimental investigation into the effect of the applied stress state on the deformation behavior of single crystal and polycrystalline shape memory alloys. Then, micro-mechanical modeling will be used to predict polycrystalline (textured and untextured) stress-strain behavior from single crystal deformation behavior. The study will require the use of *in situ* transformation observation equipment, unique triaxial testing equipment, small scale uniaxial testing equipment, and electron microscopy (SEM and TEM). The single crystals will be used to better understand the factors which govern the martensitic transformation in the absence of polycrystalline constraint. Understanding the orientation dependence of the transformation stress-strain behavior of single crystals is a crucial step in resolving stress-state effects polycrystalline materials. The *in situ* observation equipment will allow the researcher to observe the microstructural factors which govern stress state effects as they evolve. For example, it has never been determined if phase boundary motion occurs under both tensile and compressive loading. The high resolution electron microscopes will be used to determine the finer microstructural aspects of the transformation such as precipitate size, martensite plate morphology, and fracture surface characterization.

The research will also consider the effects of heat treatment (aging) on stress state effects in NiTi. This will include the study of aging effects in both single crystals and polycrystals under various applied stress states. It is expected that the stress-strain behavior and respective stress-state effects are

strongly dependent on the heat treatment (precipitate size). More explicitly, the purpose of this research is to:

1. Experimentally determine the dependence of the transformation stress-strain behavior of polycrystalline Cu-Zn-Al (with one heat treatment) on the applied stress state.
2. Experimentally determine the dependence of the transformation stress-strain behavior of polycrystalline and single crystal NiTi (with several different heat treatments) on the applied stress state and crystallographic orientation.
3. Determine the origins of stress state effects by using a micro-mechanical model to predict stress state effects in CuZnAl and NiTi polycrystalline shape memory alloys from the known constitutive response of single crystals. As an input, the model will also consider experimentally measured texture in polycrystalline NiTi.
4. Determine the role that coherent precipitates play in the stress induced martensitic transformation in aged single crystal and polycrystalline NiTi. Using micro-mechanical modeling, propose a modified Schmid law which can be used to predict the deformation behavior of aged NiTi.

1.2 COMPOSITIONS OF COMMON SMA's

1.2.1 NiTi

The maximum compositional range of the intermetallic compound NiTi is 49 to 57 at% Ni (@ 1060 °C). However, at lower temperatures, this range decreases greatly, and in order to obtain the desired shape memory properties the compositional range must be kept within 49 to 51 at% Ni

[Hodgson et al. 1990]. This limited compositional range is a direct consequence of the fact that the only intermetallic compound in the nickel-titanium phase field which undergoes the desired thermo-elastic martensitic transformation is equiatomic NiTi. When the average compositional range of an alloy is outside the NiTi phase field, precipitation of intermetallic compounds which do not demonstrate shape memory properties will occur. For example, under steady state conditions, Ti rich alloys will precipitate Ti_2Ni while Ni rich alloys will precipitate $TiNi_3$. In some cases the precipitation of these intermetallics or other quasi-steady state intermetallics is desired to improve the shape memory effect or other mechanical properties [Nishida et al. 1986]. In these cases, alloys with nickel contents as high as 52 at% are commonly employed.

1.2.2 Cu-Zn-Al

The compositional range of ternary copper based shape memory alloys is much larger than the range for binary nickel-titanium alloys. Alloys in the range 4 to 8 at% Al, 9 - 28 at% Zn, and 65 - 80 at% Cu have been the primary focus of current research efforts [Hodgson et al. 1990]. Although the main factor in selecting the composition of a NiTi alloy is to avoid or promote precipitation processes, the composition of Cu-Zn-Al alloys is usually controlled to yield a specific martensite start temperature. The martensite start temperature range for NiTi alloys is small compared to the wide range of transformation temperatures available for Cu-Zn-Al alloys, -50 °C to 110 °C versus -180 °C to 200 °C respectively. Hodgson and colleagues [1990] document the compositions that lead to specific martensite start temperatures through a ternary phase diagram with intersecting temperature contours.

1.2.3 ALLOYING ELEMENTS

NiTi alloys can be alloyed with a wide range of elements (Sc, V, Cr, Mn, Fe, Co, Cu, Pd, Au) to form Ni-Ti-X alloys. The primary reason for adding

alloying elements to NiTi is to change the martensite start temperature of the alloy [Tadaki et al. 1995]. The elements which have a large influence on the martensite start temperature (about 215 °C) are Fe, Co, Pd, and Au, while V, Sc, Cu, Mn, Cr, and Cu have a smaller effect (between 20 °C and 140 °C respectively). Additionally, Mn and Fe have the effect of promoting the R-phase transformation, while it is usually not observed in the presence of the other alloying elements [Tadaki et al. 1995].

The alloying behavior of several other elements in NiTi has been documented. Tungsten has been found to have low solubility in NiTi, and thus forms fine precipitates. The precipitates are expected to improve the two-way shape memory effect [Enami et al. 1995]. Niobium additions in NiTi have been shown to affect the martensite start temperature by as much as 100 K. The change in the martensite start temperature is a strong function of the composition of the niobium doped NiTi alloy [Paio et al. 1992]. Several studies have demonstrated the effect of hydrogen on the mechanical properties and transformation behavior of NiTi [Wu and Wayman 1988, Adachi et al. 1990, Wade et al. 1990, Hoshiya et al. 1992]. In general it was found that hydrogen slows down the shape recovery rate and causes the formation of hydrides. In addition, the heat of transformation is considerably decreased when hydrogen is present.

The most common copper-aluminum based SMA's are Cu-Al-Ni and Cu-Zn-Al. In these alloys, elements such as B, Ce, Co, Fe, Ti, V, and Zr are commonly added for grain refinement. In most cases, the elements are added in very small amounts but have dramatic effects on the mechanical properties of the copper based SMA's [Lee and Wayman 1986, Wang et al. 1991]. For example, Han and Kim [1987] have recently studied the effect of adding boron (.1 % B) to Cu-Zn-Al and have found that it decreased the grain size by about 80%, increased ductility by about 50%, and increased tensile strength by about 80%. In addition to the changes in mechanical properties, the martensite start temperatures of the alloys containing boron were much more sensitive to heat treatment. As far as the primary alloying elements,

the difference in using Zn or Ni is slight with respect to mechanical properties. A CuAl-based alloy with Ni is slightly stronger and more corrosion resistant, however, the alloy with Zn has a much larger martensite start temperature range.

1.3 MARTENSITIC PHASE TRANSFORMATIONS (MT's) IN SMA's

Undoubtedly the first observation of the product phase of a martensitic transformation was in the microstructure of quenched steels. The rapid quenching of steels created a unique needlelike microstructure which demonstrated superior mechanical properties. The microstructure was different from anything previously observed in steels, thus it was given the new name "martensite". As new martensitic microstructures began arising in many different ferrous and non-ferrous alloy systems, it was realized that martensite was not simply a microstructural constituent but rather the product of a unique transformation now called a "martensitic phase transformation." Currently, many attempts have been made to classify martensitic transformations, but the most thorough and descriptive classification scheme is one by Morris Cohen and colleagues. Probably best stated in their original words, they define a martensitic transformation as:

"A lattice-distortive, virtually diffusionless structural change having a dominant deviatoric component and associated shape change such that strain energy dominates the kinetics and morphology during the transformation." -- [Cohen et al. 1979]

In SMA's martensitic transformations are unique due to their reversibility. It has been extensively demonstrated that the main factor in the reversibility of martensitic transformations in shape memory alloys is the self-accommodating nature of the martensite plates [Tas et al. 1973, Tadaki et al. 1975, Banerjee 1990, Yang and Wayman 1992, Fukuda et al. 1992,

Madangopal et al. 1991 and 1993]. The morphology of self-accommodating martensite plates in shape memory alloys usually represents an internally twinned structure. However, Delaey and colleagues [Delaey et al. 1974] have noted that in some shape memory alloy systems the martensitic structure is made up of an array of close packed planes with a well defined stacking sequence. At any rate, for the more common shape memory alloys, there exists internal twins which minimize macroscopic shape change within a given volume of martensite. The shape minimization may also be viewed energetically as has been done by Mura et al. [1976]. Mura and colleagues demonstrated that within a spherical volume of martensite a frequent alternating twin structure minimizes the stored elastic strain energy. At any rate, the self-accommodating martensite plates form with minimal "misfit" plastic strains in the parent phase and thus are thermodynamically reversible. In the ideal case, the misfit strains created by the new martensite are exclusively elastic, hence the term "thermo-elastic martensitic transformation". In addition to the formation of thermo-elastic martensite, Wayman and Shimizu [1972] have noted that for a transformation to be reversible, the lattice invariant deformation must occur by twinning and the martensite must form from an ordered parent phase.

At this point it is appropriate to briefly discuss the thermodynamics of martensitic transformations in shape memory alloys. The thermodynamical "driving force" for martensitic transformations has long been accepted as the difference in the chemical free energy between the parent phase and the martensitic phase [Cohen et al. 1950]. Figure 1.3.1 graphically demonstrates this concept. Consistent with the free energy curves, if the material exists in the parent phase at a high temperature ($T > A_f$) then it will stay there because the state is thermodynamically favored (the parent phase has a lower chemical free energy). As the temperature is decreased the parent phase becomes less thermodynamically favored with respect to the martensitic phase. When the temperature reaches the equilibrium temperature, T_o , the parent phase and the martensitic phase are in thermodynamic equilibrium.

However, at this point the transformation to martensite does not proceed since the driving force for the transformation is zero (free energy of

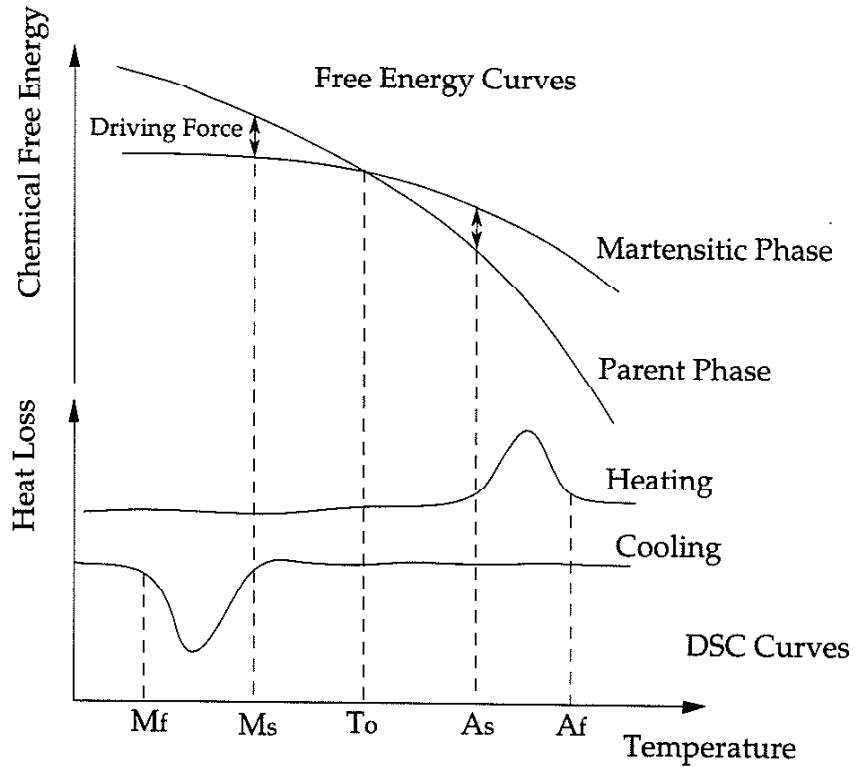


Figure 1.3.1: Free energy curves and differential scanning calorimetry curves demonstrating the critical variables in a thermally induced martensitic transformation.

martensite - free energy of parent phase = 0). As the temperature is further dropped to the martensite start temperature, M_s , the driving force for the transformation becomes large enough (for some variants) to overcome the elastic strain energy and plastic dissipation energy that will be a result of the transformation. At this point, the parent phase will begin transforming to martensite. In shape memory alloys, the reaction is athermal, meaning that the volume fraction of martensite only increases if the temperature is subsequently dropped below M_s . The transformation is complete when the temperature reaches the martensite finish temperature, M_f . Once the material exists in the martensitic phase at a low temperature, the criteria for

reverse transformation follows a similar argument. The DSC curves essentially represent a method to characterize the transformation temperatures of a particular sample, thus DSC analysis will be discussed in section 1.5.

1.4 CRYSTAL STRUCTURES OF DIFFERENT PHASES

1.4.1 NiTi

The crystal structure of the parent phase of equiatomic NiTi is an intermetallic derivative of the BCC unit cell denoted as B2 ($a_0 = 30$ nm). The unit cell has a Ti atom in the center and Ni atoms at the corners [Perkins 1981]. There are two martensitic phases in NiTi, one is a rhombohedral distortion of the B2 structure (R-phase) [Otsuka 1990] and the other is a monoclinic distortion of the B19 structure (martensitic phase) [Hehemann et al 1971, Otsuka et al 1971]. The monoclinic unit cell dimensions are: $a_0 = 28$ nm, $b_0 = 46$ nm, $c_0 = 41$ nm, $\gamma = 96.8^\circ$, with 4 atom per unit cell [Perkins 1981]. The crystallography of both transformations is well established [Nagasawa 1970, Wu and Wayman 1989], and will not be discussed here.

It is still important to note the general relationship between the two martensitic structures. In general, the R-phase transformation occurs before the martensitic transformation. In addition to the R-phase, another intermediate phase called the incommensurate (distorted cubic) phase is sometimes observed [Nishida and Wayman 1988]. Although the R-phase is commonly referred to as a "pre-martensitic phenomenon", it is not a required transformation [Perkins 1981]. That is, the R-phase transformation can occur independent of the martensitic transformation and does not necessarily lead to the martensitic transformation. In fact, the two transformations should be thought of as competing reactions rather than complimentary reactions [Otsuka 1990]. There are several methods which can be used to promote the R-phase transformation [Goldstein 1965]: 1. The introduction of rearranged dislocations due to cold work, 2. The introduction of precipitates in Ni rich

alloys aged between 400 and 500 °C, 3. Addition of elements that suppress the martensitic transformation (i.e. Fe or Al).

1.4.3 Cu-Zn-Al

The crystal structures of the parent and martensitic phases in Cu-Zn-Al are different than the structures observed in NiTi. The purpose here will not be to explain the crystallography [Adachi et al 1988] or to review the heat treatment necessary to obtain specific parent phases. Rather, this section will simply document the phases and structures which have been observed in Cu-Zn-Al alloys. The parent phase of Cu-Zn-Al is highly dependent on the temperature and Zn content [Rapacioli and Ahlers 1977]. Additionally, it is possible to obtain different parent phases dependent on the heat treatment [Delaely et al 1981, Wu 1990]. There are also various martensitic phases in Cu-Zn-Al. Delaely and colleagues [1981] have best represented the parent and martensitic phases in tabular form (Table 1.4.1). From table 1.4.1 it is clear martensitic phase in Cu-Zn-Al depends on the parent phase. In addition, the product of the martensitic transformation depends on the composition, heat

Parent Phase		Martensitic Phase	
Phase Symbol	Structure	Phase Symbol	Structure
β	A2 (BCC Disordered)	β'	9R
β_1	D0 ₃ (BCC Ordered- Fe ₃ Al type)	α_1' β_1' γ_1'	6R 18R 2H
β_2	B2 (BCC Ordered- CsCl type)	α_2' β_2'	3R 9R

Table 1.4.1: Various parent and martensitic phases which have been observed in Cu-Zn-Al and other copper based alloys [Delaely et al. 1981].

treatment, and in some cases the loading direction [Sakamoto et al. 1979, Novak et al. 1997].

1.5 CHARACTERIZATION OF MT's

1.5.1 DIFFERENTIAL SCANNING CALORIMETRY

Although there has been a recent debate [Humbrecht and Planes 1996, Morris and Lipe 1996] over the interpretation of differential scanning calorimetry (DSC) results, DSC still remains the most reliable technique for determining martensitic transformation temperatures. The DSC curves yield explicit results on the transformation start and finish temperatures (figure 1.3.1). The general theory behind DSC curves is that heat is gained or lost during the respective forward and reverse martensitic transformations. Following the cooling curve on figure 1.3.1, the heat loss is constant until the martensite start temperature, M_s . At this point the heat loss from the sample decreases significantly as the transformation to martensite proceeds. When the temperature reaches the martensite finish temperature, M_f , the transformation to martensite is complete and the heat loss becomes constant again. The transformation back to the parent phase upon heating is similar, except that heat loss increases instead of decreasing. In addition the transformation temperatures are commonly referred to as the austenite start, A_s , and finish, A_f , temperatures. The term austenite should be replaced by parent for shape memory alloys, however austenite is commonly used since it was the first observed parent phase of a martensitic transformation.

There are several important points relating to DSC that will be mentioned here. The first is with regards to the determination of transformation temperatures. Although the DSC is rather sensitive, it is not practical to define the macroscopic transformation temperatures at the exact point where the heat loss changes. The method which is universally accepted to characterize the onset or completion of the transformation is the intersecting slopes method (figure 1.5.1). In the slopes method two lines are

drawn, one parallel to the steady state heat loss and one parallel to the quasi-steady state heat loss in the peak. The intersection of these slopes is defined as

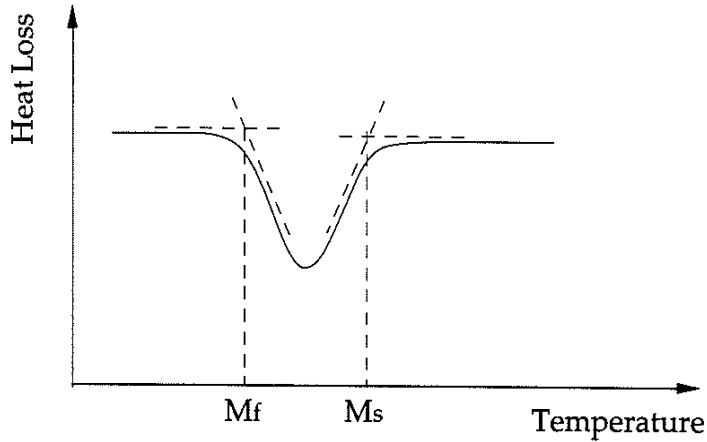


Figure 1.5.1: Intersecting slopes method used to determine transformation temperature from a DSC curve.

the transformation temperature. In addition to defining the transformation temperature correctly, it is also important to control the heating and cooling rate of the sample. If the samples are heated too fast then the peak will be very sharp, and the transformation temperatures may not be well defined. In addition, slow heating and cooling (about 10 - 20 °C/min) assures that the transformation is actually occurring athermally. If it is not an athermal transformation, then heating/cooling too fast will mask the possible isothermal (time dependent) nature of the transformation. Finally, it is crucial to have a sample of sufficient mass (about 100 mg). Otherwise the peaks will be too small and very hard to quantify.

1.5.2 CONSTRAINT CYCLING

If the only available equipment is a uniaxial test machine and a cooling device, then there is a thermo-mechanical technique which can be utilized to determine transformation temperatures [Hodgson et al. 1990]. The technique is performed as demonstrated in figure 1.5.2: First a uniaxial specimen is

stressed to a known elastic stress level, and the temperature is slowly decreased. When the transformation starts, the strain levels begin to increase as the martensite plates form in accordance with the applied stress. When the measured strain saturates, the transformation is complete, and the specimen can be re-heated to determine the austenite transformation temperatures. The temperatures obtained with this technique are slightly offset compared to the temperatures obtained with DSC curves since the applied stress alters the

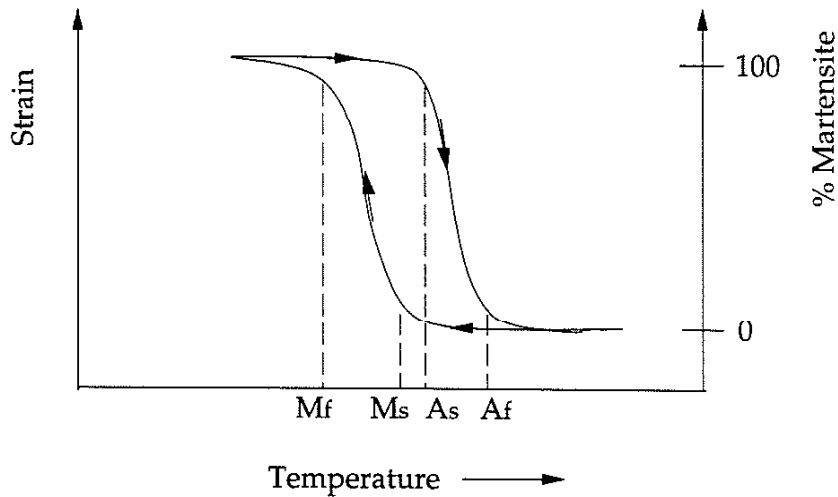


Figure 1.5.2: Transformation curve for a specimen under constant load and subjected to a fluctuating temperature.

transformation driving force. Thus to obtain “pure” transformation temperatures, the effect of the applied stress must be pre-determined. The four traditional transformation temperatures are defined on figure 1.5.2. As in the DSC plots (figure 1.3.1), the transformation temperature should be extrapolated by the method of intersecting slopes (figure 1.5.2).

1.5.3 RESISTIVITY

Historically the oldest technique, electrical resistivity versus temperature plots can be used to characterize transformation temperatures for martensitic transformations. However, as classical as the technique may be, it

is not the preferred characterization method used today. Figure 1.5.3 is a schematic of a typical resistance versus temperature curve for a specimen undergoing a martensitic transformation. Although a trained researcher may easily recognize peaks and changes in slope as transformation temperatures, is often difficult to clearly define the temperatures. Additionally, thermal cycling often changes the curves within a few cycles, making interpretation difficult.

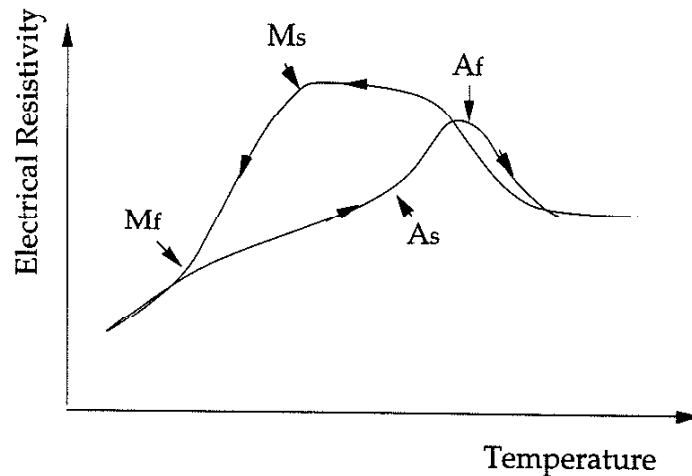


Figure 1.5.3: Typical schematic of resistivity as a function of temperature for a material undergoing a martensitic phase transformation.

1.5.4 ACOUSTIC EMISSION

Although it is not the most universally accepted or applied technique, martensitic transformations can be monitored by acoustic emission. Amengual and colleagues [1988] have determined that large amplitude acoustic bursts occur during interface movement (growth of martensite) in the parent phase. Although the bursts were primarily used to follow the motion of the martensite interface, it is clearly possible to use the results to determine transformation start and finish temperatures. With good acoustic emission equipment it is theoretically possible to determine "actual"

transformation temperatures more accurately than with other techniques. This is due to the fact that the acoustic emission technique monitors the transformation microscopically rather than macroscopically.

1.6 HEAT TREATMENT OF SMA's

1.6.1 NiTi

Shape memory alloys such as NiTi are commonly heat treated to optimize thermo-mechanical shape memory properties. In some cases heat treatment is used to simply alter the martensite start temperature, while in others it is used to promote a pre-martensitic phase such as the R-phase. For example, the R-phase is advantageous in thermal actuators due to its low transformation temperature hysteresis. At any rate, it is important to understand the effect of different heat treatments on the thermo-mechanical behavior of NiTi. However, despite the obvious relevance, the effect of heat treatment on the stress-induced martensitic transformation has sparked only minimal research interest.

In most cases, the heat treatment of near equiatomic NiTi shape memory alloys is classified as a solutionizing and subsequent aging (precipitation) heat treatment. To obtain a solid solution, the solutionizing heat treatment is commonly conducted at 1000 °C for about an hour and followed by an ambient (20 °C) water quench. If the alloy is Ti rich the solutionizing temperature should not be above 984 °C, while for Ni rich alloys the temperature should not rise above 1118 °C. The previous restrictions prevent the possible melting of any Ni-Ti constituents, with low melting temperatures, that are near the equiatomic NiTi phase field. It should also be noted that due to the poor oxidation resistance of NiTi alloys at high temperatures, heat treatments of sufficient magnitude ($T > 500$ °C, $t > 2$ h) must be carried out in a vacuum furnace or in evacuated quartz tubes.

The precipitation processes of Ni rich NiTi alloys as functions of time and temperature are well documented [Beyer et al. 1986, Nishida et al. 1986].

Conversely, the underlying precipitation processes in Ti rich alloys have not been documented even though several aging studies have utilized Ti rich alloys [Ishida et al. 1995, Thoma et al. 1995, Mertmann 1995, Filip and Mazanec 1995]. At any rate, it is appropriate here to briefly discuss the different precipitation processes involved in Ni rich NiTi alloys. The processes are divided into three separate temperature ranges, and in each range there exists unique quasi-steady state precipitates. The temperature ranges and respective precipitate reactions are given in table 1.6.1. The timescales given for the reactions indicate the approximate point where the new phase begins precipitating at the noted temperatures. It should also be mentioned that the processes in table 1.6.1 were discovered for a Ti - 52at%Ni alloy. If the Ni content is slightly less than this (i.e. 51at%Ni), the reactions will be similar but the timescale may differ considerably. As the Ni content approaches 50at%, the precipitation processes at a given temperature may

Temp. Range: T < 680 °C		timescale @ 600 °C	
NiTi + Ti ₃ Ni ₄ (Ti ₁₁ Ni ₁₄)	->	NiTi + Ti ₃ Ni ₄ + Ti ₂ Ni ₃	->
.1 hours	->	16 hours	->
			9000 hours
Temp. Range: 680 °C < T < 750 °C		timescale @ 725 °C	
NiTi + Ti ₂ Ni ₃ (Ti ₄₂ Ni ₅₈)	->	NiTi + Ti ₂ Ni ₃ + TiNi ₃	->
.25 hours	->	100 hours	->
			900 hours
Temp. Range: T > 750 °C		timescale @ 775 °C	
NiTi	->	NiTi + TiNi ₃	
0 hours	->	10 hours	

Table 1.6.1: Precipitation reactions in a Ti - 51.96 % Ni shape memory alloy. The processes will be similar in less Ni rich alloys, however, the reactions may be considerably slowed [Nishida et al. 1986].

become drastically slower, and in the limiting case they will not occur without composition gradients in the solid. In addition, if the temperature within a region is dropped below or above the cited temperatures, then the timescale of the reaction will also shift depending on the TTT curves [Nishida et al. 1986].

Following table 1.6.1, in the high temperature region, it is clear that equiatomic NiTi exists for about 10 hours. At this time, $TiNi_3$ particles become measurable, and upon further aging, the particles simply coarsen until compositional equilibrium is reached. In the mid temperature range,

As quenched: Ti - 51at%Ni [Bataillard et al. 1995, Nishida et al. 1988]						
Trans.	A_s	A_f	M_s	M_f	R_s	R_f
Temp.	-40 °C	-10 °C	-70 °C	-100 °C	-40 °C	-60 °C
As quenched: Ti - 51at%Ni [Stroz et al 1988]						
Trans.	A_s	A_f	M_s	M_f	R_s	R_f
Temp.	-32 °C	6 °C	-40 °C	-65 °C	not obs.	not obs.
As aged 1 hour @ 500 °C: Ti - 51at%Ni [Nishida et al. 1988]						
Trans.	A_s	A_f	M_s	M_f	R_s	R_f
Temp.	-10 °C	10 °C	-30 °C	-50 °C	~ 5 °C	~ 6.5 °C

Table 1.6.2: Transformation temperatures of Ti - 51 at% Ni alloys as-quenched and quenched-aged. The as quenched and quenched-aged transformation temperatures of Ti - 52 at% Ni alloys are similar [Xie et al. 1989].

Ti_2Ni_3 platelets begin to precipitate after about .25 hours. After nearly 100 hours, $TiNi_3$ particles begin to form at the expense of the coarsened Ti_2Ni_3 platelets. Once 900 hours have passed, the equilibrium $TiNi_3$ particles dominate the microstructure as the precipitated phase. In the low temperature region, almost immediately upon heating (.1 hours), widmanstatten like lenticular Ti_3Ni_4 particles can be observed in the

microstructure. However, after about 16 hours, Ti_2Ni_3 platelets begin to form in conjunction with the Ti_3Ni_4 particles. Nearly 9000 hours later, the Ti_3Ni_4 particles are completely dissolved, and the formation of the equilibrium constituent ($TiNi_3$) begins. It is expected that it will take an extremely long time to completely dissolve the Ti_2Ni_3 platelets at this low aging temperature.

The respective transformation temperatures for the aged and as quenched (as solutionized) conditions are given in table 1.6.2. It is interesting that in some studies researchers have not observed the R-phase transformation [Stroz et al. 1988] while in others [Bataillard et al. 1995, Nishida et al. 1988] the R-phase was clearly observed. This discrepancy may be caused by the misinterpretation of DSC curves, or to the blending of transformation peaks due to excessively high heating rates in the DSC. At any rate, Bataillard and Nishida produce results which are essentially in agreement. In the aged condition, the various precipitates in the NiTi matrix have unique effects on the temperature induced transformation behavior of NiTi shape memory alloys. In general the precipitated particles do not transform themselves, but rather they act as nucleation sites for both martensitic and pre-martensitic transformations. However, Nishida and Wayman [1986] have noted that Ti_2Ni_3 precipitates do undergo a orthorombic \rightarrow monoclinic transformation.

There have been several quantitative studies on the effect of aging on the transformation characteristics and temperatures of NiTi alloys [Nishida and Wayman 1988, Stroz et al. 1988, Xie et al. 1989 and 1990, Wu et al. 1994, Bataillard and Gotthardt 1995, Treppman et al. 1995, Sadrnezhad et al. 1997]. All of the aforementioned aging studies have concentrated their work in the low temperature region (table 1.6.1: $T < 680 \text{ }^\circ\text{C}$), and the results are summarized below. For very short aging times (.1 hours) the martensite start temperature slightly increases as the aging temperature increases. Additionally, the incommensurate (cubic distortion) phase transformation occurs at around $-20 \text{ }^\circ\text{C}$ for low aging ($T < 300 \text{ }^\circ\text{C}$) temperatures and at about $20 \text{ }^\circ\text{C}$ for relatively high aging temperatures ($680 \text{ }^\circ\text{C} > T > 300 \text{ }^\circ\text{C}$). At some

aging temperatures (400 °C and 500 °C), the R-phase transformation appears after only .1 hours of aging. For very long aging times (30 hours) the martensite transformation temperatures still increase with increasing aging temperature, but to a greater extent. For long aging times, high aging temperatures also decrease the martensite transformation temperature hysteresis. At aging temperatures greater than 500 °C the R-phase transformation also appeared after prolonged aging.

Much of the work in the literature has concluded that intermediate aging times (about 1 hour) optimize various shape memory properties. At these intermediate aging times there exists several unique transformation characteristics. For example, upon aging for 1 hour @ 500 °C the commensurate R-phase transformation ($R_s \sim 5$ °C) appeared in addition to the incommensurate distorted cubic phase ($I_p \sim 25$ °C) and the martensitic phase ($M_s \sim -30$ °C). Although the transformation temperatures may differ slightly, the previous statement holds true for both Ti - 51at%Ni alloys [Nishida et al. 1988] and Ti - 52at%Ni alloys [Xie et al. 1989]. The "three step" transformation (parent phase \rightarrow distorted cubic phase \rightarrow R-phase \rightarrow martensitic phase) has also been observed by Bataillard and colleagues [1995] for aging treatments of .5 hours @ 500 °C on Ti - 51.14at%Ni. The transformation temperatures for the "common" 1 hour @ 500 °C heat treatment are included in table 1.6.2. It is also interesting to note that the reverse transformation back to the parent phase normally occurs in a single peak. The temperatures obtained by the above thermal treatment are sensitive to composition. In general, the martensite and austenite transformation temperatures decrease with increasing Ni content, while the pre-martensitic transformation temperatures remain nearly the same [Honma 1986]. If the alloy reaches a composition where it becomes Ti rich then its martensite start temperature will be well above room temperature, even in the solutionized state [Filip and Mazanec 1995].

The effect of precipitation on the thermo-mechanical behavior of NiTi has been studied to a limited extent. Honma [1986] and Kaneko et al. [1993]

have both concluded that aging heat treatments of 400 °C to 500 °C for one hour dramatically increase the shape change attainable in the two way shape memory effect. The increase is primarily attributed to the formation of favorably oriented precipitates during constrained aging. Ishida and colleagues [1996] have concluded that fine Ti_3Ni_4 precipitates (about 100 nm) in thin foils increase the critical stress for inducing slip, the recoverable shape memory strain, and the thermal hysteresis. If the particles are allowed to coarsen considerably, then the recoverable strain becomes more sensitive to the matrix composition.

Chumlyakov et al. [1996] have determined the effect of fine Ti_3Ni_4 precipitates (100 nm) on mechanical behavior of NiTi single crystals. Precipitates in Ti - 50.6at%Ni and Ti - 52at%Ni crystals has been shown to weaken the orientation dependence of the shape memory effect and the inherent tension-compression asymmetry of the crystals. In aged alloys, they also observed increased pseudoelastic strains at the expense of smaller recoverable shape memory strains. Finally, crystals aged at low temperatures (1 hour @ 300 °C) showed an increase in the stress level necessary to induce a transformation, while crystals aged at higher temperatures (1 hour @ 500 °C) showed a decrease in the stress level necessary to induce the transformation. This effect is clearly due to the fact that the former treatment acts as a local stress relieving (annealing) treatment while the latter is a balance between a local stress relieving treatment and a local stress raising (precipitation) treatment. Stress raisers in NiTi act as nucleation site for martensite, and thus lower the critical transformation stresses.

The effect of work hardening before aging has been studied by several researchers [Todoroki and Tamura 1987, Abujudom et al. 1990, Legresey et al. 1991, Filip et al. 1991, Thoma et al. 1995, Filip and Mazanec 1995]. It has been determined that cold work prior to aging decreases the martensite and austenite transformation temperatures and increases the R-phase transformation temperature. In other words, cold work suppresses the martensitic transformation and promotes the R-phase transformation. The

suppression of the martensitic phase is due to an increased dislocation density which prevents interface motion [Filip et al. 1991 and 1995]. Conversely, the promotion of the R-phase is due to its ability to replace slip in the NiTi alloys [Filip et al. 1991 and 1995]. If the aging temperature is too high ($T \sim 700$ °C) then the cold work effects are sometimes nullified. To obtain a high sensitivity of transformation temperatures upon subsequent aging, the magnitude of precursory cold work should be around 7% to 9%. Cold work reductions exceeding 25% may suppress all phase transformations in NiTi. As a final note, the stress induced transformation is also triggered at higher stresses and proceeds with a steeper transformation slope in an alloy which has been cold worked prior to aging [Filip et al. 1991 and 1995].

1.6.2 Cu-Zn-Al

The heat treatment of Cu-Zn-Al differs considerably from the thermal treatments in the NiTi system. Since the heat treatment of Cu-Zn-Al alloys is very dependent on composition, the purpose here will be to provide a general discussion on heat treatment, not to document exact heat treatments. Common heat treatments which are incorporated to obtain specified stable transformation temperatures, for a given composition, are available in the literature. There are three different parent phases in Cu-Zn-Al (figure 1.4.1), one disordered high temperature phase β (A2) and two meta-stable ordered low temperature phases, β_1 (D0₃) and β_2 (B2). The existence and stability of these phases, along with the precipitation of the stable α_1 or γ_2 phases, are the major issues related to the heat treatment of Cu-Zn-Al alloys.

The first issue related to the heat treatment of Cu-Zn-Al alloys is the betatizing temperature and time. The betatizing temperature is similar to the solutionizing temperature in aged alloys because it is followed by a quench to avoid precipitation of other stable phases. In Cu-Zn-Al the precipitation of α_1 or γ_2 phases alter the local matrix composition and hence have considerable

effects on the transformation behavior of the alloy. In general, α_1 lowers the transformation temperatures while γ_2 raises them [Delaey et al. 1981]. With increasing betatizing temperatures (650 °C - 950 °C) and soak times (.15 - 1 hour), the transformation temperatures are observed to increase as much as 10 °C [Wu 1990]. The transformation temperatures are also extremely sensitive to quenching rate. If the quench rate is too slow then the martensitic phase transformations in Cu-Zn-Al will be completely suppressed by precipitation of α_1 or γ_2 [Wu 1990].

After quenching the transformation temperatures in Cu-Zn-Al are extremely unstable. In general they may increase nearly 20 °C when exposed to ambient air for less than an hour [Wu 1990]. Unfortunately the transformation temperatures are even more unstable when exposed to low or intermediate aging temperatures (200 °C - 400 °C). In this region, changes in transformation temperatures on the order of 100 °C are common [Wu 1990]. Due to this instability in transformation temperatures, a great deal of work has been done on the "stabilization" of Cu-Zn-Al martensite. Even though there has been excessive research on the stabilization of martensite, the effect is still not completely understood [Wu 1990]. One method, which has been successfully used to stabilize the martensite transformation temperatures is called "step quenching". To perform step quenching, the quench is interrupted at a typical aging temperature and held there for about an hour. After the hold period, the specimen is quenched to the ambient temperature. The advantage of step quenching over traditional quenching and aging appears to be related to the disposal of ultra-low quenching temperatures (these create possible quench distortions and cracks) and the time saved in re-heating to a subsequent aging temperature.

If quenching and subsequent aging is favored, then it is important to note that in Cu-Zn-Al alloys, both the parent and martensitic phase are metastable, and thus demonstrate aging effects [Dunne and Kennon 1981, Wu 1990]. Nevertheless, some recent research has concluded that aging in the

parent phase has little effect on transformation temperatures [Nakata et al. 1993]. At any rate, depending on composition, a Cu-Zn-Al alloy may exist in the martensitic phase or in the parent phase after quenching [Dunne and Kennon 1981]. If the parent phase results after quenching, the transformation temperatures will change during exposure to high temperatures ($T > 120$ °C). The reason for the change has been debated over the last 15 years, but one theory that is shared amongst several researchers [Dunne and Kennon 1981, Lu and Cao 1986] is based on the decomposition of the B2 phase into the $D0_3$ phase. Although the $D0_3$ phase is expected upon quenching to room temperature, quenching suppresses the formation of $D0_3$ phase in favor of the B2 phase. After heating the alloy quickly transforms to the $D0_3$ structure, thus changing the transformation temperatures [Dunne and Kennon 1991].

If the martensitic phase exists after quenching, then a similar decomposition occurs but between the martensitic B2 phase (9R) and the $D0_3$ phase. This transformation presents an irreversibility problem since the martensitic and parent phases do not “match”. In some alloys, the martensitic phase may not transform at all upon heating since it’s parent phase is B2 and the $D0_3$ parent phase is the thermodynamically favored phase. One way to overcome this problem is to step quench. This assures that the martensitic phase formed upon cooling primarily consists of 18R martensite (formed from the $D0_3$ parent phase) versus 9R martensite (formed from the B2 parent phase).

1.7 THERMO-MECHANICAL BEHAVIOR OF NiTi AND Cu-Zn-Al

1.7.1 STRESS INDUCED MARTENSITE

For nearly 75 years [Bain 1925] it has been known that the martensitic transformation in some alloys can proceed by a change in temperature or applied stress state. It has been clearly demonstrated that shape memory alloys such as NiTi [Wasilewski 1971] and Cu-Zn-Al [Nishiyama and Kajiwara 1963, Barcelo et al. 1979] fall in the class of alloys which demonstrate this

behavior. In thermodynamic terms, stress and temperature are referred to as the “state variables” which control the transformation. This is because a change in either stress or temperature alters the driving force for the transformation (the free energy difference between the parent and martensitic phases). It is common practice to construct a stress versus temperature phase diagram which indicates the phases associated with the martensitic transformation (figure 1.7.1).

In general there are three regions to the diagram. At temperatures below the martensite start temperature the material exists in the martensitic

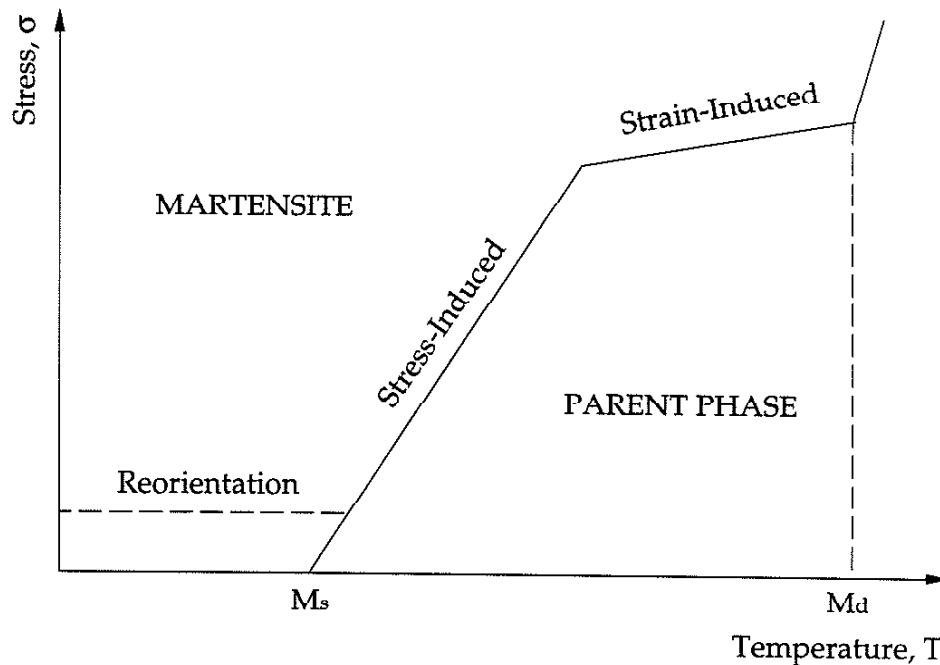


Figure 1.7.1: Stress and temperature phase diagram for materials which undergo martensitic transformations.

state under no applied stress. If stress is applied to a material which already exists in the martensitic state, the martensite plates will reorient and coalesce in favor of the applied stress state. The reorientation will occur at a relatively low stress level (note the dashed line on figure 1.7.1). At very high temperatures the applied stress state generally cannot trigger the

transformation prior to causing excessive plasticity in the parent phase. In this case, the dislocation pileups and plastic strain gradients in the parent phase locally nucleate the transformation. Generally this type of transformation is deemed “strain-induced” (figure 1.7.1). If the temperature is raised high enough (to the deformation induced temperature limit, M_d), then the transformation will never occur. Since the temperature is extremely high, the free energy difference between the phases is so large that even localized plasticity cannot trigger the transformation. The highly localized plasticity in the high temperature case will most likely fracture the specimen before any significant transformation occurs.

In the mid-temperature range, the transformation is “purely” stress induced. In other words, it is in this region where the formation of thermoelastic martensite occurs by the action of an applied stress at any given temperature. This temperature realm is classically called the “stress-induced martensite temperature range”. The slope of the stress induced transformation phase boundary in the stress-induced martensite temperature range is often modeled using a Clausius-Clapeyron equation:

$$\frac{d\sigma}{dT} \approx \frac{\Delta H}{T_o \Delta V} \quad [\text{Wollants et al. 1979}] \quad 1.7.1$$

$$\frac{d\sigma}{dT} \approx \frac{\Delta H}{T \epsilon_o} \quad [\text{Otsuka et al. 1976}] \quad 1.7.2$$

In the above equation, ϵ_o is the uniaxial transformation strain due to the applied stress and ΔV is the volume change caused by the transformation. Additionally, ΔH is the enthalpy of the transformation, and T_o is the equilibrium temperature: $T_o = \frac{1}{2}(M_s + A_s)$. Unfortunately, the meaning of T in Otsuka’s equation is slightly unclear. They are attempting to forward an equation which predicts a straight line in stress-temperature space, however, the slope shows a dependence on T. In Wollants equation there is also a

discrepancy with the ΔV term. The volume change upon transformation is always positive or negative regardless of the applied stress level. However, under compressive load the slope predicted by equation 1.7.1 must be negative. At any rate, equations 1.7.1 and 1.7.2 qualitatively predict that the phase boundary between the parent phase and the martensite is a straight line in stress-temperature space, which is consistent with experimental observations.

1.7.2 PSEUDOELASTICITY

Pseudoelasticity (superelasticity) was first discovered a year after the shape memory effect was observed [Reynolds and Bever 1952]. However, it was some time before pseudoelasticity was completely understood, and it even took over 25 years before a universal term for the behavior was accepted [Otsuka et al. 1979]. Much of the work which has laid a foundation for the current understanding of pseudoelasticity was performed on Cu-Zn-Al single crystals [Schroeder and Wayman 1979, Otsuka and Shimizu 1986]. These fundamental studies demonstrated that pseudoelastic behavior was a result of a reversible stress induced martensitic transformation (figure 1.7.2). They also demonstrated that the recoverable pseudoelastic strain magnitude is dependent on the temperature and level of strain generated. Recently, pseudoelasticity in NiTi has also been extensively studied as a function of temperature and strain level [Tobushi et al. 1993].

Figure 1.7.2 is a schematic diagram of pseudoelasticity as caused by a stress induced martensitic transformation. Of course, pseudoelasticity primarily occurs in stress-induced martensite temperature range (figure 1.7.1). Upon loading the parent phase transforms to martensite and demonstrates a linear hardening behavior in stress-strain space. After unloading, the large transformation strains (sometimes up to 10%) are recovered. This elastic-like recovery of strains is the reason for the term "pseudoelasticity". From figure 1.7.2 it is clear that the reverse transformation does not occur immediately

upon unloading. This dissipation is often attributed to the interfacial energy (friction) required to create new austenite interfaces or remove existing austenite and martensite interfaces. There may also be some dissipation due to small amounts of plastic flow. However, the interfacial friction has been determined to dominate the dissipation. It should be noted that

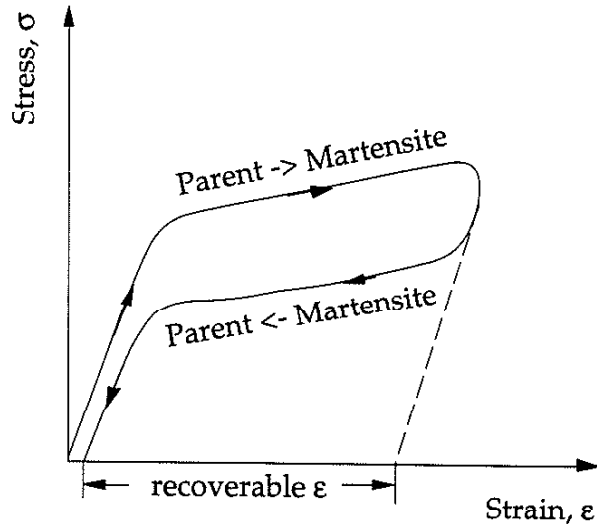


Figure 1.7.2: Schematic diagram of pseudoelasticity.

pseudoelasticity can also occur as the result of a martensite to martensite transformation [Otsuka and Shimizu 1981] or as a result of martensite reorientation. In the case of multiple martensite transformations, there will be several stress-strain plateaus depending on the number of martensitic transformations in Cu-Zn-Al or pre-martensitic transformations in NiTi. When pseudoelasticity occurs by martensite reorientation it is sometimes called ferroelasticity or rubberlike behavior. Currently it is accepted to simply call the phenomenon pseudoelasticity by martensite reorientation.

1.7.3 SHAPE MEMORY EFFECT

Shape memory alloys owe their name to the infamous shape memory effect. The shape memory effect (also called the one-way shape memory

effect) refers to the ability of a material to remember its original unreformed shape. Following figure 1.7.3, a stress is applied to a sample in the martensitic phase. When the critical stress for martensite reorientation and coalescence is reached, the sample macroscopically deforms. Upon unloading there exists a large unrecovered strain. However, if the sample is subsequently heated above its austenite start temperature, then the strains are recovered via a transformation back to the parent phase [Wayman 1981]. Two precursor steps are crucial in the development of the shape memory effect: 1. The original shape of the specimen must be decided while the material exists in the parent phase, 2. The material must be cooled to form thermally induced martensite with little or no macroscopic shape change. At this point the specimen can be stressed and the shape memory effect can be observed (figure

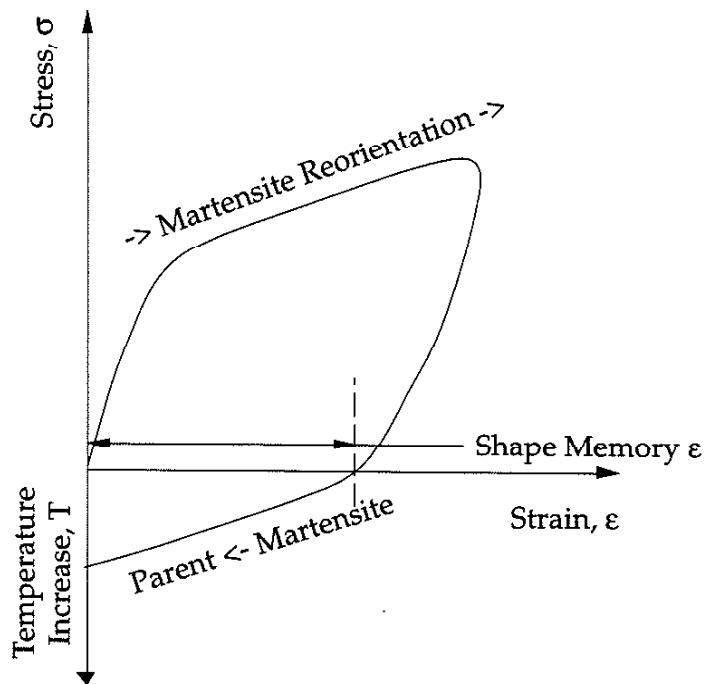


Figure 1.7.3: Schematic diagram of the shape memory effect.

1.7.3). The ability of the material to remember the exact ordering of its parent phase, even from a reoriented (deformed) martensitic phase has been studied extensively from a crystallographic point of view [Wayman 1981]. It should

also be noted that the shape memory effect has been observed in the case of stress induced martensite that is "held" in a meta stable state. In these cases there is either more accommodating plastic deformation in the matrix, or the test temperature is in between the martensite and austenite start temperatures.

1.7.4 TWO-WAY SHAPE MEMORY EFFECT

The two way shape memory effect is not an inherent characteristic of shape memory alloys [Delaey et al. 1974]. To obtain the two way shape memory effect a particular thermo-mechanical treatment must be performed on the specimen. The two way shape memory effect has strong applications in actuator sciences, thus it has been a strong focus of current research efforts. The macroscopic behavior of the two way shape memory effect is demonstrated in figure 1.7.4. As expected, upon cooling the specimen transforms from the parent phase to the martensitic phase, and after heating the specimen transforms back to the parent phase. However, in the case of the two way shape memory effect, the thermally activated transformation is

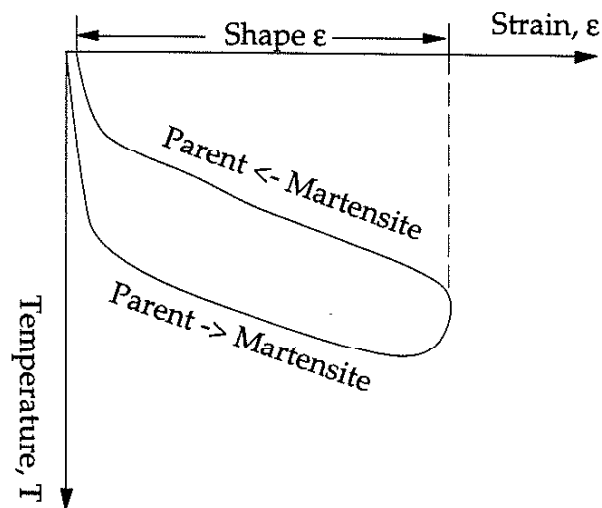


Figure 1.7.4: Schematic diagram of the two-way shape memory effect.

associated with a macroscopic shape change. The shape change is "trained" into a sample by creating favorable nucleation sites for the transformation through a repeated thermo-mechanical treatment. These sites result in the formation of a small number of martensite variants which transform in a way similar to stress-induced martensite variants. This leads to an accompanying macroscopic "shape" strain under repeated thermal cycling [Delaely et al. 1974].

1.7.5 MECHANICAL FATIGUE

Whenever a shape memory alloy component is subjected to a series of repetitive loads, mechanical fatigue must be considered. Loads are applied to shape memory alloy components in order to obtain pseudoelasticity or the shape memory effect. In the first situation, a stress-induced martensitic transformation occurs, while in the latter one, a pre-existing martensite structure is reoriented. Although martensites in shape memory alloys are thermo-elastic in nature, plastic deformation always accompanies the transformation to some degree. As expected, the accompanying plastic deformation leads to fatigue. It should be noted that in the traditional sense, the "fatigue life" of shape memory alloy components is high compared to their "yield strength". This is due to the fact that the "yield strength" of shape memory alloys is simply a critical transformation stress level, not a stress level which induces damaging plastic deformation. However, in the case of shape memory alloys, researchers are less concerned with the "fatigue life" *per se*. In most cases the degradation of shape memory properties (i.e. recoverable strain levels) is the primary concern. However, it does follow that an increase in the "fatigue life" of an alloy leads to an increase in the "stability of recoverable strains" since both are artifacts of plastic deformation.

In both NiTi [Miyazaki et al. 1986, Sade and Hornbogen 1988] and Cu-Zn-Al [Sade et al. 1985] it has been demonstrated that mechanical cycling decreases the magnitude of recoverable pseudoelastic strains. The level of

degradation is a function of several variables [Sade et al. 1986]: heat treatment, surface condition, crystallographic orientation, test frequency, stress amplitude, test temperature, and stress state. Miyazaki and colleagues [1986] have used thermo-mechanical treatments to improve the stability of recoverable pseudoelastic strains in NiTi. In Cu-Zn-Al, grain-refinement techniques have been used to improve fatigue life and thus increase the stability of recoverable strains [Jansses et al. 1982]. The effect of cycling on pseudoelasticity by martensite reorientation or "rubberlike behavior" has been studied in Cu-Zn-Al [Ahlers and Barcelo 1979]. They determined that mechanical cycling lowered the critical stress level which triggers reorientation, and increased the reorientation stress-strain slope.

Recently work has been completed on the fatigue life of NiTi using a traditional rotating bending apparatus [Tobushi et al. 1997]. Consistent with other studies, this study indicates that the higher the test temperature, the lower the fatigue life. However, the study also concludes that the fatigue life of the NiTi is highly dependent on the resulting phase formed during cycling. Cycling through the R-phase transformation leads to a fatigue life of about 10 million cycles. However, cycling through the full martensitic transformation greatly decreases the fatigue life, depending on the applied strain level. For example, at 2% strain, the fatigue life is about 2000 cycles at room temperature.

1.7.6 THERMAL FATIGUE

Thermal fatigue occurs because of cyclic plastic strains which are induced by cyclic changes in temperature. To obtain plastic deformation in the absence of applied loads, the material of interest must have either a heterogeneous temperature or microstructural distribution which generates internal stress fields. To obtain a heterogeneous temperature distribution a component must be subjected to local heat sources or be rapidly heated or cooled exclusively at the specimen surface. A heterogeneous microstructure

can exist in the case of a polycrystalline body or a material with second phase microstructural constituents. In the case of shape memory alloys, thermal fatigue can occur due to the polycrystalline constraint or second phase constituents (martensites). When a polycrystalline shape memory alloy is heated, the adjacent grains attempt to expand different amounts depending on the crystallographic orientations of the grains. Since compatibility holds the grains together, a temperature dependent internal stress field is created, and the polycrystalline alloy is subjected to thermal fatigue. In the case of martensite formation, the internal stress field is created by a lack of pure "thermo-elastic" martensite formation along with thermal expansion coefficient mismatch between the martensite and the parent phase. In either case the end result is plastic deformation, thermal fatigue, and a subsequent degradation in shape memory properties.

In shape memory alloys, thermal fatigue is a problem during both the one way or two way shape memory effects. In both situations, the temperature is cycled in order to transform a component from the parent phase to the martensitic phase and vice versa. In NiTi Tamura and colleagues [1986] have extensively studied the effect of thermal cycling on the transformation behavior during the two way shape memory effect. They concluded that after 10,000 cycles the recovering force decreased between 5% and 40% depending on the constraint strain level and test temperature. It was also observed that the recovering force decreased much less when the temperature was cycled through the R-phase transformation compared to the martensitic transformation. For the R-phase transition, a linear decrease in the recovering force with the number of cycles was observed while no such relationship was observed for the martensitic relationship. However, although recovering forces due to the martensitic transformation are less stable during thermal cycling, the attainable forces are higher. It should be noted that the above research applies to the two-way shape memory effect. However, the degradation of shape memory properties due to thermal cycling

has also been observed for the one way shape memory effect [Furuya et al. 1992].

The thermal fatigue behavior of Cu-Zn-Al is much more complicated due to martensite stabilization issues (see section 1.6.2). Aside from stabilization problems, the mechanisms of thermal fatigue in Cu-Zn-Al are similar to NiTi. Because of this similarity, thermal fatigue of Cu-Zn-Al will not be covered here. However, there exists recent work on the topic which may be sought after for a deeper understanding of the topic [Thumann and Hornbogen 1988].

1.7.7 STRESS-STATE EFFECTS

There is a shortage of work on stress state effects. This gap in research efforts is most likely due to the fact that the first large scale application of shape memory alloys was in orthodontics [Andreason and Morrow 1978]. The small NiTi wires used in braces provided little motivation for the full scale testing of shape memory alloys under compression or even three dimensional stress states. Currently, there are many new applications which constitute the need for a more thorough understanding of stress state effects on shape memory alloy stress-strain behavior.

The first researchers to note the dependence of stress-induced martensitic transformations on the applied uniaxial stress state were Kulin and colleagues [Kulin et al. 1952]. In this groundbreaking work it was discovered that a higher compressive stress is needed to macroscopically trigger a stress-induced martensitic transformation in steels. Only a year later Burkhart and Read [Burkhart and Read 1953] extended this result to another metal system when they found that the compressive stress at transformation was significantly higher than the tensile stress at transformation in In-Tl single crystals. The first report of different tensile and compressive transformation stress-strain curves for a common polycrystalline shape memory alloy (NiTi) was by Wasilewski [Wasilewski 1971]. Since then there

has been numerous studies which confirm that transformation in tension is favored over compression in several shape memory alloy systems [Lieberman et al 1975, Melton 1990, Vacher and Lexcellent 1991, Chumljakov and Starenchenko 1995, Oregas et al. 1995, Jacobus et al. 1996]. Additionally, it has also been observed that the torsion transformation yield point is well below the tensile point in NiTi [Melton 1990]. Nevertheless, in some alloy systems researchers have found that the applied stress state has little or no effect on the transformation behavior [Nakanishi et al. 1973]. In addition to this, Sakamoto and his colleagues [Sakamoto et al. 1979] have observed that compression is favored over tension in CuAlNi single crystals. Recently Novak et al. [1997] have studied the effect of tension/compression on CuZnAl and determined that different martensitic phases form under tension versus compression.

There are a limited number of experimental investigations which consider the effect of multi-dimensional stress states on martensitic transformations in shape memory alloys. There is some recent experimental work on the bi-axial loading of shape memory alloys [Chu and James 1993]. However, this research does not clearly layout the differences in the transformation stress-strain behavior caused by bi-axial and uniaxial loading states. Most of the research on multi-dimensional stress states focuses on the effect of pure hydrostatic pressure on martensitic transformation behavior. This area of study was sparked by the work of Patel and Cohen some 40 years ago [Patel and Cohen 1953]. Since then, it has been agreed on that hydrostatic pressure alters M_s in both steels [Nishiyama 1978] and shape memory alloys [Kakeshita et al. 1988 and 1992]. In the above research efforts, the hydrostatic pressure was ramped to a specified value, the temperature was cycled, and M_s was determined using resistivity-temperature curves. In the absence of an applied effective stress, it was found that pure hydrostatic pressure decreases M_s for materials exhibiting a positive volume change upon transformation, and increases M_s for materials with a negative volume change. If the pressure is large enough, then the transformation can be triggered without

any effective stress, provided that the M_s temperature is moving towards the test temperature.

The effect of hydrostatic pressure on the effective stress level necessary to induce the transformation can be explained in terms of a Clausius-Clapeyron line in stress-temperature space. If pure hydrostatic pressure exists before an effective stress is applied, then M_s is altered and the Clausius-Clapeyron line is uniformly *shifted* left or right in stress-temperature space. However, regardless of the initial value of the hydrostatic pressure, as an effective stress is applied the hydrostatic pressure may increase, decrease, or not change at all. The effect of hydrostatic pressure has been accounted for in thermodynamically based transformation continuum yield criteria [Sun and Hwang 1991, Boyd and Lagoudas 1996]. Furthermore, it has been shown that the modified yield criteria can be used to develop a Clausius-Clapeyron line with a hydrostatic stress dependent *slope* [Jacobus et al. 1996]. In either case, hydrostatic pressure increases the effective stress necessary for transformation in materials which have positive volume changes during transformation, and decreases the effective stress necessary for transformation in materials which have negative volume changes during transformation. Nevertheless, when comparing some stress states, the macroscopic transformation behavior follows the reverse of the above behavior [Jacobus et al. 1996]. This inconsistency is caused by stress-state dependent crystallographic effects which overshadow the dependence of the transformation behavior on the volume change during the transformation [Patoor et al. 1995].

1.7.8 STRAIN RATE EFFECTS

In shape memory alloys the applied strain (stress) rate influences the transformation behavior. For the most part, increasing the applied strain rate widens the transformation hysteresis [Otsuka et al. 1976], increases the transformation yield point [Mukherjee et al. 1985, Leo et al. 1993, Jacobus et al. 1995], and changes the shape of the transformation stress-strain curve

[Mukherjee et al. 1985, Leo et al. 1993]. There are two fundamental mechanisms which cause strain rate effects: (1) local temperature rises during the "quick" loading of shape memory alloy specimens in the elastic regime, (2) interactions between the nucleation and propagation of phase boundary interfaces and test machine crosshead motion. The former effects have been primarily observed in polycrystalline shape memory alloys specimens, and the latter effects have been observed mostly on single crystals specimens. However, it is clear that both effects might exist in either polycrystals or single crystals depending on the specimen geometry (ability to transfer away latent heat), applied strain rate, applied stress state, and alloy system.

The increase in the transformation yield stress level due to local temperature rises in the specimen is clearly explained using a Clausius-Clapeyron equation (1.7.1 and 1.7.2). Equations 1.7.1 and 1.7.2 state that the change in the critical transformation stress level over the change in temperature is a positive constant. Thus, if the temperature is raised, and the constant on the right hand side remains virtually the same, the critical applied stress level must also increase. The interaction of the transformation with the moving test machine crosshead has been studied by Otsuka et al. [1976]. If the critical resolved shear stress required for nucleation is high and the resulting interface propagation is must faster than the crosshead speed, then the stress strain behavior exhibits upper and lower yield points as in mild steels. In these cases, increasing the strain rate increases the transformation slope and hysteresis since interface motion much match the increased crosshead speed. This can only be accomplished by an increased applied stress level. If the critical resolved shear stress required for nucleation is low and the resulting interface propagation is must slower than the crosshead speed, then the stress strain behavior exhibits a smooth yield point. Since the interface motion is inherently slow, numerous variants must nucleate throughout the specimen length in order to "match" the crosshead speed. If the strain rate is increased, more variants must be activated to keep up with the crosshead, and the same increase in stress levels is necessary.

1.7.9 SINGLE CRYSTALS AND ORIENTATION DEPENDENCE

In engineering applications, polycrystalline samples are preferred due

Alloy (at%)	Researcher	Orientations	Heat Treatments
Ti-50.45%Ni	Chumlyakov 1996-2	[111] [100]	As Quenched
Ti-50.50%Ni	Miyazaki 1984	[111] Many [100] [110]	As Quenched 1 h @ 400°C
Ti-50.80%Ni	Chumlyakov 1996-2	[111] [321] [100] [110]	As Quenched 1h @ 400, 500°C 1.5h400, 15h500°C
Ti-51.00%Ni	Chumlyakov 1995, 1996-2	[111] [100]	As Quenched 1h @ 300 °C, 500 °C
Ti-51.30%Ni	Chumlyakov 1996-2,4	[111] [321] [100]	As Quenched 1h @ 300 °C, 400°C, 500 °C
Ti-Ni-Mo	Chumlyakov 1996-1,4	[111] [321] [100] [110]	As Quenched
Ti-Ni-Fe	Chumlyakov 1996-4	[100]	Not Cited
Ti-Ni-Cu	Chumlyakov 1996-3,4	[111] [100] [110]	As Quenched As Oven Cooled

Table 1.7.1: Summary of the experimental work on NiTi single crystals. The times and temperatures cited under heat treatments are aging treatments after quenching.

to their low cost and isotropic deformation behavior. However, the mechanical behavior of single crystals is still of great interest to the research community since single crystals allow for the intense study of the underlying

deformation phenomenon. In the case of shape memory alloys, it has been demonstrated that the transformation stress-strain behavior is dependent on the applied stress state. For example, in polycrystalline NiTi and CuZnAl the critical stress level required to trigger a perceivable transformation is always greater in compression versus tension [Jacobus 1996]. In single crystals, the transformation stress level depends not only on the applied stress state, but also on the crystallographic orientation of the test sample [Miyazaki et al. 1984, Chumlyakov et al. 1995, 1996-1,2,3,4]. The microscopic transformation behavior of single crystals and polycrystals only differs due to internal stress and strain fields caused by crystallographic misorientations. In the simplest case, the macroscopic deformation behavior of polycrystalline materials can be estimated by averaging the single crystal stress-strain response over all possible orientations. With this, it is clear that studying the orientation dependence of single crystal shape memory alloys can help explain stress-state effects in polycrystalline shape memory alloys.

There have been several experimental studies which focused on the orientation dependence of the deformation behavior of NiTi single crystal shape memory alloys. Chumlyakov and colleagues have studied the tensile and compressive behavior of aged and as quenched NiTi single crystals with several compositions and alloying elements (table 1.7.1). In all of the alloy systems listed in table 1.7.1 it has been found that aging time, orientation, test temperature, and loading direction all have a profound effect on transformation behavior. Most of the results from Chumlyakov's papers are qualitative, and it is appropriate here to summarize some of his findings. In general, the [111] orientation deforms in a very ductile manner, with extremely large transformation strains. Conversely, the [100] orientation is very brittle, showing little or no evidence of transformation [Chumlyakov et al. 1996-1]. The magnitude of ductility for a specific orientation increases as test temperature is increased, while the recoverable pseudoelastic or shape memory strain decreases [Chumlyakov et al. 1996-2]. In addition, the critical transformation stress level increases with increasing test temperature.

The effect of different aging treatments on the transformation behavior of NiTi single crystals is quite unique. For example, after some aging treatments the R-phase transformation is observed, while in others it not [Chumlyakov et al. 1996-2]. At any rate, Chumlyakov and colleagues have concluded that intermediate aging temperatures and times (1-1.5 hour @ 400-500°C) lead to a decrease in the orientation dependence of the critical transformation stress level and a weakening of the tension-compression asymmetry of any particular orientation. Additionally, intermediate aging treatments lead to the appearance of pseudoelasticity which is not observed in as quenched crystals (they demonstrate shape memory properties). If the crystals are overaged, then shape memory again replaces pseudoelasticity [Chumlyakov et al. 1996-2]. Although the above results are extremely valuable, it is still necessary to better “quantify” the orientation dependence of NiTi single crystals. At this point it is not clear precisely what treatments are “optimum” for which alloy compositions. Miyazaki et al. [1984] have also studied the strain recoverability of Ti-50.5at%Ni single crystals subjected to an aging treatment of 400°C for 1 hour. However, they have not mentioned that any of the crystals tested demonstrated pseudoelasticity. Finally, it is also important that the response of polycrystalline samples with the same heat treatments is critically compared to the single crystal results.

There has also been some recent work on the mathematical modeling of the transformation behavior of single crystal NiTi [Cizek 1989, Buchheit and Wert 1994, 1996]. One of the latter models [Buchheit and Wert 1996] is the most comprehensive since it considers both the parent to martensite transformation (the phenomenological theory of martensitic transformations), and reorientation (detwinning) effects. All of the models do predict that the [111] orientation has the largest resulting transformation strain. To obtain the largest transformation strain the [111] orientation must have a variant oriented with a Schmid factor larger than the other orientations, thus resulting in the lowest transformation stress level. This is consistent with experimental observations. However, the mathematical

models do not include the interaction between martensite formation and accommodating plasticity. Crystallographic orientations which have a lack of slip systems to accommodate the martensite formation may fail in a brittle manner. Modeling of the transformation has also proved difficult since the pre-martensitic R-phase transformation occurs after some heat treatments.

1.7.10 PHASE BOUNDARY MOTION

At the electron microscope resolution level, a martensitic transformation always proceeds through the propagation of a parent/martensite interface [Saburi and Nenno 1986, Xu et al. 1995]. However, in some cases the transformation proceeds through a "macroscopic" propagation of the parent/martensitic phase interface. This type of transformation is commonly called phase boundary motion, and it has been observed in NiTi polycrystals [Jacobus 1986, Shaw and Kyriakides 1997] and single crystals [Chumlyakov et al. 1995] and in Cu-based single crystals [Otsuka et al. 1976]. In polycrystals, macroscopic phase boundary motion results in a stress strain curve which is characterized by a flat transformation slope. In single crystals the stress strain curve usually demonstrates upper and lower yield points and a very jagged transformation slope.

The occurrence of macroscopic phase boundary motion is also dependent on the applied strain rate. At extremely fast strain rates the macroscopic phase boundary motion may not occur due to the formation of many parent/martensite interfaces [Otsuka et al. 1976, Shaw and Kyriakides 1997]. Additionally, most of the studies to date have focused on the tensile stress states, thus it is not certain if phase boundary motion occurs under compression. It is also interesting to note that phase boundary motion does not occur in CuZnAl polycrystals under tension or compression [Jacobus et al. 1986].

REFERENCES

- Abujudom D N, Thoma P E, and Fariabi S, "The effect of Cold Work and Heat Treatment on the Phase Transformations of Near Equiatomic NiTi Shape Memory Alloy," *ICOMAT - 89*, pp. 565 - 70, 1989.
- Adachi K, Perkins J, Wayman C M, "Type II twins in self-accommodating martensite plate variants in a Cu-Zn-Al shape memory alloy.," *Acta Metall.*, vol 34, no 12, pp. 2471-85, 1986.
- Adachi K, Perkins J, Wayman C M, "The crystallography and boundary structure of interplate-group combinations of 18R martensite variants in Cu-Zn-Al shape memory alloys.," *Acta Metall.*, vol 36, no 5, pp. 1343-64, 1988.
- Adachi Y, Wade N, Hosoi Y, "Effect of hydrogen on the shape memory effect and transformation behavior of Ti-Ni alloy.," *J. Jpn. Inst. Met.*, vol 54, no 5, pp. 525-31, 1990.
- Ahlers M and Barcelo G, "The influence of Cycling on the Rubberlike behavior in CuZnAl Martensite," *ICOMAT - 79*, pp. 649, 1979.
- Amengual A, Garcias F, Marco F, Segui C, Torra V, "Acoustic emission of the interface motion in the martensitic transformation of Cu-Zn-Al shape memory alloy.," *Acta Metall.*, vol 36, no 8, pp. 2329-34, 1988.
- Andreason G F and R. E. Morrow, *Am. J. Orth.*, vol. 73, pp. 142, 1978.
- Bain E C, *Trans. Am. Soc. Steel Treat.*, vol. 8, pp. 14, 1925.
- Banerjee M K S, "The self-accommodating morphology of NiTi shape memory alloy martensite.," *Scr. Metall. Mater.*, vol 24, no 12, pp. 2291-6, 1990.
- Barcelo G, M. Ahlers and R. Rapacioli, "The Stress-Induced Phase Transformation in Martensitic Single Crystal of Cu-Zn-Al Alloys," *Z. Metallkde*, vol. 70, pp. 732, 1979.
- Bataillard L, Gotthardt R, "Influence of thermal treatment on the appearance of a three step martensitic transformation in NiTi.," *J. Phys. IV, Colloq.*, vol 5, no C8, pt 2, pp. 647-52, 1995.
- Beyer J, Brakel R A, and Lloyd J R T, "Precipitation Process in NiTi near Equiatomic Alloy," *ICOMAT - 86*, pp. 703 - 8, 1986.
- Boyd J G and D.C. Lagoudas, *Int. J. Plasticity*, vol. 12-6, 805, 1996 .

- Boyd J G and D.C. Lagoudas, *Int. J. Plasticity*, vol. 12-7, 843, 1996 .
- Buchheit T E, Wert J A, "Modeling the Effects of Stress State and Crystal Orientation on the Stress-Induced Transformation of NiTi Single Crystals," *Metall. Mater. Trans. A*, vol 25 A, no 2, pp. 2383-2389, 1994.
- Buchheit T E, Wert J A, "Predicting the orientation-dependent stress-induced transformation and detwinning response of shape memory alloy single crystals.," *Metall. Mater. Trans. A*, vol 27A, no 2, pp. 269-79, 1996.
- Buehler W J, Gilfrich J V, and Wiley R C, "Effect of Low-Temperature Phase Changes on the Mechanical Properties of Alloys near Composition NiTi," *J. Appl. Phys.*, vol. 34, pp. 1475, 1963.
- Burkart M W and Read T A, *Trans. Met. Soc. AIME*, vol. 197, 1516, 1953 .
- Chang L C and Read T A, *Trans. AIME*, vol. 191, pp. 47, 1951.
- Chernenko V A, Babii O M, Kokorin V V, Lotkov A I, Grishkov V N, "Martensitic transformations in NiTi-based alloys under high hydrostatic pressures.," *Phys. Met. Metallogr.*, vol 81, no 5, pp. 549-52, 1996.
- Chu C and R.D. James, *Experiments in Smart Materials and Structures*, AMD vol. 181, 61, 1993 .
- Chumljakov J I, Starenchenko S V, "Stress induced martensitic transformation in aged titanium nickel single crystals.," *J. Phys. IV, Colloq.*, vol 5, no C8, pt 2, pp. 803-7, 1995.
- Chumlyakov Y I, Surikova N S, Korotaev A D, "Orientation Dependence of Strength and Plasticity of Titanium Nickelide Single Crystals," *Phys. Met. Metall.*, vol. 82, pp. 102-9, 1996-1.
- Chumlyakov Y I, Kireeva I V, Lineytsev V N, and Chepel E V, "Aging influence on the shape memory effects and Superelasticity in Titanium-Nickel Singel crystals," Siberian Physical Technical Institute Report, 1996-2.
- Chumlyakov Y I, Kireeva I V, Zuev Y I, and Lyisyuk A G, "Shape memory effect and pseudoelasticity in Ti-40%Ni-10%Cu (at%) single crystals," Siberian Physical Technical Institute Report, 1996-3.
- Chumlyakov Y I, Kireeva I V, Lineytsev V N, Chepel E V, Zuev Y I, Lyisyuk A G, and Surikova N S "Shape memory effect and superelasticity in NiTi single crystals," Siberian Physical Technical Institute Report, 1996-4.

Cizek P, "Orientation dependence of reversible strain in the shape memory effect in NiTi alloy.," *Met. Mater.* vol 27, no 1, pp. 52-6, 1989.

Cohen M, Machlin E S, Paranjpe V G., "Thermodynamics of the Martensitic Transformation, *Thermodynamics in Physical Metallurgy*, ASM, pp. 242-70, 1950.

Cohen M, G.B. Olsen and PP.C. Clapp, "On the Classification of Displacive Phase Transformations," *Proceedings, International Conference on Martensitic Transformations*, Cambridge, Mass., pp.1, 1979.

Delaey L, V. Krishnan, H. Tas and H. Warlimont, "Review: Thermoelasticity, pseudoelasticity and the memory effects associated with martensitic transformations, part 1 structural and microstructural changes associated with the transformations," *J. Mat. Sci.*, vol. 9, pp. 1521 - 35, 1974.

Delaey L, V. Krishnan, H. Tas and H. Warlimont, "Review: Thermoelasticity, pseudoelasticity and the memory effects associated with martensitic transformations, part 2 the macroscopic mechanical behavior," *J. Mat. Sci.*, vol. 9, pp. 1536 - 44, 1974.

Delaey F, J. Van Humbeeck, M. Chandraesederan, J. Janssen, M. Andrade, and N. Mwamba, "The Cu-Zn-Al Shape Memory Alloys," *Metals Forum*, vol. 4, pp. 164, 1981.

Dunne D P and N. F. Kennon, "Ageing of Copper-Based Shape Memory Alloys" *Metals Forum*, vol 4, pp. 176, 1981.

Enami K, Hara M, Maeda H, "Effect of W addition on the martensitic transformation and shape memory behaviour of the TiNi-base alloys.," *J. Phys. IV, Colloq.*, vol 5, no C8, pt 2, pp. 629-33, 1995.

Filip P, Rusek J, Mazanec K, "The effect of heat treatment on the structural stability of TiNi alloys.," *Z. Met.kd.*, vol 82, no 6, pp. 488-91, 1991.

Filip P, Mazanec K, "Influence of work hardening and heat treatment on deformation behaviour of TiNi shape memory alloys.," *Scr. Metall. Mater.*, vol 32, no 9, pp. 1375-80, 1995.

Fukuda T, Saburi T, Doi K, Nenno S, "Nucleation and self-accommodation of the R-phase in Ti-Ni alloys.," *Mater. Trans. JIM*, vol 33, no 3, pp. 271-7, 1992.

Furuya Y, Yun Chul Park, "Thermal cyclic deformation and degradation of shape memory effect in Ti-Ni alloy.," *Nondestruct. Test. Eval.* vol 8-9, pp. 541-54, 1992.

- Goldstein D M, Naval Ordnance Lab Technical Report # 64-235, 1965.
- Han Y S, Kim Y G, "The effects of boron and aging on mechanical properties and martensitic temperatures in Cu-Zn-Al shape-memory alloys," *Scr. Metall.*, vol 21, no 7, pp. 947-52, 1987.
- Hehemann R F and G.D. Sandrock, "Relation Between the PreMartensitic Instability and the Martensitic Structure in TiNi," *Scripta Met.* vol. 5, pp. 801, 1971.
- Hodgson D E, M.H. Wu and R.J. Biermann, "Shape memory alloys," ASM Handbook, vol. 2, pp. 897, 1990.
- Honma T, "The Effect Aging on the Spontaneous Shape Change and the All-Round Shape Memory Effect in Ni-Rich TiNi Alloy," *ICOMAT-86*, pp. 709 - 16, 1986.
- Hoshiya T, Den S, Katsuta H, Ando H, "Effect of hydrogen on transformation characteristics and deformation behavior in a TiNi shape memory alloy.," *J. Jpn. Inst. Met.*, vol 56, no 7, pp. 747-56, 1992.
- Humbecck J V and Planes A, "On the interpretation of differential scanning calorimetry results for thermoelastic martensitic transformations: athermal versus thermally activated kinetics," *Scr. Metall.* , vol. 34, pp1357-60, 1996.
- Ilyin A A, Kollerov M Yu, Mamonov A M, Krastilevsky A A, Makarenkov D Yu, "Hydrogen influence on martensitic transformation and shape memory effect in titanium alloys.," *J. Phys. IV, Colloq.*, vol 5, no C8, pt 2, pp. 1145-50, 1995.
- In Sang Chung, Kyeung Chae Park, Seoung Lee, "Changes of shape memory ability, microstructure and crystal structure by thermal cycling in Cu-Zn-Al shape memory alloy.," *J. Korean Inst. Met.*, vol 26, no 11, pp. 1013-20, 1988.
- Ishida A, Sato M, Takei A, Miyazaki S, "Effect of heat treatment on shape memory behavior of Ti-rich Ti-Ni thin films.," *Mater. Trans. JIM*, vol 36, no 11, pp. 1349-55, 1995.
- Ishida A, Sato M, Takei A, Nomura K, Miyazaki S, "Effect of aging on shape memory behavior of Ti-51.3 at. pct Ni thin films.," *Metall. Mater. Trans. A*, vol 27A, no 12, pp. 3753-9, 1996.
- Jacobus J K, "An experimental investigation of the effect of stress state on the stress-induced martensitic transformation in Cu-Zn-Al and Ni-Ti shape memory alloys," PhD Thesis, University of Illinois, 1995 .

Jacobus K, Sehitoglu H, Balzer M, "Effect of stress state on the stress-induced martensitic transformation in polycrystalline Ni-Ti alloy.," *Metall. Mater. Trans. A*, vol 27A, no 10, pp. 3066-73, 1996.

Jansses J, Willems F, Verelst B, Maertens J, and Delaey L., *ICOMAT-82*, pp. 809, 1982.

Kaneko K, Uehara M, Aoki H, Kubo M, Suzuki T, Yoshida A, "Effects of composition and heat treatment on shape memory effect of a Ni-Ti alloy.," *J. Soc. Mater. Sci. Jpn.*, vol 42, no 480, pp. 1103-8, 1993.

Kakeshita T, Y. Yoshimura, K. Shimizu, S. Endo, Y. Akahama and F.E. Fujita, *Trans. JIM*, 29, 781, 1988 .

Kakeshita T, Shimizu K, Nakamichi S, Tanaka R, Endo S, Ono F, "Effect of hydrostatic pressures on thermoelastic martensitic transformations in aged Ti-Ni and ausaged Fe-Ni-Co-Ti shape memory alloys.," *Mater. Trans. JIM*, vol 33, no 1, pp. 1-6, 1992.

Kulin S A, M. Cohen, and B.L. Averbach, "Effect of Applied Stress on the Martensitic Transformation," *J. Metals.* , vol. 4, pp. 661, 1952.

Lee J S, Wayman C M, "Grain refinement of Cu-Zn-Al shape memory alloys.," *Metallography.*, vol 19, no 4, pp. 401-19, 1986.

Legresy J M, Prandi B, Raynaud G M, "Effects of cold-rolling and post-deformation annealing on the martensitic transformation of a TiNi shape memory alloy.," *J. Phys. IV, Colloq.*, vol 1, no C4, pp. 241-6, 1991.

Leo P H, Shield T W, Bruno O P, "Transient Heat Transfer Effects on the Pseudoelastic behavior of Shape Memory Wires," *Acta. Metall.*, vol. 41, pp. 2477, 1993.

Lieberman D S, M.A. Schmerling and R.W. Karr, Shape Memory Effects in Alloys, J. Perkins, Ed., Plenum Press, 203, 1975 .

Lu X Y, Cao M S, "Step Quenching of A Cu-Zn-Al shape memory alloy-discussion of stabilization of martensite," *ICOMAT - 86*, pp. 856, 1986.

Madangopal K, Singh J, Banerjee S, "Self-accommodation in Ni-Ti shape memory alloys.," *Scr. Metall. Mater.*, vol 25, no 9, pp. 2153-8, 1991.

Madangopal K, Tiwari R, Banerjee S, "Microscopic self-accommodation in shape memory alloy martensites.," *Scr. Metall. Mater.*, vol 28, no 8, pp. 991-6, 1993.

Melton K N, Engineering Aspects of Shape Memory Alloys, Michigan State University, USA, Eds. T. W. Duerig, K. N. Melton, D. Stockel and C.M. Wayman, 21, 1990 .

Mertmann M, Bracke A, Hornbogen E, "Influence of the thermal treatment on the stability of partially constrained recovery of NiTi actuator wire.," *J. Phys. IV, Colloq.*, vol 5, no C8, pt 2, pp. 1259-64, 1995.

Min Piao, Miyazaki S, Otsuka K, Nishida N, "Effects of Nb addition on the microstructure of Ti-Ni alloys.," *Mater. Trans. JIM*, vol 33, no 4, pp. 337-45, 1992.

Miyazaki S, Kimura S, Otsuka K, Suzuki Y, "The habit plane and transformation strains associated with the martensitic transformation in Ti-Ni single crystals," *Scr. Metall.*, vol. 18, pp. 883-8, 1984.

Miyazaki S and Ohtsuka K, Shape Memory Alloys, Ed. Funakubo H, Gordon and Breach Science, 1988.

Miyazaki S, T. Imai, Y. Igo, and K. Otsuka, "Effect of Cyclic Deformation on the Pseudoelastic Character of Ti-Ni Alloys," *Met. Trans. A* , vol. 17A, pp. 115, 1986.

Morris A, Lipe T, "Comments on the interpretation of differential scanning calorimetry results for thermoelastic martensitic transformations: athermal versus thermally activated kinetics.," *Scr. Mater.*, vol 34, no 9, pp. 1361-3, 1996.

Mukherjee K, Sircar S, Dahotre N B, "Thermal Effects Associated with Stress-Induced Martensitic Transformation in a Ti-Ni Alloy," *Mater. Sci. Eng.*, vol. 74, pp. 75, 1985 .

Mura T, Mori T, Kato M, "The Elastic Stress Field Caused by a General Ellipsoidal Inclusion and the Application to Martensite Formation," *Mech. Phys. Solids*, vol. 24, pp. 303 - 18, 1976.

Nagasawa A, "Crystallography of the Ni-Ti Alloy System," *J. Phys. Soc. Jpn.* vol. 29, pp. 1386, 1970.

Nakanishi N, T. Mori, S. Miura, Y. Murakami and S. Kachi, *Phil. Mag.*, vol. 28, 277, 1973 .

Nakata Y, Yamamoto O, Shimizu K, "Effect of aging in Cu-Zn-Al shape memory alloys.," *Mater. Trans. JIM*, vol 34, no 5, pp. 429-37, 1993.

Nishiyama Z and S. Kajiwara, "Stress-Induced Martensitic Transformation in Cu-Zn-Al Alloys," *Japp. J. Appl. Phys.*, vol. 2, pp. 478, 1963.

- Nishiyama Z, Martensitic Transformation, Academic Press, 1978 .
- Nishida M, Wayman C M, Honma T, "Precipitation processes in near-equiatomic TiNi shape memory alloys.," *Metall. Trans. A.*, vol 17A, no 9, pp. 1505-15, 1986.
- Nishida M, Wayman C M, "R-phase type transformation of Ti₂Ni₃ precipitates in aged Ti-52at%Ni," *ICOMAT - 86*, pp. 653-658, 1986.
- Nishida M, Wayman C M, "Electron microscopy studies of the 'premartensitic' transformations in an aged Ti-51 at.%Ni shape memory alloy.," *Metallography.*, vol 21, no 3, pp. 255-73, 1988.
- Nishida M, Wayman C M, Chiba A, "Electron microscopy studies of the martensitic transformation in an aged Ti-51 at.%Ni shape memory alloy.," *Metallography.*, vol 21, no 3, pp. 275-91, 1988.
- Novak V, Sittner P, Zarubova N, "Anisotropy of Transformation Characteristics of Cu-Base Shape Memory Alloys," *To be published Mat. Sci. Eng. A*, 1997.
- Orgeas L, Favier D, "Non-symmetric tension-compression behaviour of NiTi alloy.," *J. Phys. IV, Colloq.*, vol 5, no C8, pt 2, pp. 605-10, 1995.
- Otsuka K, T. Sawamura and K. Shimizu, "Crystal Structure and Internal Defects of Equiatomic TiNi Martensite," *Phys. Status Solidi, a* vol. 5, pp. 457, 1971.
- Otsuka K, Wayman C M, Nakai K, Sakamoto H, Shimizu K, "Superelasticity and Stress-Induced Martensitic Transformations in Cu-Al-Ni alloys," *Acta. Metall.*, vol. 24, pp. 207-226, 1976.
- Otsuka K, Sakamoto H, Shimizu K, *Acta. Metall.*, vol. 27, pp. 585, 1979.
- Otsuka K and K. Shimizu, "Pseudoelasticity", *Metals Forum*, vol 4, pp. 142, 1981.
- Otsuka K and K. Shimizu, "Pseudoelastic Effects in Cu-Zn Single Crystals," *Int. Metals Review* , vol 31, pp. 93, 1986.
- Otsuka K, "Introduction to the R-Phase Transition," Engineering Aspects of Shape Memory Alloys, pp. 36-45, 1990.
- Paio M, Miyazaki S, Otsuka K, Nishida N, "Effects of Nb additions on the microstructure of Ti-Ni alloys," *Mat. Trans. JIM*, vol. 33, pp. 337-45, 1992.

- Patel J R and M. Cohen, "Criterion for the Action of Applied Stress in the Martensitic Transformation," *Acta Met.*, vol. 1, pp. 531, 1953.
- Patoor E, El Amrani M, Eberhardt A, Berveiller M, "Determination of the origin for the dissymmetry observed between tensile and compression tests on shape memory alloys," *J. Phys. IV*, vol 5, no C2, pp. 495-500, 1995.
- Perkins J, "Ti-Ni and Ti-Ni-X Shape Memory Alloys," *Metals Forum*, vol. 4, pp. 153, 1981.
- Rapacioli R and M. Ahlers, "Ordering in Ternary β Phase Cu-Zn-Al Alloys," *Scripta Met.*, vol 11 pp. 1147, 1977.
- Reynolds J E, Bever M B, *Trans. Met. Soc. AIME*, vol. 194, pp. 1065, 1952.
- Saburi T and Nenno S, "In situ observations of the nucleation and growth of the thermoelastic martensite in a Ti-Ni-Cu alloy," *ICOMAT-86*, pp. 671-8, 1986.
- Sade M, R. Rapacioli, M. Ahlers, "Fatigue in Cu-Zn-Al Single Crystals," *Acta. Met*, vol 33, pp. 487, 1985.
- Sade M, Lovey F C, Ahlers M, "Fatigue in CuZnAl Single Crystals Stressed in Compression," *ICOMAT-86*, pp. 934, 1986.
- Sade M, Hornbogen E, "Fatigue of single and polycrystalline beta -CuZn-base shape memory alloys," *Z. Met.kd.*, vol 79, no 12, pp. 782-7, 1988.
- Sakamoto H, M. Tanigawa, K. Otsuka and K. Shimizu, Proceedings International Conference on Martensitic Transformations, ICOMAT 79, Cambridge, MA, 633, 1979 .
- Sadrnezhaad K, Mashhadi F, Sharghi R, "Heat treatment of Ni-Ti alloy for improvement of shape memory effect," *Mater. Manuf. Process.*, vol 12, no 1, pp. 107-15, 1997.
- Schroeder T A and C.M. Wayman, "Pseudoelastic Effects in Cu-Zn Single Crystals," *Acta Met.*, vol. 27, pp. 405, 1979.
- Shaw J A, Kyriakides S, "On the nucleation and propagation of phase transformation fronts in a NiTi alloy," *Acta Mater.*, vol 45, no 2, pp. 683-700, 1997.
- Shimizu K, Tadaki T, Shape Memory Alloys, Ed. Funakubo H, Gordon and Breach Science, 1988.

Stroz D, Kwarciak J, Morawiec H, "Effect of ageing on martensitic transformation in NiTi shape memory alloy.," *J. Mater. Sci.* vol 23, no 11, pp. 4127-31, 1988.

Sun Q P and K. C. Hwang, *J. Mech. Phys. Solids*, vol. 39, pp. 507, 1991 .

Tadaki T, M. Tokoro and K. Shimizu, "Thermoelastic Nature and Crystal Structure of the Cu-Zn Martensite Related to the Shape Memory," *Trans. JIM* vol. 16, pp. 285, 1975.

Tadaki T, Nakata Y, Shimizu K, "Occupancy Sites of Constituent Atoms and their Effects on the Martensitic Transformations in some Cu-Based and NiTi-Based Ternary Alloys.," *J. Phys. IV, Colloq.*, vol 5, no C8, pt 2, pp. 81-90, 1995.

Tamura H, Suzuki Y, Todoroki T, "Fatigue Properties of NiTi Alloy in Thermal Cycling Mode," *ICOMAT-86*, pp. 736, 1986.

Tas H, Delaey L, Deruyttere, A, *Met Trans*, vol. 4, pp. 2833, 1973.

Thoma P E, Angst D R, Schachner K D, "The effect of cold work, heat treatment, and composition on the austenite to R-phase transformation temperature of Ni-Ti shape memory alloys.," *J. Phys. IV, Colloq.*, vol 5, no C8, pt 2, pp. 557-62, 1995.

Thumann M, Hornbogen E, "Thermal and mechanical fatigue in Cu-base shape memory alloys.," *Z. Met.kd.* vol 79, no 2, pp. 119-26, 1988.

Tobushi H, Tanaka K, Hori T, Sawada T, Hattori T, "Pseudoelasticity of TiNi shape memory alloy dependence on maximum strain and temperature .," *JSME Int. J. A, Mech. Mater. Eng.*, vol 36, no 3, pp. 314-18, 1993.

Tobushi H, Hachisuka T, Yamada S, Lin P H, "Rotating-Bending Fatigue of a NiTi Shape Memory Alloy Wire," *ICF-9*, pp. 1741, 1997.

Todoroki T, Tamura H, "Effect of heat treatment after cold working on the phase transformation in TiNi alloy.," *Trans. Jpn. Inst. Met.*, vol 28, no 2, pp. 83-94, 1987.

Treppmann D, Hornbogen E, Wurzel D, "The effect of combined recrystallization and precipitation processes on the functional and structural properties in NiTi alloys.," *J. Phys. IV, Colloq.*, vol 5, no C8, pt 2, pp. 569-74, 1995.

Vacher P and C. Lexcellent, Proceedings, Mechanical Behavior of Materials IV, VI, USA, ed. M. Jono , Plenum Press, 231, 1991 .

- Van Humbeeck J, Planes A, "On the Interpretation of Differential Scanning Calorimetry Results for Thermoelastic Martensitic Transformations: Athermal Versus Thermally Activated Kinetics.," *Scr. Mater.*, vol 34, no 9, pp. 1357-60, 1996.
- Wade N, Adachi Y, Hosoi Y, "A role of hydrogen in shape memory effect of Ti-Ni alloys.," *Scr. Metall. Mater.*, vol 24, no 6, pp. 1051-5, 1990.
- Wang F T, Chen F X, Wei Z G, Yang D Z, "The effects of microelements on the grain refining and the grain growth behaviors of Cu-Zn-Al shape memory alloy.," *Scr. Metall. Mater.*, vol 25, no 11, pp. 2565-70, 1991.
- Wasilewski R J, "Stress-Assisted Martensite Formation in NiTi," *Scripta Met*, vol. 5, pp. 127-30, 1971.
- Wasilewski R J, "The effect of Applied Stress on the Martensitic Transformation in NiTi," *Met. Trans. A*, vol. 2, pp. 2973-81, 1971.
- Wasilewski R J, "The 'Yield' Behavior of Stoichiometric TiNi Across the Martensitic Transformation Range ," *Scripta Met*, vol. 5, pp. 131-36, 1971.
- Wayman C M and Shizmizu K, *Met. Sci.*, vol. 6, pp. 175, 1972.
- Wayman C M, *J. Metals*, vol. 32, pp. 129, 1980.
- Wayman C M, "The Shape Memory Effect" *Metals Forum*, vol 4, pp. 135, 1981.
- Wollants P, De Bonte M, Roos, J, *Z. Metallkde*, vol. 70, pp. 113, 1979.
- Wu, M H "Cu-Based Shape Memory Alloys," Engineering Aspects of Shape Memory Alloys, pp. 69-88, 1990.
- Wu S K, Wayman C M, "Interstitial ordering of hydrogen and oxygen in TiNi alloys.," *Acta Metall.*, vol 36, no 4, pp. 1005-13, 1988.
- Wu S K, Wayman C M, "On the reciprocal lattice of the 'premartensitic' R-phase in TiNi shape memory alloys.," *Acta Metall.*, vol 37, no 10, pp. 2805-13, 1989.
- Wu X Z, Wang S D, Zhang J P, Su H Q, Jin J L, Zhang J G, "Transformation characteristics of aged NiTi shape memory alloy obtained by rapid solidification.," *Scr. Metall. Mater.*, vol 31, no 1, pp. 53-6, 1994.

Xie C Y, Zhao L C, Lei T C, "Effect of precipitates on the electrical resistivity-temperature curves in an aged Ti-51.8 at.% Ni shape memory alloy.," *Scr. Metall.*, vol 23, no 12, pp. 2131-6, 1989.

Xie C Y, Zhao L C, Lei T C, "Effect of Ti_3Ni_4 precipitates on the phase transitions in an aged Ti-51.8 at.% Ni shape memory alloy.," *Scr. Metall. Mater.*, vol 24, no 9, pp. 1753-8, 1990.

Xu Y B, Wang R J, Wang Z G, "In-situ investigation of stress-induced martensitic transformation in the Ti-Ni shape memory alloy during deformation.," *Mater. Lett.*, vol 24, no 6, pp. 355-8, 1995.

Yang J H, Wayman C M, "On secondary variants formed at intersections of in martensite variants.," *Acta Metall. Mater.*, vol 40, no 8, pp. 2011-23, 1992.

CHAPTER 2: EXPERIMENTAL TECHNIQUES

PREVIEW

Experimental techniques related to the preparation and mechanical testing of shape memory alloy specimens are discussed. Miniature polycrystalline and single crystal specimens were uniaxially loaded using a small scale testing apparatus. The apparatus was also equipped with heating and cooling sources in order to run tests at low and high temperatures. A unique triaxial test machine was used to apply three dimensional stress states to single crystal and polycrystalline samples. The preparation of samples for microscopy was accomplished using mechanical, chemical, and electrochemical methods. The heat treatment of the alloys was performed in evacuated quartz tubes.

2.1 SMALL SCALE TEST EQUIPMENT

The necessity of a small scale testing apparatus was due to the fact that the single crystal specimens had to be cut (sometimes transversely) from a long cylindrical single crystal which was about 30 mm in diameter. The mechanical test machine employed was a screw driven ATS run by a SOMAT controller capable of running in stress, strain, or displacement control modes. To properly measure the small testing loads, the ATS machine was equipped with 1010-AF Interface load cell (2500 pound load limit). The setup of the small scale testing device is shown in figure 2.1.1. At the top of the picture the load cell (cylindrical shaped with bolts) is hardly visible, while at the bottom of the picture, the light colored cylindrical actuator is clearly in view. Directly connected to the load cell and actuator are Universal double taper collet chucks. The collet chucks were incorporated to hold small scale mechanical grips (figures 2.1.2 and 2.1.3) instead of connecting the small scale

grips directly to the actuator and load cell. If the small scale grips were

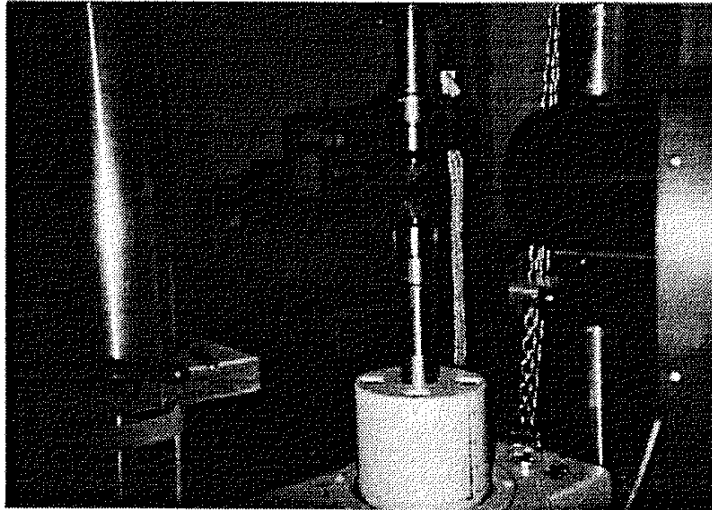


Figure 2.1.1: Picture of the small scale testing machine.

threaded directly to the load cell and the actuator, then the grips could not be rotationally aligned without depending on thread position for alignment. Additionally, the double taper collets allow the collet chuck to effectively hold the small scale grips designed to apply either tensile (figure 2.1.2) or compressive (figure 2.1.3) loads.

The small mechanical grips are shown in figures 2.1.2 and 2.1.3. The tension sample grips are designed to clamp and test a thin flat specimen, while the compressive grips simply crush a rectangular specimen. Both grips were designed to be held at the bottom by a 7/16 inch collet so that they could be used in any test machine that is already equipped with a cylindrical specimen gripping system. The small scale grips were made from a 17-4 precipitation hardened stainless steel available from Jorgensen Steel. The grips were machined in the annealed state and subsequently aged for 1 hour @ 482 °C. The small grips were then air cooled to obtain a final average Rockwell C hardness of about 44 (yield strength of about 1400 MPa).

The basic design of the grips was adapted from various research reports

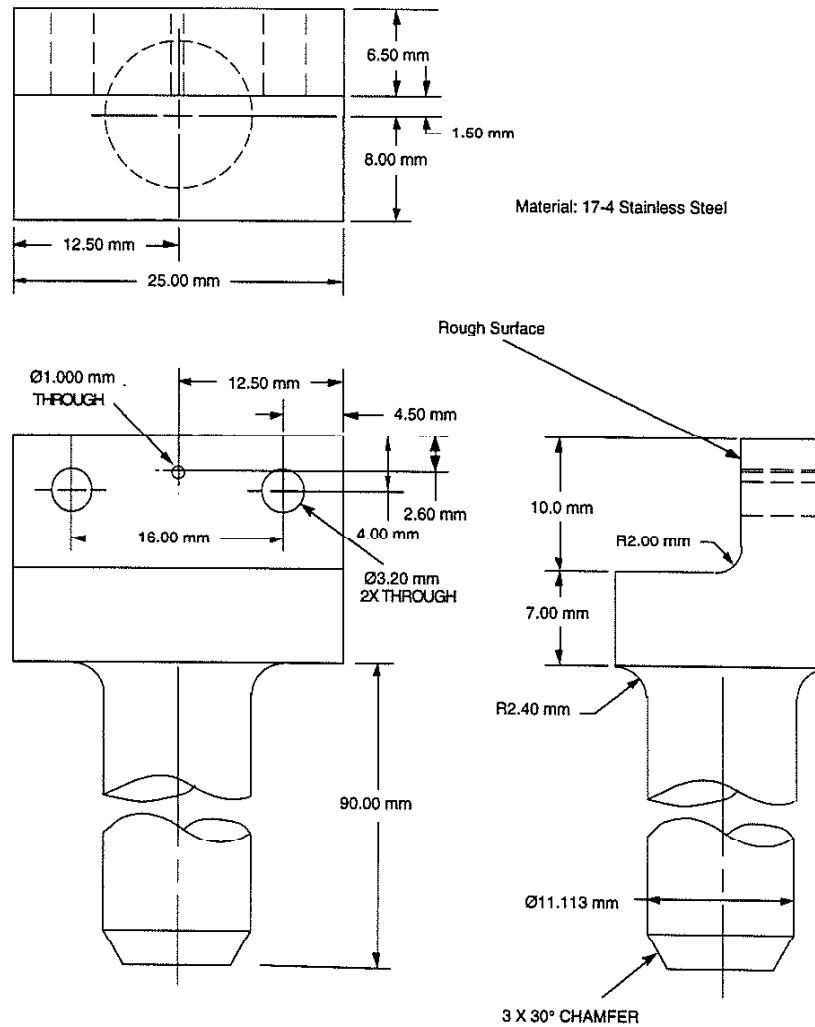


Figure 2.1.2: Small scale specimen grips used for tensile testing. The connecting clasp is not show.

of the ASTM E-10 Committee on Nuclear Technology and Applications. In the nuclear materials testing industry the specimens must be kept extremely small (~ 3mm long) to avoid excessive human radiation exposure. The primary concern of small scale testing is related to the alignment of the small specimens. For tensile specimens, most researchers used pins to align the specimens. Conversely, the compressive gripping systems were normally

“self aligning” since the compressive blocks have more freedom than the clamped tensile specimens. For the tensile grips, the pin/hole approach was

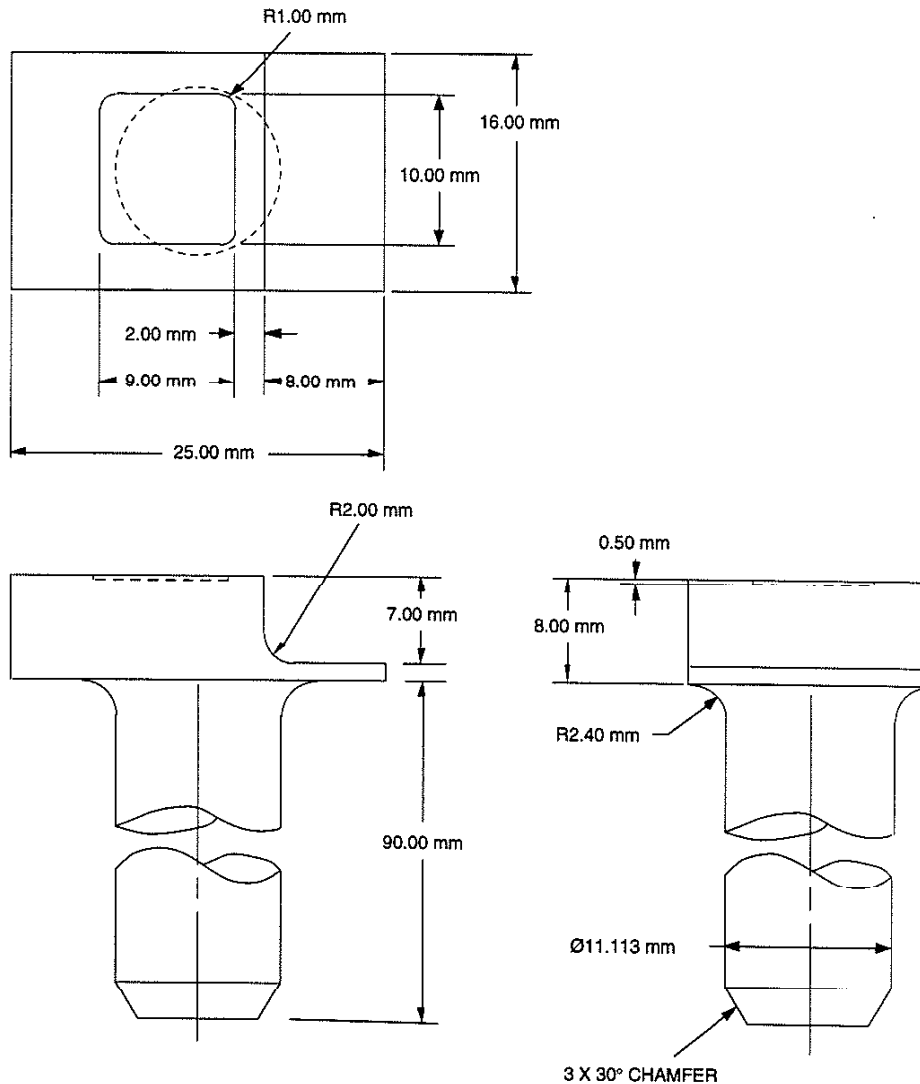


Figure 2.1.3: Small scale specimen grips used for compressive testing.

employed here. Looking at the bottom right view, in figure 2.1.2, the thin specimens (figure 2.2.1) are placed flat on the face marked “rough surface”. They are then lightly clamped in place with a square connecting block and two bolts through the 3.2 mm holes. Before clamping, the specimens are held

in place by a small pin placed through the 1 mm hole. At this point the specimens are lightly loaded in the tensile direction. Since the pin hole is aligned with the actuator axis, this preload assures proper alignment during the final clamping of the specimen.

The strains in the tests are measured with a miniature extensometer (MTS model 632.29F-20). Both the tensile and compressive grips were designed to accommodate the miniature extensometer. In addition a Questar QM-100 microscope is used to observe transformation fronts *in situ* via surface relief phenomenon. The far end of the Questar microscope is visible on the right side of figure 2.1.1. The microscope is kept approximately 3 inches from the specimen to obtain maximum contrast and resolution. Notably, this is closer than the 6 inch distance which Questar claims is the "minimum working distance." To obtain high quality bright field images from the optical microscope, it is crucial that the line of sight of the microscope and the face of the clamped small specimen be perpendicular. To accomplish this the microscope was placed in a fixed position and the collet was loosened. With the microscope focused on the center of the tension or compression specimen, the small mechanical grip was rocked through an angle range near the perpendicular condition. The rotational position which resulted in the largest light return (brightest viewing screen) was the desired grip position. The small grip was kept in this position and the collet was tightened. Then, the top grip was aligned with the secured bottom grip.

In order to run tests at different temperatures, the small scale test apparatus was also accommodated with heating and cooling sources. The heating source used here was water cooled induction heating coils. The coils were circled around the bases of both collet chucks, and heat conduction through the chucks into the specimen provided the heating source. Copper tubes wrapped tightly around the connecting end of the collet chucks, and around the clasps of the small scale specimen grips were used to cool the specimens. Liquid nitrogen was passed through the tubes and both the collet chucks and the small scale specimens were substantially cooled.

2.2 SMALL SCALE SPECIMENS

The single crystal and polycrystalline NiTi specimens used in this study are shown in figure 2.2.1. For compression tests it is feasible to use the square blocks shown in figure 2.2.1 or to use thicker tension sample specimens. The specimens were electrical discharge machined and one surface was mechanically polished to a mirror finish (final polish: .5 μm paste) to allow for the *in situ* viewing of martensite surface relief phenomenon.

The preparation of single crystal specimens of different orientations required unique preparation techniques (figure 2.2.2). The single crystal was received from Tomsk University in Russia with a random orientation. The orientation of the crystal was determined by using Kikuchi maps formed in

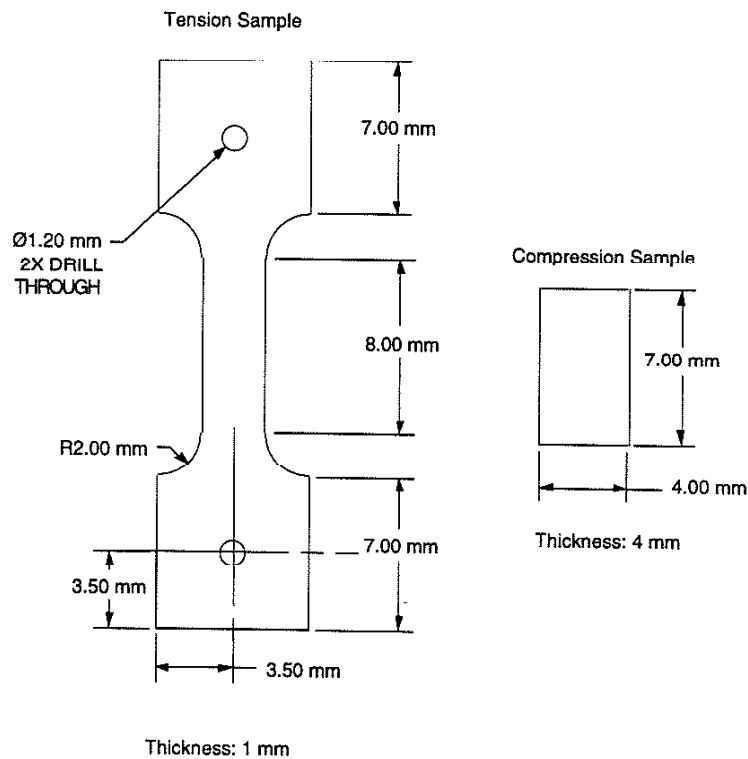


Figure 2.2.1: Small scale specimens designed for tensile or compressive loading.

the scanning electron microscope (electron backscatter diffraction mode). With the orientation information it was then possible to determine the angle between the $\{1 -1 0\}$ plane and the primary axis of the cylinder. Then, multiple thin slices were made parallel to the $\{1 -1 0\}$ plane. The slices were 1.2 mm thick for tension specimens and 5.1 mm thick for compression

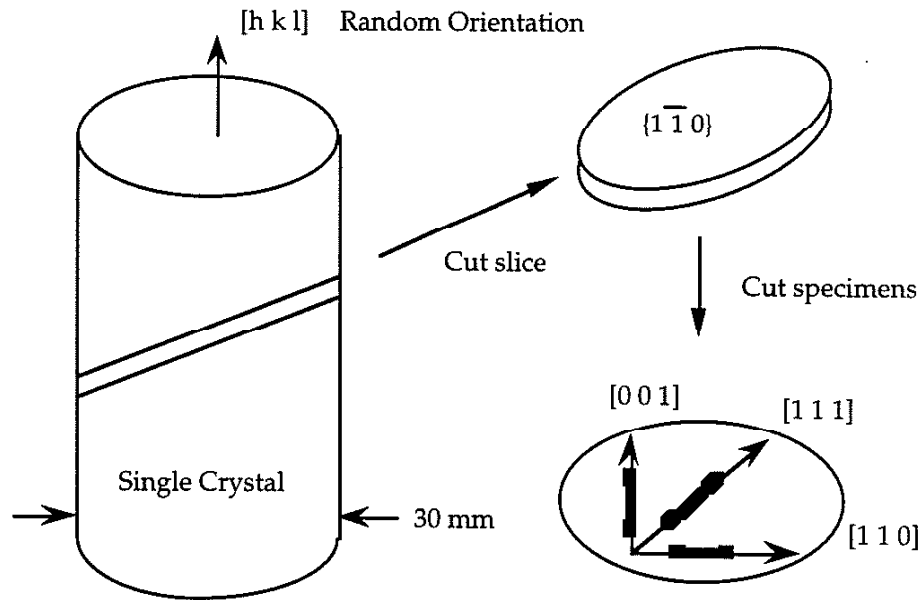


Figure 2.2.2: Preparation of single crystal specimens of different orientations.

specimens. The $\{1 -1 0\}$ plane is desired because it contains several crystallographic orientations which respond drastically different under applied loads: $[001]$, $[111]$, and $[110]$. Specimens of these three orientations were subsequently cut out of the $\{1 -1 0\}$ slice as shown in figure 2.2.2. Each slice produced two tension and ten compressive specimens (figure 2.2.1) of the same orientation. It is also helpful to note that when the single crystal specimens are etched (see section 2.4), visible "grooves" form along the $[1 1 0]$ direction. These grooves can be used as a secondary check of the crystallographic orientation of the sample before testing.

2.3 TRIAXIAL TESTING EQUIPMENT

An MTS servohydraulic test machine fitted with a unique high pressure vessel was used for triaxial testing of single crystal and polycrystalline shape memory alloy specimens. The schematic of the test system is provided in figure 2.3.1. As figure 2.3.1 indicates, axial stresses were applied to the specimen by the servohydraulic actuator of the MTS test

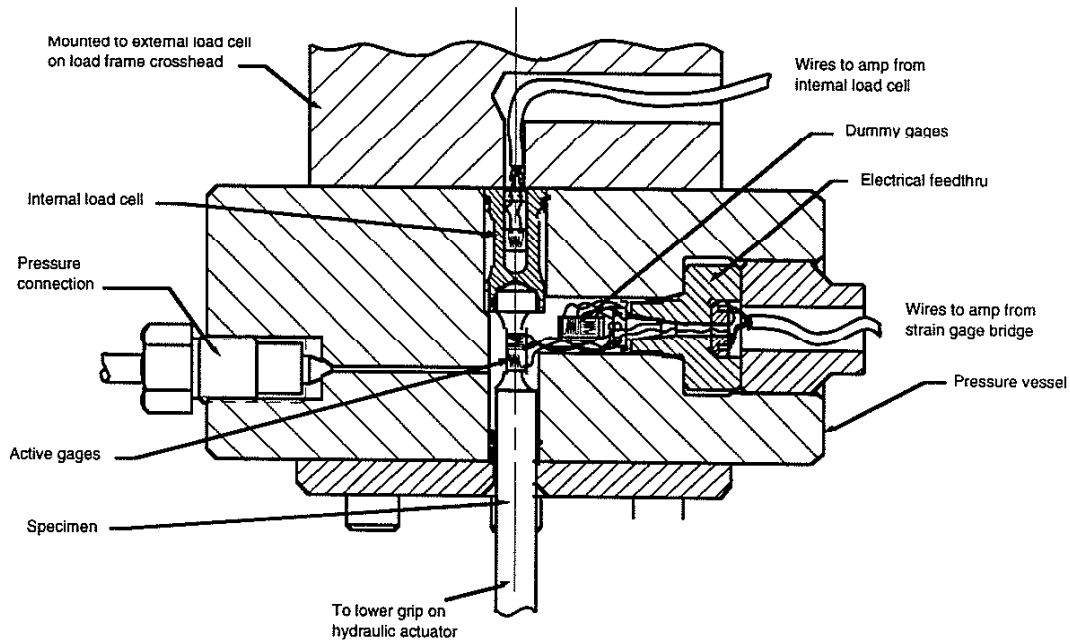


Figure 2.3.1: Cross sectional view of the triaxial test apparatus [Balzer and Sehitoglu 1997].

machine and diametral stresses were applied to the specimen through the introduction of pressurized fluid into the pressure vessel. Specimen strains (axial and diametral) were monitored by a pair of foil strain gages bonded to the specimen gage section; pressure effects on the strain gage output were eliminated by wiring a strain gaged dummy specimen into the bridge circuit inside the vessel. A miniature strain gage load cell placed in the top section of the pressure vessel was used to measure axial specimen load. This allowed

the measurement of load without having to account for seal friction. Diametral specimen pressure was monitored by a pressure transducer.

Control of the high pressure testing setup was accomplished with two independent control loops - one for the MTS axial actuator and a second for the servohydraulic pressure intensifier. The independent control loops allow for the application of any desired axial stress/lateral stress ratio within load and specimen stability limits. The ability of the present triaxial testing apparatus to simultaneously ramp the transverse and axial stresses on the specimen represents one of its main advantages over previous triaxial research efforts. In previous works, hydrostatic compression was typically applied first and the uniaxial stress was increased in a secondary operation. The present scheme circumvents any arguments regarding the role of initial hydrostatic compression on the material behavior [Radcliffe 1970]. More details of the pressure intensifier, load and strain measurements can be found in a recent publication [Balzer and Sehitoglu 1997].

2.4 MICROSCOPY SAMPLE PREPARATION

Cu-Zn-Al specimens were electropolished with a 2:1 Methanol/Nitric acid solution at -30°C and 70 Volts. The low temperature is imperative since the electropolish solution is explosive at higher temperatures. The chemical etchant used to view the martensite plates was $5\text{g FeCl}_3 + 50\text{ ml HCl} + 100\text{ ml H}_2\text{O}$. NiTi specimens were etched with a $3\text{HNO}_3 + 2\text{H}_2\text{O} + 1\text{HF}$ solution to remove surface impurities from electrical discharge machining or to view the internal martensite structures. For aged samples twice the amount of HF was necessary to obtain reasonable etching times. TEM specimens of NiTi were prepared by thinning a slice down to $150\ \mu\text{m}$ with the mentioned etchant, punching 3 mm disks, and twin jet electropolishing with a 20% H_2SO_4 - 80% methanol solution. The optimum electropolish was accomplished at $0\ ^{\circ}\text{C}$ and the other parameters of the polish were $V = 40\ \text{Volts}$ ($I = .25\ \text{Amps}$), flow

rate = 5, and photo sensitivity = 2. It should be noted that preparation of TEM samples by dimple grinding was, for the most part, unsuccessful.

2.5 Cu-Zn-Al and NiTi SPECIMEN COMPOSITIONS

Polycrystalline $\text{Cu}_{59.1}\text{Zn}_{27.0}\text{Al}_{13.8}$ (with $\text{Zr}_{0.1}$ for grain refinement) weight percent alloy was employed for the study. The average grain size of the polycrystalline Cu-Zn-Al was about 250 μm . The polycrystalline and single crystal NiTi alloy have a composition of approximately Ti - 50.9at%Ni (Ti - 56.0wt%Ni). The single crystals have a slightly higher Ni content due to the small evaporation of Ti when re-melting the polycrystalline material and growing the single crystals. The average grain size in the polycrystalline NiTi was about 20 μm .

2.6 HEAT TREATMENT TECHNIQUES

Due to the poor oxidation resistance of nickel at high temperatures, NiTi quickly develops very thick oxide layers when exposed to high

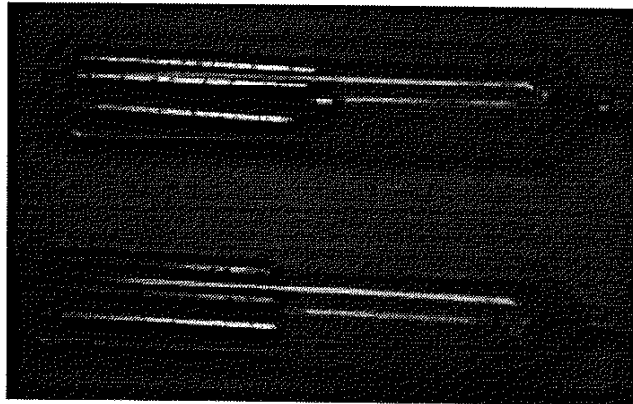


Figure 2.6.1: Two evacuated quartz tubes holding long cylindrical high pressure specimens wrapped in nickel wire. The tubes are broken upon quenching.

temperatures. Because of this, solutionizing heat treatments were conducted in evacuated quartz tubes (figure 2.6.1). The specimens were wrapped in

nickel wire to prevent them from welding together and to prevent silicon from diffusing into the samples through contact points with the quartz tubes. The samples were solutionized as thin disks for uniaxial tests or as straight cylinders for high pressure specimens. The solution treatment was performed for 2 hours @ 1000°C. At completion of the heating cycle, the tubes were quenched into ambient water and quickly broken with pliers. Aging heat treatments were performed in the furnace atmosphere on the as machined samples. It should be noted that the single crystal specimens also required a 24 hour homogenization @ 1000 °C to dissolve their coarse dendritic structure. The transformation temperatures of the samples were determined by the University of Illinois microanalysis laboratory using a Perkins-Elmer differential scanning calorimeter.

REFERENCES

Balzer M and H. Sehitoglu, *Experimental Mechanics*, vol. 37-1, (1997).

Radcliffe S V, The Mechanical Behavior of Materials Under Pressure, ed. H.L.D. Pugh, Elsevier, New York, NY, 638, (1970).

CHAPTER 3: ANALYTICAL MODELING APPROACH

PREVIEW

A micro-mechanical model which will be used to predict stress state effects in shape memory alloys is developed. The model exclusively considers the monotonic (forward transformation) stress-strain behavior. Using internal variable theory and the phenomenological theory of martensitic transformations, the constitutive equations for single crystals are derived from the complementary free energy. The polycrystalline stress-strain behavior is predicted by incorporating the single crystal constitutive equations into the self-consistent method. The important equations in the chapter are in the section 3.6. Predictions of the micro-mechanical model for Cu-Zn-Al are presented in chapter 4, while results for NiTi are included in chapter 5.

3.1 CONSTITUTIVE MODELING

The constitutive modeling of material behavior is generally motivated by one of two separate needs: (1) To predict the macroscopic stress-strain behavior of engineering components in service, i.e. constitutive relations developed for use in finite element codes; (2) To predict the macroscopic stress-strain behavior of a specific material as a function of microscopic variables. The former need is usually satisfied through phenomenological modeling, while the latter problem is usually solved by micro-mechanical modeling. Figure 3.1.1 schematically demonstrates the basis of both phenomenological and micro-mechanical modeling. Phenomenological stress-strain models incorporate simple mathematical equations with constants determined (curve fit) from the "macroscopic mechanical behavior" of a particular material. The advantage of phenomenological models is often due to the simplicity of the governing equations. For

example, the equations are usually simple enough to be incorporated into mathematically complex analysis tools such as the finite element method.

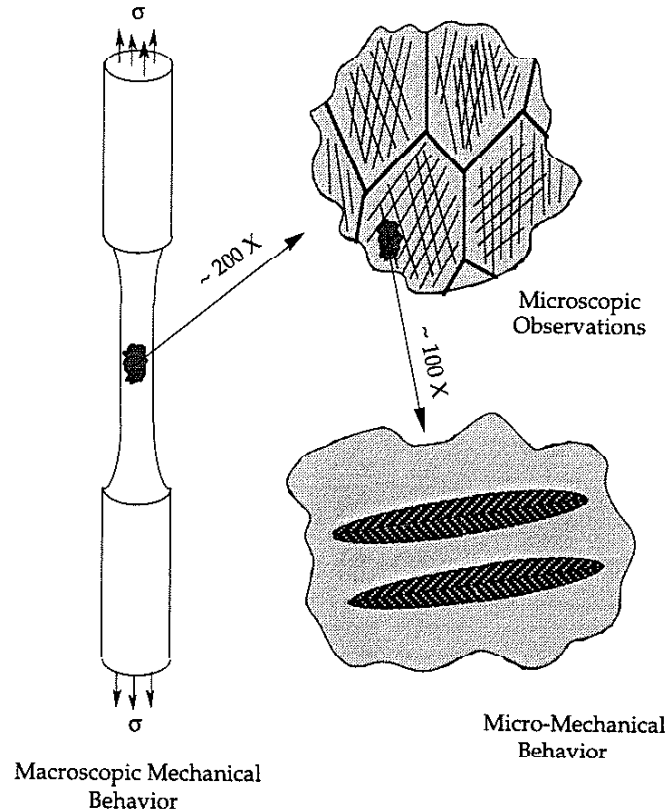


Figure 3.1.1: Schematic of shape memory alloy deformation phenomenon at various length scales.

The disadvantage of phenomenological models is that they do not consider the physics of the underlying deformation phenomenon. However, micro-mechanical models incorporate both "microscopic observations" of the material structure and "micro-mechanical behavior" of material constituents to predict macroscopic deformation behavior. Micro-mechanical models are extremely useful when it is necessary to quantify the effect of different microstructural phenomenon on macroscopic stress-strain behavior. Unfortunately, micro-mechanical models hardly ever result in explicit constitutive equations that can be used as an analysis tool on "engineering

applications” problems. At any rate, micro-mechanical modeling is an extremely valuable tool which can be used to understand and improve the macroscopic behavior of a material through a deeper quantification of the effects of microscopic variables on the deformation behavior. In the following sections, a micro-mechanical model is developed that will predict the monotonic stress-strain behavior of shape memory alloys under different stress-states.

3.2 NOTATION AND SYMBOLS USED IN MODELING

Before discussing the modeling it is appropriate to document the meanings of the symbols used in the model. Where possible, the notation is kept consistent with current models of shape memory alloy stress-strain behavior.

3.2.1 STRESS-STRAIN VARIABLES

$\epsilon_{ij} = f(\text{position})$ Local position dependent strain field within a grain.

$\sigma_{ij} = f(\text{position})$ Local position dependent stress field within a grain.

$E_{ij} = \frac{1}{V} \int_{\Omega} \epsilon_{ij} dV$ Average strain field in a single crystal of volume V .

$\Sigma_{ij} = \frac{1}{V} \int_{\Omega} \sigma_{ij} dV$ Average stress field in a single crystal of volume V .

$\bar{E}_{ij} = \frac{1}{V_i} \int_D E_{ij} dV_i$ Average strain field in a polycrystal of volume V_i .

$\bar{\Sigma}_{ij} = \frac{1}{V_i} \int_D \Sigma_{ij} dV_i$ Average stress field in a polycrystal of volume V_i .

\bar{E}_{ij}^{tr} Average transformation strain in a polycrystal.

E_{ij}^{tr} Average transformation strain in a single crystal.

E_{ij}^e Average elastic strain in a single crystal.

$\varepsilon_{ij}^{dist-tr}$	Local disturbance strain (transformation).
$\varepsilon_{ij}^{dist-e}$	Local disturbance strain (elastic).
σ_{ij}^{dist}	Local disturbance stress.
C_{ijkl}	Elasticity tensor.
S_{ijkl}	Eshelby tensor.

3.2.2 TRANSFORMATION VARIABLES

f'	“Hardening” parameter for the transformation flow rule.
f	Total transformed volume fraction of martensite.
f^n	Volume fraction of martensite for the n^{th} variant.
g	Maximum displacement magnitude of transformation.
m	Transformation direction.
n	Habit plane normal.
α_{ij}^n	Orientation tensor of n^{th} variant.
u	Displacement from parent to martensitic phase.
V	Volume of a single crystal of the parent phase.
V_m	Volume of fully transformed martensitic phase.
V'_m	Volume of partially transformed martensitic phase.
V_p	Volume of the partially untransformed parent phase.
V_r	Volume of polycrystalline body.
ΔV	Volume change from parent to martensitic phase.
x	Position vector in parent phase coordinate system.
x, y, z	Coordinate system in the parent phase

3.2.3 THERMODYNAMIC VARIABLES

B	Constant of proportionality for chemical free energy.
F^n	Thermodynamic driving force for the n^{th} variant.
F_c	Critical driving force for the transformation.
τ_{cons}	Initial constraint stress.
T	Current temperature.
T_o	Reference temperature.
Ψ	Complementary free energy.
ΔG_{chem}	Chemical free energy difference.
W_{mech}	Total elastic strain energy.
W_{inter}	Interface energy between the martensite and parent phase.
\int_{Ω}	Integration over a single crystal of volume V .
\int_D	Integration over a polycrystal of volume V_i .

3.3 PHENOMENOLOGICAL THEORY OF MT's

At the lowest level, all micro-mechanical models are essentially phenomenological. For example, even if a deformation mechanism is modeled by "fundamental" atomic movements, it can still be argued that atoms are simply phenomenological models of electron, neutron, and proton positions. Nevertheless, it is obvious that time and computing limitations prevent the development of a micro-mechanical model which incorporates all of the observations from solid state physics down to the "quark" level. The stopping point of this model will be the phenomenological theory of martensitic transformations. The basis of the theory is demonstrated in

Figure 3.3.1. The phenomenological theory of MT's is based on microscopic shape changes which have been observed for transforming martensite plates.

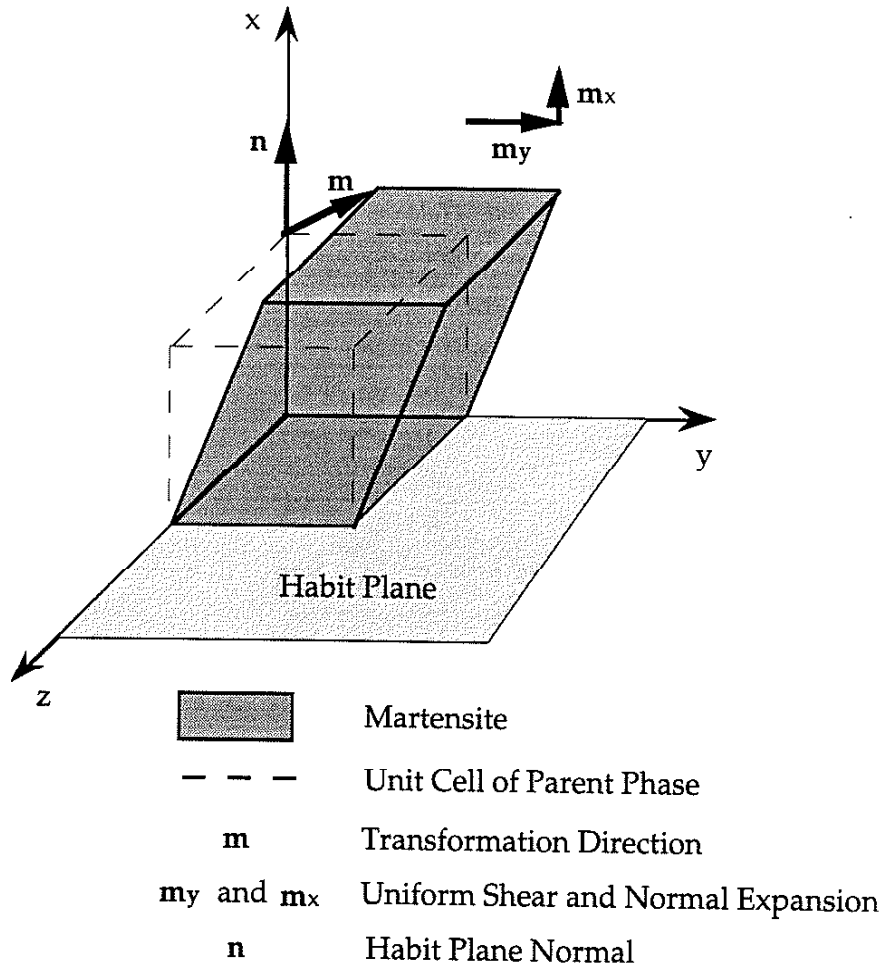


Figure 3.3.1: Basic definitions in the phenomenological theory of martensitic phase transformations.

This is in contrast to the crystallographic theory of MT's which focuses on the actual atomic movements associated with the transformation. In the phenomenological theory, the transformation variables are traditionally defined with respect to a coordinate system attached to the parent phase. Following figure 3.3.1, the habit plane of the transformation is defined as the plane which remains undistorted during the transformation. The unit vector characterizing the normal of the habit plane is denoted as n . The

transformation direction is described by a unit vector denoted m . In figure 3.3.1 the transformation direction m lies in the xy -plane, and the habit plane normal lies along the x direction. In reality, m and n may be arbitrarily oriented with respect to the parent phase coordinate system.

At any rate, the transformation in figure 3.3.1 can be broken into two components, a shear along m_y and an expansion perpendicular to the habit plane along m_x . In this case the resulting local strain field is trivial to calculate since the habit plane normal and the transformation direction are both close to the principal crystallographic axes of the parent phase. However, for the general case, the resultant strain due to the transformation of a unit volume of parent phase is derived below. To derive the general relationships, only one martensite variant will initially be considered. Following this, the derived relationships will be extended to the general multi-variant case.

The displacement vector from the parent phase to the deformed phase (martensitic phase) is given by:

$$u_i = gm_i x_k n_k \quad (3.3.1)$$

where g is the maximum magnitude of the displacement and x_k is the position vector of the martensite defined in the parent phase's coordinate system. The small strain tensor is defined as:

$$\varepsilon_{ij} = \frac{1}{2} \left(\frac{\partial u_i}{\partial x_j} + \frac{\partial u_j}{\partial x_i} \right) \quad (3.3.2)$$

Combining equations 3.3.1 and 3.3.2 the following result is obtained for the overall transformation strain:

$$E_{ij}^{tr} = g \frac{1}{2} (m_i n_j + m_j n_i) = g \alpha_{ij} \quad (3.3.3)$$

The α_{ij} term is commonly called the orientation tensor for the transforming martensite variant. Equation 3.3.3 gives a closed form result for the transformation strain resulting from the complete transformation of a unit volume of the parent phase, V , into a unit volume of the martensitic phase, V_m . The volumetric strain due to the transformation is computed as the trace of the transformation strain tensor:

$$\frac{\Delta V}{V} = \frac{V_m - V}{V} = E_{kk}^{tr} = g m_k n_k \quad (3.3.4)$$

In reality, it is possible that the martensitic transformation does not proceed throughout the entire volume of the parent phase, V , and only occupies the volume V'_m , where $V'_m = V - V_p$ (V_p is the untransformed volume of the parent phase). In this case it is feasible to use the rule of mixtures to approximate the average transformation strain in the volume V resulting from the partial transformation of V'_m :

$$E_{ij}^{tr} = g \alpha_{ij} \frac{V'_m}{V} = g \alpha_{ij} f \quad (3.3.5)$$

where f is the volume fraction of the martensite, and E_{ij}^{tr} is the average transformation strain in the unit volume V . In reality the average transformation strain in the unit volume V will be affected by the elastic constraint that the parent phase imposes on the transformed volume fraction of martensite. However, in the case of martensitic transformations in shape memory alloys, the elastic constraint is minimized due to the formation of thermo-elastic martensites. Therefore, it is proposed that equation 3.3.5 gives

a good approximation of the transformation strain in the parent phase resulting from the partial transformation of a single martensite variant.

In the case where multiple variants are active, the total transformation strain in the parent phase is given by the summation of transformation strains from all of the active variants:

$$E_{ij}^r = g \sum_n \alpha_{ij}^n f^n \quad (3.3.6)$$

The total transformed volume fraction of the crystal is the sum of the individual martensite variant volume fractions:

$$f = \sum_n f^n \quad (3.3.7)$$

The total volume fraction of martensite cannot exceed 1, thus equation 3.3.7 is restricted to $f \leq 1$. The summation only holds for martensite variants which are currently active. In NiTi and Cu-Zn-Al shape memory alloys, there are 24 possible martensite variants.

3.4 THERMODYNAMICAL CONSIDERATIONS

To derive a constitutive relationship for the transformation from the parent phase to the martensitic phase a thermodynamical approach is incorporated. It should be noted that the derivation has been adapted from the works of Patoor et al. [1993] and Huang et al. [1997]. Since the state variables in martensitic transformations are stress and temperature, the complementary free energy is chosen as the representative thermodynamic potential:

$$\Psi(\Sigma_{ij}, T, f) = -\Delta G_{chem} - W_{mech} - W_{inter} + \Sigma_{ij} E_{ij} \quad (3.4.1)$$

where ΔG_{chem} is the chemical free energy difference between the parent phase and the martensitic phase, W_{mech} is the total elastic strain energy that will exist as a result of the transformation, W_{inter} is the interfacial energy between the new martensite and parent phase, and $\Sigma_{ij}E_{ij}$ represents the dependence of the transformation on the macroscopic applied stresses. When equation 3.4.1 is greater than zero, then the transformation from the parent phase to the martensitic phase occurs. While the material exists in the parent phase, the applied stress term $\Sigma_{ij}E_{ij}$ promotes the transformation, while the resultant elastic strain energy, W_{mech} , and interfacial energy, W_{inter} , of the transformation prevent it. In addition, the chemical free energy difference between the parent phase and the martensitic phase, ΔG_{chem} , can prevent or promote the transformation. The latter term, ΔG_{chem} is a function of temperature and will become negative if the temperature is dropped below the equilibrium temperature of the two phases, T_o . In this case the $-\Delta G_{chem}$ in equation 3.4.1 will become positive and the transformation will occur when $\Delta G_{chem} + \Sigma_{ij}E_{ij}$ overcomes $-W_{inter}$ and $-W_{mech}$. In summary, the only way equation 3.4.1 can become positive is by applying a stress or lowering the temperature. This is consistent with experimental observations on martensitic transformations.

The chemical free energy is often interpolated linearly with temperature and the volume fraction of transformed martensite:

$$\Delta G_{chem} = B(T - T_o)f \quad (3.4.2)$$

The interfacial surface energy term, W_{inter} , has been determined to be negligible, and is often ignored [Huang and Brinson 1997]. The total elastic strain energy is defined as:

$$W_{mech} = \frac{1}{2V} \int_{\Omega} \sigma_{ij} \epsilon_{ij}^e dV \quad (3.4.3)$$

The local stress field is the superposition of the average macroscopic stress in the single crystal and the local stress disturbance due to the transforming martensite inclusions:

$$\sigma_{ij} = \Sigma_{ij} + \sigma_{ij}^{dist} \quad (3.4.4)$$

Similarly, the local strain field is the superposition of the average strain in the single crystal and the local strain disturbance due to the transforming martensite inclusions: $\epsilon_{ij} = E_{ij} + \epsilon_{ij}^{dist}$. The total strain may be broken into elastic and transformation (plastic) portions as follows:

$$\epsilon_{ij} = E_{ij} + \epsilon_{ij}^{dist} = E_{ij}^e + \epsilon_{ij}^{dist-e} + E_{ij}^{tr} + \epsilon_{ij}^{dist-tr} \quad (3.4.5)$$

The elastic portion is clearly given by:

$$\epsilon_{ij}^e = E_{ij}^e + \epsilon_{ij}^{dist-e} \quad (3.4.6)$$

Substituting 3.4.6 and 3.4.4 into 3.4.3, one obtains:

$$\begin{aligned} W_{mech} &= \frac{1}{2V} \int_{\Omega} (\Sigma_{ij} + \sigma_{ij}^{dist})(E_{ij}^e + \epsilon_{ij}^{dist-e}) dV \\ &= \frac{1}{2V} \int_{\Omega} (\Sigma_{ij} + \sigma_{ij}^{dist})(E_{ij}^e + \epsilon_{ij}^{dist} - \epsilon_{ij}^{dist-tr}) dV \\ &= \frac{1}{2V} \int_{\Omega} \Sigma_{ij} E_{ij}^e - \frac{1}{2V} \int_{\Omega} \sigma_{ij}^{dist} \epsilon_{ij}^{dist-tr} dV + \frac{1}{2V} \int_{\Omega} \Sigma_{ij} (\epsilon_{ij}^{dist} - \epsilon_{ij}^{dist-tr}) dV + \int_{\Omega} \sigma_{ij}^{dist} (E_{ij}^e + \epsilon_{ij}^{dist}) dV \end{aligned}$$

The latter two terms can be shown to equal zero by incorporating boundary conditions and the equation of equilibrium [Huang and Brinson 1997]. With this one obtains:

$$= \frac{1}{2V} \int_{\Omega} \Sigma_{ij} E_{ij}^e - \frac{1}{2V} \int_{\Omega} \sigma_{ij}^{dist} \epsilon_{ij}^{dist-tr} dV$$

$$W_{mech} = \frac{1}{2} \Sigma_{ij} E_{ij}^e - \frac{1}{2V} \int_{\Omega} \sigma_{ij}^{dist} \epsilon_{ij}^{dist-tr} dV \quad (3.4.7)$$

Substituting the simplified energy terms into equation 3.4.1, the following result is obtained:

$$\begin{aligned} \Psi(\Sigma_{ij}, T, f) &= -B(T - T_o)f - \frac{1}{2} \Sigma_{ij} E_{ij}^e + \frac{1}{2V} \int_{\Omega} \sigma_{ij}^{dist} \epsilon_{ij}^{dist-tr} dV + \Sigma_{ij} E_{ij} \\ &= -B(T - T_o)f - \frac{1}{2} \Sigma_{ij} E_{ij}^e + \frac{1}{2V} \int_{\Omega} \sigma_{ij}^{dist} \epsilon_{ij}^{dist-tr} dV + \Sigma_{ij} (E_{ij}^e + E_{ij}^{tr}) \end{aligned}$$

$$\Psi(\Sigma_{ij}, T, f) = -B(T - T_o)f + \frac{1}{2} \Sigma_{ij} E_{ij}^e + \Sigma_{ij} E_{ij}^{tr} + \frac{1}{2V} \int_{\Omega} \sigma_{ij}^{dist} \epsilon_{ij}^{dist-tr} dV \quad (3.4.8)$$

Equation 3.4.8 represents the complementary free energy for a single crystal of volume V transforming into a single martensite variant. The latter term is commonly referred to as the “interaction energy”. It carries with it the energy caused by the interaction of the transforming martensite plates with themselves and with the surrounding untransformed parent phase.

To extend equation 3.4.8 to a multi-variant case, equations 3.3.6 and 3.3.7 must be incorporated:

$$\Psi(\Sigma_{ij}, T, f^n) = -B(T - T_o) \sum_n f^n + \frac{1}{2} \Sigma_{ij} E_{ij}^e + \Sigma_{ij} \sum_n g \alpha_{ij}^n f^n + \frac{1}{2V} \int_{\Omega} \sigma_{ij}^{dist} \epsilon_{ij}^{dist-tr} dV \quad (3.4.9)$$

For the studies here, the above form of the complementary free energy is further reduced since the tests are all run at constant temperatures ($T = T_o$):

$$\Psi(\Sigma_{ij}, T, f^n) = \frac{1}{2} \Sigma_{ij} E_{ij}^e + \Sigma_{ij} \sum_n g \alpha_{ij}^n f^n + \frac{1}{2V} \int_{\Omega} \sigma_{ij}^{dist} \epsilon_{ij}^{dist-tr} dV \quad (3.4.10)$$

The above equation is the final form of the complementary free energy used in this model. It represents the thermodynamic potential for the multi-variant transformation from the parent phase to the martensitic phase in a single crystal of volume V which is under an applied stress Σ_{ij} .

The thermodynamic driving force acting on an internal variable is obtained by the partial differentiation of equation 3.4.10 with respect to the variable of interest:

$$F^n = \frac{\partial \Psi}{\partial f^n} = g \Sigma_{ij} \alpha_{ij}^n + \frac{\partial}{\partial f^n} \left[\frac{1}{2V} \int_{\Omega} \sigma_{ij}^{dist} \epsilon_{ij}^{dist-tr} dV \right] \quad (3.4.11)$$

When the thermodynamical force (equation 3.4.11) is greater than a critical value, the transformation proceeds. However, it is difficult to accurately calculate the interaction energy term. In the case of shape memory alloys the interaction term is minimized, due to the formation of thermo-elastic martensites. The most accurate method currently used to calculate the interaction term is in the analysis of Huang and Brinson [1997]. They considered self accommodating variant groups and used the Mori-Tanaka method to determine a form for the interaction energy. Patoor et al. [1993] dealt with the interaction term by using an "interaction matrix". In the analysis here, the interaction matrix approach will be incorporated. The analysis was even made simpler by considering the interaction of variants with the matrix but not with each other. With this, equation 3.4.11 is reduced to:

$$F^n = g \sum_{ij} \alpha_{ij}^n - f f^n \quad (3.4.12)$$

The above equation is similar to the constitutive equation for plastic flow that includes primary hardening, but does not consider latent hardening. The minus sign in front of the volume fraction evolution term is crucial since the martensite formation must be stable. As martensite forms it must become harder to form more martensite, thus the previously formed martensite lowers the "actual" thermodynamic force caused by the applied stresses and resulting strains. If this were not the case then the transformation stress-strain curve would have a negative (unstable) slope. Since this model only considers monotonic loading, with no martensite initially present, equation 3.4.12 is further reduced to:

$$F^n = g \sum_{ij} \alpha_{ij}^n \quad (3.4.13)$$

When equation 3.4.13 exceed a critical value, F_c , the transformation proceeds for the n^{th} variant. Equation 3.4.13 can also be written as a transformation criteria:

$$g \sum_{ij} \alpha_{ij}^n \geq F_c \quad (3.4.14)$$

Equation 3.4.14 is the transformation criterion for the n^{th} variant. Notably, it is possible that the left hand side of equation 3.4.14 may be negative for a given applied stress state and variant orientation tensor. In this case, the variant will never transform under the applied stress state. This asymmetry is not observed in the case in slip, and is one of the key factors governing stress state effects in shape memory alloys. In some studies it is reasonable to incorporate an initial "constraint stress" into equation 3.4.14:

$$|g_{\Sigma_{ij}}\alpha_{ij}^n \pm \tau_{cons}| \text{Sign}(\Sigma_{ij}\alpha_{ij}^n) \geq F_c \quad (3.4.15)$$

The constraint stress, τ_{cons} , has proven effective in predicting results for quenched steels undergoing martensitic transformations. In the case of quenched steels, the meta-stable austenite is normally under a large constraining pressure due to the formation of athermal martensite plates. This pressure may prohibit or promote the transformation depending on the volume change of the transformation.

To determine the flow rate of the transformation, the consistency condition is applied to equation 3.4.12:

$$\frac{\partial \dot{F}^n}{\partial \Sigma_{ij}} \dot{\Sigma}_{ij} + \frac{\partial \dot{F}^n}{\partial f^n} \dot{f}^n = g \alpha_{ij}^n \dot{\Sigma}_{ij} - f \dot{f}^n \quad (3.4.16)$$

When equation 3.4.16 is equal to zero, then the consistency condition is satisfied and the volume fraction evolution rate of martensite is obtained:

$$\dot{f}^n = \frac{g \alpha_{ij}^n \dot{\Sigma}_{ij}}{f'} \quad (3.4.17)$$

Finally, the single crystal flow rule can be written by combining equation 3.4.17 with the incremental form of equation 3.3.6:

$$\dot{E}_{ij}^{tr} = \frac{g^2}{f'} \sum_n \alpha_{ij}^n \alpha_{kl}^n \dot{\Sigma}_{kl} \quad (3.4.18)$$

Equation 3.4.18 can be used to predict the stress-strain behavior of a single crystal of a parent phase transforming to a martensitic phase. The summation over n only holds for variants which satisfy the yield criteria

(equation 3.4.14). Although much more complicated micro-mechanical models do exist, this model is sufficient to help understand stress-state effects in shape memory alloys.

3.5 POLYCRYSTALLINE TRANSITION

In the previous section a constitutive law for single crystal shape memory alloys ($\dot{\Sigma}_{ij} \leftrightarrow \dot{E}_{ij}$) was developed. However, stress-state effects have also been observed in polycrystalline shape memory alloys, and polycrystalline materials are primarily used in applications. To develop a micro-mechanical model for the macroscopic stress-strain behavior of polycrystalline shape memory alloys ($\dot{\Sigma}_{ij} \leftrightarrow \dot{\bar{E}}_{ij}$), the self-consistent method is employed [Mura 1987].

In a polycrystalline body undergoing a stress induced martensitic phase transformation, there exist grains which are oriented favorably and unfavorably with respect to the applied stress state. The misorientation will result in unbalanced transformation strain magnitudes for neighboring grains. In turn, the difference in transformation strain levels leads to local (position dependent) stress and strain fields throughout the polycrystalline body. The self consistent method assumes that the magnitude of the resulting internal stress and strain fields can be estimated by the difference in the average transformation strain of the polycrystalline matrix and the local transformation strain in any particular grain. It should be noted that although elastic property mismatch also causes internal stress and strain fields, this effect will be ignored here to simplify calculations.

The mismatch strain between the local transformation strain within a grain (volume V) and the average strain in the polycrystalline matrix (volume V_i) is written as:

$$E_{ij}^r - \bar{E}_{ij}^r \quad (3.5.1)$$

The constraint strain on the transforming grain caused by the above mismatch can be calculated using the Eshelby tensor, S_{ijkl} :

$$S_{ijkl}(E_{kl}^{rr} - \bar{E}_{kl}^{rr}) \quad (3.5.2)$$

The actual strain field is a superposition of the above constraint strain and the average strain in the polycrystalline matrix:

$$E_{ij} = C_{ijkl}^{-1}\bar{\Sigma}_{kl} + \bar{E}_{ij}^{rr} + S_{ijkl}(E_{kl}^{rr} - \bar{E}_{kl}^{rr}) \quad (3.5.3)$$

The following decomposition of the strain field in the single grain can also be made:

$$E_{ij} = C_{ijkl}^{-1}\Sigma_{kl} + E_{ij}^{rr} \quad (3.5.4)$$

Combining equations 3.5.3 and 3.5.4, a unique expression is obtained:

$$C_{ijkl}^{-1}\Sigma_{kl} + E_{ij}^{rr} = C_{ijkl}^{-1}\bar{\Sigma}_{kl} + \bar{E}_{ij}^{rr} + S_{ijkl}(E_{kl}^{rr} - \bar{E}_{kl}^{rr}) \quad (3.5.5)$$

Multiplying both sides by C_{ijkl} and rearranging, the following result is obtained:

$$\Sigma_{ij} = \bar{\Sigma}_{ij} + C_{ijkl} [S_{klmn}(E_{mn}^{rr} - \bar{E}_{mn}^{rr}) - (E_{kl}^{rr} - \bar{E}_{kl}^{rr})] \quad (3.5.6)$$

The above equation is traditionally referred to as the self consistent equation.

Multiplying both sides by $g\alpha_{ij}^n$ one obtains:

$$g\alpha_{ij}^n \Sigma_{ij} = g\alpha_{ij}^n \bar{\Sigma}_{ij} + g\alpha_{ij}^n C_{ijkl} [S_{klmn}(E_{mn}^{rr} - \bar{E}_{mn}^{rr}) - (E_{kl}^{rr} - \bar{E}_{kl}^{rr})] \quad (3.5.7)$$

Using equations 3.3.6 and 3.4.17, equation 3.5.7 is transformed into:

$$f\dot{f}^n = g\alpha_{ij}^n \bar{\Sigma}_{ij} + g\alpha_{ij}^n C_{ijkl} \left[S_{klmn} (g \sum_n \alpha_{mn}^n f^n - \bar{E}_{mn}^{tr}) - (g \sum_n \alpha_{kl}^n f^n - \bar{E}_{kl}^{tr}) \right] \quad (3.5.8)$$

Rearranging the above equation yields:

$$\begin{aligned} & g\alpha_{ij}^n \bar{\Sigma}_{ij} - g\alpha_{ij}^n C_{ijkl} S_{klmn} \bar{E}_{mn}^{tr} + g\alpha_{ij}^n C_{ijkl} \bar{E}_{kl}^{tr} \\ & = f\dot{f}^n - g^2 \alpha_{ij}^n C_{ijkl} S_{klmn} \sum_n \alpha_{mn}^n f^n + g^2 \alpha_{ij}^n C_{ijkl} \sum_n \alpha_{kl}^n f^n \end{aligned} \quad (3.5.9)$$

Or in incremental form:

$$\begin{aligned} & g\alpha_{ij}^n \dot{\bar{\Sigma}}_{ij} - g\alpha_{ij}^n C_{ijkl} S_{klmn} \dot{\bar{E}}_{mn}^{tr} + g\alpha_{ij}^n C_{ijkl} \dot{\bar{E}}_{kl}^{tr} \\ & = f\dot{f}^n - g^2 \alpha_{ij}^n C_{ijkl} S_{klmn} \sum_n \alpha_{mn}^n \dot{f}^n + g^2 \alpha_{ij}^n C_{ijkl} \sum_n \alpha_{kl}^n \dot{f}^n \end{aligned} \quad (3.5.10)$$

Equation 3.5.10 is the form of the self consistent formula that will be used to generate the polycrystalline stress-strain behavior for NiTi and Cu-Zn-Al shape memory alloys. Equation 3.5.10 is only used when the first variant within a grain reaches the critical transformation value (equation 3.4.14). Additionally, the summations only hold for variants which subsequently satisfy equation 3.4.14.

In its most general form, equation 3.5.10 represents a 24 by 24 system of linear equations to be solved for each load increment in each grain. On average, 100 to 1000 randomly oriented (α_{ij}^n rotated) grains were used to model a polycrystalline material. To simplify the Eshelby tensor the grains were assumed to be spherical in shape. The variables on the left hand side of the equation represent the known quantities at each load step, while the right hand side carries the only unknown, the volume fraction evolution of

martensite, f^n . For a given applied stress increment, $\dot{\Sigma}_{ij}$, f^n is calculated for each variant in every grain. Subsequently, the incremental form of equation 3.3.6 is used to calculate the transformation strain increment in each grain, \dot{E}_{ij}^{tr} . Finally, the values of \dot{E}_{ij}^{tr} are averaged to obtain $\dot{\bar{E}}_{ij}^{tr}$. The solution method is of the pure incremental (Euler) type since the average strain from the previous load increment is used to calculate the average strain of the current step. However, the accumulated errors are minimized by choosing extremely small applied stress increments.

In some applications of this model related to steels, plastic deformation was included in the model to properly predict experimental trends and microstructural observations. Plasticity was accounted for by adding a phenomenologically calculated average plastic strain rate onto the average calculated transformation strain value, \dot{E}_{ij}^{tr} . In the studies on shape memory alloys, plasticity will not be included in the model.

3.6 SUMMARY OF IMPORTANT EQUATIONS

Average transformation strain in a single crystal of the parent phase with n partially transformed martensite variants with volume fractions denoted f^n :

$$\text{Equation (3.3.6)} \quad E_{ij}^{tr} = g \sum_n \alpha_{ij}^n f^n$$

Transformation criteria for the n^{th} martensite variant:

$$\text{Equation (3.4.14)} \quad g \sum_j \alpha_{ij}^n \geq F_c$$

Martensite evolution rate for the n^{th} variant:

$$\text{Equation (3.4.17)} \quad \dot{f}^n = \frac{g \alpha_{ij}^n \dot{\Sigma}_{ij}}{f'}$$

Flow rule for a single crystal undergoing a martensitic transformation:

Equation (3.4.18)
$$\dot{E}_{ij}^{rr} = \frac{g^2}{f'} \sum_n \alpha_{ij}^n \alpha_{kl}^n \dot{\Sigma}_{kl}$$

Self consistent relationship for determining polycrystalline behavior.

Equation (3.5.10)
$$g \alpha_{ij}^n \dot{\Sigma}_{ij} - g \alpha_{ij}^n C_{ijkl} S_{klmn} \dot{E}_{mn}^{rr} + g \alpha_{ij}^n C_{ijkl} \dot{E}_{kl}^{rr} = f \dot{f}^n - g^2 \alpha_{ij}^n C_{ijkl} S_{klmn} \sum_n \alpha_{mn}^n \dot{f}^n + g^2 \alpha_{ij}^n C_{ijkl} \sum_n \alpha_{kl}^n \dot{f}^n$$

3.7 CRYSTALLOGRAPHIC DATA

The crystallographic data for the model is only available for the more prominent martensitic phase transformations in NiTi (B2 -> B19, table 3.7.1) and Cu-Zn-Al (B2 -> 9R, table 3.7.2). To obtain habit plane normal and the transformation direction for the other 24 variants, cyclic permutation is used [Patoor et al. 1995]. It is clear that the crystallographic parameters in the literature ($m, n, \Delta V / V$) demonstrate some scatter. The differences in the crystallographic parameters are most likely due to small experimental measurement error. For Cu-Zn-Al Patoor et al. [1995] have shown that when

Researcher	Habit Plane Normal	Transformation Direction	g	$\Delta V / V$ (%)
Buchheit and Wert (1994)	n1 = 0.889 n2 = 0.215 n3 = -0.404	m1 = -0.411 m2 = 0.763 m3 = -0.498	---	+0.000
Matsumoto et al. (Experimental) (1987)	n1 = -0.868 n2 = 0.269 n3 = 0.414	m1 = 0.458 m2 = 0.771 m3 = 0.443	0.14	-0.088
Matsumoto et al. (Theoretical) (1987)	n1 = -0.889 n2 = 0.215 n3 = 0.404	m1 = 0.435 m2 = 0.754 m3 = 0.487	0.13	-0.341

Table 3.7.1: The habit plane normal and transformation direction for the martensitic transformation (B2 -> B19) in a NiTi shape memory alloy.

the different crystallographic parameters from table 3.7.2 are used in the model, a similar macroscopic stress-strain behavior is predicted. However,

they did note that in some cases crystallographic parameters which were close in magnitude and direction to the experimentally measured parameters, did significantly change the macroscopic stress-strain response. This indicates that in some cases, the model is extremely sensitive to the crystallographic parameters.

The results of the modeling of NiTi will be discussed in chapter 5, while the results of the modeling of Cu-Zn-Al are discussed in chapter 4. It should also be noted that the crystallographic data cited here is not entirely sufficient for modeling stress state effects in shape memory alloys. It is necessary to develop phenomenological crystallographic parameters for the observed pre-martensitic transformations in NiTi and numerous other martensitic transformations observed in Cu-Zn-Al. Recently it has been reaffirmed that in Cu-Zn-Al different martensitic transformations occur under tension versus compression [Sittner et al. 1997]. When the

Researcher	Habit Plane Normal	Transformation Direction	g	$\Delta V/V$ (%)
De Vos et al. (1978)	n1 = 0.182 n2 = 0.669 n3 = 0.721	m1 = 0.165 m2 = -0.737 m3 = 0.655	0.23	+0.211
Armanie El (1994)	n1 = 0.182 n2 = 0.669 n3 = 0.721	m1 = 0.163 m2 = -0.744 m3 = 0.649	0.23	+0.000
Saburi and Wayman (1979)	n1 = 0.200 n2 = 0.680 n3 = 0.705	m1 = 0.182 m2 = -0.746 m3 = 0.641	0.19	-0.356

Table 3.7.2: The habit plane normal and transformation direction for the martensitic transformation (B2 \rightarrow 9R) in a Cu-Zn-Al shape memory alloy.

crystallographic data is documented for the less common transformations, then they can be incorporated into the micro-mechanical model. The occurrence of the less common, and often “phenomenologically smaller” transformations, is simply due to a thermodynamic favoring of the

transformations over the “larger transformations”. If the crystallographic data was available for these transformations then the model would be able to predict the formation of different martensitic phases under different applied stress states. It should be noted that the crystallographic parameters in the above table are only for one variant of martensite. In chapters 5 and 6 the parameters for the other 23 variants are determined by rotating indices.

REFERENCES

- Armani, El, Ph.D. Thesis. *Universite de Metz, France*, 1994.
- Buchheit T E and Wert J A, "Modeling the Effects of Stress State and Crystal Orientation on the Stress-Induced Transformation of NiTi Single Crystals," *Mett. Trans.*, vol. 25A, 2383-2389, 1994.
- De Vos J, Aernoudt E and Delaey L, *Z. Metallkde*, vol 69, 438-444, 1978.
- Huang M and Brinson L C, "A Multivariant Model for Single Crystal SMA Behavior," *Submitted to J. Mech. Phys. Solids*, 1997.
- Jacobus K, Sehitoglu H, Balzer M, "Effect of stress-state on the stress-induced martensitic transformation in polycrystalline Ni-Ti- alloy," *Metall. Mater. Trans.*, vol. 27A, 3066-3073, 1996.
- Matsumoto O, Miyazaki S, Otsuka K, and Tamura, H, "Crystallography of Martensitic Transformations in Ti-Ni Single Crystals," *Acta. Mett.*, vol. 35, 2137, 1987.
- Mura T, Micromechanical of Defects in Solids, Kluwer Academic Publishers, 1987.
- Patoor E, Eberhardt A, and Berveiller M, "Micromechanical Modeling of Superelasticity on Shape Memory Alloys," *Pitman Research Notes*, 296, 38 - 54, 1993.
- Patoor E, Amrani El M, Eberhardt A, and Berveiller M, "Determination of the Origin for the Dissymmetry Observed between Tensile and Compression Tests on Shape Memory Alloys," *J. D. Physique*, vol. 5-C2, 495-500, 1995.
- Saburi T and Wayman C M, *Acta. Mett.*, vol. 27, 979, 1979.
- Sittner P, Novak V, and Zarubova N, "Anisotropy of Transformation Characteristics of Cu-Based Shape Memory Alloys," *To be published in Mat. Sci. Eng. A*, 1997.

CHAPTER 4: STRESS STATE EFFECTS IN POLY. CuZnAl

PREVIEW

The effect of different uniaxial and triaxial stress states on the stress-induced martensitic transformation in CuZnAl was investigated. Under uniaxial loading it was found that the compressive stress level required to macroscopically trigger the transformation was 34% larger than the required tensile stress. The triaxial tests produced effective stress-strain curves with transformation yield points in between the tensile and compressive results. It was found that pure hydrostatic pressure was unable to experimentally trigger a stress-induced martensitic transformation due to the large pressures required. Traditional continuum based transformation theories, with yield functions and Clausius-Clapeyron equations modified to depend on the volume change during transformation, could not properly predict stress state effects in CuZnAl. Considering a combination of hydrostatic (volume change) effects and crystallographic effects (number of transforming variants), an accurate model was used to predict the dependence of the critical macroscopic transformation yield stress on the stress-state.

4.1 BACKGROUND

The experimental study of reversible stress-induced martensitic phase transformations has evolved greatly since the discovery of the shape memory effect by Chang and Read in the early 50's. Countless researchers have conducted uniaxial monotonic and cyclic tests in the temperature range where stress-induced martensitic transformations occur (temperatures greater than the martensite start temperature and below the martensite deformation induced temperature, $M_s < T < M_d$). These experiments have determined the uniaxial stress-strain response of many different shape memory alloy systems. It is widely accepted that stress-induced martensitic transformations produce

two different macroscopic stress-strain responses, pseudoelasticity and the shape memory effect [Delaely et al. 1974]. Although pseudoelasticity and shape memory are sometimes a result of martensite reorientation, this work will focus on stress-induced martensitic transformations.

To utilize the beneficial properties of shape memory alloys in engineering applications, it is essential to conduct experimental studies to understand the effect of temperature, strain rate, cyclic loading conditions, and stress state on the critical transformation stress level. Although the effect of temperature (Clausius-Clapeyron relationship), strain rate [Otsuka et al. 1976, Leo et al. 1993, Mukherjee et al. 1985], and cyclic deformation [Ahlers 1979, Brown 1979 and 1982, Sakamoto et al. 1981, Ikai et al. 1982, Sure and Brown 1984, Sade et al 1985, Miyazaki et al. 1986, Tadaki et al. 1988, Rodriguez and Guenin 1990, Picornell et al. 1990, Beyer et al. 1990] on pseudoelasticity and shape memory are all well established, there is a shortage of work on stress state effects. This gap in research efforts is most likely due to the fact that the first large scale application of shape memory alloys was in orthodontics [Andreason and Morrow 1978]. The small NiTi wires used in braces provided little motivation for the full scale testing of polycrystalline shape memory alloys under compression or even three dimensional stress states. Unfortunately, it is not an easy task to experimentally impose multi-dimensional stress states on specimens. However, there are many new applications which constitute the need for a more thorough understanding of stress state effects on polycrystalline shape memory alloy stress-strain behavior.

In many new shape memory alloy components [ICOMAT 1986 and 1990] there exist three dimensional tensile and compressive stress states during the stress-induced martensitic transformation. For example, shape memory alloys which are embedded in composite structures for active vibration control [Boyd and Lagoudas 1994] and in pressure vessels for hoop stress control [Paine and Rogers 1995] are subjected to three dimensional stress states. To properly control either parameter, the transformation yield stress

level and stress-strain response of the alloy under a constraining hydrostatic pressure must be known. Shape memory alloys are also being widely used in the medical field for endoscopic tools with increased kink resistance [Duering et al. 1996]. To precisely control bending deformation of the tool it is imperative to have a thorough understanding of the tensile and compressive behavior of the alloy. Finally, the design of components with complex geometry's requires the use of the finite element method. To implement a shape memory alloy constitutive relationship into a finite element code, the yield function must be complete in stress space.

The first researchers to note the dependence of stress-induced martensitic transformations on the applied uniaxial stress state were Kulin and colleagues [1952]. In their work it was discovered that a higher compressive stress was needed to macroscopically trigger a stress-induced martensitic transformation in steels. Only a year later Burkhart and Read [1953] discovered that the compressive stress at transformation was significantly higher than the tensile stress at transformation in In-Tl single crystals. The first report of different tensile and compressive transformation stress-strain curves for a common polycrystalline shape memory alloy (NiTi) was by Wasilewski [Wasilewski 1971]. Since then there has been numerous studies which confirm that transformation in tension is favored over compression in several shape memory alloy systems [Lieberman et al 1975, Melton 1990, Vacher and Lexcelent 1991, Chumljakov and Starenchenko 1995, Jacobus et al. 1996]. Additionally, it has also been observed that the torsion transformation yield point is well below the tensile point in NiTi [Melton 1990]. Nevertheless, in some alloy systems researchers have found that the applied stress state has little or no effect on the transformation behavior [Nakanishi et al. 1973]. In addition to this, Sakamoto and colleagues [Sakamoto et al. 1979] observed that compression is favored over tension in CuAlNi single crystals.

There are a limited number of experimental investigations which consider the effect of multi-dimensional stress states on martensitic

transformations in shape memory alloys. There is some recent experimental work on the biaxial loading of shape memory alloys [Chu and James 1993]. However, there is little research on the triaxial loading of shape memory alloys. Most of the research on multi-dimensional stress states focuses on the effect of pure hydrostatic pressure on the martensite start temperature. This area of study was sparked by the work of Patel and Cohen some 40 years ago [1953]. Since then, it has been agreed on that hydrostatic pressure alters M_s in both steels [Nishiyama 1978] and shape memory alloys [Kakeshita et al. 1988 and 1992]. In many of the above research efforts, the hydrostatic pressure was ramped to a specified value, the temperature was cycled, and M_s was determined using resistivity-temperature curves. In the absence of an applied effective stress, it was found that pure hydrostatic pressure decreases M_s for materials exhibiting a positive volume change upon transformation, and increases M_s for materials with a negative volume change. If the pressure is large enough, then the transformation can be triggered without any effective stress, provided that the M_s temperature is moving towards the test temperature.

The effect of hydrostatic pressure on the effective stress level necessary to induce the transformation can be explained in terms of a Clausius-Clapeyron line in stress-temperature space. If pure hydrostatic pressure exists before an effective stress is applied, then M_s is altered and the Clausius-Clapeyron line is uniformly *shifted* left or right in stress-temperature space. However, regardless of the initial value of the hydrostatic pressure, as an effective stress is applied the hydrostatic pressure may increase, decrease, or not change at all. The effect of hydrostatic pressure has been accounted for in thermodynamically based continuum transformation yield criteria [Sun and Hwang 1991, Boyd and Lagoudas 1996]. Furthermore, it has been shown that the modified yield criteria can be used to develop a Clausius-Clapeyron line with a hydrostatic stress dependent *slope* [Jacobus et al. 1996]. In either case, hydrostatic pressure increases the effective stress necessary for transformation

in materials which have positive volume changes during transformation, and decreases the effective stress necessary for transformation in materials which have negative volume changes during transformation. Nevertheless, when comparing the experimental results under some stress states, the macroscopic transformation behavior follows the reverse of the above behavior [Jacobus et al. 1996]. This inconsistency is caused by stress-state dependent crystallographic effects which overshadow the dependence of the transformation behavior on the volume change during the transformation [Patoor et al. 1994]. This issue will be discussed in the micro-mechanical modeling section of this work.

Despite this background, there is still a shortage of experimental work which focuses on the effect of the applied stress state on the mechanical behavior of shape memory alloys. Many of the current 3-D transformation constitutive models are simple extensions of 1-D models based on tensile stress-strain observations [Brandon and Rogers 1992, Sun and Hwang 1993, Kafka 1994, Barrett and Sullivan 1995, Baburaj et al. 1996]. Although many of the 1-D models are quite extensive they all fail to capture 3-D stress state effects or tension-compression asymmetry. A detailed review of the physical basis and micro-mechanics of the current 1-D models was recently published by Brinson and Huang [Brinson and Huang 1996]. It should be noted that there are several models [Sun and Hwang 1991, Patoor et al. 1994, Boyd and Lagoudas 1996] which include a dependence on the applied stress state. These models will be discussed within the context of this paper. In addition, the researchers here will lay further foundation to the doctrine that shape memory alloy transformation stress-strain behavior is dependent on the applied stress state. More explicitly, the paper will:

- (1) Examine the monotonic stress-strain behavior of CuZnAl (at a constant temperature above the martensite start temperature, and below the martensite deformation induced temperature, $M_s < T < M_d$) under tensile, compressive, and three dimensional stress states.

(2) Use microscopically observed phenomenon and micro-mechanical modeling to discuss the origins of stress state effects in CuZnAl.

4.2 EXPERIMENTAL TECHNIQUES

Polycrystalline $\text{Cu}_{59.1}\text{Zn}_{27.0}\text{Al}_{13.8}$ (with $\text{Zr}_{0.1}$ for grain refinement) weight percent alloy was employed for the study. The average grain size of the polycrystalline specimens after heat treatment was 250 μm . Upon complete transformation from the parent phase to the martensitic phase, it was experimentally determined that this CuZnAl alloy demonstrates a negative change in volume, $\Delta V/V \approx -0.3\%$. The scanning electron microscope images were created from electropolished and chemically etched samples. The optimum electropolish (with a 2:1 Methanol/Nitric acid solution) was achieved at -30°C and 70 Volts. The chemical etchant used to "view" the martensite plates was 5g FeCl_3 + 50 ml HCl and 100 ml H_2O .

To study the effect of the applied stress state on stress-induced martensitic transformations, it is imperative that the transformation be triggered by the applied stress. To do this, it is important to stress the specimen when it is above the martensite start temperature, M_s , but below the martensite deformation induced temperature, M_d . The former constraint inhibits the spontaneous nucleation of martensite before the stress is applied, while the latter avoids excessive plastic deformation in the parent phase during the early stages of the transformation. This type of deformation leads to strain-induced martensitic transformations. The magnitude of M_s was carefully controlled using heat treatments, and the resulting temperature value was verified using a Differential Scanning Calorimeter (DSC) analysis. The heat treatment was accomplished for one hour at 800°C and followed by a water quench. From several specimens, the average values of the critical transformation temperatures are: martensite start temperature, $M_s \approx -10^\circ\text{C}$,

martensite finish temperature, $M_f \approx -32\text{ }^\circ\text{C}$, austenite start temperature, $A_s \approx$

Test Number & Description	Applied Stress State	Relative Hydrostatic Pressure
(#1) Pure Tension	$\sigma_{ij} = \begin{bmatrix} \sigma & 0 & 0 \\ 0 & 0 & 0 \\ 0 & 0 & 0 \end{bmatrix}$	$\sigma_h = -0.33\sigma_{eff}$
(#2) Zero Hydrostatic	$\sigma_{ij} = \begin{bmatrix} 2\sigma & 0 & 0 \\ 0 & -\sigma & 0 \\ 0 & 0 & -\sigma \end{bmatrix}$	$\sigma_h = 0.00\sigma_{eff}$
(#3) Pure Compression	$\sigma_{ij} = \begin{bmatrix} -\sigma & 0 & 0 \\ 0 & 0 & 0 \\ 0 & 0 & 0 \end{bmatrix}$	$\sigma_h = +0.33\sigma_{eff}$
(#4) Triaxial Compression	$\sigma_{ij} = \begin{bmatrix} -3\sigma & 0 & 0 \\ 0 & -\sigma & 0 \\ 0 & 0 & -\sigma \end{bmatrix}$	$\sigma_h = +0.83\sigma_{eff}$
(#5) Triaxial Compression	$\sigma_{ij} = \begin{bmatrix} -2\sigma & 0 & 0 \\ 0 & -\sigma & 0 \\ 0 & 0 & -\sigma \end{bmatrix}$	$\sigma_h = +1.33\sigma_{eff}$
(#6) Triaxial Compression	$\sigma_{ij} = \begin{bmatrix} -1.7\sigma & 0 & 0 \\ 0 & -\sigma & 0 \\ 0 & 0 & -\sigma \end{bmatrix}$	$\sigma_h = +1.76\sigma_{eff}$
(#7) Pure Hydrostatic	$\sigma_{ij} = \begin{bmatrix} -\sigma & 0 & 0 \\ 0 & -\sigma & 0 \\ 0 & 0 & -\sigma \end{bmatrix}$	$\sigma_h = +\infty\sigma_{eff}$

Table 4.2.1: Uniaxial (1 & 3) and three dimensional (2 & 4-7) stress states applied to the polycrystalline CuZnAl specimens. The tests have increasing values of applied hydrostatic pressure with respect to the applied effective stress. Note that the hydrostatic *stress* is negative while the hydrostatic *pressure* is positive.

-15 °C, austenite finish temperature, $A_f \approx 5$ °C. The tests in this study were conducted at room temperature where the sample is fully austenitic ($T > A_f$).

Uniaxial loading of CuZnAl was performed on an Instron 1331 servohydraulic test machine operating in axial strain control. For tensile tests, an extensometer with a 25.4 mm gage length was used to monitor axial strains and a diametral extensometer was used to monitor the diametral strains. For compression tests, axial and diametral strains were monitored with electrical resistance strain gages bonded to the specimen gage section. An MTS servohydraulic test machine fitted with a unique high pressure vessel was used for triaxial testing of CuZnAl specimens. Axial and diametral strains were monitored by a pair of strain gages bonded to the specimen gage section. Pressure effects on the strain gage output were eliminated by wiring a gaged dummy specimen into the circuit inside the vessel. A miniature strain gage load cell placed in the top section of the pressure vessel was used to measure axial specimen load. This allowed the measurement of load without having to account for seal friction. Diametral specimen pressure was monitored by a pressure transducer.

Control of the high pressure testing setup was accomplished with two independent control loops - one for the MTS axial actuator and a second for the servohydraulic pressure intensifier. The independent control loops allow for the application of any desired axial stress/lateral stress ratio within load and specimen stability limits. The ability of the present triaxial testing apparatus to simultaneously ramp the lateral and axial stresses on the specimen represents one of its main advantages over previous triaxial research efforts. In previous works, hydrostatic compression was typically applied first and the uniaxial stress was increased in a secondary operation. The present scheme circumvents any arguments regarding the role of initial hydrostatic pressure on the material behavior [Radcliffe 1970] (i.e. initial changes in M_s). More details of the pressure intensifier, load and strain

measurements can be found in a recent publication [Balzer and Sehitoglu 1996].

To allow for comparisons between uniaxial and triaxial tests, the loading rates in the triaxial tests were selected such that they imposed effective strain rates in the elastic regime equivalent to those utilized in the uniaxial tests: 10^{-4} s^{-1} . The effective stress required to bring about the austenite to martensite transformation, σ_{eff}^y , was determined from effective stress vs. effective strain plots using several strain offsets. The effective stress and strain values were calculated with the following relationships.

$$\sigma_{eff} = \frac{\sqrt{2}}{2} \left[(\sigma_{11} - \sigma_{22})^2 + (\sigma_{11} - \sigma_{33})^2 + (\sigma_{22} - \sigma_{33})^2 \right]^{1/2} \quad (4.2.1)$$

$$\varepsilon_{eff} = \frac{\sqrt{2}}{3} \left[(\varepsilon_{11} - \varepsilon_{22})^2 + (\varepsilon_{11} - \varepsilon_{33})^2 + (\varepsilon_{22} - \varepsilon_{33})^2 \right]^{1/2} \quad (4.2.2)$$

The relationship between the effective stress values and the hydrostatic stress values as a function of the applied stress state are demonstrated in Table 4.2.1. It should be noted that both the axial and diametral strains were measured.

4.3 EXPERIMENTAL RESULTS

The first stress-strain curves presented are the uniaxial tension and compression curves (figure 4.3.1). The tensile specimens were loaded until failure (about 8% strain), while the compressive specimens were unloaded at 8% strain to avoid buckling. Since the slope of all four curves remained constant after about 1% strain, only the small strain portions of the curves are shown in figure 4.3.1. The tensile specimens fractured in a ductile manner, indicating that there was considerable plastic deformation during the latter portion of the transformation. If there were no plastic deformation, then stress-strain curves would have bent upward marking the completion of the

transformation and the beginning of the elastic deformation of the martensite. Alternatively, the curve could have continued along its present

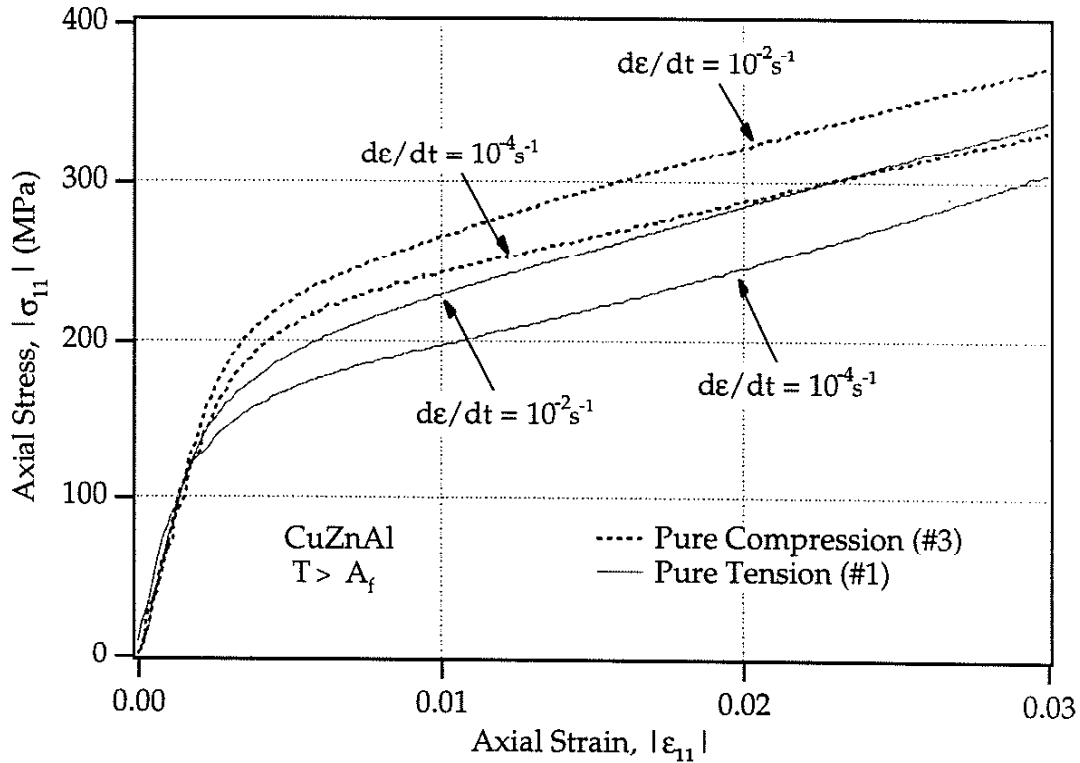


Figure 4.3.1: Uniaxial stress-strain plots for a polycrystalline CuZnAl shape memory alloy specimen above the austenite finish temperature, A_f . The plot demonstrates the asymmetry between tensile and compressive loading at high and low strain rates.

path if the fully transformed martensitic structure reoriented itself. The existence of plastic deformation is reaffirmed by the stress-strain behavior of the compressive specimens. When the material was compressed to large strains (8%), and unloaded, large permanent strains (nearly 7%) were left in the specimen. In other words, the excessive plastic strains decrease the magnitude of the recoverable pseudoelastic strains in CuZnAl to about 1%. However, if the deformation was limited to 3% then the recoverable strain magnitude is nearly 2.5% (figure 4.3.2). It is clear that the plastic strains mask the thermoelastic nature of the martensite, hence decreasing recoverability.

The onset of the transformation in the specimens is dependent on both the applied stress state (tension or compression) and the strain rate

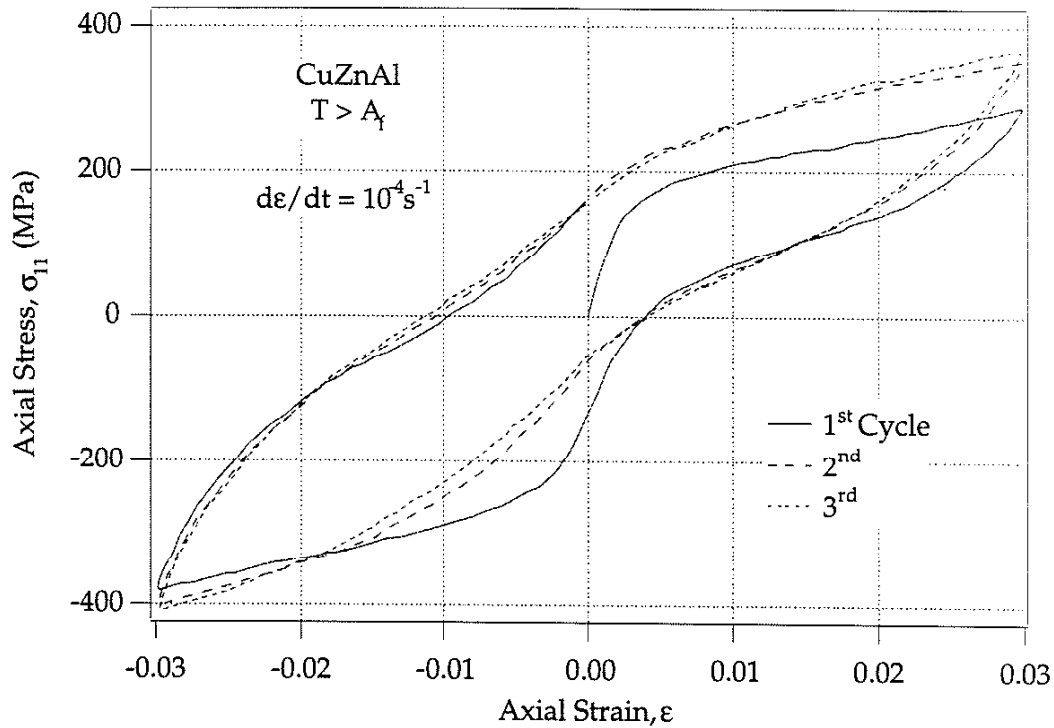


Figure 4.3.2: Cyclic ($R = -1$) stress-strain loops for a polycrystalline CuZnAl shape memory alloy specimen above the austenite finish temperature, A_f . The plot demonstrates the existence of the pseudoelastic effect for strains up to 3% and the asymmetry between tensile and compressive behavior during cyclic loading.

($\dot{\epsilon} = 10^{-4} s^{-1}$ or $10^{-2} s^{-1}$). For both strain rates a higher compressive stress is needed to macroscopically trigger the stress-induced martensitic transformation. Although this paper does not focus on the cyclic behavior of CuZnAl, it should be noted that tension-compression asymmetry can also be seen in $R = -1$ cyclic stress-strain loops (figure 4.3.2). The stress-strain results for several different triaxial tests (Table 4.2.1) are presented in figure 4.3.3. For the sake of clarity, some of the tests which produced similar results are not included in figure 4.3.3. The stress-strain curves in figure 4.3.3 are cut off at 3% strain due to the continuity of the slopes in the post yielding regime. The

unloading behaviors of the zero hydrostatic and triaxial compression tests are the same as the pure compression test. Namely, quasi-elastic unloading with

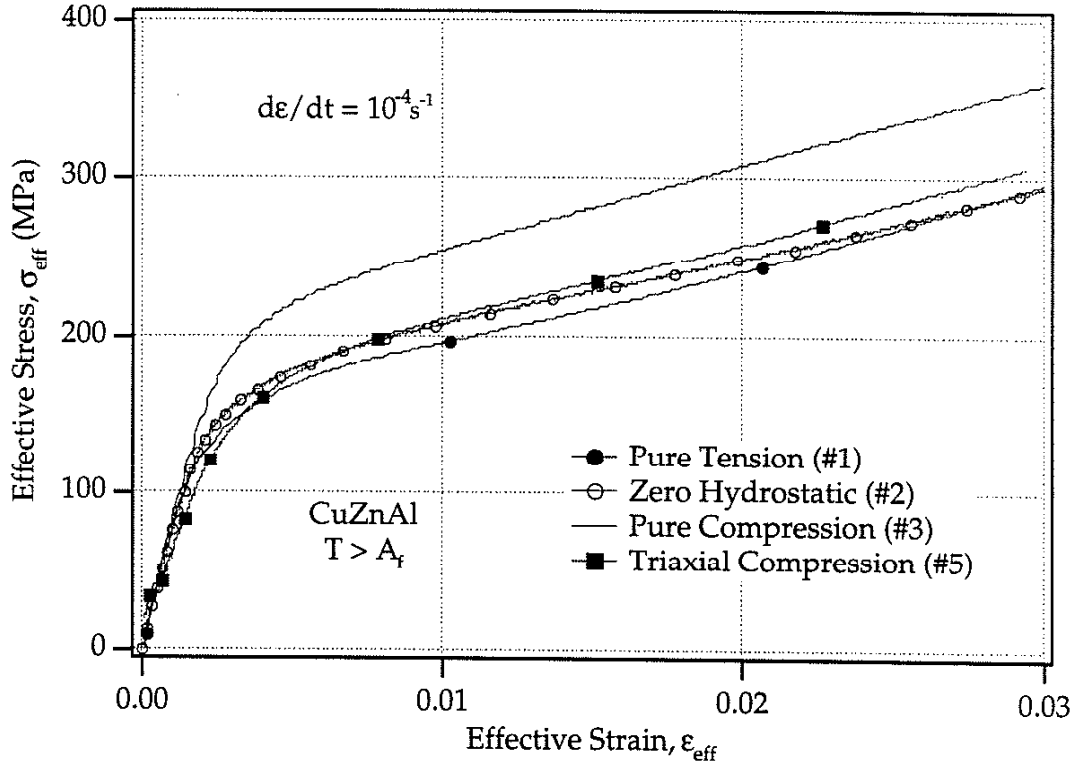


Figure 4.3.3: Effective stress-strain plots for a polycrystalline CuZnAl shape memory alloy specimen above the austenite finish temperature, A_f . The plot demonstrates the effect of several different three dimensional stress states on the transformation behavior.

large residual strains upon complete load removal from 8% strain. Once again, small magnitude of recoverable strains is due to the decrease in thermoelastic martensite. For comparisons sake, the results of the tension and compression tests are included in figure 4.3.3. All of the triaxial stress states in this study produced effective stress-strain responses in between effective tensile and compressive responses of the material.

A composite plot of the effective stress at the onset of the transformation (σ_{eff}^y) versus the hydrostatic stress at the onset of the transformation (σ_h^y) is shown in figure 4.3.4. The transformation criteria [Sun

and Hwang 1991, Boyd and Lagoudas 1996] which assume that increasing hydrostatic pressure raises or lowers the stress at transformation (for positive

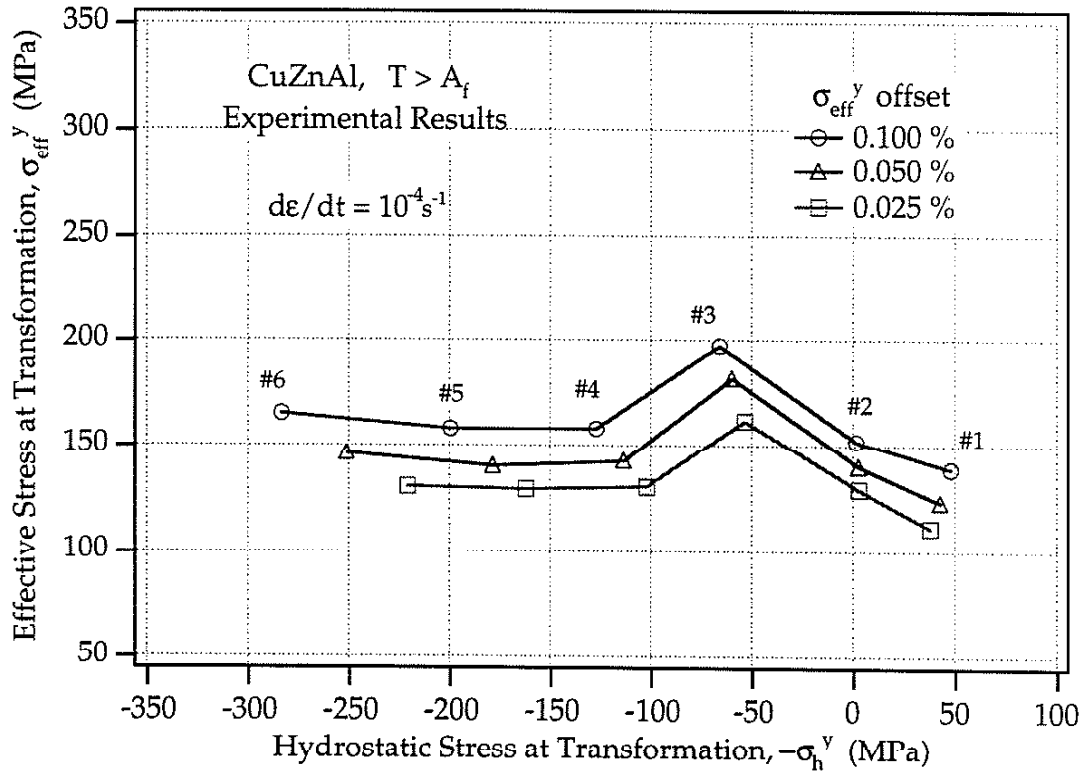


Figure 4.3.4: Plot of the effective stress at the onset transformation versus the hydrostatic stress at the onset transformation for a polycrystalline CuZnAl shape memory alloy specimen above the austenite finish temperature, A_f . The negative sign in front of σ_h^y converts the hydrostatic pressure into hydrostatic stress.

and negative volume changes during transformation respectively) cannot predict the experimental trends observed in figure 4.3.4. A study of the transforming microstructure along with micro-mechanical modeling is needed to help explain and predict stress state effects in CuZnAl.

The effect of pure hydrostatic pressure on the deformation of CuZnAl is shown in figure 4.3.5. The loading and unloading curves lie directly on top of each other. The stress-strain behavior of CuZnAl is completely elastic up to hydrostatic pressures of 700 MPa. The axial and diametral strain are nearly identical with some texture effects providing the difference. The elastic

behavior reveals that the hydrostatic pressure is not large enough to raise M_s

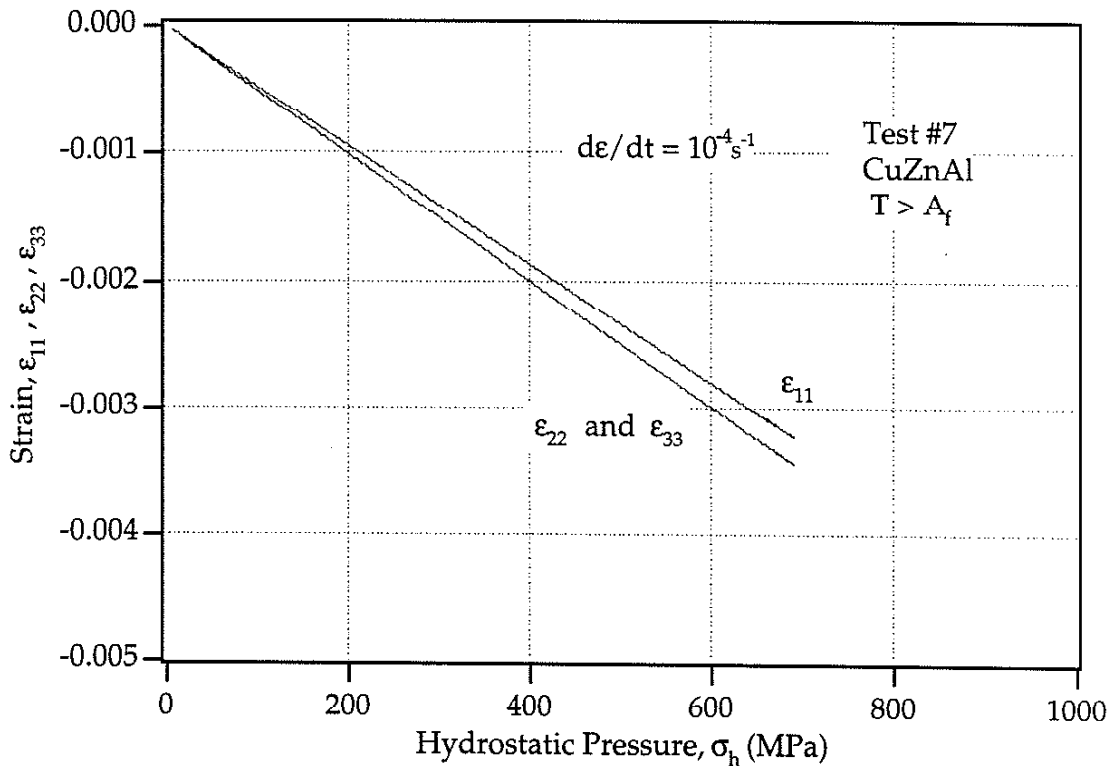


Figure 4.3.5: Response of a polycrystalline CuZnAl shape memory alloy, above the austenite finish temperature, A_f , to pure hydrostatic pressure. No stress-induced martensitic transformation is observed for pressures up to 700 MPa. The difference in the axial, ϵ_{11} , and diametral, ϵ_{22} and ϵ_{33} , strains is an artifact of texture induced during the drawing of the bars.

to room temperature and thermally trigger the transformation; to reach room temperature M_s would have to rise by 35 °C. This fact, coupled with the magnitude of the pressure change used in this study, $\Delta\sigma_h \approx 700\text{MPa}$, indicate that hydrostatic pressure has little effect on the M_s temperature in CuZnAl. The change in M_s with pure hydrostatic pressure lies within the range $0.00 < \Delta M_s / \Delta\sigma_h < 0.05$ °C/MPa. The former bound indicates that M_s increases for a CuZnAl alloy with a negative volume change during transformation, while the latter bound is formed by taking the ratio of the temperature raise needed and the pressure applied. Since M_s is rather insensitive to hydrostatic pressure, it is further reaffirmed that the stress state effects experimentally

observed here are caused by something other than the small hydrostatic pressure induced changes in the Clausius-Clapeyron line.

4.4 MICROSCOPIC OBSERVATIONS

It has been determined that hydrostatic pressure differences between stress states are not solely responsible for the stress state effects in CuZnAl. Patoor and colleagues have postulated that the hydrostatic pressure effects are being overshadowed by crystallographic effects unique to transformation twinning [Patoor et al. 1994]. In a real CuZnAl grain, there are up to 24 different microscopic martensite plates, or crystallographic variants, which can contribute to the macroscopic growth of the martensite [Schroeder and

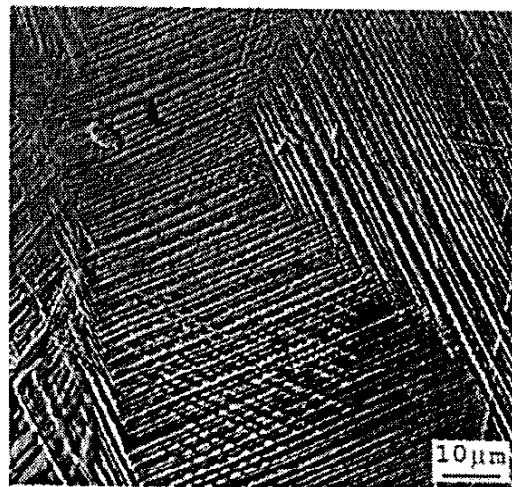


Figure 4.4.1: Scanning electron microscope image of several partially transformed CuZnAl grains. The needle like lines are 2-D cross sections of martensite plates (variants). The raised appearance of the plates is due to the deep etching of the parent phase. The picture demonstrates that the formation of martensite variants between grains is highly dependent on the crystallographic orientation of the grains.

Wayman 1979]. Although there are 24 variants available for transformation, not all of these microscopic variants will contribute to the macroscopic martensite growth. The applied stress state in a single crystal, or the internal stress field in a polycrystalline material, favor the activation of a small number of specific variants martensite [Schroeder and Wayman 1979].

The number of variants activated per grain, and the activation of different variants in different grains is demonstrated here in a scanning electron microscope (SEM) micrograph. Figure 4.4.1 is a SEM micrograph of the intersection of several grains of CuZnAl. The martensite plates are the thin needlelike features on the image. The raised appearance of the plates is due to the deep etching of the surface. The micrograph clearly shows that grains with different crystallographic orientations promote the growth of martensite variants with different orientations. The variants which are chosen for nucleation and growth are the ones which are oriented most favorably with respect to the intergranular stress field. It is clear that about two variants control the transformation from austenite to martensite. Generally, the average number of active stress-induced variants per grain was two. In very few cases there was only one dominant variant, and hardly ever more than three dominant variants.

4.5 MICRO-MECHANICAL MODELING

Most of the 3-D transformation criteria which include a dependence on the applied stress-state [Sun and Hwang 1991, Boyd and Lagoudas 1996] still produce results which are contrary to experimental trends [Jacobus et al. 1996]. In both models* a single martensite plate (single inhomogeneity), and its volume fraction evolution rate, control the transformation for the entire polycrystalline constitutive element. The simplification of a single transforming variant cannot account for the directionality of twinning. The reason that the transformation behavior cannot be smeared out at the microstructural level is due to the directionality and low symmetry of twinning. In a given twin system, twinning only occurs along the specified direction. This is in contrast to slip where shearing may occur along

* The Boyd and Lagoudas model has the framework to consider several internal variables (volume fractions of martensite in this case). However, they choose not to use several martensitic volume fractions so that they can derive explicit constitutive expressions for the transformation stress-strain behavior.

conjugate directions depending on the direction of the resolved shear stress. This result has been micro-mechanically demonstrated by considering the elastic strain energy created by twins in conjugate directions [Kumosa 1991]. As a result, twin systems which activate under a particular stress state may never activate under a different stress state. Intuitively, this effect should be averaged out in a polycrystalline specimen. However, the low symmetry of the 24 twin systems in shape memory alloys prevent this [Patoor et al. 1995].

To better understand the origins of stress state effects in CuZnAl, thermodynamics and the phenomenological theory of martensitic transformations are used to develop a micro-mechanical model. In the case where multiple variants are active, the total transformation strain rate in a single crystal of the parent phase is:

$$\dot{E}_{ij}^{tr} = g \sum_n \alpha_{ij}^n \dot{f}^n \quad (4.5.1)$$

where g is the magnitude of the shape strain, α_{ij}^n is the orientation tensor of the n^{th} variant defined as: $\alpha_{ij}^n = \frac{1}{2}(m_i^n n_j^n + m_j^n n_i^n)$, f^n is the volume fraction of martensite for the n^{th} variant, and m^n and n^n are unit vectors characterizing the transformation direction and habit plane normal for the n^{th} variant. The parameters used to model this CuZnAl alloy are: $n^n = (0.200, 0.680, 0.705)$, $m^n = (0.182, -0.746, 0.641)$, and $g = .19$. The transformation direction and slip plane normal for the other 23 directions are obtained through cyclic permutation. The total transformed volume fraction of martensite in the crystal is the sum of the individual martensite variant volume fractions:

$$f = \sum_n f^n \quad (4.5.2)$$

The total volume fraction of martensite cannot exceed 1, thus equation 4.5.2 is restricted to $f \leq 1$. The summation only holds for martensite variants which are currently active.

The isothermal transformation criteria for individual variants is written as:

$$g \Sigma_{ij} \alpha_{ij}^n \geq F_c \quad (4.5.3)$$

Where F_c is an experimentally determined constant, and Σ_{ij} is the applied stress state. The constant F_c is analogous to the critical resolved shear stress in the phenomenological theory of slip. It should be noted that the left hand side of equation 4.5.3 may not be positive for a specific variant under a given applied stress state. In this case, that particular variant is not *available* for the transformation. The volume fraction evolution rate for the n^{th} variant is given as.

$$\dot{f}^n = \frac{g \alpha_{ij}^n \dot{\Sigma}_{ij}}{f'} \quad (4.5.4)$$

where f' is a constant which describes the “hardening” of the transforming variant. It quantifies the increase in the applied stress, Σ_{ij} , necessary to continue the transformation. In the present simulations the authors did not account for variant interaction due to the complexity of the phenomenon. A model for the interaction of martensite variants has been developed by Fassi-Fehri and colleagues [Fassi-Fehri et al. 1987]. The interaction term does help the micro-mechanical model to predict transformation stress-strain slopes slightly better. However, the purpose of this model is to help understand stress state effects in the early phases of the transformation, and not to predict the shape of stress strain curves at higher strains.

The previous relationships for the transformation criteria and flow rate describe a martensitic transformation in a single crystal. In a polycrystalline body undergoing a stress induced martensitic phase transformation, there exists many single crystals (grains) which are oriented favorably and unfavorably with respect to the applied stress state. The misorientation will result in unbalanced transformation strain magnitudes for neighboring grains. In turn, the difference in transformation strain levels leads to local (position dependent) stress and strain fields throughout the polycrystalline body. The self consistent method [Mura 1987] assumes that the magnitude of the resulting internal stress and strain fields can be estimated by the difference in the average transformation strain of the polycrystalline matrix and the local transformation strain in any particular grain ($E_{mn}^{tr} - \epsilon_{mn}^{tr}$). The self consistent method then uses the mismatch strain ($E_{mn}^{tr} - \epsilon_{mn}^{tr}$) as the eigenstrain for the Eshelby inclusion problem. Along with the elastic constitutive relationship, this allows the derivation of a general relationship relating average stress and strain of the polycrystalline body to the local stress and strain in each grain. The most general form of the self consistent equation is given as [Mura 1987].

$$\Sigma_{ij} = \sigma_{ij} + C_{ijkl} [S_{klmn} (E_{mn}^{tr} - \epsilon_{mn}^{tr}) - (E_{kl}^{tr} - \epsilon_{kl}^{tr})] \quad (4.5.5)$$

where S_{ijkl} is the Eshelby tensor [Mura 1987] and C_{ijkl} is the elasticity tensor. The upper case symbols represent local stresses and strains and the greek symbols represent average stresses and strain in the polycrystalline body. Multiplying equation 4.5.5 by $g\alpha_{ij}^n$ and employing equations 4.5.1 and 4.5.4, equation 4.5.5 can be written as:

$$\begin{aligned} & g\alpha_{ij}^n \dot{\sigma}_{ij} - g\alpha_{ij}^n C_{ijkl} S_{klmn} \dot{\epsilon}_{mn}^{tr} + g\alpha_{ij}^n C_{ijkl} \dot{\epsilon}_{kl}^{tr} \\ & = f \dot{f}^n - g^2 \alpha_{ij}^n C_{ijkl} S_{klmn} \sum_n \alpha_{mn}^n \dot{f}^n + g^2 \alpha_{ij}^n C_{ijkl} \sum_n \alpha_{kl}^n \dot{f}^n \end{aligned} \quad (4.5.6)$$

Equation 4.5.6 is used to generate the polycrystalline stress-strain behavior for CuZnAl shape memory alloys. Equation 4.5.6 is only implemented when the first variant within a grain reaches the critical transformation value (equation 4.5.3). Additionally, the summations only hold for variants which subsequently satisfy equation 4.5.3.

In its most general form, equation 4.5.6 represents a 24 by 24 system of linear equations to be solved for each load increment in each grain. On average, 100 to 1000 randomly oriented (α_{ij}^n rotated) grains were used to model a polycrystalline material. To simplify the Eshelby tensor the grains were assumed to be spherical in shape. The variables on the left hand side of the equation represent the known quantities at each load step, while the right hand side carries the only unknown, the volume fraction evolution of martensite, f^n . For a given applied stress increment, $\dot{\sigma}_{ij}$, f^n is calculated for each variant in every grain. Subsequently, equation 4.5.1 is used to calculate the transformation strain increment in each grain, \dot{E}_{ij}^{tr} . Finally, the values of \dot{E}_{ij}^{tr} are averaged to obtain $\dot{\epsilon}_{ij}^{tr}$.

4.6 DISCUSSION

Figure 4.6.1 is a numerical simulation of the experimental results shown in figure 4.3.4. It is clear that the micro-mechanical model predicts the general trends in stress state effects, however, it is still necessary to analyze some of the microscopic factors which contribute to this agreement. Figure 4.6.2 is a plot of the average martensite volume fraction as a function of the applied effective stress level. The model predicts that the evolution of martensite will be quickest in pure tension, subsequently slower in triaxial compression, and even slower in pure compression. This difference in microscopic martensite evolution rates is one reason that the experimental stress-strain plots are different for different stress states. For example, if the

martensite is evolving faster in the case of pure tension than the transformation strain will also accumulate faster, as seen in figure 4.3.3.

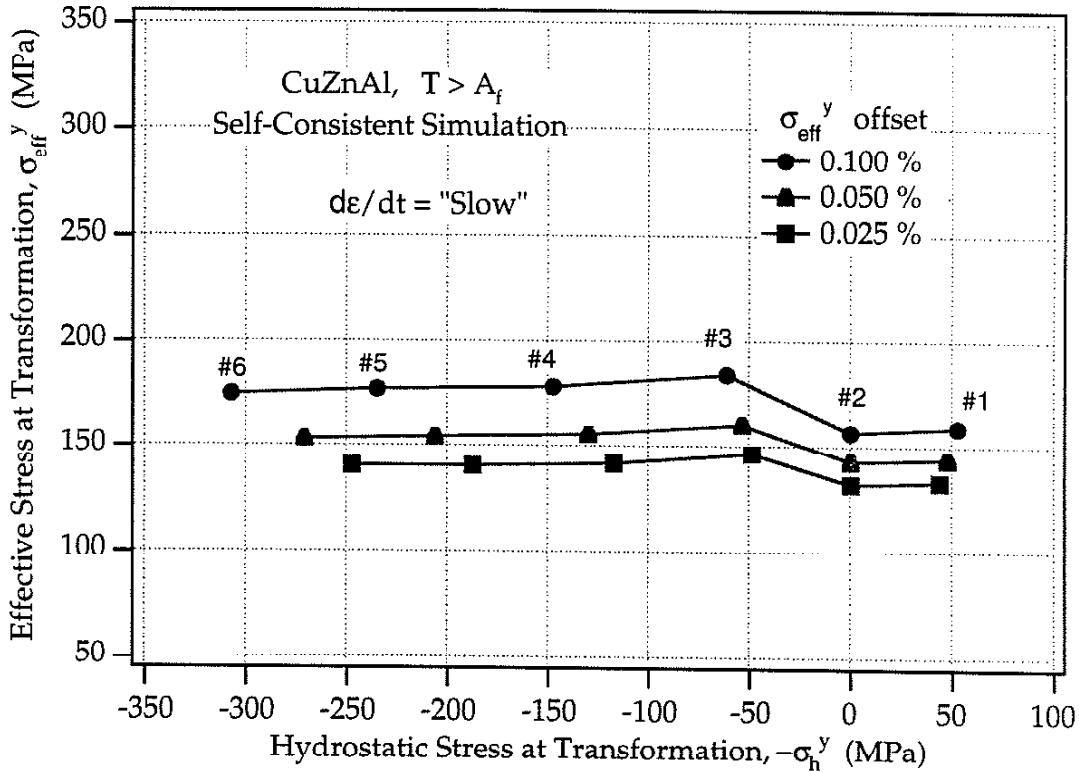


Figure 4.6.1: Plot of the effective stress at the onset of transformation versus the hydrostatic stress at the onset transformation for a polycrystalline CuZnAl shape memory alloy. The plot was generated from effective stress-strain plots created using a self-consistent scheme similar to the model of Patoor et al. 1994. The numerical model predicts the general experimental trends observed in this CuZnAl alloy.

At the microscopic level, the differences in the martensite evolution rates are due to the fact that in some stress states there are more martensite variants *available* for the transformation. Recall that a variant is available for the transformation if the left hand side of equation 4.5.3 is positive under the applied stress state. Clearly from equation 4.5.3, the variants available under tension will never activate under compression. For example, consider a single cubic crystal of CuZnAl with the three cubic axes aligned along the three principal stress axes. Under pure tension 16 of the 24 possible variants are available for transformation. Conversely, under pure compression, only 8

of the variants are available for transformation. The 8 variants which

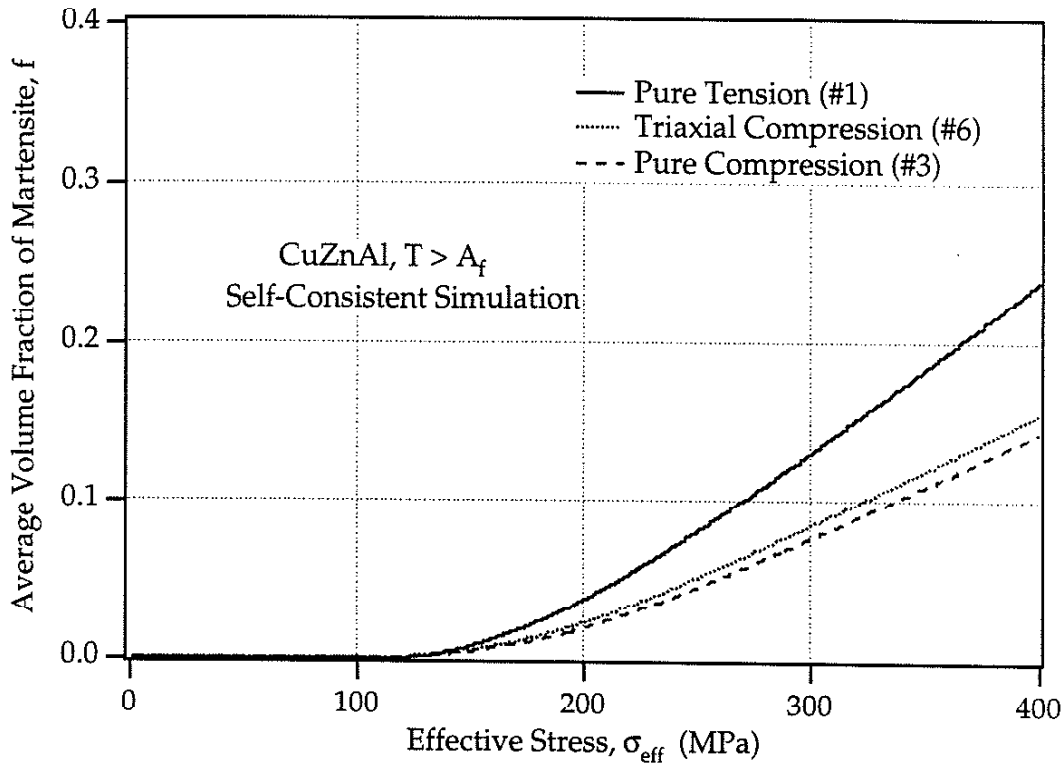


Figure 4.6.2: Plot of the average volume fraction of martensite versus the applied effective stress for a polycrystalline CuZnAl shape memory alloy. The plot was generated using a self-consistent scheme similar to the model of Patoor et al. 1994. For the growth of martensite, pure tension is the most favorable stress state while pure compression is the least favorable.

activate under compression will never contribute to the transformation under tension and vice versa. Under any other three dimensional stress state the number of active variants depends on the ratios and directions of the three applied stresses. As the crystallographic orientation of the single crystal is changed, with respect to the principal stress axes, the number of available variants corresponding to a particular stress state changes.

The combination of many single crystals with different crystallographic orientations creates a polycrystalline material which favors different stress states. Using the present numerical model, it can be shown that the number of variants which activate per grain in polycrystalline CuZnAl is also dependent on the applied stress state (figure 4.6.3). The largest number of

active variants occurs in tension, followed by triaxial compression, and finally by compression. From figure 4.6.3 it is also clear that the average number of active variants per grain quickly approaches about 2, as observed microscopically (figure 4.4.1). The small offset in the curves at the very start

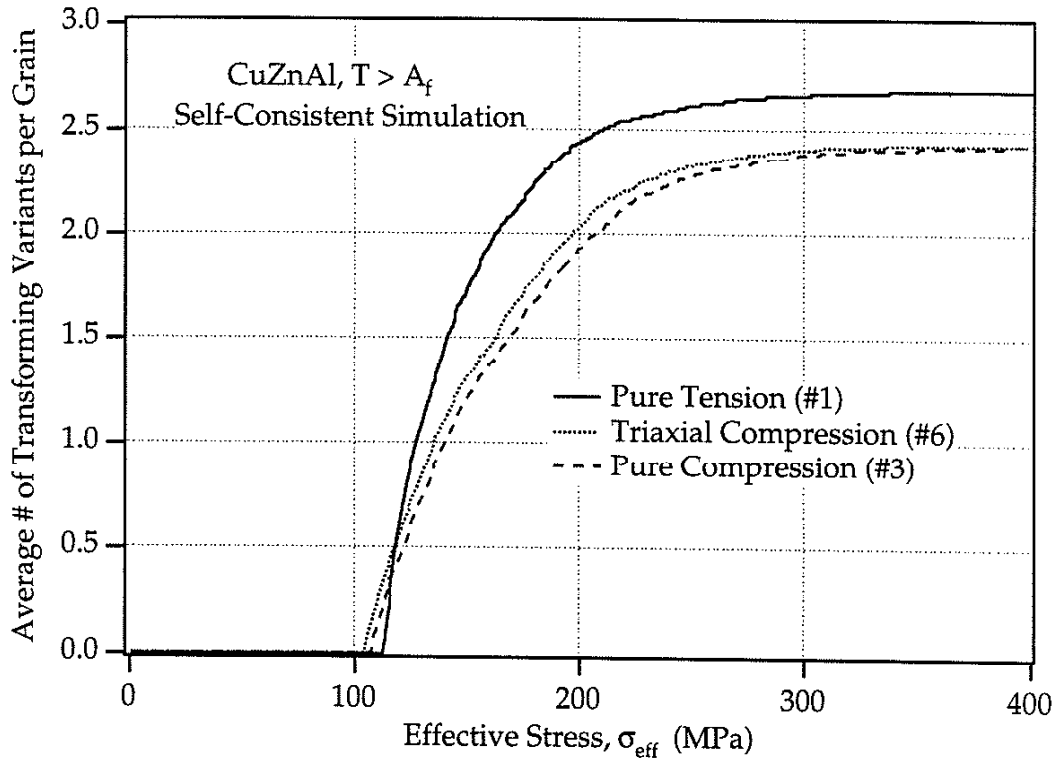


Figure 4.6.3: Plot of the average number of active martensite variants versus the applied effective stress for a polycrystalline CuZnAl shape memory alloy. The plot was generated using a self-consistent scheme similar to the model of Patoor et al. 1994. At a given applied stress level, pure tension activates the largest number of martensite variants followed by triaxial compression and then pure compression.

of the transformation is due to the hydrostatic stress differences between the stress states. When comparing tensile and compressive loading, the small offset caused by hydrostatic differences between the stress states is quickly overshadowed. In summary, the stress states which have a smaller average number of variants transforming per grain (figure 4.6.3) clearly have slower martensite growth rates (figure 4.6.2) and consequently higher offset transformation yield stress values (figures 4.3.4 and 4.6.1). The above

argument which states that different stress states activate different quantities of martensite variants during transformation is deemed here the 'crystallographic' stress state effect.

At this point it is useful to discuss the relationship of figure 4.6.1 to the transformation behavior of other stress states as discovered in experiments and predicted by continuum based models. Figure 4.6.1 predicts that pure compression has the highest yield point and that pure tension has the lowest. In addition, the stress-strain curves for the triaxial tests have yield points in between the tensile and compressive behaviors. Although it is not shown on figure 4.6.1, the model also predicted that pure hydrostatic pressure would trigger the transformation at around 2900 MPa, and that negative hydrostatic pressure would never cause the transformation. This indicates that, for large changes in the hydrostatic pressure, the crystallographic model agrees with experimental results and the continuum based models on the *overall* effect of hydrostatic pressure on the transformation yield stress level. However, this agreement breaks down for small changes in hydrostatic pressure (i.e. the hydrostatic pressures range in figure 4.6.1), where the continuum based models cannot predict asymmetry between stress states. It should be noted here that lowering the temperature or increasing the hydrostatic pressure are thermodynamically equivalent. That is, along with the effective stress, hydrostatic pressure and temperature are both state variables which change the free energy barrier to transformation.

It is now obvious that the primary advantage of the crystallographic model is that it captures experimental stress state trends for any change in hydrostatic pressures between stress states. This is due to the fact that the crystallographic model microscopically accounts for both crystallographic (number of transforming variants) and hydrostatic (volume change) effects on stress states. It is important to note that the transformation behavior is still dependent on the hydrostatic pressure as originally observed. More specifically, increasing the hydrostatic pressure lowers the effective stress for transformation while decreasing the hydrostatic pressure raises the effective

stress necessary for transformation. However, it should be noted that the dependence of the effective stress at transformation on the hydrostatic stress is very small. At very high (positive) hydrostatic pressures the effective transformation yield stress approaches zero, while at very low (negative) hydrostatic pressures the effective transformation yield stress approaches infinity. Recall that this previous statement is only true since this CuZnAl alloy undergoes a negative volume change during the transformation. It is this response to hydrostatic pressure that may cause researchers to incorrectly link the pure tension and compression asymmetry to hydrostatic stress differences between the two stress states.

At the microscopic level, the crystallographic (number of transforming variants) and hydrostatic (volume change) effects are clearly defined. When a particular stress state is applied, and the transformation criteria is satisfied for several preferred variants, the variants begin to transform. If the stress state is crystallographically favored then more variants will activate than if it is not. In general, the crystallographic effect favors stress states which have dominant principal stresses in tension. Regardless of the number of variants which activate, the hydrostatic pressure imposed on the individual variants is also playing a role in the nucleation and subsequent transformation. If the selected variants are attempting to expand while growing then the hydrostatic pressure will hinder nucleation and growth. Conversely, if the selected variants are attempting to contract while growing then the hydrostatic pressure will promote nucleation and growth.

At the macroscopic level, it is insightful to simply "view" stress state effects in this CuZnAl alloy as a balance between crystallographic (number of transforming variants) and hydrostatic pressure (volume change) effects. Both effects always play a role in determining the transformation stress-strain response of the CuZnAl. The importance of one effect over the other depends on the relative change in the hydrostatic pressure between the stress states. For example, the difference in hydrostatic pressure (at the yield point) between tension and compression is about 100 MPa. If the approximate scale

for hydrostatic effects is taken to be about 2900 MPa, then the relative change in hydrostatic pressure between tension and compression is about 3%. Clearly, in this example, crystallographic effects are dominant and hydrostatic effects are negligible. Figure 4.6.1 represents a section of the yield criterion where crystallographic effects are more pronounced. If the horizontal scale in figure 4.6.1 was increased by a factor of ten then the hydrostatic effects would become more clear. The yield line would appear as a continuous curve passing through the point with zero effective stress and -2900 MPa hydrostatic stress. The yield curve would also bend up towards infinity as the hydrostatic stress was increased. The kinks in the curve due to crystallographic effects would be so small that they would become indistinguishable.

As a final note, it is obvious that the model predicts the general experimental stress state trends. However, the magnitude of the asymmetry between the yield points for different tests is slightly different in the model. The difference in the locations of the triaxial data points, with respect to the experimental points, is believed to be an artifact of texture. Additional discrepancy is created in the transition from the single crystal behavior to the polycrystalline behavior. The isotropic self-consistent method employed here ignores stresses and strains caused by elastic property mismatch between grains with different crystallographic orientations. At small transformation strains, when elastic constraint dominates, this effect should not be ignored. However, as a first approximation the isotropic self-consistent method still produces very insightful results. Additionally, the model employed here is restricted to strains less than about 3% since it does not account for plastic deformation.

4.7 CONCLUSIONS

(1) The monotonic stress-strain behavior of CuZnAl (at a constant temperature above the martensite start temperature, and below the martensite deformation induced temperature, $M_s < T < M_d$) is dependent on

the applied stress-state. The stress necessary to macroscopically trigger a perceivable transformation is 34 % larger in pure compression, versus pure tension. Several other triaxial tests produced effective stress-strain plots with yield points in between the tensile and compressive results.

(2) Pure hydrostatic pressure was unable to experimentally trigger the martensitic transformation up to pressures of 700 MPa. From this, the change in the martensite start temperature, M_s , with pure hydrostatic pressure was calculated to be within the range $0.00 < \Delta M_s / \Delta \sigma_h < 0.05$ °C/MPa. Using a numerical model it was predicted that the transformation should occur at a hydrostatic pressure of 2900 MPa, and never occur under negative hydrostatic pressures.

(3) It was numerically predicted and experimentally confirmed that on average only 2 to 3 martensite plates (variants) per grain control the stress-induced martensitic transformation. The orientation of martensite variants which activate in different grains are since the martensite transforms to accommodate the applied stress state.

(4) Theories based on the volume change during the transformation or on a single transforming martensite variant, are unable to properly predict experimental stress state results in CuZnAl. A micro-mechanical self-consistent model with up to 24 available martensite variants per grain was able to capture the stress state effects.

(5) Stress state effects in this CuZnAl alloy are a balance between crystallographic effects (number of transforming variants) and hydrostatic pressure (volume change) effects. The crystallographic effects are more pronounced when two stress states have a small difference in hydrostatic stress levels. The hydrostatic pressure effects become evident when there are extremely large differences in hydrostatic pressures between stress states.

REFERENCES

- M. Ahlers and G. Barcelo, ICOMAT-79, Massachusetts, Ed. W.S. Owen, 649, 1979 .
- G. F. Andreason and R. E.Morrow, *Am. J. Orth.*,vol. 73,pp. 142, 1978 .
- V. Baburay, M. Kawai, K. Kinoshita and T Koga, *J. Int. Mat. Sys. Struct.*, vol 7, pp. 145, 1996 .
- M. Balzer and H. Sehitoglu, *Experimental Mechanics*, vol. 37, 1997 .
- D.J. Barrett and B.J. Sullivan, *J. Int. Mat. Sys. Struct.*, vol 6, pp. 831, 1995 .
- J. L. Bassani, T. Y. Wu and C. Laird, *Proc. R. Soc. Lond.*, vol. 435, pp. 1, 1991 .
- J. Beyer, B. Koopman, P.A. Besselink and P.F. Willemse, *Materials Science Forum*, vol. 56-58, pp. 773, 1990 .
- J. G. Boyd and D.C. Lagoudas, *J. Int. Mat. Sys. Struct.*, vol. 5, pp. 333, 1994 .
- J. G. Boyd and D.C. Lagoudas,*Int. J. Plasticity*, vol. 12-6, pp. 805, 1996 .
- J. G. Boyd and D.C. Lagoudas,*Int. J. Plasticity*, vol. 12-7, pp. 843, 1996 .
- D. Brandon and R.C. Rogers, *J. Int. Mat. Sys. Struct.*, vol. 3, pp. 255, 1992 .
- L. C. Brinson and M.S. Huang, *J. Int. Mat. Sys. Struct.*, vol. 7, pp. 108, 1996 .
- L.C. Brown, *Met Trans. A*, vol. 10A, pp. 217, 1979 .
- L.C. Brown, *Met. Trans. A*, vol. 13A, pp. 25, 1982 .
- M. W. Burkart and T. A. Read, *Trans. Met. Soc. AIME*, vol. 197, pp. 1516, 1953 .
- L.C. Chang and T.A. Read, *Trans. AIME*, vol. 191, pp. 47, 1951 .
- C. Chu and R.D. James, *Experiments in Smart Materials and Structures*, AMD vol. 181, pp. 61, 1993 .
- J.J. Chumlijakov and S.V. Starenchenko, *J. Physique IV*, vol. 5, pp. 803, 1995 .
- L. Delaely, V. Krishnan, H. Tas and H. Warlimont, *J. Mat. Sci.*, vol. 9, pp. 1521, 1974 .

- L. Delaely, V. Krishnan, H. Tas and H. Warlimont, *J. Mat. Sci.*, vol. 9, pp. 1536, 1974 .
- T. W. Duerig, A. R. Pelton and D. Stockel, International conference on Displacive Phase transformations and their applications to materials engineering, University of Illinois, 1996 .
- ICOMAT-86, Proceedings of the 5th International Conference on Martensitic Transformations, Nara, Japan, Ed. I. Tamura, 1986 .
- ICOMAT-90, "Proceedings of the 6th International Conference on Martensitic Transformations", Sidney, Australia, Ed. B.C. Muddle, 1989 .
- Y. Ikai, K. Murakami and K. Mishima, Proceedings, International Conference on Martensitic Transformations, Leuven, Belgium, C4, 1982 .
- K. Jacobus, H. Sehitoglu and M. Balzer, *Met. Trans.*, vol. 27A, pp. 3066, 1986 .
- V. Kafka, *J. Int. Mat. Sys. Struct.*, vol. 5, pp. 815, 1994 .
- T. Kakeshita, Y. Yoshimura, K. Shimizu, S. Endo, Y. Akahama and F.E. Fujita, *Trans. JIM*, vol. 29, pp. 781, 1988 .
- T. Kakeshita, K. Shimizu, S. Nakamichi, R. Tanaka, S. Endo and F. Ono, *Mat. Trans. JIM*, vol. 33, pp. 1, 1992 .
- S.A. Kulin, M. Cohen and B.L. Averbach, *J. Metals*. 4, pp. 661, 1952 .
- M. Kumosa, *J. Phys.*, 24, pp. 1816, 1991 .
- P. H. Leo, T. W. Shield and O .P. Bruno, *Acta. Met.*, 41, pp. 2477, 1993 .
- D. S. Lieberman, M.A. Schmerling and R.W. Karr, Shape Memory Effects in Alloys, J. Perkins, Ed., Plenum Press, pp. 203, 1975 .
- K. N. Melton, Engineering Aspects of Shape Memory Alloys, Michigan State University, USA, Eds. T. W. Duerig, K. N. Melton, D. Stockel and C.M. Wayman, 21, 1990 .
- S. Miyazaki, T. Imai, Y. Igo and K. Otsuka, *Met. Trans. A* vol. 17A, pp. 115, 1986 .
- K. Mukherjee, S. Sircar and N.B. Dahotre, *Mater. Sci. and Eng.*, vol. 74, pp. 75, 1985 .
- T. Mura, Micromechanics of Defects in Solids, Kluwer, 1987 .

- N. Nakanishi, T. Mori, S. Miura, Y. Murakami and S. Kachi, *Phil. Mag.*, vol. 28, pp. 277, 1973 .
- Z. Nishiyama, Martensitic Transformation, Academic Press, 1978 .
- J. S. N. Paine and C. A. Rogers, *J. Int. Mat. Sys. Struct.*, vol. 6, pp. 210, 1995 .
- J. R. Patel and M. Cohen, *Acta Met.*, vol. 1, pp. 531, 1953 .
- E. Patoor, A. Eberhardt and M. Berveiller, Mechanics of Phase Transformations and Shape Memory Alloys, eds. L.C. Brinson and B. Moran, ASME, New York, NY, vol. 23, 1994 .
- E. Patoor, M. El Amrani, A. Eberhardt and M Berveiller, *J. De Physique*, vol. 5, pp. 495, 1995 .
- C. Picornell, E. Cesari and M. Sade, *Materials Science Forum*, vol. 56-58, pp. 741, 1990 .
- S. V. Radcliffe: The Mechanical Behavior of Materials Under Pressure, ed. H.L.D. Pugh, Elsevier, New York, NY, 638, 1970 .
- P. Rodriguez and G.J. Guenin, *Materials Science Forum*, vol. 56-58, pp. 541, 1990 .
- M. Sade, R. Rapacioli and M. Ahlers, 1985 , *Acta. Met.*, vol. 33, pp. 487, 1985 .
- H. Sakamoto, M. Tanigawa, K. Otsuka and K. Shimizu, Proceedings, International Conference on Martensitic Transformations, ICOMAT 79, Cambridge, MA, pp. 633, 1979 .
- H. Sakamoto, H. Shimizu, and K. Otsuka, *Trans. JIM*, vol. 28, pp. 579, 1981 .
- T.A. Schroeder and C.M. Wayman, "Pseudoelastic Effects in Cu-Zn Single Crystals" *Acta Met.* vol. 27, pp. 405, 1979 .
- Q. P. Sun and K. C. Hwang, *J. Mech. Phys. Solids*, vol. 39, pp. 507, 1991 .
- Q. P. Sun and K. C. Hwang, *J. Mech. Phys. Solids*, vol. 41, pp. 1, 1993 .
- Q. P. Sun and K. C. Hwang, *J. Mech. Phys. Solids*, vol. 41, pp. 19, 1993 .
- G.N. Sure and L.C. Brown, *Met. Trans. A*, vol. 15A, pp. 1613, 1984 .
- T. Tadaki, K. Otsuka and K. Shimizu, *Ann. Rev. Mater. Sci.*, 18, vol. 25, 1988 .

P. Vacher and C. L'excellent, Proceedings, Mechanical Behavior of Materials IV, VI, USA, ed. M. Jono , Plenum Press, pp. 231, 1991 .

R. J. Wasilewski, *Met. Trans. A*, vol. 2, pp. 2973, 1971 .

CHAPTER 5: STRESS STATE EFFECTS IN POLY. NiTi

PREVIEW

A micro-mechanical model is used to uncover the origins of stress-state effects on the forward stress-induced martensitic transformation in polycrystalline NiTi. At the microscopic level the model considers a self-accommodating multi-variant martensitic transformation. The model also accounts for the unidirectional nature of the shear deformation across the martensite habit plane which is responsible for the strong orientation dependence of NiTi single crystals. To predict the macroscopic polycrystalline stress-strain response, the model incorporates single crystal transformation behavior and experimentally measured polycrystalline texture into the self consistent formulation. The predicted results of the model are extremely consistent with experimental findings on polycrystalline NiTi. Ultimately, the unidirectional nature of the transformation coupled with strong crystallographic texture are deemed responsible for stress state effects in polycrystalline NiTi.

1.1 NOMENCLATURE

A_s	Austenite start temperature.
B	Constant in the chemical free energy term.
C_{ijkl}	Elasticity tensor.
E_{int}	Interaction Energy.
$E_{ij}^{tr} = \frac{1}{V} \int_{\Omega} \epsilon_{ij}^{tr} dV$	Average trans. strain in a single crystal of volume V .
$E_{ij} = \frac{1}{V} \int_{\Omega} \epsilon_{ij} dV$	Average total strain in a single crystal of volume V .
$\bar{E}_{ij}^{tr} = \frac{1}{V_p} \int_D E_{ij}^{tr} dV_p$	Average trans. strain in a polycrystal of volume V_p .
$\bar{E}_{ij} = \frac{1}{V_p} \int_D E_{ij} dV_p$	Average total strain in a polycrystal of volume V_p .
f	Volume fraction of martensite in a single crystal.
f_{ave}	Volume fraction of martensite in a polycrystal.
f^n	Volume fraction of martensite for the n^{th} variant.

F^n	Thermodynamic driving force for the n^{th} variant.
F_c	Critical driving force for the transformation.
g	Transformation magnitude.
H^{mn}	Interaction energy matrix.
M_s	Martensite start temperature.
m	Unit vector characterizing the transformation direction.
n	Unit vector characterizing the habit plane normal.
S_{ijkl}	Eshelby tensor.
T	Test temperature.
T_o	Phase equilibrium temperature.
x, y, z	Coordinate system in the parent phase
α_{ij}^n	Orientation tensor of the n^{th} martensite variant.
ϵ_{ij}^n	Intrinsic transformation strain for the n^{th} variant.
$\epsilon_{ij}^{\text{tr}}$	Local transformation strain.
ϵ_{ij}	Local total strain.
ϵ_{ijk}	Permutation tensor.
μ	Shear modulus.
Ψ	Complementary free energy.
σ_{ij}	Local stress.
$\Sigma_{ij} = \frac{1}{V} \int_{\Omega} \sigma_{ij} dV$	Average stress in a single crystal of volume V .
$\bar{\Sigma}_{ij} = \frac{1}{V_p} \int_D \Sigma_{ij} dV_p$	Average stress in a polycrystal of volume V_p .
\sum_m	Summation from 1 to m .

5.2 BACKGROUND

Shape memory alloys such as NiTi are rapidly becoming technologically important engineering materials. To date, the applications of NiTi range from pipe couplings and heat engines to kink resistant endoscopic medical tools and orthodontic wires. At any rate, the use of NiTi has expanded due to its large recoverable pseudoelastic and shape memory strains, along with its excellent resistance to fatigue and corrosion. However, there are several unresolved issues related to the mechanical behavior of NiTi. For example, it is still necessary to thoroughly understand and quantify the factors which govern stress state effects in NiTi (Orgeas and Favier, 1995; Jacobus *et al.*, 1996; Schetky, 1996; Plietsch and Ehrlich, 1997) Certainly, as NiTi

becomes a candidate material for more geometrically complex engineering components, the effect of different stress states on the mechanical behavior of NiTi is becoming increasingly important.

At the single crystal level several experimental studies have shown that the deformation behavior of NiTi is highly dependent on the applied stress state and crystallographic orientation (Miyazaki *et al.*, 1984; Chumlyakov *et al.*, 1995 and 1996). Under tensile loading, the [111] orientation is characterized as “soft” since it demonstrates extremely large uniaxial transformation strains and low critical transformation stress levels. Conversely, the [100] orientation is characterized as “hard” under tension since it demonstrates small uniaxial transformation strain levels and begins transformation at a significantly higher stress (Miyazaki *et al.*, 1984; Chumlyakov *et al.*, 1995 and 1996). Under compression the mechanical behavior of NiTi single crystals is reversed, i.e. the [111] orientation is hard and the [100] orientation is soft. It should also be noted that Chumlyakov and colleagues (1995 and 1996) have concluded that intermediate aging temperatures and times (1-1.5 hour @ 400-500°C) lead to a decrease in the orientation dependence of the critical transformation stress level and a weakening of the tension/compression asymmetry of any particular orientation. However, this decrease in the orientation dependence of the transformation parameters was only observed for intermediate precipitate sizes (peak aging). When the specimens weren't peak aged the original orientation dependence was observed. At any rate, the phenomenological theory of martensitic transformations has proven somewhat effective in modeling the tension/compression asymmetry and orientation dependence of the deformation behavior of NiTi single crystals which are not peak aged (Cizek, 1989; Buchhiet and Wert, 1994 and 1996).

The stress induced transformation behavior of polycrystalline NiTi has also been observed to exhibit a dependence on the applied stress state. Several researchers have concluded that when compared to tensile results, compressive stress-strain plots demonstrate smaller recoverable strain levels,

steeper transformation stress-strain slopes, and higher critical transformation stress levels (Wasilewski, 1971; Orgeas *et al.*, 1995; Jacobus *et al.*, 1996; Schetky, 1996; Plietsch and Ehrlich, 1997). In addition, it has also been observed that the torsion transformation yield point is well below the tensile point in NiTi (Melton, 1990). The effect of pure hydrostatic pressure on the stress induced transformation in NiTi has been studied by Kakeshita and colleagues (1992). It was determined that positive hydrostatic pressures slightly increase the martensite start temperature in NiTi compared to its value at atmospheric pressure. Clearly, if the martensite start temperature is lower than the test temperature then an extremely large hydrostatic pressure can trigger the stress induced martensitic transformation in NiTi. The effect of three dimensional stress states on the stress induced transformation in NiTi was recently studied by the present authors (Jacobus *et al.*, 1996). It was concluded that increasing the hydrostatic pressure increased the effective stress level required to trigger the transformation.

Although experimental stress state effects in both single crystal and polycrystalline NiTi are well documented, there has been little or no attempt to properly include these effects into recent phenomenological constitutive modeling efforts (Brandon and Rogers, 1992; Sun and Hwang, 1993; Kafka, 1995; Barrett and Sullivan, 1995; Baburaj *et al.*, 1996). Some of the more comprehensive phenomenological models which include a dependence on the applied stress state (Sun *et al.*, 1991; Boyd and Lagoudas, 1996) do not properly predict fundamental stress state effects such as tension/compression asymmetry (Jacobus *et al.*, 1996). The shortcoming of these phenomenological models is that they overlook the underlying deformation phenomenon responsible for stress state effects. With this, several researchers have used micro-mechanical modeling in order to incorporate the actual microscopic deformation mechanisms into shape memory alloy constitutive models. With the proper physical framework, it is expected that micro-mechanical models can capture a wide range of experimentally observed macroscopic deformation phenomenon such as stress state effects. Some of the earlier

micro-mechanical models (Falk, 1989; Ono *et al.*, 1989) were successful in predicting recoverable strain levels and critical transformation stress levels of polycrystalline shape memory alloys from single crystal data. The single variant model of Ono *et al.* (1989) considered the orientation dependence of the transformation behavior of single crystals. However, it predicted that the critical macroscopic stress level required for transformation in texture free polycrystalline NiTi would be smaller in compression versus tension. Unfortunately, all experimental observations on the deformation behavior of NiTi follow the reverse of this predicted behavior (Wasilewski, 1971; Orgeas *et al.*, 1995; Jacobus *et al.*, 1996; Schetky, 1996; Plietsch and Ehrlich, 1997). More recent micro-mechanical models (Amrani, 1994; Patoor *et al.*, 1996; Huang and Brinson, 1997) are multi-variant transformation models with self-accommodating variants. The multi-variant model of Patoor and colleagues has been successful in predicting stress state effects in Cu-Zn-Al alloys (Amrani, 1994; Patoor *et al.*, 1996; Gall *et al.*, 1997) however, there has been no attempt to quantitatively predict stress state effects in textured or untextured NiTi.

With this background, it is clear that stress state effects in NiTi are not properly accounted for. Consequently, the purpose of the present study is to provide a thorough understanding of the origins of stress state effects in NiTi. Stress state effects in polycrystalline NiTi are certainly linked to the strong orientation dependence of NiTi single crystals. Thus, stress state effects will be studied by considering the microscopic aspects of the transformation through a multi-variant micro-mechanical model. The model utilizes the known constitutive behavior of NiTi single crystals, experimentally measured polycrystalline texture, and the self consistent scheme. The model is used to predict the constitutive response of polycrystalline NiTi undergoing a forward stress induced martensitic transformation under different applied stress states. To verify the predictions of the model, the results are critically compared to previous experimental results of the present authors on

polycrystalline NiTi (Jacobus *et al.*, 1996). As a first approximation, only tensile and compressive loading will be considered.

5.3 MICRO-MECHANICAL MODELING

The framework of the micro-mechanical model used here to predict the stress-strain behavior of polycrystalline NiTi is the phenomenological

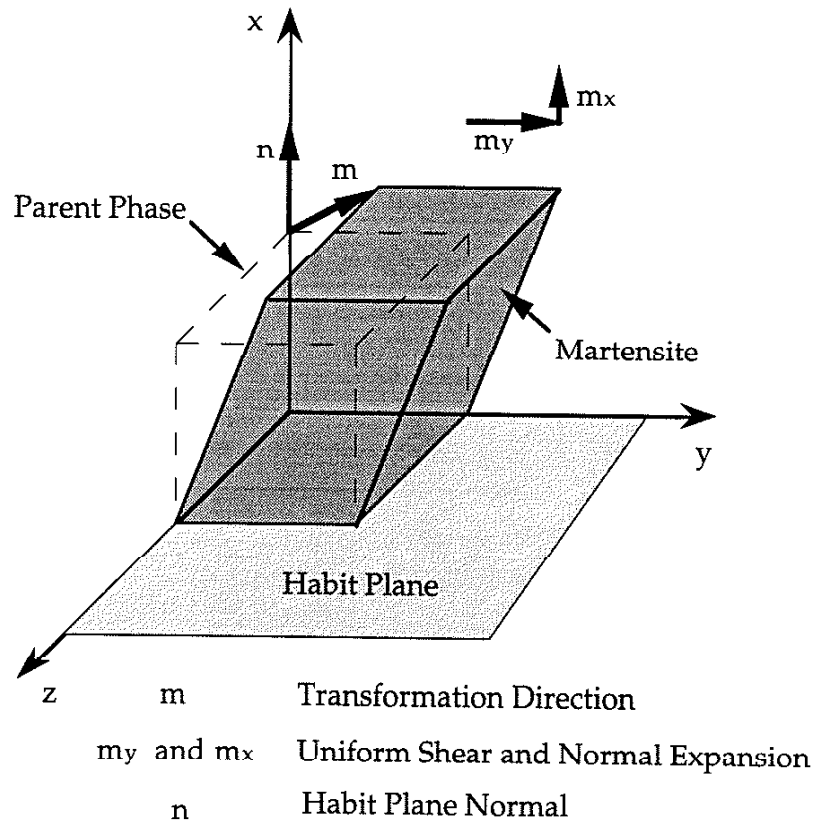


Figure 5.3.1: Transformation parameters in the phenomenological theory of martensitic transformations. For this simple example the martensite is favorably oriented with respect to the coordinate system chosen in the parent phase.

theory of martensitic transformations. Figure 5.3.1 is a schematic of a martensitic transformation in a single crystal of a parent phase. Following figure 5.3.1, the habit plane of the transformation is defined as the plane which remains undistorted during the transformation. The unit vector

characterizing the normal of the habit plane is denoted as n . The transformation direction is described by a unit vector denoted m . The transformation in figure 5.3.1 can be broken into two components, a shear along m_y and an expansion perpendicular to the habit plane along m_x . In the case where several arbitrarily oriented martensite variants transform, the average transformation strain is written as:

$$E_{ij}^{tr} = \sum_n g \alpha_{ij}^n f^n = \sum_n \epsilon_{ij}^n f^n \quad (5.3.1)$$

where g is the magnitude of the transformation, α_{ij}^n is the orientation tensor of the n^{th} martensite variant defined as $\alpha_{ij}^n = \frac{1}{2}(m_i^n n_j^n + m_j^n n_i^n)$, ϵ_{ij}^n is the intrinsic transformation strain of the n^{th} variant, and f^n is the volume fraction of the n^{th} variant. The crystallographic data for the 24 martensite variants in NiTi are given in Table 5.3.1 (Matsumoto *et al.*, 1987). These transformation parameters are not valid for NiTi materials with intermediate precipitate sizes (Miyazaki *et al.*, 1984). However, the heat treatment given to the polycrystalline material to be modeled here (Jacobus *et al.*, 1996) is not capable of causing such intermediate precipitate sizes since the material is annealed and never fully solutionized. To circumvent any arguments that stress state effects may be linked to the volume change upon transformation, the small expansion perpendicular to the habit plane has been removed in table 5.3.1. Buchheit and Wert (1994) have performed a similar operation and demonstrated that the volume change has a negligible effect on the predicted transformation behavior of single crystal NiTi. The total transformed volume fraction of martensite in a single crystal is the sum of the individual martensite variant volume fractions:

$$f = \sum_n f^n \quad (5.3.2)$$

The total volume fraction of martensite cannot exceed 1, thus equation 5.3.1 is only valid for $f \leq 1$.

V#	Habit Plane Normal, n			Transformation Direction, m		
				g = 0.13078		
1	-0.8889	-0.4044	0.2152	0.4114	-0.4981	0.7633
2	-0.4044	-0.8889	-0.2152	-0.4981	0.4114	-0.7633
3	0.8889	0.4044	0.2152	-0.4114	0.4981	0.7633
4	0.4044	0.8889	-0.2152	0.4981	-0.4114	-0.7633
5	-0.8889	0.4044	-0.2152	0.4114	0.4981	-0.7633
6	0.4044	-0.8889	0.2152	0.4981	0.4114	0.7633
7	0.8889	-0.4044	-0.2152	-0.4114	-0.4981	-0.7633
8	-0.4044	0.8889	0.2152	-0.4981	-0.4114	0.7633
9	0.2152	0.8889	0.4044	0.7633	-0.4114	0.4981
10	0.2152	-0.8889	-0.4044	0.7633	0.4114	-0.4981
11	-0.2152	-0.4044	-0.8889	-0.7633	-0.4981	0.4114
12	-0.2152	0.4044	0.8889	-0.7633	0.4981	-0.4114
13	-0.2152	0.8889	-0.4044	-0.7633	-0.4114	-0.4981
14	-0.2152	-0.8889	0.4044	-0.7633	0.4114	0.4981
15	0.2152	0.4044	-0.8889	0.7633	0.4981	0.4114
16	0.2152	-0.4044	0.8889	0.7633	-0.4981	-0.4114
17	0.8889	-0.2152	0.4044	-0.4114	-0.7633	0.4981
18	-0.8889	-0.2152	-0.4044	0.4114	-0.7633	-0.4981
19	0.4044	0.2152	0.8889	0.4981	0.7633	-0.4114
20	-0.4044	0.2152	-0.8889	-0.4981	0.7633	0.4114
21	0.8889	0.2152	-0.4044	-0.4114	0.7633	-0.4981
22	-0.8889	0.2152	0.4044	0.4114	0.7633	0.4981
23	-0.4044	-0.2152	0.8889	-0.4981	-0.7633	-0.4114
24	0.4044	-0.2152	-0.8889	0.4981	-0.7633	0.4114

Table 5.3.1: Crystallographic data for the 24 martensite variants in NiTi (Matsumoto *et al.*, 1987). The small expansion perpendicular to the habit plane has been removed (Buchheit and Wert, 1984).

To derive a constitutive relationship for the transformation from the parent phase to the martensitic phase a thermodynamical approach is necessary (Sun *et al.*, 1991; Amrani, 1994; Patoor *et al.*, 1996; Huang and Brinson, 1997). For a single crystal undergoing a multi-variant martensitic

transformation, the complimentary free energy takes the following form (Patoor *et al.*, 1996; Huang and Brinson, 1997):

$$\Psi(\Sigma_{ij}, T, f^n) = B(T_0 - T) \sum_n f^n + \frac{1}{2} \Sigma_{ij} C_{ijkl} \Sigma_{kl} + \Sigma_{ij} \sum_n \epsilon_{ij}^n f^n + \frac{1}{2V} \int_{\Omega} \sigma_{ij} \epsilon_{ij}^{tr} dV \quad (5.3.3)$$

where Σ_{ij} is the average applied stress, B is a constant, T is the test temperature, T_0 is the phase equilibrium temperature, C_{ijkl} is the elastic constant tensor, ϵ_{ij}^{tr} is the local transformation strain, and σ_{ij} is the local stress due to the martensite inclusions. From equation 5.3.3 it is clear that lowering the temperature below T_0 or applying a stress equivalently raise the free energy difference between the two phases and promote the forward martensitic transformation. The only possible "barrier" to the forward transformation is the integral term in equation 5.3.3. In shape memory alloy constitutive models, this term is commonly called the interaction energy, E_{int} (Amrani, 1994; Patoor *et al.*, 1996; Huang and Brinson, 1997). Micro-mechanical derivations of the interaction energy have been completed for both single variant (Sun *et al.*, 1991) and multi-variant (Amrani, 1994; Patoor *et al.*, 1996; Huang and Brinson, 1997) constitutive models. Although there has been some difficulty with the resulting sign of the interaction energy term (Sun *et al.*, 1991), it is clear that at least one term in equation 5.3.3 must work against the transformation. Without internal resistance to the transformation, the martensite formation would be unstable and the true stress-strain curves would demonstrate negative transformation slopes.

A micro-mechanical analysis can be used to prove that the interaction energy does in fact restrain the forward transformation (i.e. the interaction energy is negative). Consider a single variant transformation where the resulting martensite variant is approximated as an ellipsoidal inclusion. For simplicity, it can also be assumed that the martensite variant is oriented in such a way that the resulting shear strain field is aligned with the coordinate

axis chosen in the parent phase (i.e. the martensite in figure 5.3.1). Ignoring the small expansion normal to the habit plane, the resulting transformation strain is trivial to calculate, and interaction energy can be estimated as:

$$E_{\text{int}} = \frac{1}{2V} \int_{\Omega} \sigma_{ij} \epsilon_{ij}^{\text{tr}} dV = \frac{1}{2} \sigma_{12} \epsilon_{12} f \quad (5.3.4)$$

Considering that the shear moduli of the martensite is about half that of the parent phase, the stress field in the martensite inclusion can be written as (Tanaka and Mura, 1982):

$$\sigma_{12} = -\frac{1}{3} \mu \epsilon_{12} \quad (5.3.5)$$

where μ is the shear modulus of the parent phase. Equation 5.3.5 states that a spontaneous local transformation strain will always give rise to internal stresses which oppose the strain. By substituting equation 5.3.5 into equation 5.3.4 the following result is obtained for the interaction energy, E_{int} :

$$E_{\text{int}} = -\frac{1}{6} \mu (\epsilon_{12})^2 f \quad (5.3.6)$$

Clearly equation 5.3.6 predicts that the interaction energy will always be negative regardless of the magnitude or direction of the intrinsic transformation shear strain.

Although the above result was obtained for a single, favorably oriented martensite inclusion, the interaction energy must be negative even during a multi-variant martensitic transformation. Patoor and colleagues (1996) determined that for a multi-variant martensitic transformation, the interaction energy can be approximated by a so-called interaction energy matrix. With this, equation 5.3.3 becomes:

$$\Psi(\Sigma_{ij}, T, f^n) = B(T_0 - T) \sum_n f^n + \frac{1}{2} \sum_{ij} C_{ijkl} \Sigma_{kl} + \sum_{ij} \sum_n \epsilon_{ij}^n f^n - \sum_{n,m} H^{nm} f^n f^m \quad (5.3.7)$$

The interaction energy matrix, H^{nm} , is a matrix of positive constants which represent the decrease in the complimentary free energy due to the formation of multiple interacting martensite variants. The terms in H^{nm} are a function of the shear modulus of the parent phase, and the martensite variant morphology. It is also important to note that the H^{nm} matrix accounts for the self-accommodation of the martensite variants, as will be further discussed.

Mutually transforming variants n and m are considered perfectly self-accommodating if the resulting net intrinsic strain tensor ($\epsilon_{ij}^n + \epsilon_{ij}^m$) has only dilational components (Wayman, 1986). Consequently, the degree of self-accommodation (strong versus weak) for imperfect self-accommodating groups can be estimated through the magnitude of the shear terms in the net intrinsic strain tensor. Martensite variants which are thermally induced into NiTi form in nearly perfect self-accommodating three variant groups (Wayman, 1986). However, in the case of stress-induced martensites, it is more appropriate to estimate the degree of self-accommodation between random variant pairs rather than groups. As a first approximation it can be assumed that two variants will either be strongly self-accommodating (compatible) or weakly self-accommodating (incompatible). Although it is possible to determine which variants will be compatible (have relatively small net intrinsic shear strains) by crystallographic inspection (Wayman, 1986), it is more systematic to use a modified version of the strain compatibility equation (Amrani, 1994):

$$\epsilon_{ijk} \epsilon_{pqr} (\epsilon_{kr,jq}^n - \epsilon_{kr,jq}^m) = 0 \quad (5.3.8)$$

where ϵ_{ij}^n is the intrinsic transformation strain for the n^{th} variant, ϵ_{ij}^m is the

V #	1	2	3	4	5	6	7	8	9	10	11	12	13	14	15	16	17	18	19	20	21	22	23	24
1	C	C	C	C	C	I	C	I	I	I	I	C	I	I	C	I	C	I	I	I	C	I	I	I
2	C	C	C	C	I	C	I	C	C	I	I	I	C	I	I	I	I	I	C	I	I	I	I	C
3	C	C	C	C	C	I	C	I	I	I	C	I	I	I	I	C	I	C	I	I	I	C	I	I
4	C	C	C	C	I	C	I	C	I	C	I	I	I	C	I	I	I	I	I	C	I	I	C	I
5	C	I	C	I	C	C	C	C	I	I	C	I	I	I	I	C	C	I	I	I	C	I	I	I
6	I	C	I	C	C	C	C	C	C	I	I	I	C	I	I	I	I	I	I	C	I	I	C	I
7	C	I	C	I	C	C	C	C	I	I	I	C	I	I	C	I	I	C	I	I	I	C	I	I
8	I	C	I	C	C	C	C	C	I	C	I	I	I	C	I	I	I	I	C	I	I	I	I	C
9	I	C	I	I	I	C	I	I	C	C	C	C	C	C	I	I	I	C	I	I	C	I	I	I
10	I	I	I	C	I	I	I	C	C	C	C	C	C	C	I	I	C	I	I	I	I	C	I	I
11	I	I	C	I	C	I	I	I	C	C	C	C	I	I	C	C	I	I	C	I	I	I	C	I
12	C	I	I	I	I	I	C	I	C	C	C	C	I	I	C	C	I	I	I	C	I	I	I	C
13	I	C	I	I	I	C	I	I	C	C	I	I	C	C	C	C	C	I	I	I	I	C	I	I
14	I	I	I	C	I	I	I	C	C	C	I	I	C	C	C	C	I	C	I	I	C	I	I	I
15	C	I	I	I	I	I	C	I	I	I	C	C	C	C	C	C	I	I	C	I	I	I	C	I
16	I	I	C	I	C	I	I	I	I	I	C	C	C	C	C	C	I	I	I	C	I	I	I	C
17	C	I	I	I	C	I	I	I	I	C	I	I	C	I	I	I	C	C	C	C	C	C	I	I
18	I	I	C	I	I	I	C	I	C	I	I	I	I	C	I	I	C	C	C	C	C	C	I	I
19	I	C	I	I	I	I	I	C	I	I	C	I	I	I	C	I	C	C	C	C	C	I	I	C
20	I	I	I	C	I	C	I	I	I	I	I	C	I	I	I	C	C	C	C	C	C	I	I	C
21	C	I	I	I	C	I	I	I	C	I	I	I	I	C	I	I	C	C	I	I	C	C	C	C
22	I	I	C	I	I	I	C	I	I	C	I	I	C	I	I	I	C	C	I	I	C	C	C	C
23	I	I	I	C	I	C	I	I	I	I	C	I	I	I	C	I	I	I	C	C	C	C	C	C
24	I	C	I	I	I	I	I	C	I	I	I	C	I	I	I	C	I	I	C	C	C	C	C	C

Table 5.3.2: Compatibility (H^{mn}) matrix for NiTi. The interaction energy matrix, H^{mn} , is created by assigning compatible variants interaction energies of $C = \mu/3000$, and incompatible variants interaction energies of $I = \mu/750$. The resulting 24 by 24 matrix can be directly implemented into equation 5.3.13 where the summations over H^{mn} only hold for variants which are currently transforming.

intrinsic transformation strain for the m^{th} variant, and ϵ_{ijk} is the permutation tensor.

Martensite variants n and m which satisfy equation 5.3.8 have compatible orientations α_{ij}^n and α_{ij}^m (strong self-accommodation). Variant pairs n and m which do not satisfy equation 5.3.8 have incompatible orientations α_{ij}^n and α_{ij}^m (weak self-accommodation). Table 5.3.2 demonstrates the compatibility matrix calculated for NiTi using equation 5.3.8 coupled with the crystallographic data from table 5.3.1. In table 5.3.2, "I" indicates that two variants are incompatible and "C" indicates that two variants are compatible. Since the compatibility of variant pairs is proportional to the net intrinsic shear strains, it follows that compatible variants will mutually transform with small interaction energy magnitudes while incompatible variants will mutually transform with large interaction energy magnitudes. As a first approximation, the compatible variants are assumed to form with an interaction energy on the order of $C = \mu/3000$ while the incompatible variants are assumed to form with an interaction energy about four times higher, $I = \mu/750$. These two values were estimated by using the previous interaction energy values calculated for Cu-Zn-Al (Patoor *et al.*, 1996) weighed by the smaller transformation magnitude in NiTi. The values for Cu-Zn-Al were calculated using a multi-variant micro-mechanical approach similar to the one variant approach presented here (equation 5.3.6). It should also be noted that if the transformation parameters are substituted into equation 6 then the magnitude of the interaction energy is on the order of $\mu/1000$ for one variant. The insertion of the C and I values into the compatibility matrix converts table 5.3.2 into the interaction energy matrix, H^{nm} . The influence of H^{nm} on the transformation behavior will be further discussed as the model is developed and utilized.

The thermodynamic driving force acting on the n^{th} martensite variant is obtained by the partial differentiation of equation 5.3.7 with respect to the volume fraction of martensite, f^n :

$$F^n = \frac{\partial \Psi}{\partial f^n} = B(T_0 - T) + \sum_{ij} \epsilon_{ij}^n - \sum_m H^{nm} f^m \geq F_c \quad (5.3.9)$$

When the thermodynamical force acting on the n^{th} variant, F^n , is greater than a critical value, F_c , the transformation from the parent phase to the martensitic phase proceeds for the n^{th} variant. Assuming that a linear relationship exists between the critical stress and temperature required to induce the transformation, the constants F_c and B can be uniquely determined from two experimental tests. The most effective way to determine the constants is from a room temperature tensile test and a stress free cool down test. The constants should be determined at the single crystal level, however, their magnitude can be estimated by using polycrystalline data and considering extremely small offset levels. For the modeling results presented here, the constants F_c and B were estimated from previous polycrystalline tensile test results (Jacobus *et al.*, 1996). The data for the polycrystalline NiTi which will be used is as follows: $M_s = -18.1$ °C, $A_s = -0.3$ °C, $T_0 = -9.2$ °C, and $\bar{\Sigma}_y \sim 400$ MPa (at deviation from linearity). Utilizing these values, equation 5.3.9, and assuming that at least one favorably oriented variant ($\epsilon_{ij}^n = 0.5g$) begins to transform at the first deviation from linearity, the following parameters are determined for the modeling of NiTi: $B \sim 0.607$ MPa/°C and $F_c \sim 5.4$ MPa.

The role that the interaction energy matrix, H^{nm} , plays in the transformation criteria (equation 5.3.9) is critical. The relative magnitudes between the terms in the interaction energy matrix account for the self-accommodation of the martensite variants. For example, consider that due to an increasing applied stress level variant 1 is the first variant to satisfy equation 5.3.9 (i.e. it has the highest $\sum_{ij} \epsilon_{ij}^n$ value at a constant test temperature). Subsequently, it can be assumed that variant 1 evolves to a specific volume fraction denoted f^1 . Then consider a second variant, say variant 10, which is favored for subsequent transformation (i.e. it has the

second highest $\sum_{ij}\epsilon_{ij}^n$ value). If variants 1 and 10 are compatible then $H^{10,1}$ is relatively small and the $H^{10,1}f^1$ term will not affect the transformation driving force (equation 5.3.9) for variant 10. However, if variants 10 and 1 are incompatible then $H^{10,1}$ is relatively large and the transformation driving force for variant 10 will be significantly reduced by the presence of variant 1. Appropriately, variant 10 may not subsequently transform even though it is favored by the applied stress state since it is not compatible (or strongly self-accommodating) with variant 1.

The volume fraction evolution rate of the martensite, \dot{f}^n , is determined from the consistency condition:

$$\frac{\partial \dot{F}^n}{\partial \Sigma_{ij}} \dot{\Sigma}_{ij} + \frac{\partial \dot{F}^n}{\partial f^n} \dot{f}^n + \frac{\partial \dot{F}^n}{\partial T} \dot{T} = -B\dot{T} + \dot{\Sigma}_{ij}\epsilon_{ij}^n - \sum_m H^{nm}\dot{f}^m = 0 \quad (5.3.10)$$

Solving for \dot{f}^n the following result is obtained:

$$\dot{f}^n = \sum_m H^{nm-1} [\dot{\Sigma}_{ij}\epsilon_{ij}^m - B\dot{T}] \quad (5.3.11)$$

After the transformation criteria is satisfied, equation 5.3.11 determines the volume fraction evolution rate of the martensite for the n^{th} variant. In equation 5.3.11 the magnitudes of the terms in the H^{nm} matrix account for the experimentally observed hardening behavior of single crystal shape memory alloys (Chumlyakov *et al.*, 1995 and 1996). If the values in H^{nm} are set to zero then the single crystal stress-strain curves will have zero slope. As the values within H^{nm} are equivalently increased, the slopes of the single crystal transformation stress-strain curves will increase. It should be kept clear that the magnitude of all the terms in H^{nm} are responsible for the hardening of the single crystal stress-strain curves, while the relative magnitudes between the terms in H^{nm} account for the compatibility of variant pairs. Equations

5.3.1, 5.3.2, 5.3.9, and 5.3.11 completely describe the forward multi-variant stress induced martensitic transformation for a NiTi single crystal. When equation 5.3.9 is satisfied for n variants, equation 5.3.11 determines the volume fraction evolution rate for the variants and equation 5.3.1 yields the resulting transformation strain.

In a polycrystalline body undergoing a stress induced martensitic phase transformation, there exists grains which are oriented favorably and unfavorably with respect to the applied stress state. This misorientation results in unbalanced transformation strain magnitudes for neighboring grains. In turn, the difference in transformation strain levels leads to local stress and strain fields throughout the polycrystalline body. The self consistent method can be used to estimate the magnitudes of the internal stress and strain fields in the polycrystalline body. This is accomplished by using the difference in the average transformation strain in a hypothetical isotropic polycrystalline matrix and the local transformation strain in any particular grain as the eigenstrain in the Eshelby method (Mura, 1987).

In the most general form, the incremental self-consistent relationship is written as (Mura, 1987):

$$\dot{\Sigma}_{ij} = \dot{\bar{\Sigma}}_{ij} + C_{ijkl} \left[S_{klmn} (\dot{E}_{mn}^{tr} - \dot{\bar{E}}_{mn}^{tr}) - (\dot{E}_{kl}^{tr} - \dot{\bar{E}}_{kl}^{tr}) \right] \quad (5.3.12)$$

where Σ_{ij} and E_{ij}^{tr} are the average stress and transformation strain magnitudes in a single grain, $\bar{\Sigma}_{ij}$ and \bar{E}_{ij}^{tr} are the average stress and transformation strain magnitudes in the polycrystalline body, and S_{ijkl} is the fourth order Eshelby tensor. By multiplying both sides of equation 5.3.12 by ϵ_{ij}^n , and incorporating equations 5.3.1 and 5.3.9, the following result is obtained:

$$\sum_m H^{mn} \dot{f}^m + B\dot{T} = \epsilon_{ij}^n \dot{\bar{\Sigma}}_{ij} + \epsilon_{ij}^n C_{ijkl} \left[S_{klop} \left(\sum_q \epsilon_{op}^q \dot{f}^q - \dot{\bar{E}}_{op}^{tr} \right) - \left(\sum_q \epsilon_{kl}^q \dot{f}^q - \dot{\bar{E}}_{kl}^{tr} \right) \right] \quad (5.3.13)$$

where \sum_m and \sum_q represent summations from 1 to m and 1 to q respectively.

Equation 5.3.13 is the form of the self consistent relationship that is used to generate the polycrystalline stress-strain behavior for NiTi shape memory alloys. Equation 5.3.13 is only implemented when the first variant within a grain reaches the critical transformation value (equation 5.3.9). Additionally, all summations only hold for variants which subsequently satisfy equation 5.3.9.

When n martensite variants have satisfied the transformation criteria (equation 5.3.9), equation 5.3.13 represents a n by n system of linear equations to be solved for every load increment in each grain. For an untextured material, 2000 randomly oriented (α_{ij}^n rotated) grains are used to model a polycrystalline material. When a textured material is modeled, the grain orientations are extracted from experimental pole figures using popLA, a texture analysis software. The grains were assumed to be spherical in shape. For a given average stress increment, $\dot{\bar{\Sigma}}_{ij}$, equation 5.3.13 is used to calculate \dot{f}^n for each transforming variant in every grain. Subsequently, the incremental form of equation 5.3.1 is used to calculate the transformation strain increment in each grain, \dot{E}_{ij}^{tr} . Finally, the values of \dot{E}_{ij}^{tr} are averaged to obtain $\dot{\bar{E}}_{ij}^{tr}$. The solution method is of the pure incremental (Euler) type since the average transformation strain from the previous load increment is used to calculate the average transformation strain of the current step. However, the accumulated errors are minimized by choosing extremely small applied average stress increments ($\dot{\bar{\Sigma}}_{ij} = 0.2$ MPa).

5.4 TEXTURE ANALYSIS

To properly use the current micro-mechanical model to predict the experimental stress-strain behavior of polycrystalline NiTi, it is first necessary

to quantify the crystallographic texture of the candidate mechanical test specimens. The samples employed for the texture analysis were obtained from previous NiTi mechanical test specimens of the present authors (Jacobus *et al.*, 1996). Prior to mechanical testing the samples from the experimental study were cold drawn, annealed, straightened, centerless ground, aged .25 hours at 550 °C, and machined into dogbone specimens with the loading axis parallel to the drawing direction. The details of the mechanical testing conditions are covered in a recent publication (Jacobus *et al.*, 1996). Since the authors are only concerned with the overall orientation distribution of the grains in the polycrystalline NiTi specimen, the method chosen here to determine the crystallographic texture is x-ray diffraction. The experimental pole figures resulting from the x-ray analysis are presented in figures 5.4.1a and 5.4.1b. Figure 5.4.1a is stereographic projection of the intensity of reflections from the {110} crystallographic planes, while figure 5.4.1b represents the intensity of reflections from the {100} planes. The experimental pole figure resulting from the {111} reflections was also measured, but is not shown here. Figures 5.4.1a and 5.4.1b are both presented in times-normal format, where the center of both figures represents a direction parallel to the loading axis of the test specimens. From the experimental pole figures it is clear that a strong crystallographic texture is present in NiTi.

Along the loading axis, figures 5.4.1a and 5.4.1b demonstrate that compared to a polycrystal with a random distribution of grain orientations, there is about 1.5 times the expected {110} reflections, and less than .44 times the expected {100} reflections. To obtain discrete information from the experimental pole figures it is necessary to combine the information stored in the three figures using the texture analysis software popLA. First, using the three experimentally measured pole figures, the orientation distribution function (ODF) is calculated for the NiTi specimen. Following this, the ODF is used to create a data file consisting of about 2,000 grains with individual Euler angle triplets and corresponding weights. To verify the ODF and the

resulting Euler angles, the grains with large weights were used to create a

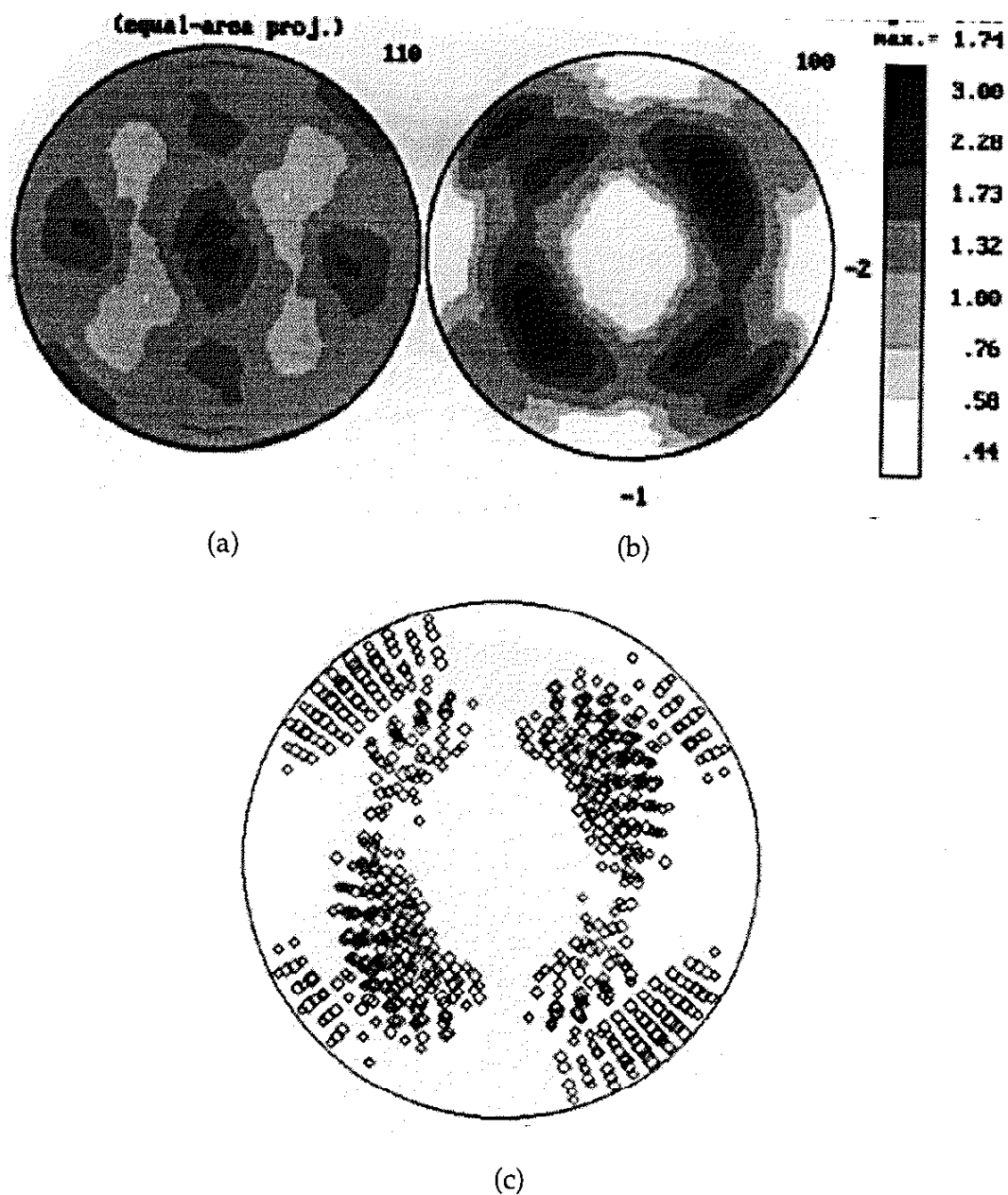


Figure 5.4.1: a. Normalized experimental {110} pole figure. b. Normalized experimental {100} pole figure. c. Discretized {100} pole figure derived from figures a, b, and the {111} pole figure. The experimental figures were all taken from a polycrystalline NiTi sample with the reference direction (the center of the projection) chosen parallel to the loading axis of the specimen.

discretized {100} pole figure shown in figure 5.4.1c. As expected, figure 5.4.1c predicts the locations of the strong reflections present in the experimental {100} pole figure shown in figure 5.4.1b.

The effect of crystallographic texture on the deformation behavior of polycrystalline alloys is dependent on the observed anisotropy at the single crystal level. Table 5.4.1 demonstrates the maximum value of the orientation

	Maximum α_{ij}^n value		
	[1 0 0] direction	[1 1 0] direction	[1 1 1] direction
Tension	0.21	0.41	0.45
Compression	0.40	0.37	0.25

Table 5.4.1: Maximum value of the orientation tensor (maximum resolved shear stress factor) for several crystallographic orientations of NiTi.

tensor, α_{ij}^n , (maximum resolved shear stress factor) for several different crystallographic orientations. The values are determined from the data in table 5.3.1. Under a specific applied stress state, large α_{ij}^n values correspond to soft crystallographic orientations while small α_{ij}^n values correspond to hard crystallographic orientations. From table 5.4.1 it is clear that if crystallographic texture is developed in any of the three directions, the transformation will be heavily biased with respect to the loading direction. Notably, a major texture in the [111] or [100] directions would create a larger bias than a texture in the [110] direction. With this it is quite obvious that the deformation behavior of polycrystalline NiTi is quite sensitive to crystallographic texture. Using the popLA software it was determined that parallel to the loading direction the major texture was of the {110} <111> type. Since this crystallographic orientation is soft in tension and hard in compression (table 5.4.1), the texture analysis qualitatively predicts that transformation in tension is favored over transformation in compression in these polycrystalline NiTi test specimens.

5.5 DISCUSSION

Before analyzing the results of the micro-mechanical model it is important to briefly discuss the origin of stress state effects in NiTi single crystals as predicted by the phenomenological theory of martensitic transformations. Assuming that the initial test specimen is martensite free, the uniaxial transformation criteria for the n^{th} martensite variant (equation 5.3.9) can be written as:

$$B(T_0 - T) + \Sigma_{11} g \alpha_{11}^n \geq F_c \quad (5.5.1)$$

For the following discussion, it is assumed that the test temperature remains fixed and that the chemical free energy term behaves as a constant that can be combined with F_c . Equation 5.5.1 is unique since it only allows the n^{th} variant to transform if the resolved shear stress (neglecting the small volume change) is along the same direction as the prescribed twin direction. If the two directions do not coincide, then the left hand side of equation 5.5.1 will always be negative and will never overcome the positive constant F_c . This is in opposition to the case of slip where conjugate slip directions are allowed and the left hand side of equation 5.5.1 is contained within an absolute value function. The unidirectional nature of twin formation has been experimentally observed in NiTi single crystals under different stress states (Chumlyakov *et al.*, 1995 and 1996). In addition, it has been proven that for BCC materials such as NiTi, conjugate twins are forbidden since the resulting stored elastic strain energy is higher when the shear strain is along a direction opposite to the prescribed twin direction (Kumosa, 1991).

Figure 5.5.1 demonstrates the effect of the unidirectional transformation criteria on the stress-strain behavior of NiTi single crystals under different stress states. In the schematic both crystals are oriented along the [100] direction, however, the crystal on the right is loaded in compression while the crystal on the left is loaded in tension. The trace of the habit plane

(elliptical curve) and the prescribed transformation direction (solid arrow) of the first variants to satisfy equation 5.5.1 are shown at the center of both

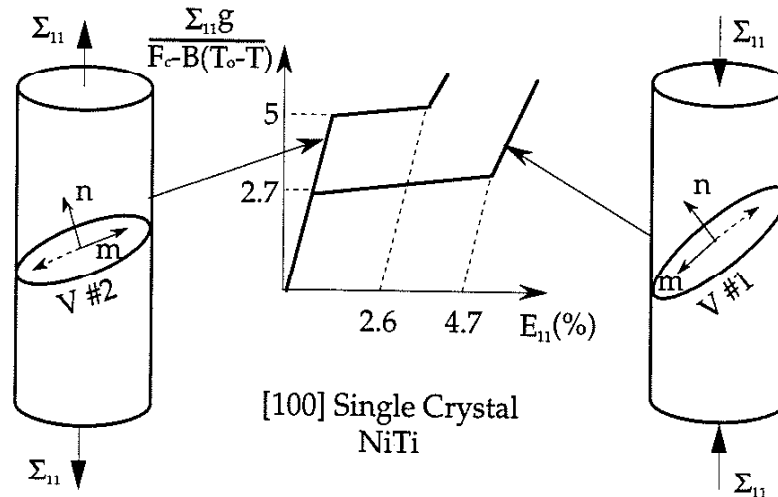


Figure 5.5.1: Schematic demonstrating the origin of stress state effects in a single crystal of NiTi.

specimens. The conjugate (forbidden) transformation directions are demonstrated by dashed lines. Under compression variant #1 (see table 5.3.1) is the first variant to satisfy equation 5.5.1. Since the habit plane of variant #1 is oriented close to 45° , variant #1 is favorably oriented with respect to the loading axis, i.e. $|\alpha_{11}^1|$ is large. Consequently, under compression, the critical transformation stress level is small and the transformation strain magnitude is large. However, if a crystal of the same orientation is loaded under tension the resolved shear stress acting across the habit plane of variant #1 is along the dashed line. Since transformation along this direction is not energetically favored, variant #1 will not activate under tension. Instead, the first variant to satisfy equation 5.5.1 under tension will be variant #2 (see table 5.3.1). Unfortunately, variant 2 is not favorably oriented with respect to the loading axis, i.e. $|\alpha_{11}^2|$ is small. Consequently, under tension, the critical transformation stress level is large and the transformation strain magnitude is small.

To study the effect of the applied stress state on the deformation behavior of polycrystalline NiTi it is necessary to analyze the predictions of the micro-mechanical model. Figure 5.5.2 demonstrates the predicted stress-strain curves for both textured (solid lines) and untextured (dashed lines)

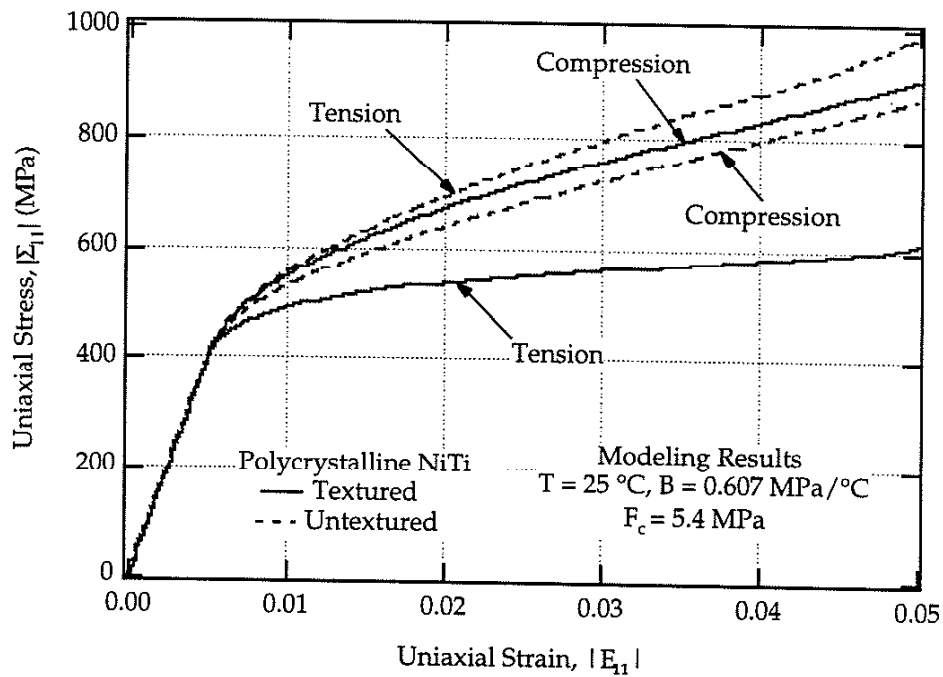


Figure 5.5.2: Modeling results for polycrystalline NiTi demonstrating the effect of the experimentally measured texture on the predicted stress-strain curves.

NiTi. The textured results were generated by implementing the 2000 discrete grain orientations (figure 5.4.1c) extracted from the experimental pole figures while the untextured results represent a body containing 2000 randomly oriented grains. In the untextured case, the stress-strain curves demonstrate low levels of asymmetry between tensile and compressive loading. In fact, at the macroscopic level, transformation in compression occurs at a slightly lower stress level than transformation in tension. This is consistent with the predictions of Ono *et al.* (1989) on untextured polycrystalline NiTi. However, when the crystallographic texture is implemented into the model the locations of the tensile and compressive stress-strain curves are reversed. In

the textured case the compressive stress-strain lies slightly above the untextured curve, while the textured tensile curve is well below the

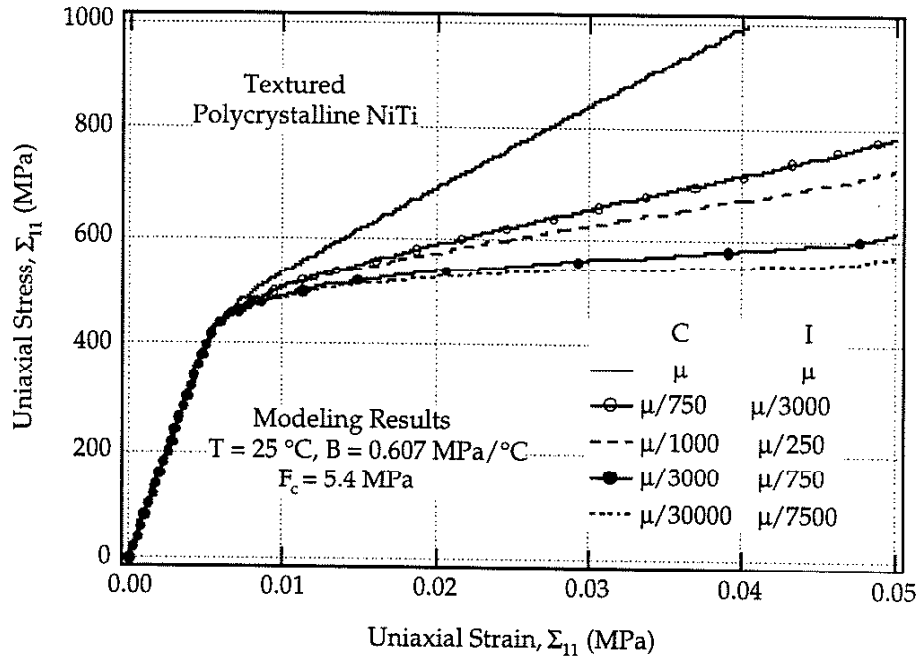


Figure 5.5.3: Modeling results for polycrystalline NiTi demonstrating the effect of various interaction energy magnitudes on the predicted tensile stress-strain curves.

untextured tensile result. For the remainder of this discussion, the textured results will be utilized since they best represent the actual experimental NiTi test specimens. Most of the transformation modeling parameters (m , n , g , F_c , and B) are taken from experimental results on polycrystalline (Jacobus *et al.*, 1996) and single crystal (Matsumoto *et al.*, 1987) NiTi. The only parameters estimated from an analytical standpoint are the terms in interaction energy matrix, H^{mn} . Since H^{mn} is not an experimental parameter *per se*, it is appropriate to study the effect of varying H^{mn} on the predicted polycrystalline stress-strain behavior. Figure 5.5.3 demonstrates the variations in the tensile stress-strain behavior as a function of C and I , the constants which represent the interaction energies of the compatible and incompatible variants within H^{mn} . From figure 5.5.3 it is clear that altering

the magnitudes of the C and I terms has a profound effect on the predicted tensile stress-strain behavior. For this discussion, the values $C = \mu/3000$ and $I = \mu/750$ are chosen as the “reference” constants (solid circles in figure 5.5.3).

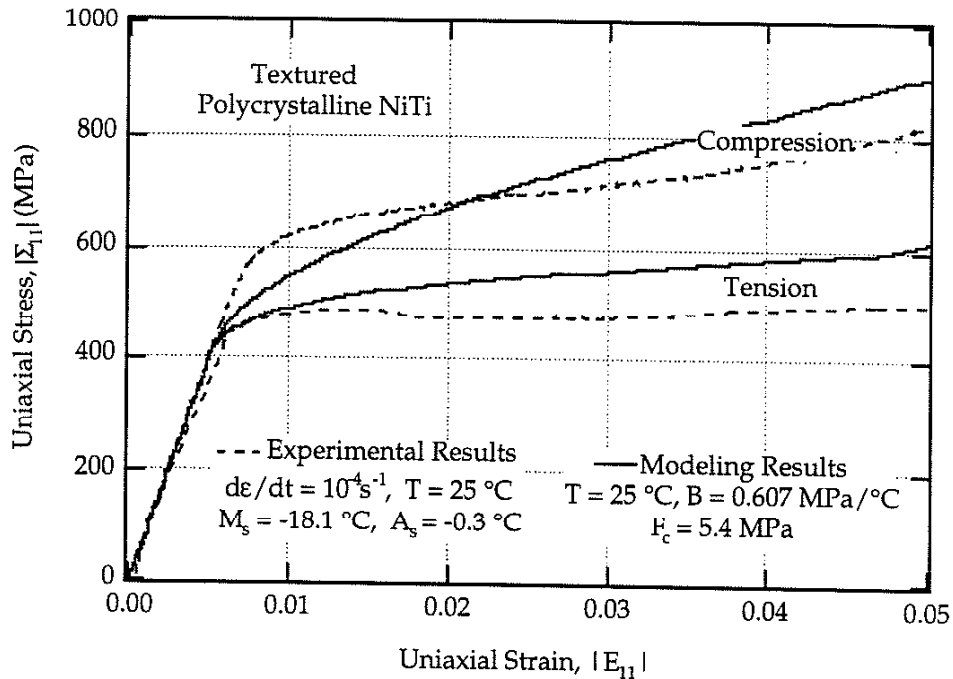


Figure 5.5.4: Comparison of modeling results with experimental results for polycrystalline NiTi.

As the values of C and I are equivalently decreased ($C = \mu/30000$ and $I = \mu/7500$) the predicted polycrystalline stress-strain curve demonstrates a slightly smaller transformation stress-strain slope. If the magnitudes of C and I are equivalently increased above the reference value ($C = \mu/1000$, μ and $I = \mu/250$, μ) the slopes of the transformation stress-strain curves dramatically increase. Since the magnitudes of the constants C and I quantify the hardening behavior of single crystals, the above effect is consistent with expectations. A more interesting effect is discovered if the values for C and I are switched. By switching the magnitudes of the two terms, variants which were found to be compatible are now treated as incompatible variants and

vice versa. The stress-strain curve corresponding to this situation is shown by the hollow circles on figure 5.5.3. When the incompatible (non self-accommodating) variants are biased for joint transformation, the stress-strain curve shows considerably more hardening over the case where the compatible variants are allowed to transform together (solid circles). At any rate, the chosen values for C and I yield reasonable stress-strain predictions thus they will be used for the remainder of the discussion.

At this point it is imperative to discuss the relationship between the predictions of the micro-mechanical model and the experimentally observed mechanical behavior. Figure 5.5.4 gives a comparison of previous experimental stress-strain curves (Jacobus *et al.*, 1996) (dashed lines) and the predicted stress-strain curves (solid lines) for textured polycrystalline NiTi. The experimental and predicted stress-strain curves demonstrate considerable asymmetry between tensile and compressive loading. Both the predicted and experimental curves show that under compression, the transformation occurs at a higher stress level and with a larger transformation stress-strain slope. Although the model does not capture the exact shape of the experimental stress-strain curves, it does an excellent job predicting the overall asymmetry between tensile and compressive loading. Under tensile loading the model predicts that the transformation will occur with a very small transformation stress-strain slope. This observation is consistent with the experimentally observed transformation slope under tension. Under compression, both the experimental and modeling results show that the transformation proceeds with considerable hardening when compared to the tensile results. The model also does a fairly good job predicting the difference in the critical macroscopic stress required to induce transformation in tension versus compression. In the small strain regime the tension/compression asymmetry is slightly larger in the experimental results versus modeling results. This is an artifact of the self-consistent averaging scheme which is only an approximation of the real polycrystalline behavior. At any rate, the model is extremely valuable since it can predict the strong asymmetry

between tensile and compressive loading given constants experimentally determined exclusively under tensile loading.

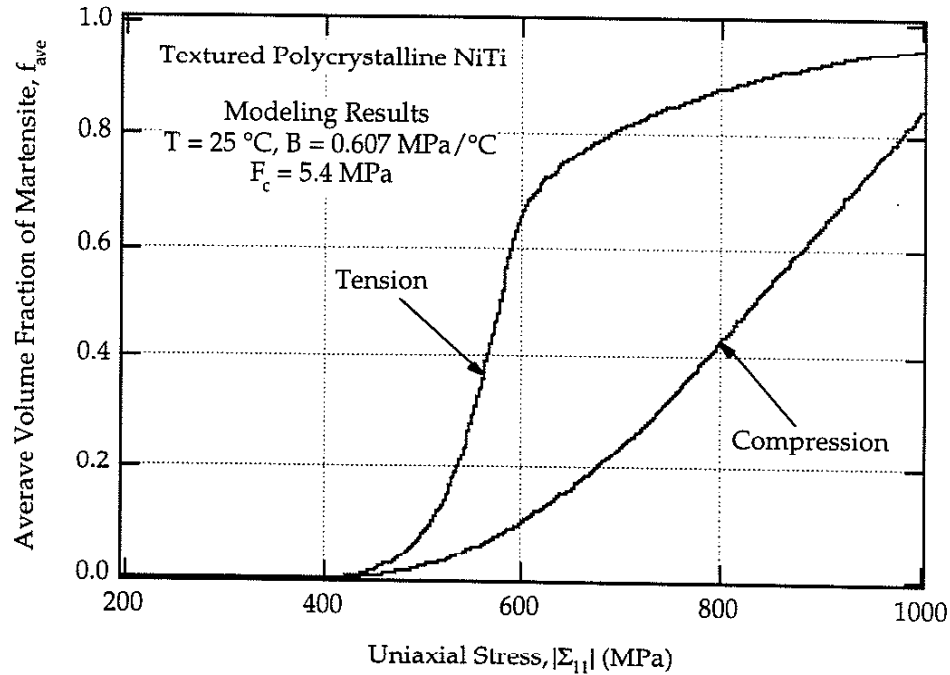


Figure 5.5.5: Plot of average volume fraction of martensite versus the applied uniaxial stress level as predicted by the model.

Although it is clear that the micro-mechanical model predicts the proper experimental trends, it is still necessary to analyze some of the microscopic factors (as predicted by the model) which lead to this agreement. Figure 5.5.5 is a plot of the average volume fraction of martensite in the polycrystalline body, f_{ave} , versus the average applied uniaxial stress level. The average volume fraction of martensite in the polycrystalline body represents an average of the individual volume fractions of martensite, f , in the 2000 grains. Under tension the model predicts that once the applied stress reaches a critical macroscopic value, the martensite evolves very quickly with respect to a small increase in the applied stress level. Conversely, under compression, the martensite evolves as a much weaker function of the average applied stress level. At any rate, there is considerable asymmetry

in the average macroscopic evolution rate of martensite in tension versus compression. The strong difference in martensite evolution rates under tension and compression (figure 5.5.5) is clearly responsible for the asymmetry observed between the tensile and compressive stress-strain curves (figure 5.5.4).

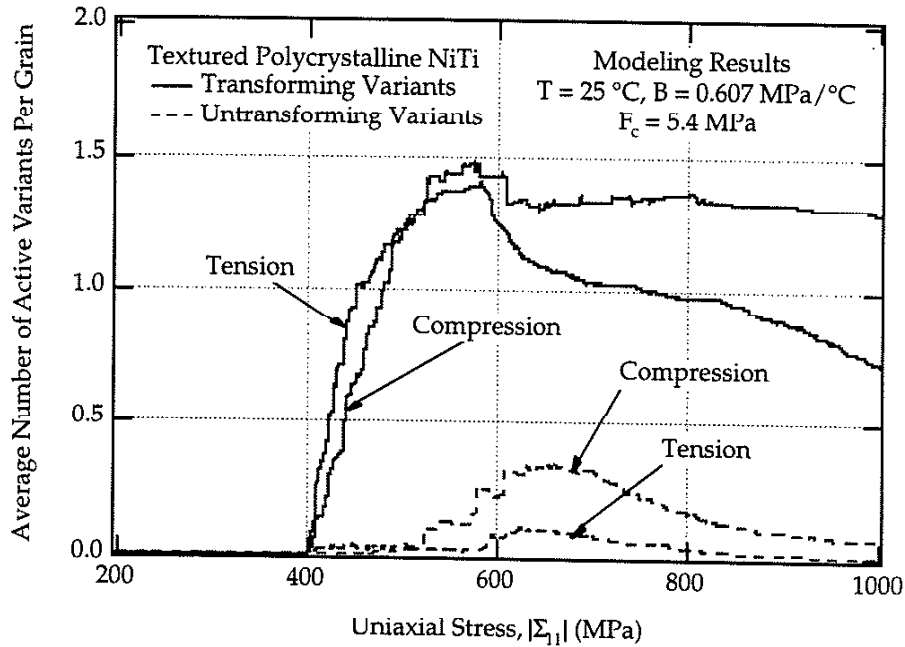


Figure 5.5.6: Plot of average number of active martensite variants per grain versus the applied uniaxial stress level as predicted by the model.

The difference in martensite evolution rates in tension versus compression is strongly linked to stress state effects at the single crystal level. Figure 5.5.6 demonstrates the average number of active variants per grain (variants which are undergoing a forward or reverse martensitic transformation) versus the applied uniaxial stress level. At the microscopic level the transformation is triggered at the same applied stress level under tensile and compressive loading. However, the number of variants transforming under tension quickly exceeds the number of variants transforming in compression. On average, at 450 MPa every grain is

transforming under tension, while only about 65% of the grains are transforming under compression. When a large number of grains are favorably oriented for transformation under tension then there is a high probability that somewhere in the gage section all of the grains will simultaneously begin to transform. This localized deformation sometimes leads to the propagation of a macroscopic parent/martensite phase boundary. Notably, under tensile loading, phase boundary motion (Luders deformation) has been experimentally observed in polycrystalline NiTi (Shaw and Kyriakides, 1997).

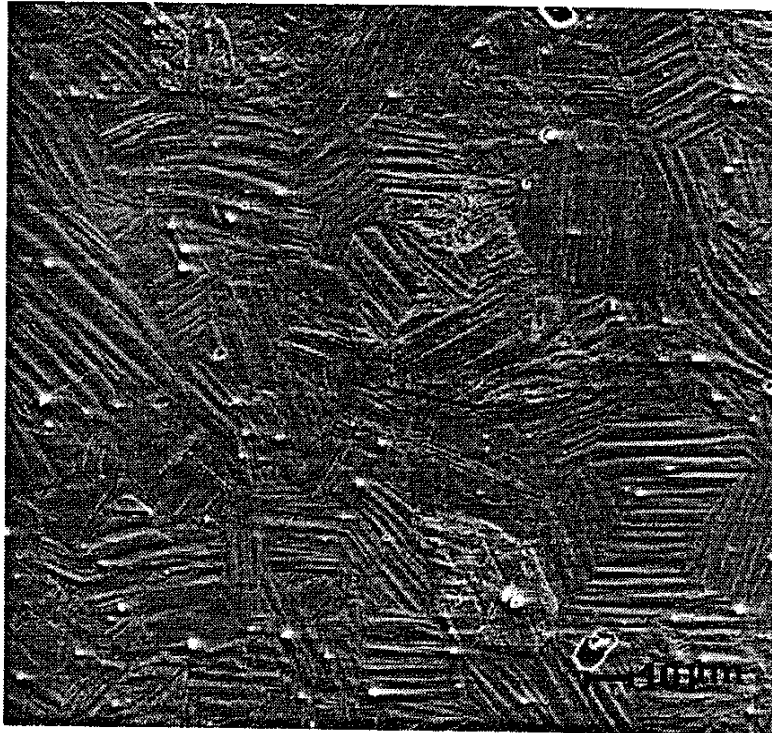


Figure 5.5.7: Scanning electron micrograph of polycrystalline NiTi deformed under tension. The number of stress induced martensite variants per grain is between one and two.

As the applied stress is increased, the number of transforming variants under compressive loading eventually surpasses the number of transforming variants under tension. However, at this point, most of the grains in the tensile specimen are fully martensitic and the number of variants

transforming under tension begins to level off and eventually decrease. The maximum number of active variants per grain in both cases is about 1.5. This small number of active variants per grain is consistent with microstructural observations in deformed polycrystalline NiTi. Figure 5.5.7 is a scanning electron micrograph of deformed NiTi. Etching has been used to reveal the martensite plates. As predicted by the model, figure 5.5.7 demonstrates that most of the grains contain at least one, and sometimes two martensite variants. It is also interesting to note that under both tensile and compressive loading the micro-mechanical model predicts the local unloading (untransforming) of martensite variants. The untransformation of martensite variants is caused by the strong local stress field generated in a polycrystalline body. The effect of the local unloading on the macroscopic stress-strain response is small, and probably very difficult to measure experimentally, but nonetheless is predicted by the model.

In summary, it is clear that polycrystalline NiTi responds differently under tensile and compressive loading because of unique crystallographic effects. When a polycrystalline aggregate of NiTi single crystals (grains) is drawn, a crystallographic texture is induced that orients more single crystals favored for transformation in tension versus compression. Consequently, at the microscopic level, a larger number of variants activate under tension versus compression. This leads to a faster macroscopic martensite evolution rate under tension, resulting in a lower critical transformation stress level and a smaller transformation stress-strain slope. Since most of the NiTi used in applications today is drawn into wire or bar stock, texture induced tension-compression asymmetry is certainly an important phenomenon. At this point it is still necessary to better quantify the relationship between different amounts of cold work (% reduction) and different heat treatments (precipitate sizes) on tension/compression asymmetry. However, these topics are issues that must be resolved in future research efforts.

5.6 CONCLUSIONS

1. A multi-variant thermodynamically based constitutive model is used to predict the stress-strain behavior of textured polycrystalline NiTi undergoing a forward stress-induced martensitic transformation. The transformation criteria of the micro-mechanical model accounts for the observed unidirectional nature of the shear deformation across the martensite habit planes. Aside from the previously determined crystallographic transformation data, only two experiments are required to determine the modeling constants; a uniaxial tension test and a stress free cool down test.
2. Using a pair interaction scheme two distinct interactions are predicted between the 24 NiTi martensite variants. Some variants are found to strongly self-accommodate (incompatible variants) while others are found to weakly self-accommodate (compatible variants). Using an interaction energy matrix the model accounts for self-accommodation by promoting the mutual transformation of compatible variants and hindering the mutual transformation of incompatible variants. If the incompatible variants are allowed to transform together then the predicted transformation stress-strain behavior demonstrates excessive hardening.
3. For a randomly oriented polycrystal the model predicts that the applied stress state has a negligible effect on the resulting stress-strain behavior. When experimentally measured crystallographic texture of the $\{110\}\langle 111\rangle$ type is incorporated into the micro-mechanical model, it is found that transformation in tension is strongly favored over transformation in compression. As experimentally observed, the model predicts that transformation in tension is macroscopically triggered at a lower applied stress level and subsequently proceeds with a smaller transformation stress-strain slope.

4. The model predicts that a more abrupt martensite evolution in tension versus compression is responsible for the asymmetric tensile/compressive stress-strain responses. The quicker martensite evolution rate under tension is further attributed to the fact that more grains (or martensite variants) are favorably oriented for transformation in tension versus compression. Under tension the large percentage of favorably oriented variants per grain indicates that there is a high probability for the simultaneous yield of all grains across a portion of the gage section. Under these localized conditions, it is predicted that macroscopic phase boundary motion may occur in polycrystalline NiTi under tensile loading.

REFERENCES

- Amrani M. El. (1994), Micromechanical aspects of thermoelastic martensites., *University de Metz*, Ph.D. Thesis.
- Baburaj, V., M. Kawai, K. Kinoshita and T. Koga (1996), An accurate prediction of specific damping capacity of TiNi SMA composite through a three-dimensional constitutive model., *J. Int. Mat. Sys. Struct.*, **7**, 145.
- Barrett, D. J. and B.J. Sullivan (1995), A three dimensional phase transformation model for shape memory alloys., *J. Int. Mat. Sys. Struct.*, **6**, 831.
- Boyd, J. G. and D.C. Lagoudas (1996), A thermodynamical constitutive model for shape memory materials. Part 1. The monolithic shape memory alloy., *Int. J. Plasticity*, **12**, 805.
- Boyd, J. G. and D.C. Lagoudas (1996), A thermodynamical constitutive model for shape memory materials. Part 2. The SMA composite material., *Int. J. Plasticity*, **12**, 843.
- Brandon, D. and R. C. Rogers (1992), Constitutive laws for pseudo-elastic materials., *J. Int. Mat. Sys. Struct.*, **3**, 255.
- Buchheit T. E., J. A. Wert (1994), Modeling the Effects of Stress State and Crystal Orientation on the Stress-Induced Transformation of NiTi Single Crystals., *Metall. Mater. Trans.*, **25A**, 2383.
- Buchheit T. E., J. A. Wert (1996), Predicting the orientation-dependent stress-induced transformation and detwinning response of shape memory alloy single crystals., *Metall. Mater. Trans.*, **27A**, 269.
- Chumlyakov Y. I. and S. V. Starenchenko (1995), Stress induced martensitic transformation in aged titanium nickel single crystals., *J. Phys. IV, Colloq*, **5**, 803.
- Chumlyakov Y. I., I. V. Kireeva, V. N. Lineytsev, and E. V. Chepel (1996), Aging influence on the shape memory effects and superelasticity in Titanium-Nickel Single crystals, *Siberian Physical Technical Institute Report*.
- Cizek, P. (1989), Orientation dependence of reversible strain in the shape memory effect in NiTi alloy., *Met. Mater.*, **27**, 52.
- Falk, F. (1989), Pseudoelastic stress-strain curves of polycrystalline shape memory alloys calculated from single crystal data., *Acta. Metall.*, **27**, 277.

- Gall K., H. Sehitoglu, H. J. Maier, and K. Jacobus (1997), Stress-induced martensitic phase transformations in polycrystalline Cu-Zn-Al shape memory alloys under different stress states., *Submitted to Act. Mett.*
- Huang, M. and L. C. Brinson (1997), A multivariant model for single crystal SMA behavior, *Submitted to J. Mech. Phys. Solids.*
- Jacobus, K., H. Sehitoglu, and M. Balzer (1996), Effect of stress state on the stress-induced martensitic transformation in polycrystalline Ni-Ti alloy., *Metall. Mater. Trans.*, **27A**, 3066.
- Kafka, V. (1995), Shape memory, A new concept of explanation and of mathematical modeling. Part II: Mathematical modeling of the SM effect and of pseudoelasticity., *J. Int. Mat. Sys. Struc*, **5**, 815.
- Kakeshita T., K. Shimizu, S. Nakamichi, R. Tanaka, S. Endo, F. Ono (1992), Effect of hydrostatic pressures on thermoelastic martensitic transformations in aged Ti-Ni and ausaged Fe-Ni-Co-Ti shape memory alloys., *Mater. Trans. JIM*, **6**, 1.
- Kumosa, M. (1991), Strain energy of a mechanical twin in α iron., *J. Phyc*, **24**, 1816.
- Melton, K. N. (1990), *Engineering Aspects of Shape Memory Alloys*, Eds. T. W. Duerig, K. N. Melton, D. Stockel and C.M. Wayman.
- Miyazaki S., S. Kimura, K. Otsuka, Y. Suzuki (1984), The habit plane and transformation strains associated with the martensitic transformation in Ti-Ni single crystals., *Scr. Mett.*, **18**, 883.
- Matsumoto O., S. Miyazaki, K. Otsuka, and H. Tamura (1987), Crystallography of martensitic transformations in Ti-Ni single crystals., *Acta. Mett.*, **35**, 2137.
- Mura, T. (1987), *Micromechanics of Defects in Solids*, Kluwer Academic Publishing, Netherlands, 2nd ed.
- Ono, N., A. Satoh, and H. Ohta (1989), A discussion on the mechanical properties of shape memory alloys based on a polycrystal model, *Mat. Trans. JIM*, **30**, 756.
- Orgeas L. and D. Favier (1995), Non-symmetric tension-compression behavior of NiTi alloy., *J. Phys. IV, Colloq.*, **5**, 605.
- Patoor, E., A. Eberhardt and M Berveiller (1996), Micromechanical modeling of superelasticity in shape memory alloys, *J. de Physique*, **6**, 277.

- Plietsch, R. and K. Ehrlich (1997), Strength differential effect in pseudoelastic NiTi shape memory alloys, *Acta Mater.*, **45**, 2417.
- Shaw J. A. and S. Kyriakides (1997), On the nucleation and propagation of phase transformation fronts in a NiTi alloy., *Acta Mater*, **45**, 683.
- Sun, Q. P., K. C. Hwang, and S. W. Yu (1991), A micromechanics constitutive model of transformation plasticity with shear and dilation effect, *J. Mech. Phys. Solids*, **39**, 507.
- Sun, Q. P. and K. C. Hwang (1993), Micromechanics modeling for the constitutive behavior of polycrystalline shape memory alloys-I. Derivation of general relations., *J. Mech. Phys. Solids*, **41**, 1.
- Sun, Q. P. and K. C. Hwang (1993), Micromechanics modeling for the constitutive behavior of polycrystalline shape memory alloys-II. Study of individual phenomenon., *J. Mech. Phys. Solids*, **41**, 19.
- Schetky, L. M. (1996), *International Conference on Displacive Phase Transformations and Their Applications in Materials Engineering*, Univ. of Ill.
- Tanaka, K. and T. Mura (1982), A theory of fatigue crack initiation at inclusions, *Metall. Mater. Trans.*, **13A**, 117.
- Wasilewski, R. J. (1971), The effect of Applied Stress on the Martensitic Transformation in NiTi, *Metall. Mater. Trans.*, **2A**, 2973.
- Wayman, C. M. (1986), Phase transformations in Ni-Ti shape memory alloys, *ICOMAT 86*, 645.

CHAPTER 6: MODELING THE EFFECTS OF AGING IN NiTi

PREVIEW

Transmission electron microscopy is used to determine the microstructures of a Ti - 50.8 at% Ni alloy given different aging treatments. Two different peak-aging treatments are shown to result in finely distributed semi-coherent $\text{Ti}_{11}\text{Ni}_{14}$ precipitates with a length ranging from 50 nm to 200 nm depending on the aging temperature. For these peak-aging treatments, strong strain fields are clearly visible on the TEM micrographs. An Eshelby based model is used to predict the local stress fields due to the differences in the lattice parameters of the precipitates and surrounding matrix. The position dependent local stress fields are then resolved onto the 24 different martensite correspondence variant pairs (CVP's). It is further demonstrated due to the unique orientation relationship that exists between the precipitate variants and the martensite CVP's, the local resolved shear stresses are extremely large on some CVP's and negligible on others. When the Ni rich NiTi is over-aged, it is found that the precipitates coarsen to approximately 1000 nm, they become in-coherent, and the local stress fields disappear. It is also determined that after over-aging the average composition of the matrix drops from 50.8 at% Ni to approximately 50.4 at% Ni.

6.1 BACKGROUND

Over the last two decades, many research efforts have focused on characterizing martensitic transformations in NiTi. Consistent with the groundbreaking studies on the mechanisms of plastic slip, most researchers have turned to single crystal NiTi materials. Experimental studies on single crystal materials are extremely useful because they allow the study of fundamental deformation mechanisms without the influence of grain boundary strengthening or crystallographic texture. At this time, martensitic

transformations in solutionized NiTi are well characterized. Nearly ten years ago it was proposed that in solutionized NiTi the thermally induced self-accommodating microstructure consisted of multiple three plate groups (Wayman, 1986). At that time, this result was not understood since a four plate group resulted in a more perfect self accommodating structure (the average shear strains in the group are zero). With the help of high resolution transmission electron microscopy, it is now known that the three variant groups form through an autocatalytic process (the growth of one plate induces the nucleation of the other two plates). This process leads to the less than perfect self-accommodating plate groups experimentally observed in solutionized NiTi (Madangopal, 1997).

The transformation parameters for martensitic transformations (twinning mode, habit plane, orientation relationship, magnitude and direction of shape strain) are well documented for solutionized NiTi (Matsumoto *et al.*, 1987). From the aforementioned study the lattice invariant shear in solutionized NiTi has been identified as type II twinning. Thus the individual martensite plates in NiTi consist of a stacking of different type II twin related variants. Consequently, it is appropriate to refer to different martensite plates formed in NiTi as correspondence variant pairs (CVP's) rather than martensite variants (Buchheit and Wert, 1994). Although martensitic transformations in solutionized NiTi are relatively well understood, there still exists many unresolved issues related to aged (precipitated) NiTi materials. For some time it has been known that materials without structural defects, such as very thin films, may never form martensite even if the measured martensite start temperature of the bulk material is high. This is due to the fact that the nucleation and growth of martensite is usually heterogeneous and when defects or precipitates are present they will control the martensitic transformation (Hornbogen, 1985). It is also worthwhile to note that when NiTi is used in engineering applications it is frequently given some type of aging (or annealing) treatment which sometimes results in a precipitates microstructure.

By utilizing different soak temperatures and hold times, peak-aging heat treatments can be used to tailor the properties of shape memory alloys such as the two-way shape memory effect (Honma, 1986) and pseudoelasticity (Miyazaki *et al.*, 1982). Since aged Ni rich NiTi alloys typically have transformation temperatures near room temperature, they have been extensively used in applications and consequently are a strong focus of current research efforts. The precipitation processes in Ni rich NiTi alloys are well documented (Beyer *et al.* 1986; Nishida *et al.*, 1986). In addition to the equilibrium precipitates (TiNi_3), Nishida and colleagues determined that there are several quasi-stable precipitates which form in Ni rich NiTi. All present research efforts agree that the precipitation of coherent or semi-coherent $\text{Ti}_{11}\text{Ni}_{14}$ (sometimes referred to as Ti_3Ni_4) precipitates leads to a large change in the macroscopic mechanical properties of Ni rich NiTi alloys. It is proposed here that heat treatments of this nature should be referred to as peak-aging treatments since they lead to the most drastic changes in the mechanical properties of NiTi. Table 6.1.1 outlines the required temperatures and times, observed microstructures, and thermally induced transformation characteristics of aged NiTi. The second row in Table 6.1.1 outlines the published heat treatments which lead to the precipitation of semi-coherent $\text{Ti}_{11}\text{Ni}_{14}$ precipitates in NiTi alloys with approximately 51 at% Ni. Three other heat treatments are possible: a solutionized state, an under-aged state, or an over-aged state. In Table 6.1.1, under-aged materials are not considered, since no work has been published on them. It should be noted that the aging treatments in the last two rows of Table 6.1.1 are performed on NiTi that exists in the solutionized state.

Metallurgical studies have uncovered several of the fundamental characteristics of martensitic transformations in peak-aged NiTi. Nishida and Wayman (1988) have proposed that peak-aged NiTi undergoes several premartensitic transformations. Upon cooling, the complete transformation sequence was determined to be: parent phase (B2) \rightarrow incommensurate phase (distorted cubic) \rightarrow commensurate phase (rhombohedral) \rightarrow martensitic phase

(B19'). It is worthwhile to note that the above solid state reactions occur in increasing order of displacive magnitude, and that the distorted cubic phase transformation is usually negligible (Nishida and Wayman, 1988). For this

Approximate Heat Treatment	Material Condition	Material Microstructure	Transformation Characteristics
T ~ 840 K - 1273 K t ~ 1 hour Water Quench	solutionized	Precipitate Free Supersaturated NiTi (Recrystallization)	Heating M → A Cooling M ← A
T ~ 673 K t ~ 1 - 50 hours T ~ 773 K - 830 K t ~ 1 hour Water Quench	peak-aged	Finely Distributed Semi-coherent Ti ₁₁ Ni ₁₄ Precipitates	Heating M → A Cooling M ← R ← A
T ~ 773 K t > 15 hours Water Quench	over-aged	Coarsened Incoherent Ti ₁₁ Ni ₁₄ Precipitates	Heating M → A Cooling M ← R ← A

Table 6.1.1: Three different aging treatments for NiTi alloys with approximately 51 at% Ni. The heat treatments cited represent the combined results of several researchers on both polycrystalline and single crystal NiTi (Todoroki and Tamura, 1987; Nishida and Wayman, 1988; Abujudom *et al.* 1990; Chumlyakov and Starenchenko, 1995).

reason, this transformation has not been indicated in Table 6.1.1. Treppmann and Hornbogen (1995) have proposed that the disperse structure of dislocations and precipitates promote the R-phase transformation (rhombohedral) and impede the martensitic phase (B19'). It has also been concluded that the precipitates in aged NiTi have a dramatic effect on the martensitic transformation (Nishida *et al.*, 1988). They determined that during cooling the martensite plates in peak-aged NiTi do not form in the traditional three plate (CVP) groups originally observed by Wayman (1986). In peak-aged NiTi the thermally induced martensite morphology appeared to be dominated by one plate growing from each of the precipitate variants. They also determined that the martensite in aged alloys was comprised of

compound twins (internal defects on (100) planes) rather than type II twins (internal defects on (110) planes). Notably, it has been shown that the transformation habit plane for compound twinning is slightly different than the habit plane for type II twinning in NiTi (Miyazaki *et al.*, 1984).

At the single crystal level the effects of aging on martensitic transformations in NiTi have been modeled to some degree. It has been proposed that recoverable strain levels are smaller in peak-aged specimens because the detwinning of internally faulted martensite is inhibited. Buchheit and Wert (1996) developed a single crystal constitutive model which includes both the transformation strains due to the phenomenological theory of martensitic transformations (CVP formation), and CVP detwinning. When detwinning was prohibited in their model, the predicted recoverable strains were on the order of previously reported experimental results (Miyazaki *et al.*, 1984) for peak-aged single crystals. The aforementioned model and the study by Treppman and Hornbogen (1995) are the only works to date which model martensitic transformations in aged NiTi. Clearly then it is necessary to better understand the effect of different aging treatments on martensitic transformations in NiTi. Consequently, the present study will focus on properly explaining the effect of precipitation on critical transformation stress levels, σ_{cr} , and martensite start temperatures, M_s , in NiTi. The results of the study will be presented in two separate reports. The present paper will model the effect of aging on σ_{cr} and M_s . Chapter 7 will use the modeling results presented here to critically discuss experimental results on aged single crystal and polycrystalline NiTi. This research is superior over previous research efforts since it relates the micro-mechanisms of aging to the macroscopic deformation behavior, allowing for the extension of the results to other NiTi alloy systems. The goals of the chapter are explicitly outlined below:

1. Determine the precipitation structure in Ni rich NiTi subjected to several distinctly different aging treatments including both peak-aged and

over-aged cases. Experimentally determine the decrease in the average Ni concentration of the matrix after over-aging.

2. Discuss the local stress fields and morphological changes associated with the precipitation of $Ti_{11}Ni_{14}$ in Ni rich NiTi alloys. Use micro-mechanical modeling to predict the local resolved shear stress fields on the 24 martensite correspondence variant pairs (CVP's) near the coherent or semi-coherent precipitates in peak-aged NiTi.

6.2 EXPERIMENTAL TECHNIQUES

Polycrystalline samples were electro-discharge machined from 1" diameter cylindrical bars purchased from Special Metals Corporation. The bars were cold drawn, centerless ground, straightened, and annealed. The polycrystalline samples were given a 2 hour solutionizing (recrystallization) heat treatment at 1273 K. The heat treatment was performed in evacuated quartz tubes which were quenched and broken in ambient temperature water. The average grain size of the polycrystalline material was determined to be about 20 μm . Bars from the same material batch were melted in ingots and used to produce single crystal NiTi specimens. The single crystals were grown using the modified Bridgeman technique in an inert gas atmosphere. Following growth, the crystals were homogenized at 1273 K for 24 hours in a vacuum furnace and quenched into ambient temperature water, leaving them in the solutionized state. The compositions of both the single crystal and the polycrystalline materials were found to be approximately Ti - 50.8 at% Ni.

The solutionized polycrystalline and single crystal samples were then given subsequent aging treatments. The aging treatments were chosen to yield distinctly different microstructures. The four heat treatments utilized in this study were: as solutionized, aged 1.5 hours @ 673 K, aged 1 hour @ 773 K, and aged 15 hours @ 773 K. Table 6.1.1 lists some of the expected

characteristics of NiTi in the different aged states. When the material is quenched from a high temperature it is left in the solutionized (supersaturated) state (row 1 in Table 6.1.1). The 15 hour treatment at 773 K leaves the material in the over-aged state (row 3 in Table 6.1.1). The two remaining heat treatments both leave the material in the peak-aged state (row 2 in Table 6.1.1). However, the 673 K heat treatment will result in a R-phase transformation that is separated from the martensitic transformation. Conversely, the 773 K heat treatment will result in a R-phase transformation which is closer to the martensitic transformation (Nishida and Wayman, 1988). TEM specimens of NiTi were prepared by thinning slices down to 150 μm with a $3\text{HNO}_3 + 2\text{H}_2\text{O} + 1\text{HF}$ solution, punching 3 mm disks, and twin jet electropolishing with a 20% H_2SO_4 - 80% methanol solution. A Hitachi 8100 operated at a nominal accelerating voltage of 200 kV was used to examine the precipitate structure. Local composition measurements were made with a Phillips EDX detector.

6.3 MICROSTRUCTURE IN AGED NiTi

The microstructure in aged Ni rich NiTi depends on the aging temperature, hold time, alloy composition, and prior cold work (Treppmann *et al.*, 1995). Figures 6.3.1 (a-d) are transmission electron microscope (TEM) images of the NiTi microstructure after peak-aging (1a-1c) and over-aging 1d heat treatments. Figure 6.3.1a is a two-beam bright field imaged of a sample aged for 1.5 h @ 673 K. On the micrograph there is a strong contrast that surrounds the precipitates which indicates that internal (local) strain fields are present. The strain fields are caused by the difference in the lattice parameters of the $\text{Ti}_{11}\text{Ni}_{14}$ precipitates and the surrounding NiTi matrix. Figure 6.3.1b shows a larger magnification of the precipitates in figure 6.3.1a. The precipitates are about 75 nm (.075 μm) in length, which indicates that they are semi-coherent in this fully recrystallized matrix (Treppmann *et al.*, 1995). In Figure 6.3.1b the strong contrast due to the lattice mismatch strains

is still visible. The next micrograph (Figure 6.3.1c) is a weak beam TEM picture of NiTi aged for 1 h @ 773 K. The weak beam TEM image is superior

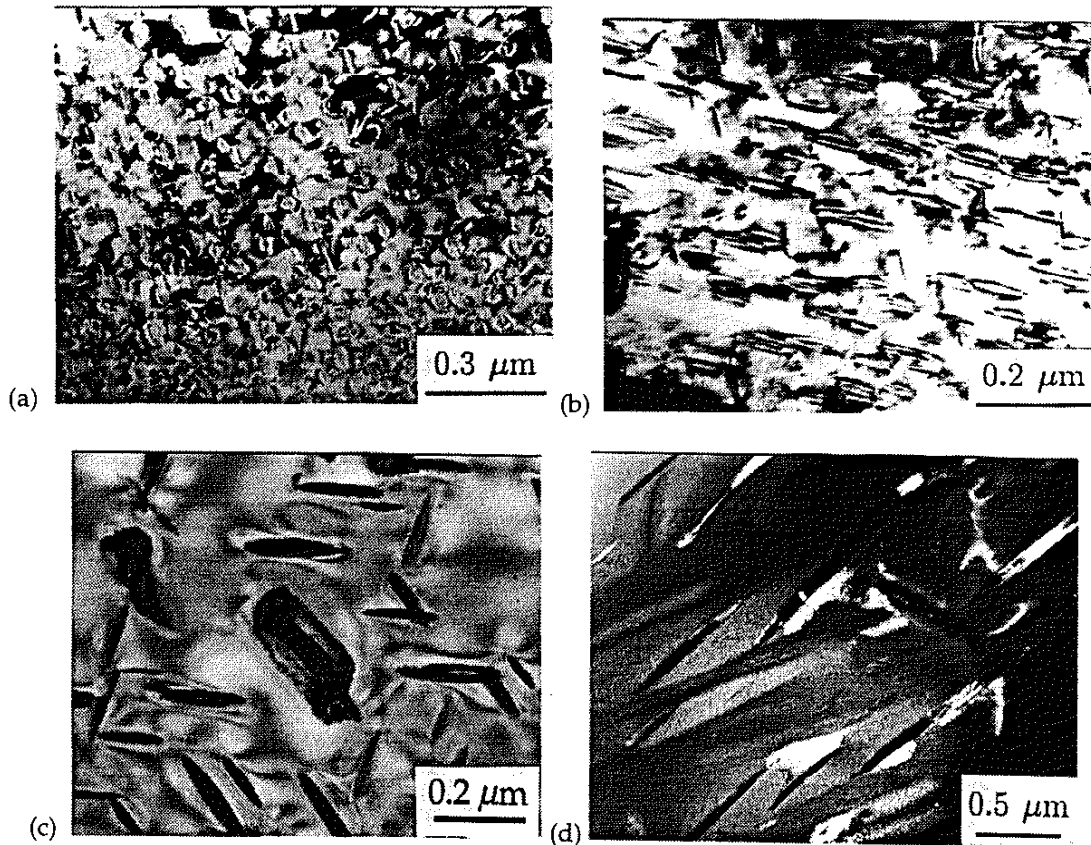


Figure 6.3.1: Microstructures in aged Ni rich NiTi: (a and b) aged 1.5 h @ 673 K, (c) aged 1 h @ 773 K, (d) aged 15 h @ 773 K. Figure c is a weak beam TEM image. The volume fraction of the precipitates in the over-aged material was determined to be approximately 0.074.

over a two-beam bright field image when attempting to determine the aspect ratio of the precipitates or the morphology. In a weak beam TEM image the contrast due to the surrounding strain fields is greatly decreased due to the choice of the diffracting beam. Consequently, the strain fields surrounding the precipitates are much stronger than Figure 6.3.1c indicates. At any rate, the precipitates in Figure 6.3.1c are about 50 nm in length. The aspect ratio of the precipitates appears to be about 7 (nm/nm). Since smaller precipitates are

always more coherent, clearly the 1.5 h @ 673 K heat treatment results in stronger local strain fields compared to the 1 h @ 773 K heat treatment.

Figure 6.3.1d is a TEM micrograph of over-aged Ni rich NiTi (15 h @ 773 K). The strong strain fields which were present in Figures 6.3.1(a-c) are completely absent in Figure 6.3.1d. Consequently, the coarsened precipitates in Figure 6.3.1d (length of about 1000 nm) are fully incoherent. This is consistent with the observation that $Ti_{11}Ni_{14}$ precipitates completely lose coherency with a fully recrystallized matrix at an average size of 300 nm (Treppmann *et al.*, 1995). In general the single crystals showed an even dispersion of all four variants of the $Ti_{11}Ni_{14}$ precipitates. Since they were aged in a stress free and undeformed state this is consistent with expectations (Li and Chen, 1997). It should be noted that in general Figures 6.3.1 (a-d) do not always show four precipitate variants. This is due to the fact that the inclusions sometimes represent several different variants which are indistinguishable in certain cross sections. The polycrystalline and single crystal materials given equivalent heat treatments all demonstrated very similar average precipitate sizes. However, it will be noted that in the polycrystalline material the precipitate structure in several grains sometimes appeared to be dominated by a single precipitate variant. In addition, there were some grains that has a sparse distribution of precipitates. The reason for the heterogeneous precipitate distribution is most likely due to the effects of intergranular constraint or local composition gradients.

6.4 MODELING TRANSFORMATIONS IN SOLUTIONIZED NiTi

To model the martensitic transformation at the "macroscopic" level, it is most appropriate to use the phenomenological theory of martensitic transformations (Lieberman *et al.*, 1955). Matsumoto and colleagues (1987) have determined the habit plane and transformation direction for the 24 correspondence variant pairs CVP's in NiTi (Table 6.4.1). In Table 6.4.1, the transformation direction is indicated by the unit vector m , and the habit

plane is indicated by the unit vector h . The magnitude of the transformation is $g = 0.13$. To obtain the orientation tensor (Schmid Factors) for the n^{th} martensite CVP in the global parent phase (B2) coordinate system, the following relationship is used:

$$\alpha_{ij}^n = \frac{1}{2}(h_i^n m_j^n + h_j^n m_i^n) \quad (6.4.1)$$

Buchheit and Wert (1994 and 1996) have noted that the small volume change during the transformation has a negligible effect on the predicted transformation behavior and can be ignored. With this, it is possible to calculate the resolved shear stresses on different CVP's due to an external stress applied to a single crystal of NiTi. For the n^{th} martensite CVP the resolved shear stress is given by:

$$\tau_{\text{rss-e}}^n = \sigma_{ij} \alpha_{ij}^n \quad (6.4.2)$$

When the resolved shear stress on a particular CVP is greater than the critical resolved shear stress, τ_{crss} then the transformation proceeds on that CVP:

$$\tau_{\text{rss-e}}^n \geq \tau_{\text{crss}}(T, c_{\text{Ni}}) \quad (6.4.3)$$

Equation 6.4.3 is directly analogous to the Schmid-Boas Law in single crystal slip theory. For martensitic transformations in solutionized NiTi τ_{crss} is a strong function of several variables, primarily the current test temperature, T , and the concentration of nickel in the alloy, c_{Ni} . It should also be noted that as the test temperature reaches the deformation induced temperature M_d , some so-called non-Schmid effects may affect the transformation. This is due to strong interactions between slip and the martensitic transformation near this temperature. At any rate equations 6.4.2

and 6.4.3 provide reasonable predictions for the orientation dependence of the

CVP Number	Habit Plane, h	Shear Direction, m
1	(-0.868, -0.414, 0.269)	[0.458, -0.443, 0.771]
2	(-0.414, -0.868, -0.269)	[-0.443, 0.458, -0.771]
3	(0.868, 0.414, 0.269)	[-0.458, 0.443, 0.771]
4	(0.414, 0.868, -0.269)	[0.443, -0.458, -0.771]
5	(-0.868, 0.414, -0.269)	[0.458, 0.443, -0.771]
6	(0.414, -0.868, 0.269)	[0.443, 0.458, 0.771]
7	(0.868, -0.414, -0.269)	[-0.458, -0.443, -0.771]
8	(-0.414, 0.868, 0.269)	[-0.443, -0.458, 0.771]
9	(0.269, 0.868, 0.414)	[0.771, -0.458, 0.443]
10	(0.269, -0.868, -0.414)	[0.771, 0.458, -0.443]
11	(-0.269, -0.414, -0.868)	[-0.771, -0.443, 0.458]
12	(-0.269, 0.414, 0.868)	[-0.771, 0.443, -0.458]
13	(-0.269, 0.868, -0.414)	[-0.771, -0.458, -0.443]
14	(-0.269, -0.868, 0.414)	[-0.771, 0.458, 0.443]
15	(0.269, 0.414, -0.868)	[0.771, 0.443, 0.458]
16	(0.269, -0.414, 0.868)	[0.771, -0.443, -0.458]
17	(0.868, -0.269, 0.414)	[-0.458, -0.771, 0.443]
18	(-0.868, -0.269, -0.414)	[0.458, -0.771, -0.443]
19	(0.414, 0.269, 0.868)	[0.443, 0.771, -0.458]
20	(-0.414, 0.269, -0.868)	[-0.443, 0.771, 0.458]
21	(0.868, 0.269, -0.414)	[-0.458, 0.771, -0.443]
22	(-0.868, 0.269, 0.414)	[0.458, 0.771, 0.443]
23	(-0.414, -0.269, 0.868)	[-0.443, -0.771, -0.458]
24	(0.414, -0.269, -0.868)	[0.443, -0.771, 0.458]

Table 6.4.1: Transformation parameters for the B2 → B19' martensitic transformation in NiTi (Matsumoto *et al.* 1987). CVP stands for correspondence variant pair.

critical stress levels, σ_{cr} , required to trigger the transformation in solutionized NiTi (Chumlyakov *et al.*, 1996). The temperature dependence of τ_{crss} follows a linear distribution in resolved shear stress-temperature space between M_s and M_d (Clausius-Clapeyron relationship). It will be noted the slopes of the Clausius-Clapeyron lines in σ_{cr} versus temperature space will be different for

different crystallographic orientations. However, if a single crystal shape memory alloy system obeys the Schmid law then the linear distribution of τ_{crss} as a function of temperature will be the same for all orientations. As the test temperature approaches the martensite start temperature, M_s , the critical resolved shear stress, τ_{crss} , is zero. Consequently, at M_s the stress required to trigger the transformation will be negligible in solutionized single crystals. It should be noted that a finite value is often reported at M_s and this value is due to the strain offset method often used to determine σ_{cr} . If the temperature is subsequently dropped below M_s then the transformation will proceed on all 24 CVP's in solutionized NiTi.

6.5 MODELING PHILOSOPHY IN AGED NiTi

The experimental results in chapter 7 demonstrate that equation 6.4.3 cannot always be used to predict the orientation dependence of the critical transformation stress levels, σ_{cr} , in aged NiTi. In addition, NiTi which is given different aging treatments demonstrates different values of M_s and σ_{cr} (at a given test temperature). In order to properly model the influence of aging on σ_{cr} and M_s in NiTi, it is first appropriate to discuss precipitation in Ni rich NiTi. The coherent $\text{Ti}_{11}\text{Ni}_{14}$ precipitates are disk shaped with a normal that is parallel to the [111] direction in both phases (Li and Chen, 1997 I, II). With this, and the fact that the disks have rotational symmetry, it is clear that the precipitates have 8 possible crystallographic variants. By further considering the mirror symmetry of the disks about their normal, the number of unique precipitate orientations is reduced to four. Figure 6.5.1 schematically demonstrates a slice of aged NiTi parallel to the $[\bar{1}01]_{\text{B}_2}$ plane. The schematic is directly analogous to the TEM micrograph of peak-aged single crystal NiTi in figure 6.3.1c. In Figure 6.5.1, the thinner (angled) lenticular inclusions are cross sections of the disk shaped precipitates parallel to their normal. The slightly wider (horizontal) lenticular inclusions are cross sections of the precipitates at an angle offset from their normal. It

should also be noted that only three different precipitate variants are visible on Figure 6.5.1. This is because the horizontal inclusions represent two

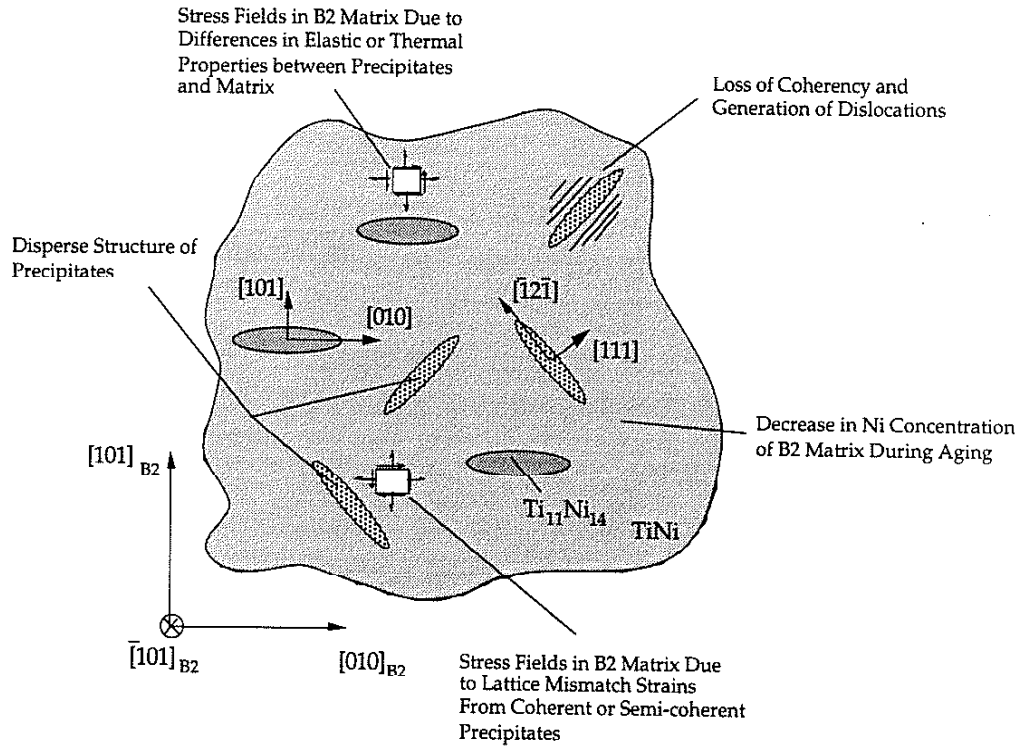


Figure 6.5.1: Schematic of possible stress fields and morphological changes associated with Ti₁₁Ni₁₄ precipitates in Ni rich NiTi.

different precipitate variants which are indistinguishable from each other in this particular cross section.

There are several microstructural changes due to the precipitation that may alter σ_{cr} and M_s in NiTi. It should be noted here that a increase in M_s is the same as a decrease in σ_{cr} (at any test temperature) as predicted by a shift of the Clausius-Clapeyron line in stress-temperature space. When coherent or semi-coherent precipitates are formed a strong local stress field is developed in the NiTi matrix due to the mismatch in lattice parameters of the precipitates versus the matrix (Figure 6.5.1). These local stress fields result in local resolved shear stresses on martensite CVP's and thus create preferential

nucleation sites for the martensitic transformation. However, during aging there usually exists a critical particle size at which the precipitates completely lose coherency with the matrix (Hornbogen, 1985). As this critical size is approached, dislocations are generated around the precipitates, and the stress fields due to the lattice mismatch strains are weakened (Martin, 1980). During aging the Ni rich NiTi matrix is also depleted of Ni (Figure 6.5.1). A decrease in the Ni concentration from 51 at% to 50 at% has been shown to raise M_s in solutionized NiTi as much as 120 K (Duerig and Pelton, 1994). Thus a change in the nominal composition of the matrix (the only material which undergoes the martensitic transformation) will affect the transformation if the Ni loss is significant. The final change that may alter σ_{cr} and M_s in aged NiTi is a difference in the thermal or elastic properties of the precipitates and the matrix (Figure 6.5.1). When the bulk material is uniformly stressed or cooled, the difference in these properties will generate local disturbance stress fields in the NiTi matrix (Mura, 1987).

Although the aforementioned mechanisms will all effect the martensitic transformation to some degree, it is proposed that only two of them will significantly affect σ_{cr} and M_s in NiTi. Li and Chen (1997 I, II) have ignored the effect of elastic and thermal property mismatch between the matrix and the precipitates and have successfully modeled the growth of these precipitates under stress. Thus, in this analysis, the elastic and thermal properties of the matrix and the precipitates will be assumed to be the same. In addition, the discussion will not consider the effect of the disperse structure of the precipitates *per se*. Calculating the stress fields resulting from precipitate interactions is not necessary to examine the effect of precipitation on σ_{cr} and M_s . However, it will be noted that any model which hopes to predict the subsequent growth of martensite plates through an aged microstructure must consider the disperse structure of the precipitates. In this paper, only the critical transformation parameters (stress, temperature) as a function of aging treatment will be considered. It should also be noted that this discussion will only consider the martensitic (B2->B19') transformation.

The effect of the preceding R-phase transformation on the subsequent martensitic transformation will not be considered. Treppmann and Hornbogen (1995) have noted that the R-phase transformation occurs in aged NiTi simply because of the disperse structure of the precipitates. In their calculations they did not consider the effect of the R-phase on the martensitic transformation. In addition to this, Nishida and Wayman (1988) have concluded that the R-phase is not precursory to the martensitic transformation. With this, the variables which are proposed to strongly affect σ_{cr} and M_s in aged NiTi alloys are: 1. The generation and subsequent degeneration of strong local stress fields due to the transition from coherent to incoherent precipitates, 2. The depletion of Ni in the matrix surrounding the precipitates.

6.6 MODELING THE EFFECT OF COHERENT PRECIPITATES

Figure 6.6.1 is a schematic of the proposed effect of the local stress fields from the coherent or semi-coherent precipitates on the martensitic transformation. In addition to the resolved shear stress due to the external loading, τ_{RSS-e}^n , there now exists a resolved shear stress due to the local stress fields around the precipitates, a so-called internal resolved shear stress, τ_{RSS-i}^n . As a first approximation the micro-mechanical modeling here will assume that the martensite which forms in the matrix surrounding the precipitates is the same as the martensite which forms in solutionized NiTi. That is, the modeling will ignore the observed formation of compound twins in aged NiTi as observed by Nishida *et al.* (1988). In Figure 6.6.1 an average internal resolved shear stress is also defined. This average internal resolved shear stress, $\bar{\tau}_{RSS-i}^n$ is necessary to properly estimate the effect of the precipitates on the macroscopic critical stress, σ_{cr} , and temperature, M_s , required to trigger the transformation. The volume, V , is chosen in a region where the martensite is expected to nucleate and grow. With this choice, $\bar{\tau}_{RSS-i}^n$ is

expected to give a first order approximation of the effect of the precipitate stress fields on the macroscopic critical transformation parameters. Using a

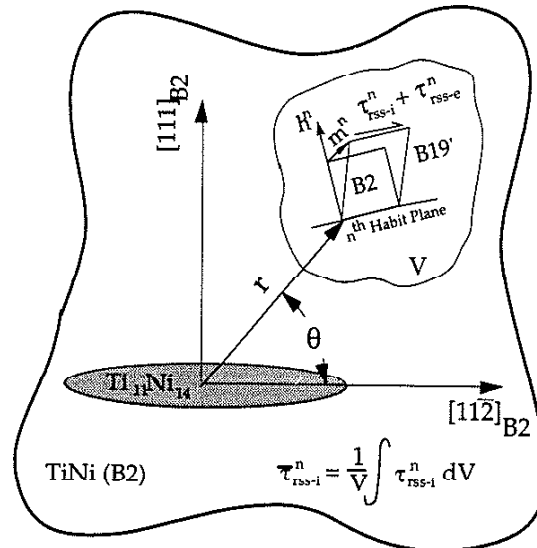


Figure 6.6.1: Schematic of the proposed effect of local lattice mismatch strains (stresses) on martensitic transformations in aged NiTi.

pointwise maximum stress value would not properly consider the fact that the martensite must be able to grow into a favorable stress field after microscopic nucleation. In addition, averaging the internal stress field over the entire volume does not properly consider the observed heterogeneous nucleation and growth characteristics of martensite plates. With this, equation 3 can be modified for peak-aged NiTi single crystals:

$$\tau_{rss-e}^n + \bar{\tau}_{rss-i}^n \geq \tau_{crss}(T, c_{Ni}) \quad (6.6.1)$$

The above equation states that the transformation will proceed when the sum of the internal and external resolved shear stresses is greater than a critical value. Equation 6.6.1 does not hold in a strict sense since it is difficult to precisely calculate the internal (local) resolved shear stress fields on the individual martensite CVP's. However, approximate values of the local

stress fields can be used along with equation 6.6.1 to estimate the effect of coherent or semi-coherent precipitates on the critical transformation stress level and martensite start temperatures.

The local stress fields outside the precipitates are caused by the lattice parameter mismatch which exists between the coherent or semi-coherent precipitates and the matrix. The general philosophy of the model proposed here is to use the difference in the lattice parameters of the two phases (Li and Chen, 1997-II) as the eigenstrain for a disk shaped inclusion in an infinite elastic matrix:

$$\varepsilon_{ij}^p = \begin{pmatrix} 0.014 & 0 & 0 \\ 0 & 0.014 & 0 \\ 0 & 0 & -0.029 \end{pmatrix} \quad (6.6.2)$$

The above eigenstrain is only valid in the principal coordinate frame for the disk shaped precipitate: $[1\bar{1}0]_{B2}$, $[11\bar{2}]_{B2}$, and $[111]_{B2}$. It will be noted that the modeling is aimed at predicting the effect of aging on transformation stress levels and temperatures at the onset of the transformation. Thus, the local stress fields from the lattice mismatch in equation 6.6.2 are exclusively considered here. As the martensite grows the lattice mismatch strains and local stress fields will change. Near the completion of the transformation the local stress fields will be governed by the lattice mismatch between the precipitates and the B19' martensite. These newly formed stress fields are responsible for the inhibition of detwinning and will also control the reverse transformation upon unloading. At any rate, the precipitates were assumed to be elliptical (oblate spheroids). The chosen length scale of the precipitates does not affect the modeling *per se*. However, the aspect ratio has a profound effect on the stress fields so it is important to consider the aspect ratio which was observed in the micrographs. For the two peak-aging treatments the aspect ratio of the precipitates was measured to be about 7 (Figure 6.3.1c). In addition, choosing an elliptical geometry is critical since a simplified spherical

geometry will not yield the expected strong position dependent (r, θ) stress fields.

Given the elliptical geometry, the elastic constants of the two mediums, and the eigenstrain (equation 6.6.2) it is possible to calculate the local stress and strain fields outside of the disk shaped precipitates (Mura, 1987):

$$\varepsilon_{ij}^{\text{local}}(r, \theta) = D_{ijkl}(r, \theta) \varepsilon_{kl}^p \quad \sigma_{ij}^{\text{local}}(r, \theta) = C_{ijkl} \varepsilon_{ij}^{\text{local}}(r, \theta) \quad (6.6.3)$$

where C_{ijkl} is the elasticity tensor, $D_{ijkl}(r, \theta)$ the Eshelby tensor for the exterior stress field, and (r, θ) indicates that the quantities are dependent on the position outside of the precipitate. Given the geometry of the precipitates and the symmetry of the eigenstrains, the local stress fields only depend on r and θ as indicated in Figure 6.6.1. The Eshelby tensor for the exterior stress fields, $D_{ijkl}(r, \theta)$, is derived by using Green's functions and depends on the distance from the precipitate, the precipitate geometry, and the elastic constants of the precipitate. For the elliptical geometry chosen $D_{ijkl}(r, \theta)$ is quite complex (Mura, 1987) and solving for the stress and strain fields in equation 6.6.3 is rather computationally intensive.

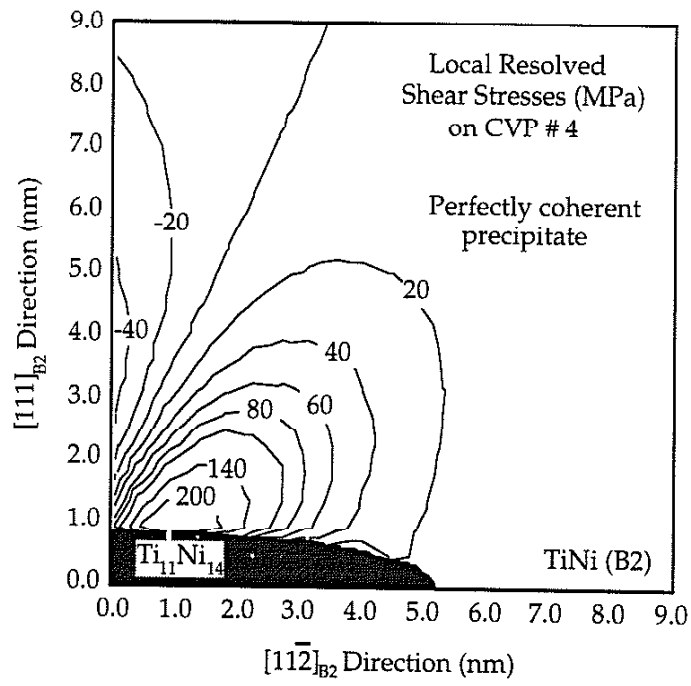
To estimate the effect of $\sigma_{ij}^{\text{local}}$ on the martensitic transformation, it is appropriate to calculate the local resolved shear stresses acting on the 24 martensite CVP's near the precipitate, $\tau_{r_{SS-i}}^n$. Once again it will be noted that it is assumed that the martensite which forms in the aged NiTi matrix is the same as the martensite which forms in solutionized NiTi. The first step in the calculation is to use equation 1 to calculate the orientation tensors for the 24 martensite CVP's. Then the 24 orientation tensors are transformed from the global coordinate system into the precipitate coordinate system ($\alpha_{ij}^{n'} = \lambda_{ik} \lambda_{jl} \alpha_{kl}^n$, where λ_{ij} is the rotation tensor between the two coordinate

frames). Finally, the local position dependent resolved shear stresses acting on the 24 martensite CVP's surrounding the precipitates are calculated through the following relationship:

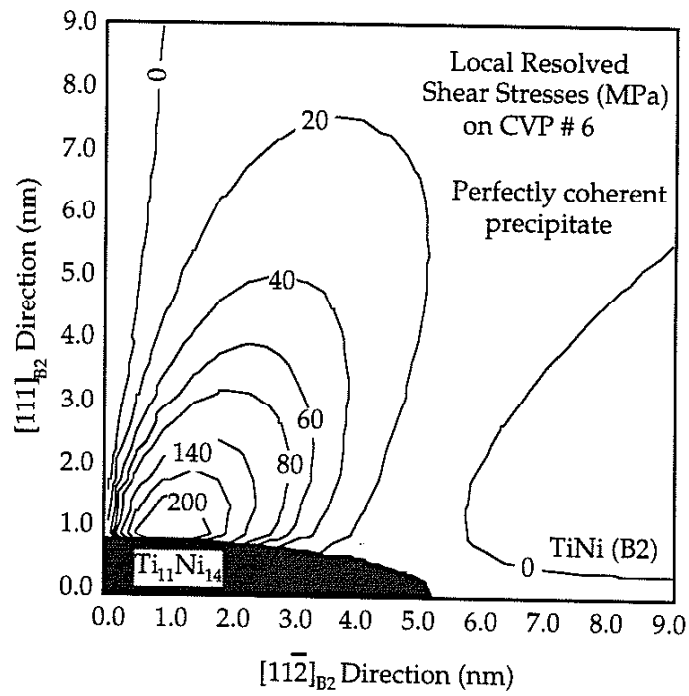
$$\tau_{\text{rss}-i}^n(\mathbf{r}, \theta) = \sigma_{ij}^{\text{local}}(\mathbf{r}, \theta) \alpha_{ij}^{n'} \quad (6.6.4)$$

Although there are 4 different precipitate variants, only one variant will be analyzed in this paper. The local stress fields outside the other three variants of the precipitates are the same, and are not necessary to draw the conclusions made in chapter 7. It should also be noted that precipitate interactions were not considered here. It is clear that the neighboring precipitates will affect the local stress and strain fields. However, the calculation of these local interactions is more pertinent to the subsequent growth of the martensite and not the critical transformation stress levels and martensite start temperatures in NiTi studied here.

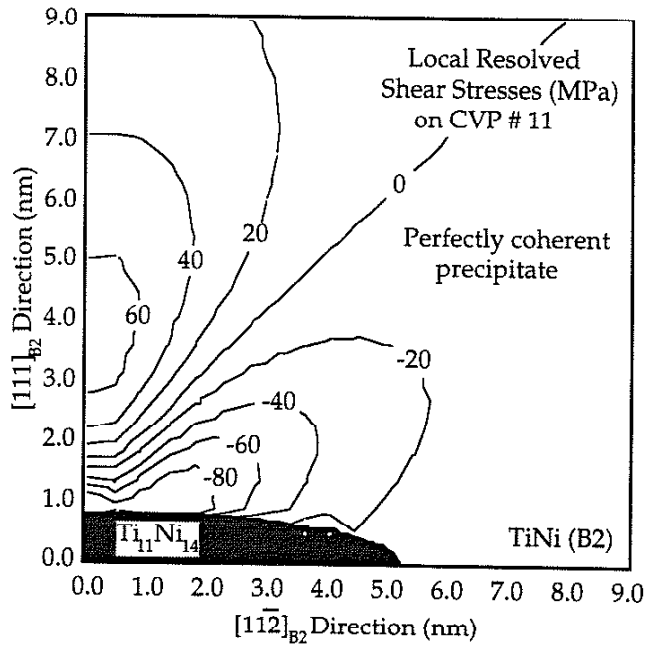
Figures 6.6.2 (a-d) are representative local resolved shear stress, $\tau_{\text{rss}-i}^n$ contour plots around the precipitates. The stress fields are resolved onto several different martensite CVP's ($n = 4, 6, 11, 20$) in order to demonstrate that not all martensite CVP's experience the same local stress distributions due to the coherent precipitates. The plots (and the precipitates themselves) are axis-symmetric about the [111] direction and possess mirror symmetry across the (111) plane. It should also be noted that the resolved shear stress fields are representative of perfectly coherent precipitates. As the precipitates coarsen, dislocations are generated, the precipitates become semi-coherent, and the stress fields are weakened (Martin, 1980). From the plots it is clear that the stress fields are usually largest right next to the precipitates and quickly diminish away from the precipitate. However, it is also clear from section 3 that the precipitates are rather close together. Hence, the stress fields due to the precipitates will overlap and only the resolved shear stress contours relatively close to the precipitate will control σ_{cr} and M_s .



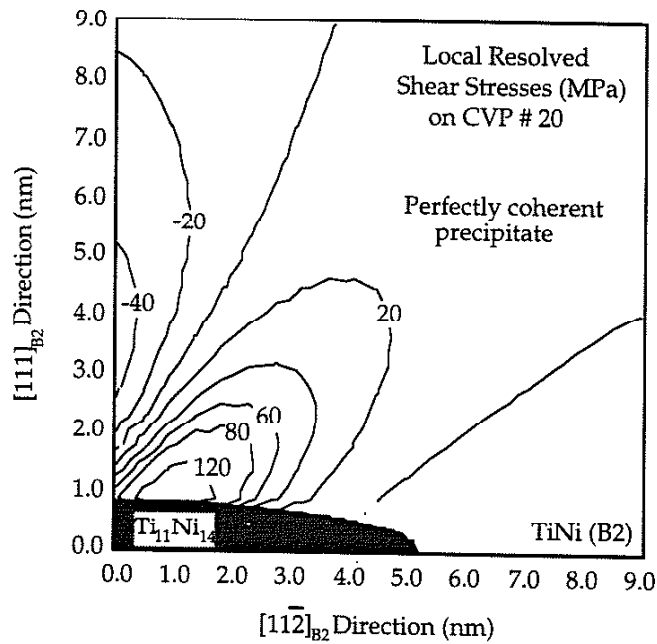
(a)



(b)



(c)



(d)

Figures 6.6.2 (a-d): Predicted resolved shear stress fields outside of perfectly coherent precipitates due to lattice mismatch strains. As the precipitates grow larger than 10 nm they become semi-coherent (Treppmann *et al.*, 1995). The plots are axis-symmetric about the [111] direction and have mirror symmetry about the (111) plane. CVP stands for correspondence variant pair.

The stress fields in all cases are negligible near the edges of the disks and more pronounced near the centers. Thus this model predicts that the

CVP Number	Maximum Local	Location	
	Resolved Shear Stress $\bar{\tau}_{\text{rSS}-i}^n$ (MPa)	r (nm)	θ (degrees)
1	20	80	30°
2	60	80	80°
3	50	80	90°
4	148	40	45°
5	0	-	-
6	148	40	45°
7	0	-	-
8	20	40	45°
9	60	80	80°
10	90	40	45°
11	60	80	90°
12	40	25	90°
13	130	40	45°
14	70	40	45°
15	10	50	30°
16	50	40	45°
17	30	35	30°
18	50	80	90°
19	50	80	90°
20	90	40	45°
21	10	120	10°
22	0	-	-
23	50	30	45°
24	0	-	-

Table 6.6.1: Summary of maximum (positive) average local resolved shear stresses for all 24 martensite CVP's (correspondence variant pairs). The tabulated results are for one precipitate variant out of 4.

martensite will nucleate near the center of the precipitate and grow outwards. In Figures 6.6.2(a, c, d) the local resolved shear stress fields are both positive and negative, while in Figure 6.6.2b the resolved shear stress fields are only positive. In the regions where the shear stresses are positive the transformation will be favored, while the transformation will be hindered in

the regions with negative shear stresses (equation 6.6.1). This is due to the well know unidirectional nature of the martensitic transformation across the habit plane (Buchheit and Wert, 1994 and 1996). Figures 6.6.2(a-d) also demonstrate that the local stress fields outside of the precipitates resolve very differently onto various martensite CVP's. For some CVP's the local resolved shear stress fields are very large (Figure 6.6.2a) while in others the shear stresses are much smaller (Figure 6.6.2c). The magnitude and relative location (r, θ defined in Figure 6.6.1) of the maximum average local resolved

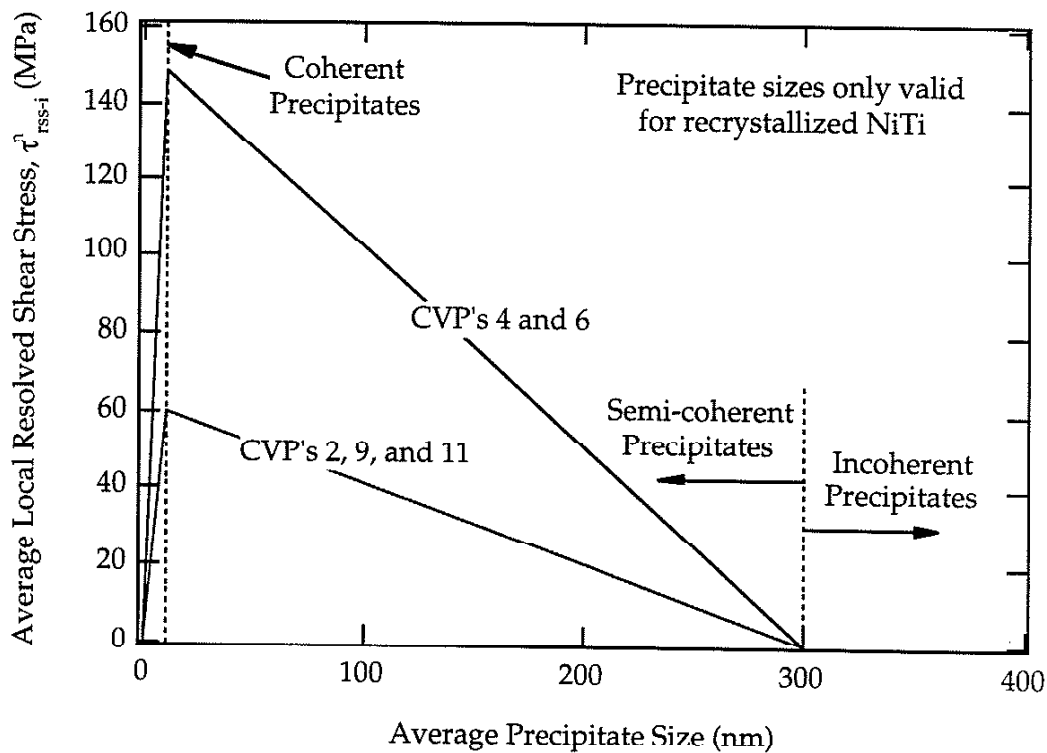


Figure 6.6.3: Plot which demonstrates the weakening of internal resolved shear stress fields due to the loss of coherency of $Ti_{11}Ni_{14}$ precipitates. The precipitate sizes for perfectly coherent precipitates (10 nm) and incoherent precipitates (300 nm) were determined by Treppmann *et al.*, (1995) for recrystallized Ti - 50.8 at% Ni.

shear stresses are summarized in Table 6.6.1. The volume over which the average resolved shear stress was calculated was kept equivalent in all

calculations in order to properly compare the magnitude of local stresses on different CVP's.

The stress fields predicted in Figure 6.6.2 and outlined in Table 6.6.1 are for perfectly coherent $Ti_{11}Ni_{14}$ precipitates. During aging the precipitates lose coherency with the B2 matrix and the stress fields are greatly weakened. Treppmann *et al.*, (1995) have determined that for recrystallized Ti - 50.8 at% Ni (the same material employed here) the precipitates are perfectly coherent at about 10 nm and completely lose coherency at about 300 nm. They also noted that in a cold worked matrix (20% CW) the precipitates will become incoherent at 150 nm. At any rate, the relationship between precipitate size and coherency level is useful in this study because it allows the researchers to quantitatively determine the weakening of the internal resolved stress fields as the sample is aged. Figure 6.6.3 shows the average local resolved shear stress, $\bar{\tau}_{RSS-i}^n$, as a function of the average precipitate size. As a first approximation, a linear dependence is assumed between the two variables although the actual effect may be slightly non-linear. Figure 6.6.3 demonstrates that for different martensite CVP's the internal resolved shear stress fields weaken at different rates. The figure is extremely valuable since the magnitude of $\bar{\tau}_{RSS-i}^n$ can be estimated for a given precipitate size. The two curves in Figure 6.6.3 are able to account for the decrease in the orientation dependence of σ_{cr} in NiTi given aging treatments that result in different precipitate sizes (this is demonstrated in chapter 7). In addition, the extremely strong local stress fields on some individual martensite CVP's ($n = 4$ and 6) accounts for the large increase in M_s (decrease in σ_{cr}) and the loss of the traditional three variant self accommodating groups in peak-aged NiTi .

6.7 ESTIMATING THE EFFECT OF Ni LOSS IN THE MATRIX

Although the internal stress fields will alter the martensitic transformation in aged NiTi, it is also proposed that compositional changes brought about by aging will also have an effect. The average composition of

the alloys was measured to be 49.2 at% Ti and 50.8 at% Ni. Although this average remains the same during aging, strong compositional gradients are developed in the alloy. In the peak-aged state accurate measurements of matrix and precipitate compositions are not possible due to the fine distribution of precipitates. However, in the over-aged materials the

	Lowest Measured Ni Concentration	Highest Measured Ni Concentration
Surrounding Matrix	51.4 at% Ti, 48.6 at% Ni	46.7 at% Ti, 53.3 at% Ni
Ti ₁₁ Ni ₁₄ Precipitates	44.1 at% Ti, 55.9 at% Ni	

Table 6.7.1: Experimentally measured compositions of precipitates and surrounding matrix in over-aged NiTi. The measurements were made on several different specimen areas.

compositions of the matrix and precipitates were successfully measured. The results of the composition analysis are shown in Table 6.7.1. The composition of the precipitates here (Table 6.7.1) matches the expected Ti₁₁Ni₁₄ composition (Nishida *et al.*, 1986). Several different compositional measurements were made in the matrix between the coarsened precipitates. In some areas the local Ni concentration was very low while in others it was very high (Table 6.7.1). The locally high concentrations of Ni in Table 6.7.1 are due to the segregation of Ni and most likely represent dissolved precipitates. However, to qualitatively determine the effect of the composition change on σ_{cr} and M_s in NiTi, it is necessary to determine the average Ni concentration in the matrix, c_{Ni} , surrounding the precipitates.

Due to the small samples of material that are studied with the TEM it is somewhat difficult to experimentally estimate the macroscopic volume fraction of the microscopic Ti₁₁Ni₁₄ precipitates, particularly in the peak-aged samples. However, it is possible to estimate the volume fraction of the

coarsened precipitates in the over-aged case. It is expected that the volume fraction of the precipitates in the over-aged case is only slightly higher than the volume fraction in the peak-aged cases. Using imaging software the volume fraction of the $Ti_{11}Ni_{14}$ precipitates in Figure 6.3.1d was determined to be about 0.074. Since the precipitates are very rich in Ni, during aging the average composition of the matrix must fall below the average composition of the alloy (50.8 at%Ni). In fact, if the average composition of the alloy is assumed to be set at 50.8 at%Ni and the composition of the precipitates is set at 55.9 at%Ni (volume fraction = 0.074), it is possible to calculate the average composition of the matrix, c_{Ni} , in the over-aged state:

$$c_{Ni} = \frac{50.8 - 55.9 * f}{(1 - f)} \text{ at\% Ni} = 50.39 \text{ at\% Ni} \quad (6.7.1)$$

A drop in the average composition of the matrix from 50.8 at%Ni to 50.4 at%Ni will have a significant effect on σ_{cr} and M_s . Figure 6.7.1 is a reproduction of the work published by Duerig and Pelton (1994) which demonstrates the dependence of M_s on the Ni concentration in the alloy. In Figure 6.7.1 the composition of the solutionized specimens and the matrix of the over-aged samples are also indicated. From figure 6.7.1 it is clear that M_s is expected to increase anywhere from 30 K to 70 K if the Ni concentration of the matrix drops about 0.4 at%Ni. Clearly an increase in M_s of that magnitude will also affect the critical transformation stress level in the alloy at any given test temperature.

The change in the composition of the matrix is a “homogeneous” effect on the martensitic transformation. That is, it will not effect the orientation dependence of single crystals or final martensite morphology in stress or temperature induced transformations. However, the decrease in the Ni concentration will raise M_s and lower σ_{cr} (at a given test temperature). It is appropriate to consider this effect in conjunction with the local stress fields from the precipitates. By considering both effects it is shown in chapter 7 that

the aging influence on σ_{cr} and M_s can be accounted for. In the peak-aged

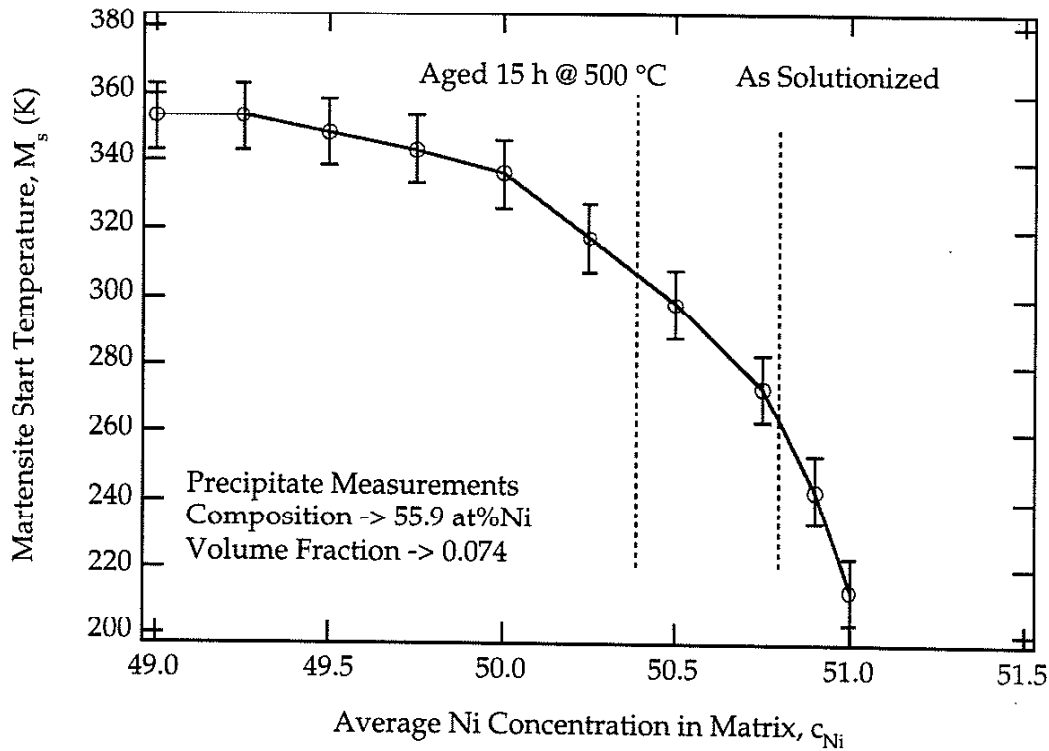


Figure 6.7.1: The martensite start temperature as a function of composition as taken from Duerig and Pelton (1994). The measured composition of the solutionized alloy and the matrix composition of the over-aged alloy (calculated from volume fraction of precipitates and known precipitate composition) are also included in the figure.

samples the local stress fields combined with the compositional changes will raise M_s and lower the critical transformation stress levels. In addition to altering M_s , it is shown that the local stress fields in the peak-aged samples will decrease the orientation dependence of the critical transformation stress levels. In the over-aged samples M_s is raised and σ_{cr} is lowered exclusively due to compositional changes.

6.8 CONCLUSIONS

1. Several different aging treatments on solutionized Ti - 50.8 at% Ni resulted in the following average precipitate sizes: 1.5 h @ 673 K (peak-aged) - > 75 nm, 1 h @ 773 K (peak-aged) -> 150 nm, 15 h @ 773 K (over-aged) -> 1000 nm. In peak-aged Ni rich NiTi materials it is observed that finely distributed semi-coherent $\text{Ti}_{11}\text{Ni}_{14}$ precipitates result in very large local strain fields. The chemical composition of the precipitates was found to be 55.9 at%Ni. By measuring the precipitate volume fraction in the over-aged state (0.074), the average decrease in the Ni concentration of the matrix was predicted to be about 0.4 at%Ni.
2. Using an Eshelby based micro-mechanical model the local stress fields due to lattice mismatch strains are calculated for a perfectly coherent $\text{Ti}_{11}\text{Ni}_{14}$ precipitate in a NiTi matrix. To estimate the effect of the local stresses on the martensitic transformation, the local stress fields outside of the precipitate are then resolved onto the 24 martensite correspondence variant pairs (CVP's). It is further demonstrated that due to the unique orientation relationship that exists between the precipitate variants and the martensite CVP's, the local resolved shear stresses are extremely large on some CVP's and negligible on others.
3. The modeling results presented here are used in chapter 7 to discuss experimental results on aged NiTi. In peak-aged NiTi the model predicts an increase in the martensite start temperature and a decrease in the critical transformation stress levels that is primarily due to the local resolved shear stresses. In over-aged NiTi the model predicts an increase in the martensite start temperature and a decrease in the critical transformation stress levels that is primarily due to local compositional changes. In addition the model is able to successfully predict the decrease in the orientation dependence of the critical transformation stress levels in peak-aged NiTi.

REFERENCES

- Abujudom D. N., Thoma P. E., and Fariabi S., 1990, "The Effect of Cold Work and Heat Treatment on the Phase Transformations of Near Equiatomic NiTi Shape Memory Alloy," *Mat. Sci. Forum*, vol. 56-58, pp. 565-570.
- Beyer, J., Brakel, R. A., and Lloyd, J. R. T., 1986, "Precipitation Processes in TiNi Near Equiatomic Alloy," *ICOMAT-86*, pp. 703-708.
- Buchheit T. E., J. A. Wert, 1994, "Modeling the Effects of Stress State and Crystal Orientation on the Stress-Induced Transformation of NiTi Single Crystals," *Metall. Mater. Trans.*, vol. 25A, pp. 2383-2389.
- Buchheit T. E., J. A. Wert, 1996, Predicting the orientation-dependent stress-induced transformation and detwinning response of shape memory alloy single crystals., *Metall. Mater. Trans*, vol. 27A, pp. 269-279.
- Chumlyakov Y. I. and S. V. Starenchenko, 1995, "Stress-induced martensitic transformation in aged titanium nickel single crystals., *J. Phys. IV, Colloq*, vol. 5, pp. 803-807.
- Chumlyakov Y. I., I. V. Kireeva, V. N. Lineytsev, and E. V. Chepel, 1996, "Aging influence on the shape memory effects and superelasticity in Titanium-Nickel Single crystals," *MRS Symposium Proceedings*, vol. 459, Boston, pp. 387-392.
- Duerig, T. W. and Pelton, A. R., 1994, "Ti-Ni Shape Memory Alloys," *Mater. Prop. Hnbk.*, ASM International, Titanium Alloys, pp. 1035-1048.
- Honma, T, 1986, "The effect of aging on the spontaneous shape change and the all-round shape memory effect in Ni-Rich TiNi alloy," *ICOMAT-86*, pp. 709-716.
- Hornbogen, E., 1985, "The effect of Variables on Martensitic Transformations Temperatures," *Acta. Mett.*, vol. 33, pp. 595-601.
- Lieberman, D. S., Wechsler, M. S., and Read, T. A., 1955, "Cubic to Orthorombic Diffusionless Phase Change-Experimental and Theoretical Studies of AuCd," *J. App. Phys.*, vol. 26, pp. 473-484.
- Li, D. Y. and Chen, L. Q., 1997-I, "Selective Variant Growth of Coherent $Ti_{11}Ni_{14}$ precipitate in a TiNi Alloy Under Applied Stress," *Acta Mater.*, vol 45, pp. 471-479.

- Li, D. Y. and Chen, L. Q., 1997-II, "Shape of a Rhombohedral Coherent $Ti_{11}Ni_{14}$ precipitate in a Cubic Matrix and its Growth and Dissolution During Constrained Aging," *Acta Mater.*, vol 45, pp. 2435-2442.
- Madangopal, K, 1997, "The Self Accommodating Martensitic Microstructure of Ni-Ti Shape Memory Alloys," *Acta Mater.*, vol 45, pp. 5347-5365.
- Martin, J. W., 1980, Micromechanisms in particle-hardened alloys, 1st edition, Cambridge University Press, Great Britian, p. 17.
- Matsumoto O., S. Miyazaki, K. Otsuka, and H. Tamura, 1987, "Crystallography of martensitic transformations in Ti-Ni single crystals.," *Acta. Mett.*, vol. 35, pp. 2137-2144.
- Miyazaki, S., Ohmi, Y., Otsuka, K., and Suzuki, Y, 1982, *J. De. Phys.*, vol. 43, pp. 255.
- Miyazaki, S., Kimura, S., Otsuka, K., and Suzuki, Y., 1984, "The Habit Plane and Transformation Strains Associated With the Martensitic Transformation in Ti-Ni Single Crystals.," *Scr. Mett.*, vol. 18, pp. 883-888.
- Mura, T, 1987, Micromechanics of Defects in Solids, 2nd edition, Kluwer Academic Publishers, The Netherlands.
- Nishida, M., Wayman, C. M., and Honma, T., 1986, "Precipitation Processes in Near-Equiatomic TiNi Shape Memory Alloys," *Met. Trans.*, vol. 17A, pp. 1505-1515.
- Nishida M, Wayman C M, 1988, "Electron microscopy studies of the 'premartensitic' transformations in an aged Ti-51 at.%Ni shape memory alloy.," *Metallography.*, vol 21, pp. 255-273.
- Nishida M, Wayman C M, Chiba A, 1988, "Electron microscopy studies of the martensitic transformation in an aged Ti-51 at.%Ni shape memory alloy.," *Metallography.*, vol 21, pp. 275-291.
- Todoroki T. and Tamura H, 1987, "Effect of Heat Treatment after Cold Working on the Phase Transformation in TiNi alloy.," *Trans. Jpn. Inst. Met.*, vol 28, no 2, pp. 83-94.
- Treppmann, D. and Hornbogen, E., 1995, "The Effect of Dislocation Substructure and Decomposition on the Course of Diffusionless Transformation," *J. D. Physique IV*, vol. 5, pp. 211-216.

Treppmann, D, Hornbogen, E, and Wurzel, D, 1995, "The effect of Combined recrystallization and precipitation processes on the functional and structural properties of NiTi alloys.," *J. De. Phys.*, vol. 5, pp. 569-574.

Wayman, C. M., 1986, Phase transformations in Ni-Ti shape memory alloys, *ICOMAT 86*, pp. 645.

CHAPTER 7: EXPERIMENTS ON AGED NiTi

PREVIEW

Stress-induced transformations in polycrystalline NiTi were found to closely resemble transformations in single crystals of the [110] and [111] orientations. Solutionized and over-aged single crystals exhibited a strong orientation dependence of the critical stress required to trigger the transformation, σ_{cr} . The Schmid law was able to accurately predict the orientation dependence of σ_{cr} in the solutionized and over-aged single crystals. Peak-aged single crystals demonstrated a much weaker orientation dependence of σ_{cr} and in general the Schmid law was not obeyed. By considering the local stress fields outside of the semi-coherent precipitates, the decrease in the orientation dependence of σ_{cr} was accounted for. The martensite start temperatures, M_s , in aged single crystal and polycrystalline NiTi were much higher than in solutionized samples. In peak-aged NiTi the increase was primarily attributed to the local stress fields outside the coherent precipitates which create preferential nucleation sites for the martensite. In the over-aged NiTi the increase in M_s was primarily attributed to the decrease in the average Ni concentration of the matrix surrounding the coarsened precipitates.

7.1 BACKGROUND

To date there are nearly twenty intermetallic alloys which possess shape memory properties (Shimizu and Tadaki, 1988; Hodgson *et al.*, 1990). However, due to several variables such as cost, strength, processability, and recoverable strain levels, only two shape memory alloy systems have been extensively used in engineering applications. Copper based shape memory alloys such as Cu-Zn-Al have provoked interest due to their moderate recoverability, low cost, and ease in processing (Wayman, 1980).

Consequently, copper based alloys with refined grain structures have been extensively used in thermal-mechanical actuator mechanisms (Wu, 1988). However, since its discovery in the early 60's by Buehler and colleagues at the Naval Ordnance Laboratory, NiTi (also referred to as NitiNOL) has dominated engineering applications. Some of the well known applications of NiTi include orthodontic wires, endoscopic surgical wires, pipe couplings, intravascular stents, space antennas, embedded wires in composites, actuators, and eyeglass frames. The extensive use of NiTi is undoubtedly due to its remarkable physical and mechanical properties such as: recoverable strains (Wasilewski, 1971), recoverable forces (Furuya *et al.* 1988), cyclic path memorization (Lim and McDowell, 1995); cyclic stability (Miyazaki *et al.*, 1986), fatigue resistance (Tobushi *et al.*, 1997), corrosion resistance (Filip *et al.*, 1994), and wear resistance (Li, 1996). A comprehensive review of the general properties of NiTi has been published by Duerig and Pelton (1994). The only apparent disadvantage of NiTi alloys is that they are somewhat expensive due to high fabrication and manufacturing costs (Perkins, 1981).

At this point, the monotonic stress-strain behavior of polycrystalline NiTi shape memory alloys has been studied quite extensively. Both classical (Wasilewski, 1971) and more recent studies (Jacobus *et al.*, 1996; Shaw and Kyriakides, 1997; Liu and Galvin, 1997) have demonstrated that the tensile behavior of polycrystalline NiTi is strongly dependent on the test temperature. Generally speaking, shape memory alloys deform through martensite reorientation at low temperatures, a stress-induced martensitic transformation at intermediate temperatures, and plastic slip at high temperatures. The transition temperatures for different deformation mechanisms are dependent on the alloy composition, heat treatment, processing, and prior thermal and mechanical cycling history (Funakubo, 1988). In addition, several unique experimental phenomenon have been observed in the stress-induced temperature range. When polycrystalline NiTi is stressed in tension it sometimes deforms through the motion of a macroscopic phase boundary and the resulting stress-strain curve is

dependent on the applied strain rate (Jacobus *et al.*, 1996; Shaw and Kyriakides, 1997). The higher the applied strain rate, the higher the critical transformation stress level and the steeper the transformation stress-strain slope. It has also been observed that the stress-induced transformation in polycrystalline NiTi exhibits a dependence on the applied stress state. Several researchers have concluded that when compared to tensile results, compressive stress-strain plots demonstrate smaller recoverable strain levels, steeper transformation stress-strain slopes, and higher critical transformation stress levels (Wasilewski, 1971; Orgeas *et al.*, 1995; Jacobus *et al.*, 1996; Plietsch and Ehrlich, 1997). This effect has been properly explained and modeled by considering the texture of the polycrystalline specimens (chapter 5).

By utilizing different soak temperatures and hold times, heat treatments can be used to tailor the properties of shape memory alloys such as the two-way shape memory effect (Honma, 1986) and pseudoelasticity (Miyazaki *et al.*, 1982). Chumlyakov and colleagues have observed that peak-aged Ni rich NiTi single crystals demonstrated a decrease in the orientation dependence and tension-compression asymmetry of critical transformation stress levels (Chumlyakov *et al.* 1995, 1996). In addition it has also been observed that the recoverable strain levels in peak-aged single crystals are significantly smaller than those in solutionized NiTi (Miyazaki *et al.* 1984). Most of the studies on aged polycrystalline NiTi have focused on the effect of different cold workings and subsequent aging treatments on thermal (Abujdom *et al.* 1990; Todoroki and Tamura, 1987) and tensile stress-induced (Filip *et al.*, 1991; Liu and Galvin, 1997) martensitic transformations. For “equiatomic” NiTi aged below the recrystallization temperature (about 823 K) increasing the percentage of cold work was found to decrease the martensite start temperature (Abujdom *et al.* 1990). For example, increasing the cold work from 6% to 55% decreases M_s from about 293 K to 263 K when the cold work is performed prior to a 1 h heat treatment at 748 K. If the cold work is performed prior to aging above 823 K then M_s may increase or decrease depending on the percent of cold work. It should be noted that the

aforementioned results are difficult to generalize to all NiTi materials since the composition of the alloy was only cited as "equiatomic" and the microstructures were not studied (Abujdom *et al.* 1990).

After a fixed percent of cold work, the effect of aging depends on the heat treatment temperature. In a Ti - 50.6 at% Ni alloy Todoroki and Tamura (1987) determined that M_s goes through three different changes as the aging temperature is increased. When the aging temperature was decreased from 625 K to 700 K M_s slightly decreased. However, if the aging temperature was increased from 700 K to about 823 K M_s increased nearly 70 K. However, when the NiTi was heat treated above 823 K M_s once again decreased. Notably, all NiTi polycrystals aged above 840 K (for 1 hour) demonstrated recrystallization, a disappearance of the R-phase, and a masking of the effects of cold work (Abujdom *et al.* 1990; Todoroki and Tamura, 1987). Several studies have considered stress-induced martensitic transformations in aged polycrystalline NiTi deformed under tension (Filip *et al.*, 1991; Liu and Galvin, 1997). As the aging temperature was increased (below the recrystallization temperature) the stress required to induce the transformation, σ_{cr} , decreased consistent with the observed increase in the martensite start temperature. Increasing the aging temperature above 840 K increased the stress required to induce the transformation. Finally, it should be noted that similar to single crystals, polycrystalline Ni rich NiTi aged in the range 673 K through 830 K also demonstrated smaller recoverable strain levels. Most researchers have attributed this effect to a decrease in the mobility (or detwinning) of martensite phase boundaries through the precipitated regions (Filip *et al.*, 1991, Buchheit and Wert, 1996). At this point, there has been no experimental studies which consider the compressive behavior of NiTi subjected to different heat treatments. The lack of experimental studies which consider compression is a concern since NiTi materials are available in wire, bar, and sheet form, and all three will experience compressive stresses through bending loads.

In an attempt to predict and better utilize the thermo-mechanical response of shape memory alloys, several phenomenological constitutive models have been developed (Sun *et al.*, 1991; Sun and Hwang, 1993; Boyd and Lagoudas, 1996). Although the aforementioned constitutive models are quite extensive, they all aim at providing simple mathematical expressions for the transformation criteria and martensite evolution rate. In doing so, they fail to properly capture several experimentally observed phenomenon such as stress state effects and the influence of aging on σ_{cr} , M_s and recoverable strain levels. All three effects are inherently linked to the microstructures in polycrystalline NiTi alloys, primarily the crystallographic texture and the precipitate structure. Although the aforementioned constitutive models are valuable, extreme caution must be used when they are used to predict the transformation behavior of shape memory alloys under different stress states, or alloys which exist in different aged states. To rectify the above situation, several researchers have developed micro-mechanical models for polycrystalline shape memory alloys (Falk, 1989; Ono *et al.*, 1989; Patoor *et al.*, 1996; chapter 4 and 5). In an attempt to better capture all of the observed experimental phenomenon, these models incorporate the actual microstructural deformation mechanisms of the transformation. The latter three models have been successful in capturing stress state effects in Cu-Zn-Al and NiTi. Strictly speaking, the model for NiTi (chapter 5) is only applicable to materials without coherent or semi-coherent precipitates. At this point, it is still necessary to incorporate the effects of aging into polycrystalline shape memory alloy constitutive models.

At the single crystal level the effects of aging on martensitic transformations in NiTi have been modeled to some degree. It has been proposed that recoverable strain levels are smaller in peak-aged specimens because the detwinning of internally faulted martensite is inhibited. Buchheit and Wert (1996) developed a single crystal constitutive model which includes both the transformation strains due to the phenomenological theory of martensitic transformations (CVP formation), and CVP detwinning.

When detwinning was prohibited in their model, the predicted recoverable strains were on the order of previously reported experimental results (Miyazaki *et al.*, 1984) for peak-aged single crystals. The aforementioned model and the study by Treppman and Hornbogen (1995) are the only works to date which model martensitic transformations in aged NiTi. Clearly then it is necessary to better understand the effect of different aging treatments on martensitic transformations in NiTi.

Consequently, the current study will focus on properly explaining the effect of precipitation on critical transformation stress levels, σ_{cr} , and martensite start temperatures, M_s , in NiTi. The present chapter is aimed at presenting a systematic set of experimental results on NiTi. The experiments will consider the effects of different aging treatments, materials (polycrystalline versus single crystal), and test temperatures. As a first approximation, the effects of cold work will not be considered. To remove the effects of previous cold workings, the polycrystalline materials were given recrystallization treatments (the single crystals were never cold worked). Since the deformation behavior of polycrystalline NiTi is very dependent on texture (chapter 5), single crystals of several different orientations will be studied. Specifically, the [111] and [110] orientations will be utilized since they are soft under tension (large transformation strains, low σ_{cr}) and the [100] orientation will be utilized since it is hard under tension (small transformation strains, high σ_{cr}). The single crystal orientation [111] is also of particular interest since the predominant texture in drawn NiTi polycrystals is of the $\langle 111 \rangle$ -[110] type (chapter 5). Microstructural observations and micro-mechanical modeling results from chapter 6 will be used to elucidate the experimental results. This research is superior over previous research efforts since it relates the micro-mechanisms of aging to the macroscopic deformation behavior, allowing for the extension of the results to other NiTi alloy systems. The goals of this chapter are explicitly outlined below:

1. Experimentally determine the critical transformation stress levels under tension and martensite start temperatures for single crystal ([111], [110], and [100] orientations) and polycrystalline NiTi exposed to different aging treatments.
2. Use micro-mechanical arguments to quantitatively predict the effect of precipitation on the critical stresses and temperatures required to trigger martensitic transformations in peak-aged and over-aged NiTi.

7.2 EXPERIMENTAL TECHNIQUES

Polycrystalline samples were electro-discharge machined from 1" diameter cylindrical bars available from Special Metals Corporation. The bars were cold drawn, centerless ground, straightened, and annealed. The polycrystalline samples were given a 2 hour solutionizing treatment at 1273 K. The heat treatment was performed in evacuated quartz tubes which were quenched and broken in ambient temperature water. The average grain size of the polycrystalline material was determined to be 20 μm . Bars from the same material batch were melted in ingots and used to produce single crystal NiTi specimens. The single crystals were grown using the modified Bridgeman technique in an inert gas atmosphere. Following growth, the crystals were homogenized at 1273 K for 24 hours in a vacuum furnace and quenched into ambient temperature water, leaving them in the solutionized state. The compositions of both the single crystal and the polycrystalline materials were found to be approximately Ti - 50.8 at% Ni. Using electron backscatter diffraction patterns, the orientation of the bulk single crystal was determined and single crystal specimens were electro-discharge machined in the [111], [110], and [100] orientations. The test samples had a gage cross section of 3 mm x 1 mm and a length of 25 mm.

The solutionized polycrystalline and single crystal samples were given subsequent aging treatments in the as machined state. The aging treatments

were chosen to yield distinctly different microstructures. The four heat treatments utilized in this study were: as solutionized, aged 1.5 hours @ 673 K, aged 1 hour @ 773 K, and aged 15 hours @ 773 K. Table 6.1.1 lists some of the expected characteristics of NiTi in the different material states. When the material is quenched from a high temperature it is left in the solutionized (supersaturated) state (row 1 in Table 6.1.1). The 15 hour treatment at 773 K leaves the material in the over-aged state (row 3 in Table 6.1.1). The two remaining heat treatments both leave the material in the peak-aged state (row 2 in Table 6.1.1). However, the 673 K heat treatment will result in a R-phase transformation that is separated from the martensitic transformation. Conversely, the 773 K heat treatment will result in a R-phase transformation which is closer to the martensitic transformation (Nishida and Wayman, 1988).

Mechanical testing was performed on a screw driven ATS machine fitted with small scale testing grips. Loads were measured with an Interface load cell. Local strains were measured with a miniature MTS extensometer with a 3 mm gage length and a +/- 8 % strain range. All tests were run at a strain rate of 5×10^{-4} /s. All critical transformation stress levels, $\sigma_{cr} = \sigma_{cr}^{.0025}$, were calculated by using the traditional .0025 strain offset method. The temperature of the specimens during the tests was monitored through a thermocouple attached directly to the sample gage section. Low temperature tests were accomplished by cooling the specimen grips and allowing heat to conduct out of the specimen. High temperature tests were performed by heating the specimen grips and allowing heat to flow into the specimen. For both high and low temperature tests the specimen was kept in an insulated chamber to prevent sudden temperature fluctuations. Before testing all NiTi specimens were lightly cleaned with a $3\text{HNO}_3 + 2\text{H}_2\text{O} + 1\text{HF}$ solution to remove surface impurities from electrical discharge machining and heat treating. Transformation temperatures were determined using a Perkin-Elmer Differential Scanning Calorimeter.

7.3 THERMALLY INDUCED MARTENSITE

The purpose of this section is to discuss the effect of aging on thermally induced martensitic transformations in single crystal and polycrystalline NiTi. It should be noted that the results of this DSC study are consistent with previously published results (Table 1). However, this is the first study which simultaneously considers single crystal and polycrystalline NiTi materials given equivalent aging treatments. Figure 7.3.1 is a composite plot of the all of the DSC curves for the different materials and heat treatments considered here. In general, the transformation temperatures are comparable for both the single crystal and polycrystalline NiTi. The small differences in transformation temperatures between the single crystal and polycrystalline materials may be attributed to small compositional changes during the growth of the crystals or intergranular constraint. It is also clear that the transformation peaks in the single crystal NiTi are generally more abrupt and well defined than the wide peaks observed in the polycrystalline NiTi. This is attributed to the fact that the transformation fronts in single crystal NiTi move more easily through the test specimens. In the polycrystalline NiTi the transformation fronts are inhibited by grain boundaries and thus the transformation proceeds more slowly as a function of the temperature.

At this point it is appropriate to briefly discuss the pertinent characteristics of the DSC curves for the four different aging treatments. The lowest DSC curve in Figure 7.3.1 represents the material in the solutionized state. The solutionized material only undergoes two transformations, a forward martensitic transformation upon cooling and a reverse martensitic transformation upon heating. Notably, the transformation temperatures in the solutionized (supersaturated) state are much lower than in any of the aged materials. The DSC curve second from the bottom represents peak-aged NiTi (1.5 h @ 673 K). Upon cooling this material undergoes a R-phase transformation near 320 K and a martensitic transformation around 260 K. Upon heating the martensitic phase transforms back into the parent phase in

one solid state transformation at around 320 K. The noteworthy feature on

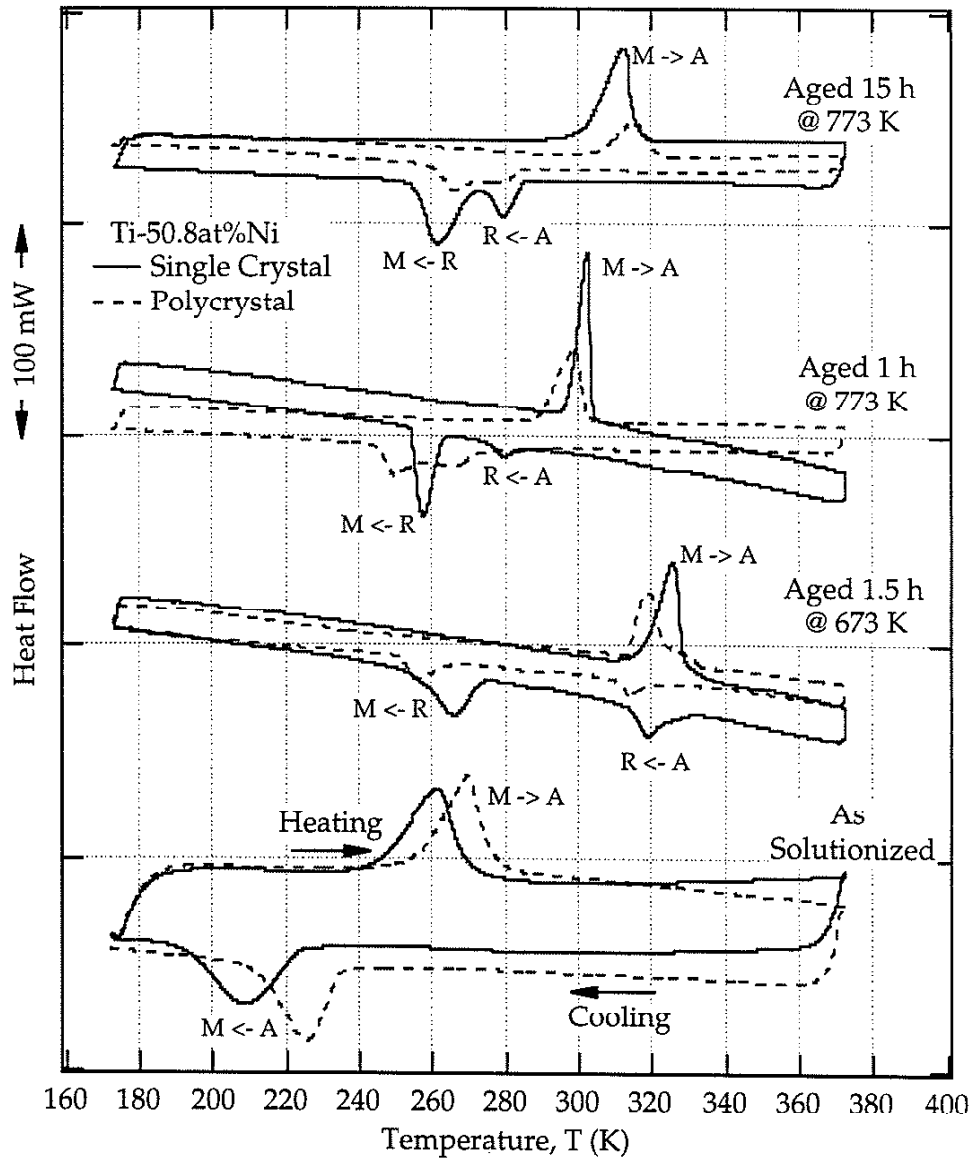


Figure 7.3.1: Differential scanning calorimetry (DSC) curves for single crystal and polycrystalline NiTi given four different heat treatments. On the plot, M is the martensitic phase (B19'), R is the commensurate phase (rhombohedral), and A is the parent phase (B2).

this DSC curve is the large separation between the R-phase transformation and the martensitic transformation. The final two DSC curves (aged 1 h @

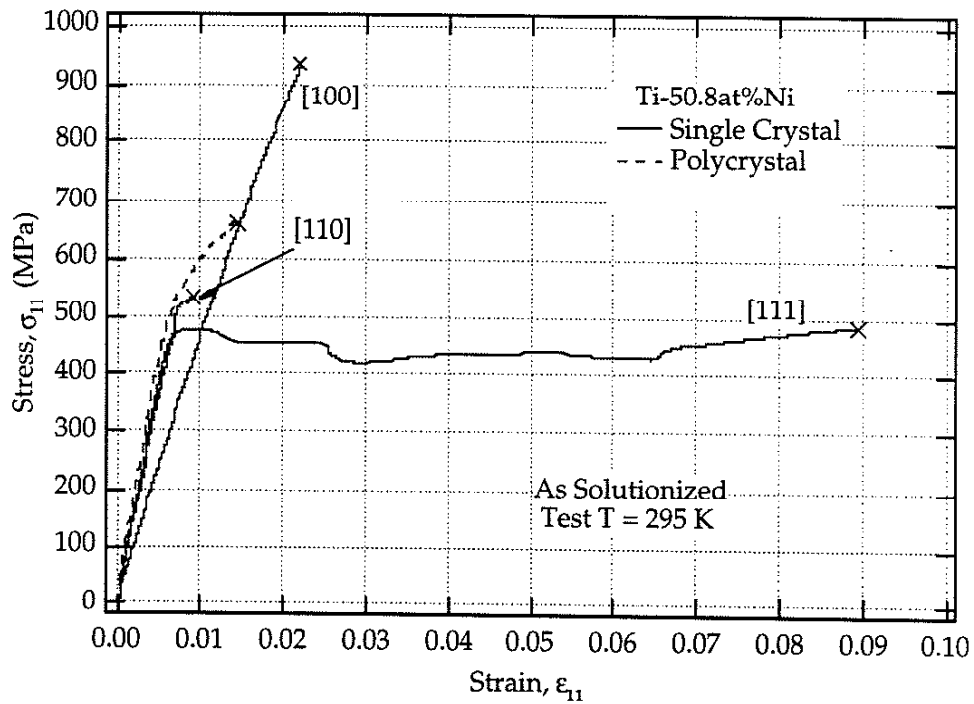
773 K and 15 h @ 773 K) have similar transformation characteristics. Upon cooling the R-phase transformation occurs at about 280 K and the martensitic transformation occurs at about 260 K. Upon heating, the martensitic phase transforms back to the parent phase in one solid state transformation at about 310 K. It should be noted that there are several differences in the two materials aged at 773 K. In the over-aged state (15 h @ 773 K), the R-phase transformation is more pronounced than in the peak-aged state (1 h @ 773 K). Additionally, the transformation temperatures are slightly higher in the over-aged case.

7.4 ROOM TEMPERATURE STRESS INDUCED MARTENSITE

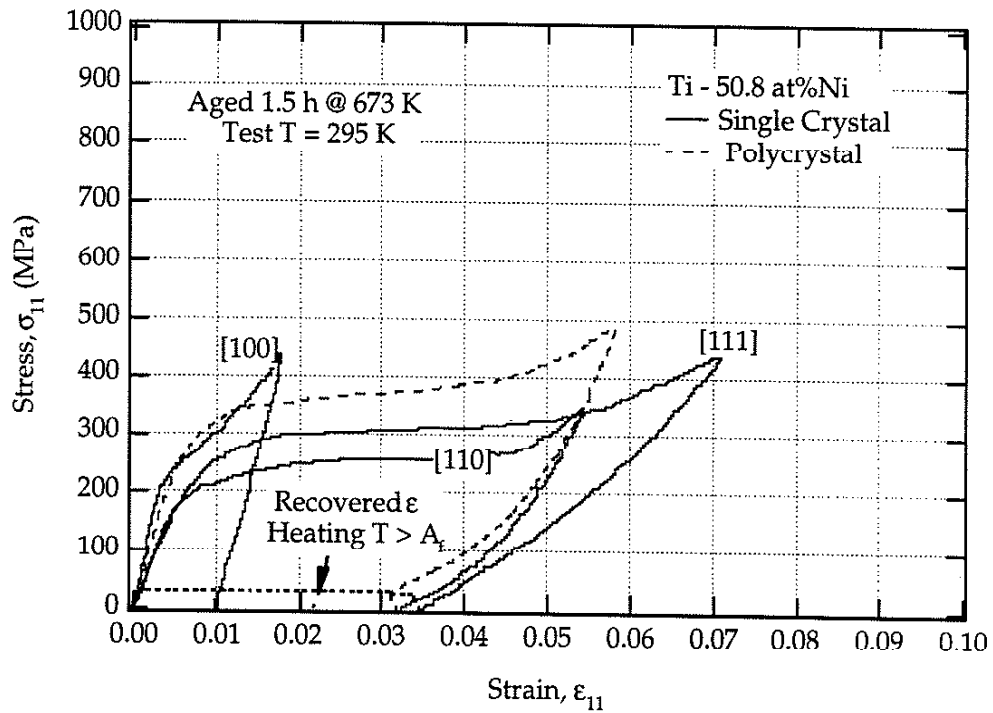
In this section, the results of tensile tests on single crystal and polycrystalline NiTi are presented. Figures 7.4.1 (a-d) demonstrate the room temperature tensile stress-strain curves for NiTi. In each figure the tensile stress-strain curves are shown for polycrystalline NiTi and three different crystallographic orientations ([100], [110], [111]) of single crystal NiTi. Figure 7.4.1a represents the material in the solutionized state. Clearly there exists a strong dependence of the deformation behavior on the crystallographic orientation. It is also clear that most of the specimens fracture soon after the transformation is initiated. This theory was confirmed by the discovery of martensite plates on the fracture surfaces of the specimens using the scanning electron microscope. It has been previously noted that solutionized NiTi alloys with high Ni concentrations have low ductility (Duering and Pelton, 1994). At any rate, the orientation dependence of critical stress levels required to trigger the transformation, σ_{cr} , in Figure 7.4.1a should be consistent with the predictions of the phenomenological theory of martensitic transformations (Schmid Law).

To determine if the specimens obey the Schmid law, it is necessary to calculate the critical resolved shear stress, τ_{crss} , in the specimens with different

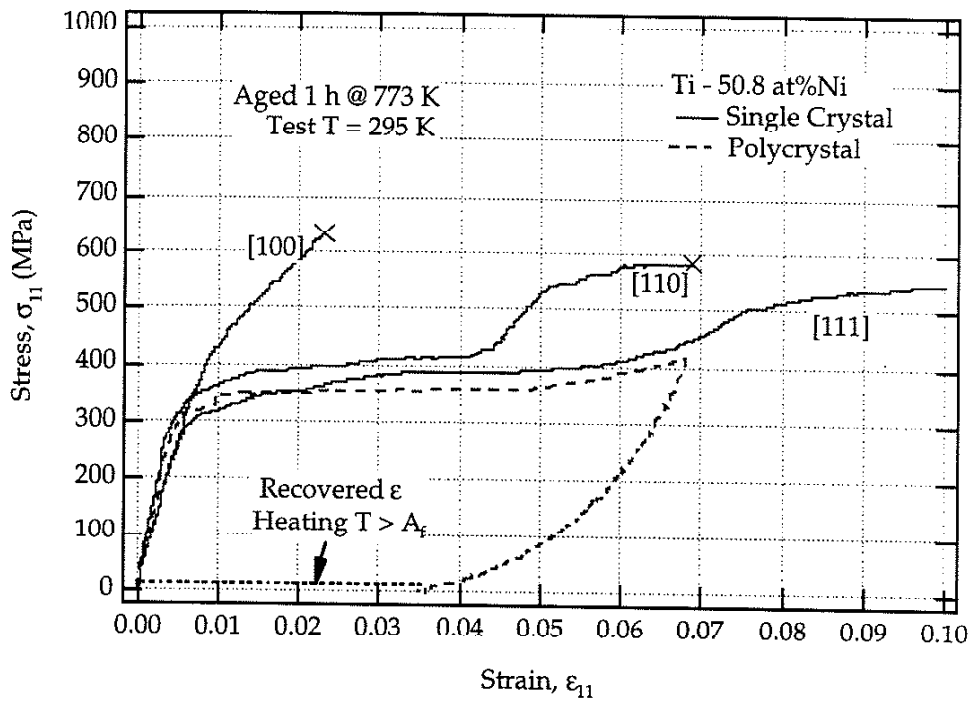
tensile axes. If the Schmid law holds then τ_{crss} should be independent of the



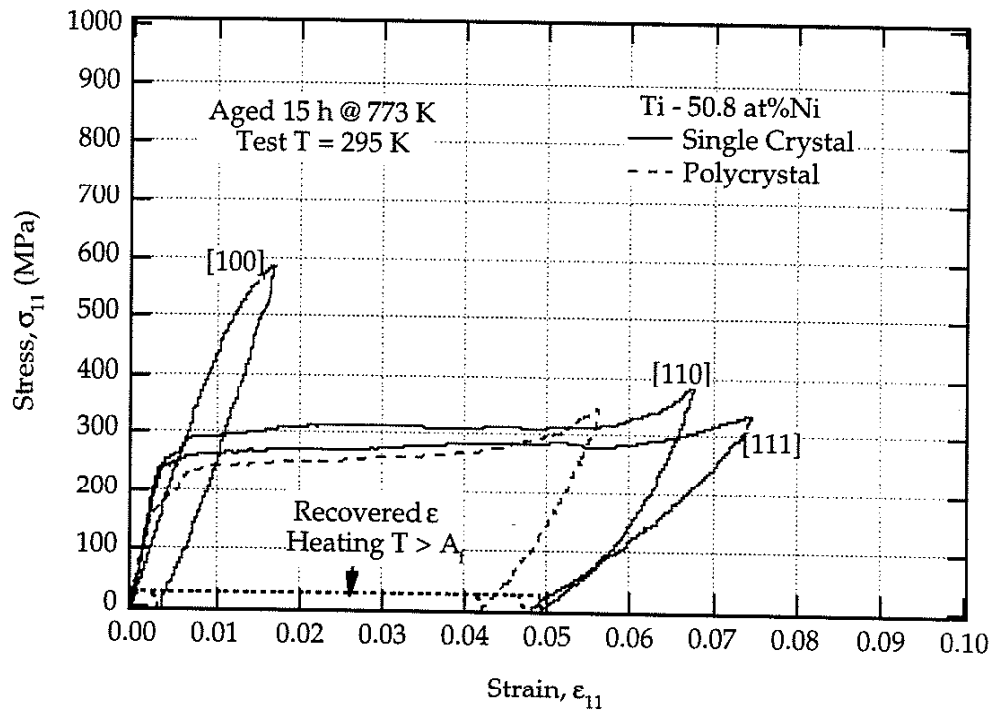
(a)



(b)



(c)



(d)

Figure 7.4.1: Room temperature tensile stress-strain curves for single crystal and polycrystalline NiTi subjected to four different aging treatments: (a) as solutionized, (b) aged 1.5 h @ 673 K, (c) aged 1 h @ 773 K, (d) aged 15 h @ 773 K.

crystallographic orientation of the tensile axes. The critical resolved shear stress, τ_{crss} , is calculated by multiplying σ_{cr} (.0025 strain offset method) by the Schmid factor, α_{11} , of the most favorably oriented martensite correspondence variant pair (CVP) for a particular orientation (Table 7.4.1). The important

Tensile Axis Orientation	[1 0 0]	[1 1 0]	[1 1 1]
Max. Schmid factor, α_{11}	0.21	0.41	0.39

Table 7.4.1: Schmid factor for the most favorably oriented martensite correspondence variant pair (CVP) for several different crystallographic orientations of NiTi loaded under tension.

parameters for all of the room temperature tests are summarized in Table 7.4.2. In the solutionized state Table 7.4.2 demonstrates that the difference in τ_{crss} is small between the two different orientations. The difference in τ_{crss} for the solutionized specimens is considered to be a measurement of the overall experimental error in the study (standard deviation of about 5.5 MPa). The deformation of the polycrystalline NiTi in Figure 7.4.1a appears to be controlled by the brittle failures observed in the [100] and [110] orientations.

Figure 7.4.1b shows the room temperature stress-strain response for NiTi aged for 1.5 hours at 673 K. At this test temperature the NiTi exists in the R-phase, and this is evident on the stress-strain curves by the different elastic moduli of the specimens (Figures 7.4.1a versus 7.4.1b). All of the specimens were unloaded and demonstrated complete recoverability upon heating above the austenite finish temperature. Two features in Figure 7.4.1b that will be focused on in this study are the drastic drop in σ_{cr} and the severe weakening of the orientation dependence of σ_{cr} . The overall drop in σ_{cr} can be explained by noting that the test temperature is much closer to the measured martensite start temperature, M_s , of the peak-aged material (Table 7.4.2).

However, the decrease in the orientation dependence of the σ_{cr} cannot be simply explained by using the DSC curves. In addition, the Schmid law

	specimen	M_s (K)	σ_{cr} (MPa)	τ_{crss} (MPa)
As Solutionized	[100]	224	934	196
	[111]	224	475	185
	polycrystal	236	583	-
Aged 1.5 hours @ 673 K	[100]	274	250	52
	[111]	274	238	93
	polycrystal	266	296	-
Aged 1 hour @ 773 K	[100]	264	451	95
	[111]	264	316	123
	polycrystal	257	343	-
Aged 15 hours @ 773 K	[100]	272	530	111
	[111]	272	260	101
	polycrystal	272	220	-

Table 7.4.2: Summary of experimentally determined critical transformation parameters for aged and solutionized NiTi. The [111] and [110] orientations are compared since they have drastically different Schmid factors (Table 7.4.1).

cannot be used to predict the critical resolved shear stress from σ_{cr} for different specimen orientations. From Table 7.4.2 it is clear that for the samples aged 1.5 hours at 673 K, the predicted τ_{crss} is dependent on the crystallographic orientation of the test specimen. The polycrystalline NiTi in Figure 7.4.1b deforms in a manner which is very similar to the deformation of the [110] and [111] orientations. However, the critical transformation stress level in the polycrystalline material is slightly higher than that of the single crystals. This is expected since the martensite start temperature, M_s , is slightly lower in the polycrystalline material versus the single crystal material (Figure 7.3.1). It will also be noted here that the peak-aged samples demonstrated a very non-linear unloading path. This is caused by the existence of strong internal stress fields due to mismatch strains between the precipitates and the fully developed martensite. These internal stress fields are what prohibit the detwinning of faulted martensite in peak-aged NiTi.

A similar decrease in the orientation dependence of σ_{cr} is observed in the NiTi given the other peak-aging treatment (Figure 7.4.1c). Once again, the σ_{cr} values from Figure 7.4.1c do not produce τ_{crss} values consistent between different crystallographic orientations (Table 7.4.2). The specimens in Figure 7.4.1c were loaded until failure to determine the orientation dependence of the room temperature fracture strains. The [111] orientation demonstrated the largest fracture strain (~30 %) while the [100] orientation demonstrated the smallest (~2 %). The single crystal materials given the 1 h @ 773 K heat treatment show a slightly larger σ_{cr} since their martensite start temperature is slightly lower than in the first peak-aging treatment (Table 7.4.2). The final room temperature stress-strain curves shown in Figure 7.4.1d are for the over-aged NiTi materials. In most of the over-aged materials two transformation points are clearly visible, the R-phase transformation and the martensitic transformation. For the over-aged polycrystalline material, σ_{cr} is lower than σ_{cr} for either of the peak-aged materials, which is consistent with the DSC results (Table 7.4.2). It is also worth noting that the transformation stress-strain slope is steeper in the peak-aged materials (Figures 7.4.1b and 2c) versus the over-aged materials (Figure 7.4.1d). This indicates that the martensite grows more freely through the over-aged materials and is consistent with the theory that martensite interfaces are immobile in peak aged samples (Buchheit and Wert, 1996).

The most intriguing feature of Figure 7.4.1d is that the original orientation dependence of σ_{cr} is similar to that of the solutionized specimens. This observation is elucidated by the fact that the separation in the experimentally measured τ_{crss} is once again on the order of experimental error (Table 7.4.2). Another noteworthy feature in Figure 7.4.1d is found on the unloading portion of the stress-strain curve. The unloading path in the over-aged materials is more linear than the unloading paths for the peak-aged materials. This indicates that the mismatch strains and resulting local stress

fields between the precipitates and the martensite are smaller in the over-aged state. It is also helpful to graphically demonstrate the dependence of τ_{crss}

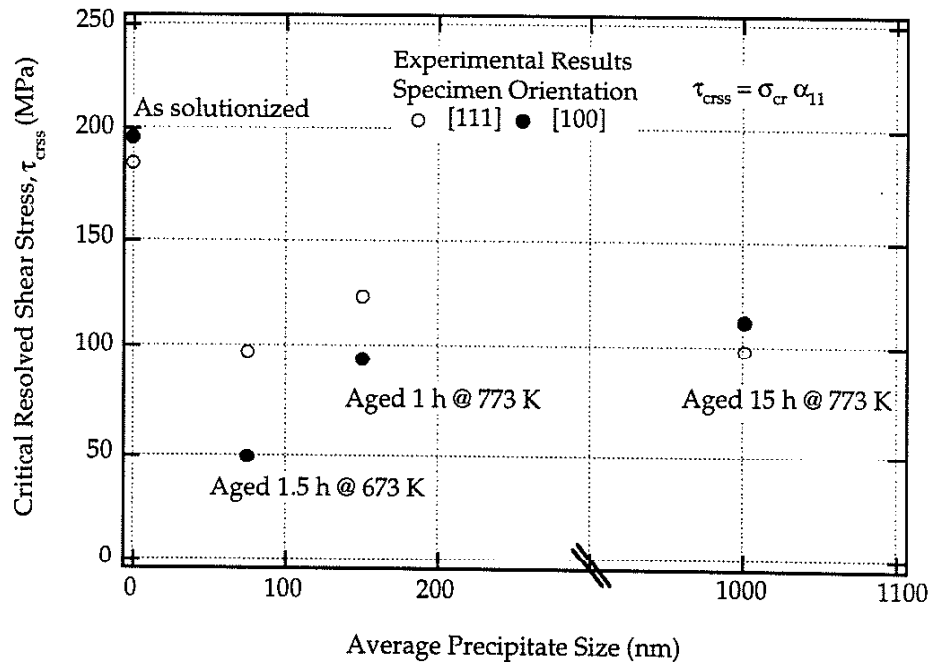


Figure 7.4.2: Effect of heat treatment on the orientation dependence of the critical resolved shear stress, τ_{crss} , under tension. In the figure α_{11} is the Schmid factor and σ_{cr} is the critical stress level at the onset of the transformation for a given orientation.

on the heat treatment (Figure 7.4.2). Figure 7.4.2 shows τ_{crss} for two different specimen orientations as a function of the precipitate size. The figure is similar to a yield stress-precipitate size plot for a precipitation hardening material. However, the plot is mirrored since precipitation lowers τ_{crss} for a constant test temperature rather than raises it. Clearly, in the peak-aged samples the separation between τ_{crss} for different specimen orientations is much more than in the case of the solutionized or over-aged samples. It should be noted that the overall trend in τ_{crss} is consistent with the different M_s values in Table 7.4.2. At a constant test temperature the specimens are in a different thermodynamic state is their M_s temperatures are different.

However, at this point it is still necessary to understand the effect of aging on the temperature dependence of σ_{cr} .

7.5 TEMPERATURE DEPENDENCE OF STRESS INDUCED MARTENSITE

To further understand the decrease in the orientation dependence of σ_{cr} in the peak-aged single crystals, tensile tests were conducted at several different test temperatures on specimens oriented in the [100] and [111] directions. Since the mechanical behavior resulting from the two peak-aging treatments is similar, only the treatment for 1 hour at 773 K is considered here. Figure 7.5.1 shows the temperature dependence of σ_{cr} for the two chosen single crystal orientations. On the plot, the martensite and austenite start temperatures (M_s and A_s) are indicated by vertical dashed lines. When the specimen is cooled below M_f and subsequently tested at any temperature below A_s the single crystal specimens deform through martensite reorientation. From the results in Figure 7.5.1 it is clear that as the test temperature is lowered, the critical stress for reorientation, σ_{cr} , increases. Additionally, it is clear that σ_{cr} for reorientation is the same for the [100] and [111] orientations. At high temperatures the [111] orientation deforms through plastic flow, while the [100] orientation undergoes neither a martensitic transformation nor plastic slip and fails in a brittle manner. This is clearly due to a lack of available slip systems when the specimen is oriented in the [100] direction.

In the stress-induced temperature range the specimen is heated above the austenite finish temperature and then cooled and tested above M_s . The critical stress required to induce the transformation, σ_{cr} , exhibits a strong linear dependence on the test temperature for both crystallographic orientations (Clausius-Clapeyron relationship). As expected the slopes of the lines in stress-temperature space are different for the [100] and [111] orientations. This is because the slope of the Clausius-Clapeyron is inversely

proportional to the recoverable strain level of a given orientation. It will be noted that caution should be exercised when determining slopes of Clausius-Clapeyron lines. As M_d is approached, plastic slip may alter the calculation

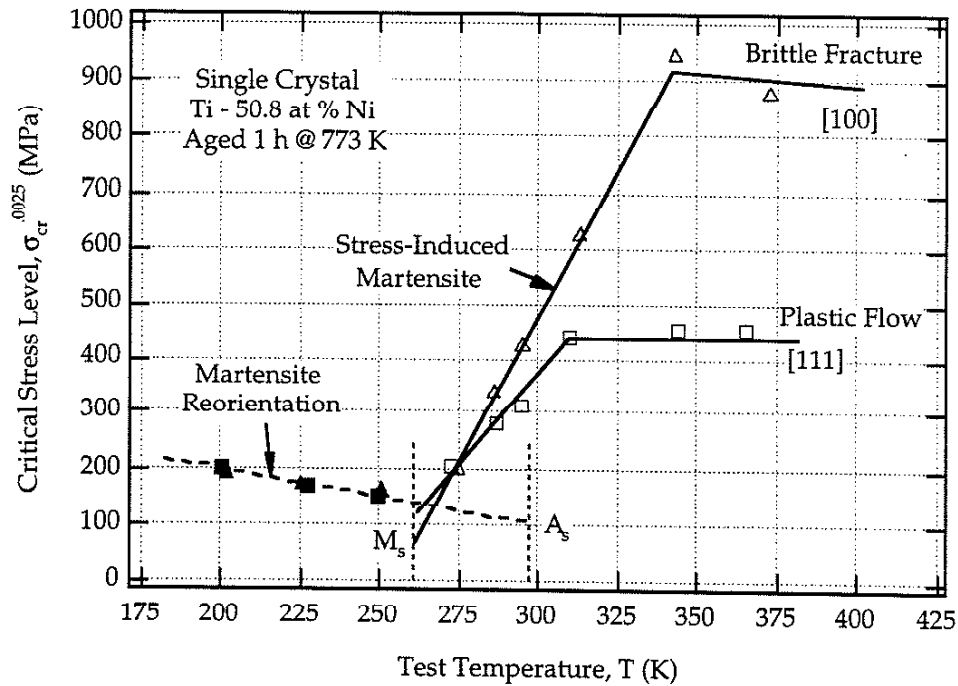


Figure 7.5.1: Orientation and temperature dependence of the critical stress required to induce the martensitic transformation under tension in peak-aged single crystal NiTi.

and give erroneous results. The slopes calculated here are just first order approximations since more test temperatures need to be considered to precisely calculate the σ_{cr} versus temperature trend. Figure 7.5.1 the slope of the Clausius-Clapeyron line for the [100] orientation is given by:

$$\frac{d\sigma_{cr}}{dT} \approx 10.6 \frac{\text{MPa}}{\text{K}} \quad (7.5.1)$$

While slope of the Clausius-Clapeyron line for the [111] orientation is given by:

$$\frac{d\sigma_{cr}}{dT} \approx 6.6 \frac{\text{MPa}}{\text{K}} \quad (7.5.2)$$

The ratio of the slope in equation 7.5.1 over the slope in equation 7.5.2 is about 1.61. However, for solutionized NiTi the individual slopes are expected to be inversely proportional to the recoverable strain levels (Schmid factors in Table 7.4.1) for a given orientation. Taking the ratio of the inverse Schmid factors for the two orientations [100] and [111] the value 1.86 is obtained. Since the theoretical difference for solutionized samples (1.86) is higher than the experimental value for the peak-aged samples (1.61), the orientation dependence of the Clausius-Clapeyron slopes is decreased by peak-aging. This ratio is expected to be even smaller for the samples peak-aged for 1.5 h @ 673 K. Using the recoverable strain levels from a previous research effort on Ti - 50.5 at% Ni given a 1 h @ 673 K heat treatment, the ratio is calculated to be about 1.22 (Miyazaki *et al.*, 1984). Another intriguing feature in Figure 7.5.1 is the different intercepts of the two lines. This difference is not expected in solutionized specimens, and its origin will be discussed later.

Another important aspect of figure 7.5.1 is the difference between σ_{cr} for a stress-induced transformation and σ_{cr} for martensite reorientation. Even at equivalent test temperatures σ_{cr} is much higher for the stress induced transformation (about 150 MPa at the equilibrium transformation temperature $T_0 = \frac{1}{2}(M_s + A_s)$). This large difference is due to the fact that there are several nucleation barriers which exist in the stress induced case and not in the case of martensite reorientation. The critical stress for reorientation is solely governed by the difficulty in moving and creating martensite interfaces. However, the critical stress level required to create new martensite is primarily controlled by the chemical free energy difference between the two phases, the interfacial energy, and the elastic strain energy. The aforementioned mechanisms are all considered “nucleation” barriers for

the formation of the new martensitic phase in the parent material. Since the second phase already exists in the case of reorientation, only the internal friction of moving boundaries contributes to the critical stress level. Notably, this internal friction decreases with increasing temperature (Figure 7.5.1).

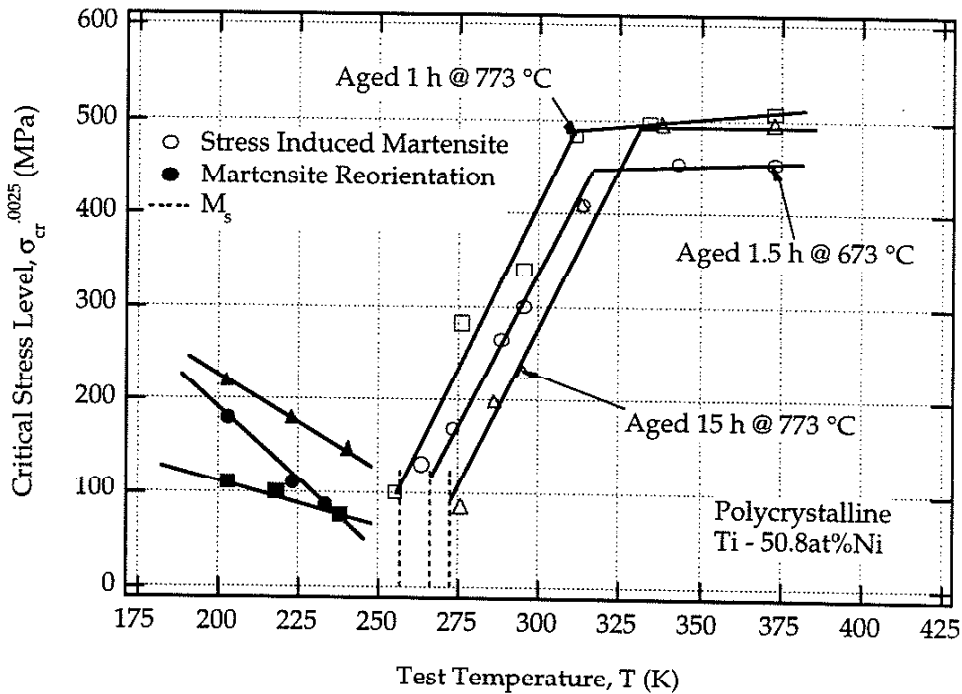


Figure 7.5.2: Temperature dependence of the critical stress required to induce the martensitic transformation in polycrystalline NiTi given several different heat treatments.

Since polycrystalline materials are commonly used in applications, the final experimental results presented here will demonstrate the temperature dependence of σ_{cr} for polycrystalline NiTi. For the two peak-aged and the over-aged materials, Figure 7.5.2 plots the temperature dependence of σ_{cr} for polycrystalline NiTi. The general characteristics of the plot are similar to Figure 7.5.1, thus they will not be discussed. It should be noted that the reverse transformation temperatures are not indicated on Figure 7.5.2 in order to conserve space. If they were, the martensite reorientation lines would be extended to intercept them. At any rate, in the low temperature

region, martensite reorientation is most difficult in the over-aged case and easiest in the samples peak-aged for 1 hour at 773 K. The samples aged for 1.5 h at 673 K lie in-between the two and exhibit a stronger dependence on the test temperature. In the high temperature region the flow strength, σ_{cr} , is higher in the samples aged at 773 K and relatively lower for the samples aged at 673 K. Finally, in the stress-induced temperature range, it generally follows that the samples aged at 773 K for 1 hour have the highest σ_{cr} , the samples aged at 673 K for 1.5 hours have intermediate levels of σ_{cr} , and the over-aged samples have the lowest levels of σ_{cr} . The slopes of the Clausius-Clapeyron lines for the polycrystalline materials given different heat treatments is given by:

$$\frac{d\sigma_{cr}}{dT} \approx 7.3 \frac{\text{MPa}}{\text{K}} \quad (7.5.3)$$

This value is consistent with previously reported values for the Clausius-Clapeyron slope in polycrystalline NiTi given different aging treatments (Duerig and Pelton, 1994; Jacobus et al., 1996; Liu and Galvin, 1997). It is also interesting to note that the value in equation 7.5.3 is similar to the value in equation 7.5.2 for a single crystal oriented along the [111] direction.

7.6 DISCUSSION OF EXPERIMENTAL RESULTS

The first experimental results to examine are the DSC curves and the room temperature tensile stress-strain curves for the single crystals. In the solutionized state Ni rich NiTi is supersaturated in Ni, thus the M_s temperature is low (Figure 7.3.1), and the room temp τ_{crss} is high (Figure 7.4.2). Additionally, since there are no precipitates, there are no local stress fields, and the Schmid law holds (Figure 7.4.2). For the two peak-aged materials, it has been microscopically observed that strong strain fields are present due to

the lattice mismatch strains between the semi-coherent precipitates and the B2 matrix (chapter 6). In the peak-aged materials, strong local resolved shear stress fields are present on the martensite correspondence variant pairs (CVP's) due to the local stress fields. In chapter 6 the magnitudes of the local resolved shear stresses were estimated for coherent and semi-coherent precipitates. A reproduction of the results are shown in table 7.6.1. Only the

CVP	Schmid Factor, α_{11}			Average Local Resolved Shear Stress $\bar{\tau}_{RSS-1}$ (MPa), for a given precipitate size		
	[100]	[110]	[111]	10 nm	75 nm	150 nm
2	0.18	-0.20	0.39	60	47	31
4	0.18	-0.20	-0.27	148	115	77
6	0.18	-0.01	-0.10	148	115	77
9	0.21	-0.37	0.39	60	47	31
11	0.21	-0.02	0.39	60	47	31
13	0.21	0.18	-0.10	130	100	67
20	0.18	0.41	-0.27	90	70	46

Table 7.6.1: Local resolved shear stresses on different martensite correspondence variant pairs due to lattice mismatch strains for a perfectly coherent precipitate (10 nm) and several semi-coherent precipitates (75 and 150 nm) (chapter 6).

CVP's which have very large average local resolved shear stresses are shown in Table 7.6.1. As the precipitates lose coherency (increase in size), these local shear stress magnitudes will decrease. In Table 7.6.1 the predicted stress fields are given for perfectly coherent precipitates (10 nm), 75 nm precipitates (aged 1.5 h @ 673 K), and 150 nm precipitates (aged 1 h @ 773 K). The increase in the transformation temperatures (Table 7.4.2) for the materials given the two peak-aging treatments is primarily controlled by the local resolved shear stresses from the precipitates.

The former reasoning indicates that M_s of the matrix material is still relatively low, however, the bulk material has a higher M_s due to the strong local stress fields. The increase in M_s is simply due to the fact that the local stress fields create preferential nucleation sites for the martensite. Since not

all of the correspondence variant pairs (CVP's) have equivalent local resolved shear stresses, the morphology of thermally induced martensite in peak-aged samples will be different. For example, as the specimen is cooled, CVP's 4 and 6 will transform much earlier (Table 7.6.1) than any the other CVP's since the thermodynamic driving force on them is offset by the local resolved shear stresses. Most likely, these variants will control the entire transformation and the resulting martensite morphology. The loss of the traditional three CVP self-accommodating groups in peak-aged NiTi is consistent with the microscopic observations of Nishida *et al.* (1988). It should also be noted that since M_s for the 1 h @ 673 K treatment is raised more than M_s for the 1 h @ 773 K treatment, the former heat treatment is proposed to result in more coherent precipitates. This is also consistent with microscopic observations (chapter 6) which show that the 1.5 h @ 673 K treatment results in smaller precipitates. The strong coherency of the precipitates after the 1.5 h @ 673 K heat treatment is also one probable cause of the extremely high R-phase transformation temperature.

When the martensite was stress-induced, both of the peak-aged materials showed a decrease in the orientation dependence of critical transformation stress levels. This effect can be explained by considering the results in Table 7.6.1. When a solutionized single crystal is stressed under tension along the [100] direction, Schmid law predicts that CVP's 9, 11, and 13 will simultaneously transform (Table 7.6.1). However, in a peak-aged single crystal of NiTi, the CVP's which will transform first are the ones which have the maximum *combination* of external (applied) and average local (precipitate) resolved shear stresses (chapter 6). Hence, for a peak-aged single crystal oriented along the [100] direction CVP's 4 and 6 will activate first under an applied stress. Conversely, for a peak-aged single crystal oriented along the [111] direction CVP's 2, 9, and 11 will activate first under tension. Clearly the local resolved shear stresses are much larger on the CVP's favored for transformation in crystals loaded along the [100] direction versus the [111] direction. Thus, crystals oriented along the [100] direction will show a much

more dramatic decrease in the applied stress required to trigger the transformation when they are peak-aged (compare Figures 7.4.1 a-c).

It is also possible to view the above argument from another perspective. The experimentally calculated critical resolved shear stresses in the peak-aged specimens are much lower in the [100] direction versus the [111] direction (Table 7.4.2). This is due to the fact that the different pre-existing local resolved shear stresses for different CVP's are not accounted for in the calculation in Table 7.4.2. Consequently, the decrease in τ_{crss} in the peak-aged materials compared to the solutionized materials is a measure of the local (internal) resolved shear stresses on the martensite CVP's which control the stress-induced transformation. Although there is some lowering of τ_{crss} due to the small compositional change, this effect is proposed to be smaller for the peak-aging treatments. The decrease in the calculated τ_{crss} for the peak-aged materials compared to the solutionized materials (Figure 7.4.2) should be on the order of the predictions in Table 7.6.1. For the 1.5 h @ 673 treatment the precipitate size is about 75 nm. With this, the [100] and [111] orientations are expected to see decreases in τ_{crss} on the order of 115 MPa and 47 MPa respectively. The experiments indicated a drop of about 150 MPa for the [100] orientation and a drop of 87 MPa for the [111] orientation. The agreement between the experiments and the modeling is offset by about 40 MPa. This difference is the same for both orientations and thus is attributed to the compositional change in the alloy during aging which raises M_s and lowers τ_{crss} at a given test temperature. A similar approach can be used to predict the changes τ_{crss} due to aging for 1 h @ 773 K. Notably, the decrease in τ_{crss} is smaller for the 1 h @ 773 heat treatment (Figure 7.4.2). However, the modeling also predicts that the internal stress fields is also weaker for the 1 h @ 773 K heat treatment (Table 7.6.1). Ultimately, it is clear that the modeling results do indicate that the local resolved shear stresses, $\bar{\tau}_{\text{TSS-i}}$, can properly account for the orientation dependent change in τ_{crss} . This orientation

dependent change can not be properly explained by just considering changes in M_s .

In the over-aged materials, the martensite transformation temperatures are comparable to the transformation temperatures of the peak-aged samples (Figure 7.3.1). However, it was also observed that the original orientation dependence of the critical transformation stress levels was recovered (Table 7.4.2). With this it must be assumed that the precipitates are no longer coherent and that the local stress fields are negligible in the over-aged case. This proposition is consistent with the fact that thermally induced martensite in over-aged NiTi reverts back to the three variant self-accommodating groups (Nishida *et al.*, 1988). If the three variant groups were visible in metallurgical studies then the local stress fields must be very weak and the precipitates must be non-coherent. In addition, given the size of the precipitates in the over-aged samples (chapter 6) they are past the critical coherent particle size (Treppmann *et al.*, 1995). With this, it becomes clear that in the over-aged state the coarsened precipitates have depleted the surrounding NiTi of enough Ni to sufficiently raise M_s (lower τ_{crss} and σ_{cr} at a constant test temperature). In figure 7.3.1 the over-aged material shows an increase in M_s of about 50 K compared to the solutionized material. From chapter 6, the change in M_s predicted by considering the volume fraction of the coarsened precipitates was between 30 K and 70 K. Although there is a significant error band in the M_s versus composition data used to make this prediction, the general agreement does imply that the compositional changes in the matrix are responsible for the increase in M_s . Finally, it should be noted that the R-phase transformation occurs in this over-aged state since the precipitates are still disperse enough to promote it (Treppman and Hornbogen, 1995).

The final experimental results which will be discussed here are the multi-temperature tests in Figure 7.5.1. The discussion will be limited to the stress-induced region in Figure 7.5.1. One of the key features of this region is

that the critical transformation stress levels, σ_{cr} , for the two different orientations extrapolate back to different lower limits. The σ_{cr} values for the [100] orientation extrapolate back to almost 70 MPa as the test temperature approaches M_s . Conversely, the σ_{cr} values for the [111] orientation extrapolate back to about 130 MPa as the test temperature approaches M_s . The former barrier (70 MPa) is most likely due to the fact that an offset value was used for determining σ_{cr} . The actual transformation may proceed at nearly 0 MPa. However, this reasoning does not explain why the [111] line extrapolates to a much higher stress. If a tensile stress is applied along the [111] direction (under 130 MPa) it has no effect on the critical temperature required to induce the transformation. Although this may seem counterintuitive, it is due to the fact that different CVP's are responsible for the transformation in the [111] orientation above and below the critical stress level (150 MPa).

For example, when the temperature is dropped below M_s in a stress free state the first CVP's to activate in both the [100] or the [111] specimen will be 4 and 6 (Table 7.6.1). Now suppose that a tensile stress of 100 MPa is applied to both the [100] and the [111] specimens and the temperature is dropped towards M_s . In the [100] specimen all of the CVP's in Table 7.6.1 will see an increased resolved shear stress of about 20 MPa due to the external stresses. This includes the CVP's with the very large local resolved shear stresses due to the precipitates (4 and 6). Thus under the small external tensile stress the transformation will be triggered at a slightly higher temperature (consistent with Figure 7.5.1). In the [111] specimen, only CVP's 2, 9, and 11 will see a positive increase in the resolved shear stress (39 MPa). However, this increase cannot overcome the already large local resolved shear stress on CVP's 4 and 6 (31 MPa + 39 MPa = 70 MPa < 77 MPa). Therefore CVP's 4 and 6 will still activate under the 100 MPa applied tensile stress and subsequent temperature drop. Since the applied stress has a small effect on CVP's 4 and 6 the temperature at which they activate will be nearly identical to that observed under no stress. Thus the continuous phase boundary line for the

[100] orientation on Figure 7.5.1 represents the transformation of the CVP's 4 and 6. However, the vertical dashed phase boundary line on Figure 7.5.1 for the [111] orientation represents the transformation of CVP 6 while the slanted solid line represents the transformation of the CVP's 2, 9, and 11.

As a final discussion point it will be noted that the precipitate coherency levels and Ni depletion levels in the matrix not only depend on the heat treatment temperature and hold time, but also the composition of the alloy and the percent of previous cold work. The theories developed in this paper may be extended to explain the effects of the nominal composition of the alloy and the percent of previous cold work on σ_{cr} and M_s in NiTi. NiTi alloys (Ni rich) with lower Ni concentrations will require longer aging times to achieve the same precipitate size as the 50.8 at% Ni alloy considered here. This is simply due to the fact that the driving force for the precipitation is lower in less Ni rich alloys. Thus, for equivalent aging times and temperatures, lower concentration Ni-rich alloys will not experience changes in M_s or σ_{cr} due to aging as large as 50.8 at% Ni alloys. Cold worked alloys have dense dislocation populations, and thus precipitates will lose coherency faster than in fully recrystallized materials (Treppman and Hornbogen, 1995). This implies that if NiTi is peak-aged below the recrystallization temperature then increasing the percentage of cold work will diminish internal stress fields for a given peak-aging treatment. Thus, for a given peak-aging treatment M_s will decrease as the percentage of cold work goes up due to the diminishing of internal stress fields in high dislocation density areas. Notably, this trend has been experimentally observed (Abujdom, 1990). If the cold worked alloys are aged near the recrystallization temperature then the aging process is more complex (Treppmann *et al.*, 1995)

7.7 CONCLUSIONS

1. Thermally induced martensitic transformations are similar in polycrystalline and single crystal materials for solutionized, peak-aged, and

over-aged NiTi. The transformation stress-strain behavior of polycrystalline NiTi is similar to that of single crystals oriented in the [111] and [110] directions for peak-aged and over-aged materials. Solutionized single crystals and polycrystals were generally brittle at the onset of the transformation due to the high concentration of supersaturated Ni.

2. Generally speaking, the peak-aged and the over-aged materials all have martensite start temperatures well above the solutionized specimens. In the peak-aged samples the difference is primarily attributed to large local stress fields on two martensite correspondence variant pairs (CVP's). In the over-aged materials the difference is primarily attributed to the depletion of Ni in the matrix material. This theory is consistent with previous microscopic observations that the three CVP thermally induced self-accommodating martensite groups are observed in over-aged but not peak-aged samples.

3. The critical transformation stress levels, σ_{cr} , in the solutionized and over-aged single crystals of different crystallographic orientations are consistent with the phenomenological theory of martensitic transformations (Schmid Law). However, σ_{cr} in the peak-aged single crystals of different crystallographic orientations do not obey the Schmid Law. Peak-aged single crystals loaded in tension along the [111] direction show a decrease in σ_{cr} . Conversely, peak-aged single crystals loaded in tension along the [100] direction show a significantly larger decrease in the σ_{cr} .

4. It has been determined that the decrease in the orientation dependence of σ_{cr} in peak-aged NiTi is caused by the precipitation of coherent or semi-coherent $Ti_{11}Ni_{14}$ particles. The local stress fields generated by the precipitates results in large resolved shear stresses on some martensite correspondence variant pairs (CVP's) and small resolved shear stresses on others. It so happens that the martensite CVP's which are oriented favorably for

transformation when the crystal is stressed along the [100] direction are exposed to large local resolved shear stresses. Conversely, the martensite CVP's which are oriented favorably for transformation when the crystal is stressed along the [111] direction are exposed to small local resolved shear stresses.

REFERENCES

- Abujudom D. N., Thoma P. E., and Fariabi S., 1990, "The Effect of Cold Work and Heat Treatment on the Phase Transformations of Near Equiatomic NiTi Shape Memory Alloy," *Mat. Sci. Forum*, vol. 56-58, pp. 565-570.
- Boyd, J. G. and D.C. Lagoudas, 1996, "A thermodynamical constitutive model for shape memory materials. Part 1. The monolithic shape memory alloy," *Int. J. Plasticity*, Vol. 12, 805.
- Boyd, J. G. and D.C. Lagoudas, 1996, "A thermodynamical constitutive model for shape memory materials. Part 2. The SMA composite material," *Int. J. Plasticity*, vol. 12, 843.
- Buchheit T. E., J. A. Wert, 1994, "Modeling the Effects of Stress State and Crystal Orientation on the Stress-Induced Transformation of NiTi Single Crystals," *Metall. Mater. Trans.*, vol. 25A, pp. 2383-2389.
- Buchheit T. E., J. A. Wert, 1996, Predicting the orientation-dependent stress-induced transformation and detwinning response of shape memory alloy single crystals., *Metall. Mater. Trans.*, vol. 27A, pp. 269-279.
- Buehler, W. J., Gilfrich, J. V., and Wiley, R. C., 1963, "Effect of Low-Temperature Phase Changes on the Mechanical Properties of Alloys near Composition TiNi," *J. App. Phys.*, vol. 34, pp. 1475-1477.
- Chumlyakov Y. I. and S. V. Starenchenko, 1995, "Stress-induced martensitic transformation in aged titanium nickel single crystals., *J. Phys. IV, Colloq*, vol. 5, pp. 803-807.
- Chumlyakov Y. I., I. V. Kireeva, V. N. Lineytsev, and E. V. Chepel, 1996, "Aging influence on the shape memory effects and superelasticity in Titanium-Nickel Single crystals," *MRS Symposium Proceedings*, vol. 459, Boston, pp. 387-392.
- Duering, T. W. and Pelton, A. R., 1994, "Ti-Ni Shape Memory Alloys," *Mater. Prop. Hnbk.*, ASM International, Titanium Alloys, pp. 1035-1048.
- Falk, F., 1989, "Pseudoelastic stress-strain curves of polycrystalline shape memory alloys calculated from single crystal data.," *Acta. Met.*, vol. 27, pp. 277.
- Filip P., Rusek J., Mazanec K., 1991, "The effect of heat treatment on the structural stability of TiNi alloys.," *Z. Met.kd.*, vol 82, pp. 488-491.

Filip, P., Tomasek, V., Mazanec, K., 1994, "Corrosion Properties of Shape Memory TiNi Alloys," *Met. Mater.*, vol. 32, pp. 63-68.

Funakubo, H., 1988, Shape Memory Alloys, Gordon and Breach Science.

Furuya, Y., Shimada, H., Tanahashi, Y., Matsumoto, M., Honma, T., 1988, "Evaluation of Recovery Bending Force of Shape Memory Ni-Ti Alloy," *Scr. Met.*, vol. 22, pp. 751-755.

Hodgson, D. E., Wu, M. H., and Biermann, R. J., 1990, "Shape Memory Alloys," *ASM Handbook*, Vol. 2, pp. 897-902.

Honma, T., 1986, "The effect of aging on the spontaneous shape change and the all-round shape memory effect in Ni-Rich TiNi alloy," *ICOMAT-86*, pp. 709-716.

Jacobus, K., H. Sehitoglu, and M. Balzer, 1996, "Effect of stress state on the stress-induced martensitic transformation in polycrystalline Ni-Ti alloy," *Metall. Mater. Trans.*, vol. 27A, pp. 3066.

Li, D. Y., 1996, "Wear Behavior of TiNi Shape Memory Alloys," *Scr. Met.*, vol. 34, pp. 195-200.

Lim, T. J. and McDowell, D. L., 1995, "Path dependence of Shape Memory Alloys During Cyclic Loading," *J. Int. Mat. Sys. Struct.*, vol. 6, pp. 817-830.

Liu, Y. and Galvin, S. P., 1997, "Criteria for Pseudoelasticity in Near-Equiatomic NiTi Shape Memory Alloys," *Acta Mat.*, vol 45, pp. 4431-4439.

Miyazaki, S., Ohmi, Y., Otsuka, K., and Suzuki, Y., 1982, *J. De. Phys.*, vol. 43, pp. 255.

Miyazaki, S., Kimura, S., Otsuka, K., and Suzuki, Y., 1984, "The Habit Plane and Transformation Strains Associated With the Martensitic Transformation in Ti-Ni Single Crystals," *Scr. Met.*, vol. 18, pp. 883-888.

Miyazaki, S., Imai, T., Igo, Y., Otsuka, K., 1986, "Effect of Cyclic Deformation on the Pseudoelastic Characteristics of Ti-Ni alloys," *Metall. Mater. Trans.*, vol. 17A, pp. 115-120.

Nishida M, Wayman C M, 1988, "Electron microscopy studies of the 'premartensitic' transformations in an aged Ti-51 at.%Ni shape memory alloy," *Metallography*, vol 21, pp. 255-273.

- Nishida M, Wayman C M, Chiba A, 1988, "Electron microscopy studies of the martensitic transformation in an aged Ti-51 at.%Ni shape memory alloy.," *Metallography*, vol 21, pp. 275-291.
- Ono, N., A. Satoh, and H. Ohta, 1989, "A discussion on the mechanical properties of shape memory alloys based on a polycrystal model.," *Mat. Trans. JIM*, vol. 30, pp. 756.
- Orgeas L. and D. Favier, 1995, "Non-symmetric tension-compression behavior of NiTi alloy.," *J. Phys. IV, Colloq.*, vol. 5, pp. 605.
- Patoor, E., A. Eberhardt and M Berveiller, 1996, "Micromechanical modeling of superelasticity in shape memory alloys.," *J. de Physique*, vol. 6, pp. 277.
- Perkins, J., 1981, "Ti-Ni and Ti-Ni-X Shape Memory Alloys," *Metals Forum*, vol. 4, pp. 153-163.
- Plietsch, R. and K. Ehrlich, 1997, "Strength differential effect in pseudoelastic NiTi shape memory alloys," *Acta Mat.*, vol. 35, pp. 2417.
- Shaw J. A., and Kyriakides S., 1997, "On the nucleation and propagation of phase transformation fronts in a NiTi alloy.," *Acta Mat.*, vol 45, pp. 683-700.
- Shimizu K, Tadaki T, 1988, Shape Memory Alloys, Ed. Funakubo H, Gordon and Breach Science.
- Sun, Q. P., K. C. Hwang, and S. W. Yu, 1991, "A micromechanics constitutive model of transformation plasticity with shear and dilation effect," *J. Mech. Phys. Solids*, vol. 39, 507.
- Sun, Q. P. and K. C. Hwang, 1993, "Micromechanics modeling for the constitutive behavior of polycrystalline shape memory alloys-I. Derivation of general relations.," *J. Mech. Phys. Solids*, vol. 41, 1.
- Sun, Q. P. and K. C. Hwang, 1993, "Micromechanics modeling for the constitutive behavior of polycrystalline shape memory alloys-II. Study of individual phenomenon.," *J. Mech. Phys. Solids*, vol. 41, 19.
- Tobushi, H., Hachisuka, T., Yamada, S., and Lin, P. H., 1997, "Rotating Bending Fatigue of a TiNi Shape Memory alloy Wire," *ICF9 Advances in Fracture Research, Sidney, Australia*, vol. 3, pp. 1741-1748.
- Todoroki T. and Tamura H, 1987, "Effect of Heat Treatment after Cold Working on the Phase Transformation in TiNi alloy.," *Trans. Jpn. Inst. Met.*, vol 28, no 2, pp. 83-94.

Treppmann, D. and Hornbogen, E., 1995, "The Effect of Dislocation Substructure and Decomposition on the Course of Diffusionless Transformation," *J. D. Physique IV*, vol. 5, pp. 211-216.

Treppmann, D, Hornbogen, E, and Wurzel, D, 1995, "The effect of Combined recrystallization and precipitation processes on the functional and structural properties of NiTi alloys," *J. De. Phys.*, vol. 5, pp. 569-574.

Wasilewski, R. J., 1971, "The effects of Applied Stress on the Martensitic Transformation in NiTi," *Metall. Mater. Trans.*, vol. 2, pp. 2973-2981.

Wayman C M, 1980, *J. Metals*, vol. 32, pp. 129.

Wu, M. H., 1988, "Cu-Based Shape Memory Alloys," Shape Memory Alloys, Ed. Funakubo H, Gordon and Breach Science, pp. 69-88.

APPENDIX A: FORTRAN PROGRAM SHAPE.F

In this appendix, the general framework of the computer code used to predict the polycrystalline response of shape memory alloys is given. Some of the sections of the program are omitted to save space. Here, the solution algorithms are only shown for one or two transforming variants. In the actual program, up to four variants are allowed to transform per grain.

```
c This program will calculate the response of a polycrystalline
c shape memory alloy from single crystal behavior using the
c self consistent formulation.

c declare variables (NOT SHOWN)

c initialize variables (NOT SHOWN)

c assign values to variables (NOT SHOWN)

c read in maximum applied stress tensor (NOT SHOWN)

c calculate maximum effective stress

      seff = SQRT(2.0)/2.0*SQRT( ( sbar(1,1)-sbar(2,2) )**2.0 +
&   ( sbar(1,1)-sbar(3,3) )**2.0 + ( sbar(2,2)-sbar(3,3) )**2.0)

c calculate mvec and nvec for all 24 unrotated slip systems (NOT SHOWN)

c calculate alpha-ij for unrotated grains (NOT SHOWN)

c rotate alpha tensor randomly through three calculated angles (NOT
c SHOWN)
c each grain has a different random rotation to simulate a polycrystalline body

c ***** MAIN PROGRAM LOOP BEGINS HERE *****
c linearly ramp all loads from zero to maximum so that they hit
c the maximum values at the same time during the loading history.

c find proper far field average load increments

      dsbar(1,1) = sbar(1,1)/incr
      dsbar(2,2) = sbar(2,2)/incr
```

```
dsbar(3,3) = sbar(3,3)/incr
dseff = seff/incr
```

c Zero out applied far field load

```
sbar(1,1) = 0.0
sbar(2,2) = 0.0
sbar(3,3) = 0.0
seff = 0.0
```

c BEGIN DO LOOP

```
DO 1000 kk = 1,incr

write(*,*) 'step ',kk,' of ',incr
```

c increment all average far field loads

```
sbar(1,1) = sbar(1,1) + dsbar(1,1)
sbar(2,2) = sbar(2,2) + dsbar(2,2)
sbar(3,3) = sbar(3,3) + dsbar(3,3)
seff = seff + dseff
```

c calculate current elastic constants

```
Elas = Em*fave + Ea*(1-fave)
mu = Elas/2.0/(1.0+nu)
```

```
H1 = mu/1100.0
H2 = 0.0
```

```
C11 = Elas*(1.0-nu)/((1.0+nu)*(1.0-2.0*nu))
C12 = Elas*nu/((1.0+nu)*(1.0-2.0*nu))
C44 = (C11-C12)/2.0
```

```
S1111 = (7.0-5.0*nu)/(15.0*(1.0-nu))
S1122 = (5.0*nu-1.0)/(15.0*(1.0-nu))
S1212 = (4.0-5.0*nu)/(15.0*(1.0-nu))
```

```
AA = 2.0*C12*S1122 + C11*S1111
BB = 2.0*S1122*(C11+C12) + 2.0*C12*S1111
DD = 2.0*C44*S1212
```

c calculate elastic strain increments in every grain

```
mean = nu/Elas*(dsbar(1,1)+dsbar(2,2)+dsbar(3,3))
```



```
deebars(1,1) = (1.+nu)/Elas*dsbar(1,1)-mean
deebars(2,2) = (1.+nu)/Elas*dsbar(2,2)-mean
deebars(3,3) = (1.+nu)/Elas*dsbar(3,3)-mean
```

```
c remember previous total plastic strain increment
```

```
tr(1,1) = depbar(1,1)
tr(2,2) = depbar(2,2)
tr(3,3) = depbar(3,3)
```

```
tr(1,2) = depbar(1,2)
tr(1,3) = depbar(1,3)
tr(2,3) = depbar(2,3)
```

```
c zero out current total plastic strain increments
```

```
depbar(1,1) = 0.0
depbar(2,2) = 0.0
depbar(3,3) = 0.0
```

```
depbar(1,2) = 0.0
depbar(1,3) = 0.0
depbar(2,3) = 0.0
```

```
c zero out martensite evolution variables
```

```
fave = 0.0
nactg = 0
nactv = 0
nactvn = 0
```

```
c LOOP THROUGH THE GRAINS
```

```
DO 2000 jj = 1,1000
```

```
c zero out plastic strain increment for grain jj
```

```
depg(1,1,jj) = 0.0
depg(2,2,jj) = 0.0
depg(3,3,jj) = 0.0
```

```
depg(1,2,jj) = 0.0
depg(1,3,jj) = 0.0
depg(2,3,jj) = 0.0
```

c loop through the slip systems and mark the transforming variants

DO 3000 ii = 1,24

c calculate the thermodynamic force the ii variant in grain jj

```
tau(ii,jj)=sbar(1,1)*alt(1,1,ii,jj)
&      +sbar(2,2)*alt(2,2,ii,jj)
&      +sbar(3,3)*alt(3,3,ii,jj)
```

c check for transformation of the particular variant

```
IF( (active(jj) .LT. 3) .AND. (ftot(jj) .LT. 1.0) ) THEN
```

```
IF ( (tau(ii,jj) .GE. taunot) ) THEN
```

c check to see if this is the first yield, and note it

```
if ( ken(ii,jj) .EQ. 0) then
    ken(ii,jj) = 1
    grain(jj) = 1
    active(jj) = active(jj) + 1
    mark(active(jj),jj) = ii
```

c give this yielding variant an intrinsic trans strain

```
epv(1,1,ii,jj) = gee*alt(1,1,ii,jj)
epv(2,2,ii,jj) = gee*alt(2,2,ii,jj)
epv(3,3,ii,jj) = gee*alt(3,3,ii,jj)
epv(1,2,ii,jj) = gee*alt(1,2,ii,jj)
epv(1,3,ii,jj) = gee*alt(1,3,ii,jj)
epv(2,3,ii,jj) = gee*alt(2,3,ii,jj)
endif
```

```
ENDIF
```

```
ENDIF
```

3000 CONTINUE

c with the information on yielding (active variants)

c calculate fdot for all of the active variants in the grain

c ONE VARIANT TRANSFORMING

IF ((ftot(jj) .LT. 1.0) .AND. (active(jj) .EQ. 1)) THEN

c calculate fdot (self consistant method)

```
fdot(mark(1,jj),jj) = ( epv(1,1,mark(1,jj),jj)*dsbar(1,1)
& +epv(2,2,mark(1,jj),jj)*dsbar(2,2)
& +epv(3,3,mark(1,jj),jj)*dsbar(3,3)
& -(AA-C11)*( epv(1,1,mark(1,jj),jj)*tr(1,1)
& +epv(2,2,mark(1,jj),jj)*tr(2,2)
& +epv(3,3,mark(1,jj),jj)*tr(3,3))
& -(BB/2.0-C12)*( epv(1,1,mark(1,jj),jj)*tr(2,2)
& +epv(1,1,mark(1,jj),jj)*tr(3,3)
& +epv(2,2,mark(1,jj),jj)*tr(3,3)
& +epv(2,2,mark(1,jj),jj)*tr(1,1)
& +epv(3,3,mark(1,jj),jj)*tr(1,1)
& +epv(3,3,mark(1,jj),jj)*tr(2,2))
& -(DD-1.0*C44)*( epv(1,2,mark(1,jj),jj)*tr(1,2)
& +epv(1,3,mark(1,jj),jj)*tr(1,3)
& +epv(2,3,mark(1,jj),jj)*tr(2,3)) ) /
& (mu/1000.0
& -(AA-C11)*( epv(1,1,mark(1,jj),jj)*epv(1,1,mark(1,jj),jj)
& +epv(2,2,mark(1,jj),jj)*epv(2,2,mark(1,jj),jj)
& +epv(3,3,mark(1,jj),jj)*epv(3,3,mark(1,jj),jj))
& -(BB-2.0*C12)*( epv(1,1,mark(1,jj),jj)*epv(2,2,mark(1,jj),jj)
& +epv(1,1,mark(1,jj),jj)*epv(3,3,mark(1,jj),jj)
& +epv(2,2,mark(1,jj),jj)*epv(3,3,mark(1,jj),jj))
& -(DD-1.0*C44)*( epv(1,2,mark(1,jj),jj)*epv(1,2,mark(1,jj),jj)
& +epv(1,3,mark(1,jj),jj)*epv(1,3,mark(1,jj),jj)
& +epv(2,3,mark(1,jj),jj)*epv(2,3,mark(1,jj),jj)) )
```

c check to see if this variant is untransforming

if (fdot(mark(1,jj),jj) .LT. 0.0) then

c can this variant untransform?

if (ftotv(mark(1,jj),jj) .LE. 0.0) then

c NO, so there is no transformation at all

fdot(mark(1,jj),jj) = 0.0

kenn(mark(1,jj),jj) = 0

kenp(mark(1,jj),jj) = 0

else

```

c      YES, let the program know that this variant is untrans
      kenn(mark(1,jj),jj) = 1
      kenp(mark(1,jj),jj) = 0

      endif
else
c      this variant is transforming if it is NOT untransforming
      kenn(mark(1,jj),jj) = 0
      kenp(mark(1,jj),jj) = 1

      endif

c      update f total for the grain

      ftotv(mark(1,jj),jj)=ftotv(mark(1,jj),jj)+fdot(mark(1,jj),jj)
      ftot(jj) = ftotv(mark(1,jj),jj)

c      add variant plastic strain to total grain plastic strain
c      weighted by the volume fraction of new martensite fdot

      depg(1,1,jj) = depg(1,1,jj)
&      + epv(1,1,mark(1,jj),jj)*fdot(mark(1,jj),jj)
      depg(2,2,jj) = depg(2,2,jj)
&      + epv(2,2,mark(1,jj),jj)*fdot(mark(1,jj),jj)
      depg(3,3,jj) = depg(3,3,jj)
&      + epv(3,3,mark(1,jj),jj)*fdot(mark(1,jj),jj)

      depg(1,2,jj) = depg(1,2,jj)
&      + epv(1,2,mark(1,jj),jj)*fdot(mark(1,jj),jj)
      depg(1,3,jj) = depg(1,3,jj)
&      + epv(1,3,mark(1,jj),jj)*fdot(mark(1,jj),jj)
      depg(2,3,jj) = depg(2,3,jj)
&      + epv(2,3,mark(1,jj),jj)*fdot(mark(1,jj),jj)

c      add this yielding variant to the total currently yielding

      nactv = nactv + kenp(mark(1,jj),jj)
      nactvn = nactvn + kenn(mark(1,jj),jj)

      ENDIF

c      TWO VARIANTS TRANSFORMING

      IF ( (ftot(jj) .LT. 1.0) .AND. (active(jj) .EQ. 2) ) THEN

```

c calculate fdot (self consistant method)

```

AVE(1) = epv(1,1,mark(1,jj),jj)*dsbar(1,1)
&      +epv(2,2,mark(1,jj),jj)*dsbar(2,2)
&      +epv(3,3,mark(1,jj),jj)*dsbar(3,3)
&      -(AA-C11)*( epv(1,1,mark(1,jj),jj)*tr(1,1)
&                  +epv(2,2,mark(1,jj),jj)*tr(2,2)
&                  +epv(3,3,mark(1,jj),jj)*tr(3,3))
&      -(BB/2.0-C12)*( epv(1,1,mark(1,jj),jj)*tr(2,2)
&                      +epv(1,1,mark(1,jj),jj)*tr(3,3)
&                      +epv(2,2,mark(1,jj),jj)*tr(3,3)
&                      +epv(2,2,mark(1,jj),jj)*tr(1,1)
&                      +epv(3,3,mark(1,jj),jj)*tr(1,1)
&                      +epv(3,3,mark(1,jj),jj)*tr(2,2))
&      -(DD-1.0*C44)*( epv(1,2,mark(1,jj),jj)*tr(1,2)
&                      +epv(1,3,mark(1,jj),jj)*tr(1,3)
&                      +epv(2,3,mark(1,jj),jj)*tr(2,3))

```

```

AVE(2) = epv(1,1,mark(2,jj),jj)*dsbar(1,1)
&      +epv(2,2,mark(2,jj),jj)*dsbar(2,2)
&      +epv(3,3,mark(2,jj),jj)*dsbar(3,3)
&      -(AA-C11)*( epv(1,1,mark(2,jj),jj)*tr(1,1)
&                  +epv(2,2,mark(2,jj),jj)*tr(2,2)
&                  +epv(3,3,mark(2,jj),jj)*tr(3,3))
&      -(BB/2.0-C12)*( epv(1,1,mark(2,jj),jj)*tr(2,2)
&                      +epv(1,1,mark(2,jj),jj)*tr(3,3)
&                      +epv(2,2,mark(2,jj),jj)*tr(3,3)
&                      +epv(2,2,mark(2,jj),jj)*tr(1,1)
&                      +epv(3,3,mark(2,jj),jj)*tr(1,1)
&                      +epv(3,3,mark(2,jj),jj)*tr(2,2))
&      -(DD-1.0*C44)*( epv(1,2,mark(2,jj),jj)*tr(1,2)
&                      +epv(1,3,mark(2,jj),jj)*tr(1,3)
&                      +epv(2,3,mark(2,jj),jj)*tr(2,3))

```

```

FD2(1,1) = mu/1100.0
&      -(AA-C11)*( epv(1,1,mark(1,jj),jj)*epv(1,1,mark(1,jj),jj)
&                  +epv(2,2,mark(1,jj),jj)*epv(2,2,mark(1,jj),jj)
&                  +epv(3,3,mark(1,jj),jj)*epv(3,3,mark(1,jj),jj))
&      -(BB-2.0*C12)*( epv(1,1,mark(1,jj),jj)*epv(2,2,mark(1,jj),jj)
&                      +epv(1,1,mark(1,jj),jj)*epv(3,3,mark(1,jj),jj)
&                      +epv(2,2,mark(1,jj),jj)*epv(3,3,mark(1,jj),jj))
&      -(DD-1.0*C44)*( epv(1,2,mark(1,jj),jj)*epv(1,2,mark(1,jj),jj)
&                      +epv(1,3,mark(1,jj),jj)*epv(1,3,mark(1,jj),jj)
&                      +epv(2,3,mark(1,jj),jj)*epv(2,3,mark(1,jj),jj))

```

```

FD2(2,2) = mu/1100.0

```

```

& -(AA-C11)*( epv(1,1,mark(2,jj),jj)*epv(1,1,mark(2,jj),jj)
&      +epv(2,2,mark(2,jj),jj)*epv(2,2,mark(2,jj),jj)
&      +epv(3,3,mark(2,jj),jj)*epv(3,3,mark(2,jj),jj))
& -(BB-2.0*C12)*( epv(1,1,mark(2,jj),jj)*epv(2,2,mark(2,jj),jj)
&      +epv(1,1,mark(2,jj),jj)*epv(3,3,mark(2,jj),jj)
&      +epv(2,2,mark(2,jj),jj)*epv(3,3,mark(2,jj),jj))
& -(DD-1.0*C44)*( epv(1,2,mark(2,jj),jj)*epv(1,2,mark(2,jj),jj)
&      +epv(1,3,mark(2,jj),jj)*epv(1,3,mark(2,jj),jj)
&      +epv(2,3,mark(2,jj),jj)*epv(2,3,mark(2,jj),jj))

```

```

FD2(1,2) =
& -(AA-C11)*( epv(1,1,mark(1,jj),jj)*epv(1,1,mark(2,jj),jj)
&      +epv(2,2,mark(1,jj),jj)*epv(2,2,mark(2,jj),jj)
&      +epv(3,3,mark(1,jj),jj)*epv(3,3,mark(2,jj),jj))
& -(BB-2.0*C12)*( epv(1,1,mark(1,jj),jj)*epv(2,2,mark(2,jj),jj)
&      +epv(1,1,mark(1,jj),jj)*epv(3,3,mark(2,jj),jj)
&      +epv(2,2,mark(1,jj),jj)*epv(3,3,mark(2,jj),jj))
& -(DD-1.0*C44)*( epv(1,2,mark(1,jj),jj)*epv(1,2,mark(2,jj),jj)
&      +epv(1,3,mark(1,jj),jj)*epv(1,3,mark(2,jj),jj)
&      +epv(2,3,mark(1,jj),jj)*epv(2,3,mark(2,jj),jj))

```

```

FD2(2,1) =
& -(AA-C11)*( epv(1,1,mark(2,jj),jj)*epv(1,1,mark(1,jj),jj)
&      +epv(2,2,mark(2,jj),jj)*epv(2,2,mark(1,jj),jj)
&      +epv(3,3,mark(2,jj),jj)*epv(3,3,mark(1,jj),jj))
& -(BB-2.0*C12)*( epv(1,1,mark(2,jj),jj)*epv(2,2,mark(1,jj),jj)
&      +epv(1,1,mark(2,jj),jj)*epv(3,3,mark(1,jj),jj)
&      +epv(2,2,mark(2,jj),jj)*epv(3,3,mark(1,jj),jj))
& -(DD-1.0*C44)*( epv(1,2,mark(2,jj),jj)*epv(1,2,mark(1,jj),jj)
&      +epv(1,3,mark(2,jj),jj)*epv(1,3,mark(1,jj),jj)
&      +epv(2,3,mark(2,jj),jj)*epv(2,3,mark(1,jj),jj))

```

```

DET2(1) = 0.0
DET2(2) = 0.0
WORK2(1) = 0.0
WORK2(2) = 0.0
IPVT2(1) = 0
IPVT2(2) = 0
INFO = 0
LDA = 2
JOB = 01

```

c imsl equation solver

```
call linrg(2,FD2,2,FD2,2)
```

$\text{fdot}(\text{mark}(1,\text{jj}),\text{jj}) = \text{FD2}(1,1)*\text{AVE}(1) + \text{FD2}(1,2)*\text{AVE}(2)$
 $\text{fdot}(\text{mark}(2,\text{jj}),\text{jj}) = \text{FD2}(2,1)*\text{AVE}(1) + \text{FD2}(2,2)*\text{AVE}(2)$

c check to see if this variant is untransforming

if ($\text{fdot}(\text{mark}(1,\text{jj}),\text{jj})$.LT. 0.0) then

c can this variant untransform?

if ($\text{ftotv}(\text{mark}(1,\text{jj}),\text{jj})$.LE. 0.0) then

c NO, so there is no transformation at all

$\text{fdot}(\text{mark}(1,\text{jj}),\text{jj}) = 0.0$

$\text{kenn}(\text{mark}(1,\text{jj}),\text{jj}) = 0$

$\text{kenp}(\text{mark}(1,\text{jj}),\text{jj}) = 0$

else

c YES, let the program know that this variant is untrans

$\text{kenn}(\text{mark}(1,\text{jj}),\text{jj}) = 1$

$\text{kenp}(\text{mark}(1,\text{jj}),\text{jj}) = 0$

endif

else

c this variant is transforming if it is NOT untransforming

$\text{kenn}(\text{mark}(1,\text{jj}),\text{jj}) = 0$

$\text{kenp}(\text{mark}(1,\text{jj}),\text{jj}) = 1$

endif

c check to see if this variant is untransforming

if ($\text{fdot}(\text{mark}(2,\text{jj}),\text{jj})$.LT. 0.0) then

c can this variant untransform?

if ($\text{ftotv}(\text{mark}(2,\text{jj}),\text{jj})$.LE. 0.0) then

c NO, so there is no transformation at all

$\text{fdot}(\text{mark}(2,\text{jj}),\text{jj}) = 0.0$

$\text{kenn}(\text{mark}(2,\text{jj}),\text{jj}) = 0$

$\text{kenp}(\text{mark}(2,\text{jj}),\text{jj}) = 0$

else

```

c      YES, let the program know that this variant is untrans
      kenn(mark(2,jj),jj) = 1
      kenp(mark(2,jj),jj) = 0

```

```

      endif
else

```

```

c      this variant is transforming if it is NOT untransforming
      kenn(mark(2,jj),jj) = 0
      kenp(mark(2,jj),jj) = 1

```

```

      endif

```

```

c      update f total for the grain

```

```

      ftotv(mark(1,jj),jj)=ftotv(mark(1,jj),jj)+fdot(mark(1,jj),jj)
      ftotv(mark(2,jj),jj)=ftotv(mark(2,jj),jj)+fdot(mark(2,jj),jj)
      ftot(jj) = ftotv(mark(1,jj),jj) + ftotv(mark(2,jj),jj)

```

```

c      add variant plastic strain to total grain plastic strain

```

```

c      weighted by the volume fraction of new martensite fdot

```

```

      depg(1,1,jj) = depg(1,1,jj)
&      + epv(1,1,mark(1,jj),jj)*fdot(mark(1,jj),jj)
&      + epv(1,1,mark(2,jj),jj)*fdot(mark(2,jj),jj)
      depg(2,2,jj) = depg(2,2,jj)
&      + epv(2,2,mark(1,jj),jj)*fdot(mark(1,jj),jj)
&      + epv(2,2,mark(2,jj),jj)*fdot(mark(2,jj),jj)
      depg(3,3,jj) = depg(3,3,jj)
&      + epv(3,3,mark(1,jj),jj)*fdot(mark(1,jj),jj)
&      + epv(3,3,mark(2,jj),jj)*fdot(mark(2,jj),jj)

```

```

      depg(1,2,jj) = depg(1,2,jj)
&      + epv(1,2,mark(1,jj),jj)*fdot(mark(1,jj),jj)
&      + epv(1,2,mark(2,jj),jj)*fdot(mark(2,jj),jj)
      depg(1,3,jj) = depg(1,3,jj)
&      + epv(1,3,mark(1,jj),jj)*fdot(mark(1,jj),jj)
&      + epv(1,3,mark(2,jj),jj)*fdot(mark(2,jj),jj)
      depg(2,3,jj) = depg(2,3,jj)
&      + epv(2,3,mark(1,jj),jj)*fdot(mark(1,jj),jj)
&      + epv(2,3,mark(2,jj),jj)*fdot(mark(2,jj),jj)

```


c add this yielding variant to the total currently yielding

```
nactv = nactv + kenp(mark(1,jj),jj)
&      + kenp(mark(2,jj),jj)
nactvn = nactvn + kenn(mark(1,jj),jj)
&      + kenn(mark(2,jj),jj)
```

ENDIF

c check to see if the grain has completely transformed

```
IF ((ftot(jj) .GE. 1.0) .AND. (active(jj) .EQ. 1)) THEN
```

```
  nactv = nactv - kenp(mark(1,jj),jj)
  nactvn = nactvn - kenn(mark(1,jj),jj)
  kenp(mark(1,jj),jj) = 0
  ken(mark(1,jj),jj) = 0
  kenn(mark(1,jj),jj) = 0
  grain(jj) = 0
  active(jj) = 0
```

ENDIF

```
IF ((ftot(jj) .GE. 1.0) .AND. (active(jj) .EQ. 2)) THEN
```

```
  nactv = nactv - kenp(mark(1,jj),jj)
&      - kenp(mark(2,jj),jj)
  nactvn = nactvn - kenn(mark(1,jj),jj)
&      - kenn(mark(2,jj),jj)
  ken(mark(1,jj),jj) = 0
  ken(mark(2,jj),jj) = 0
  kenp(mark(1,jj),jj) = 0
  kenp(mark(2,jj),jj) = 0
  kenn(mark(1,jj),jj) = 0
  kenn(mark(2,jj),jj) = 0
  grain(jj) = 0
  active(jj) = 0
```

ENDIF

c add this grain plastic e to total plastic e (NOT SHOWN)

c add volume fraction of this grain to total vol fract (NOT SHOWN)

c (to be averaged after all grains have been looped through)

c add this grain, jj, to the total number of transforming grains (NOT SHOWN)

2000 CONTINUE

c average overall plastic strains (NOT SHOWN)

c average total transformed volume fraction (NOT SHOWN)

c add plastic and elastic strain increments (NOT SHOWN)

c update plastic strain (NOT SHOWN)

c update total strain (NOT SHOWN)

c calculate current effective plastic strain (NOT SHOWN)

c calculate current effective total strain (NOT SHOWN)

c write data to the output files

1000 CONTINUE

END

APPENDIX B: RESOLVED SHEAR STRESS CONTOURS

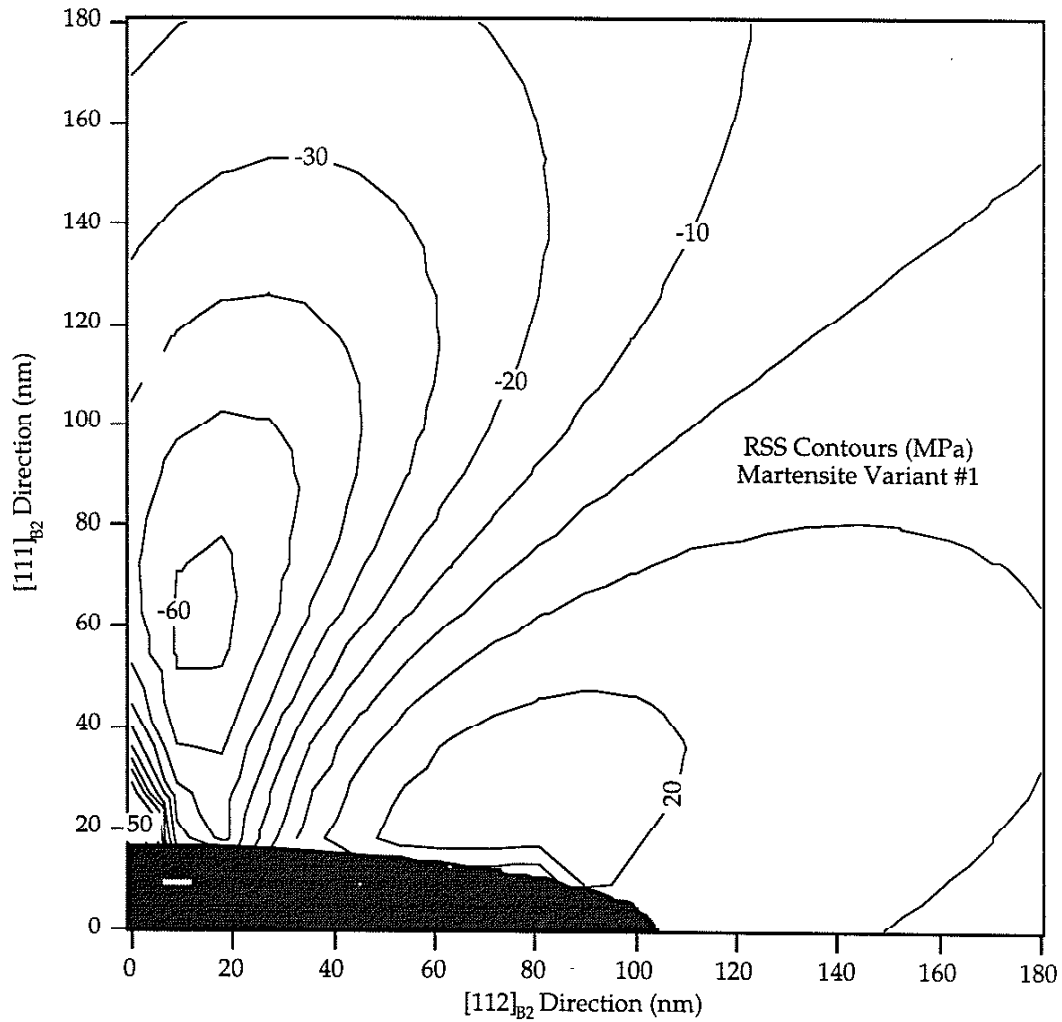


Figure B.1: Resolved shear stress contours due to lattice mismatch strains around a $Ti_{11}Ni_{14}$ precipitate in a NiTi matrix. The resolved shear stresses are calculated on martensite variant #1. The plot is axessymmetric around the $[111]$ axes and posses mirror symmetry about the $[111]$ plane.

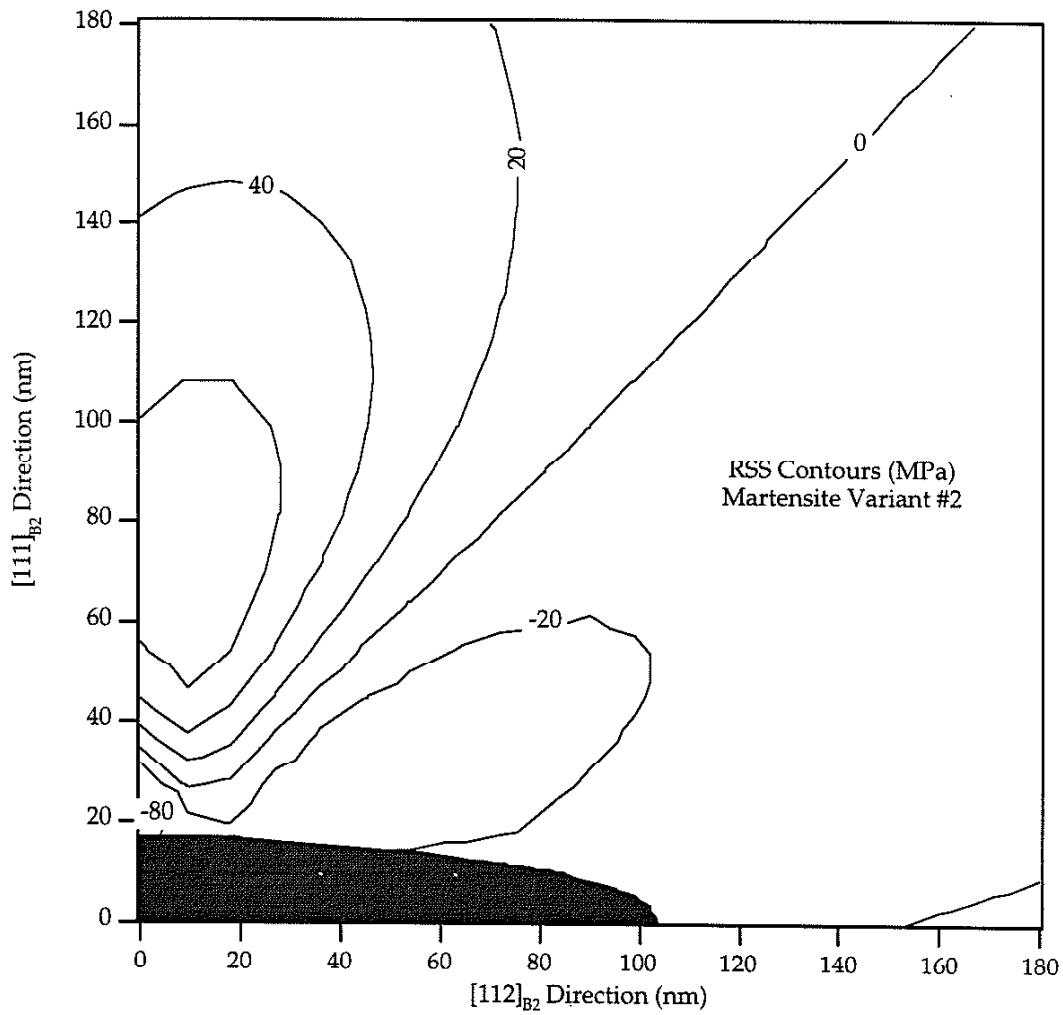


Figure B.2: Resolved shear stress contours due to lattice mismatch strains around a $\text{Ti}_{11}\text{Ni}_{14}$ precipitate in a NiTi matrix. The resolved shear stresses are calculated on martensite variant #2. The plot is axially symmetric around the $[111]$ axes and possesses mirror symmetry about the $[111]$ plane.

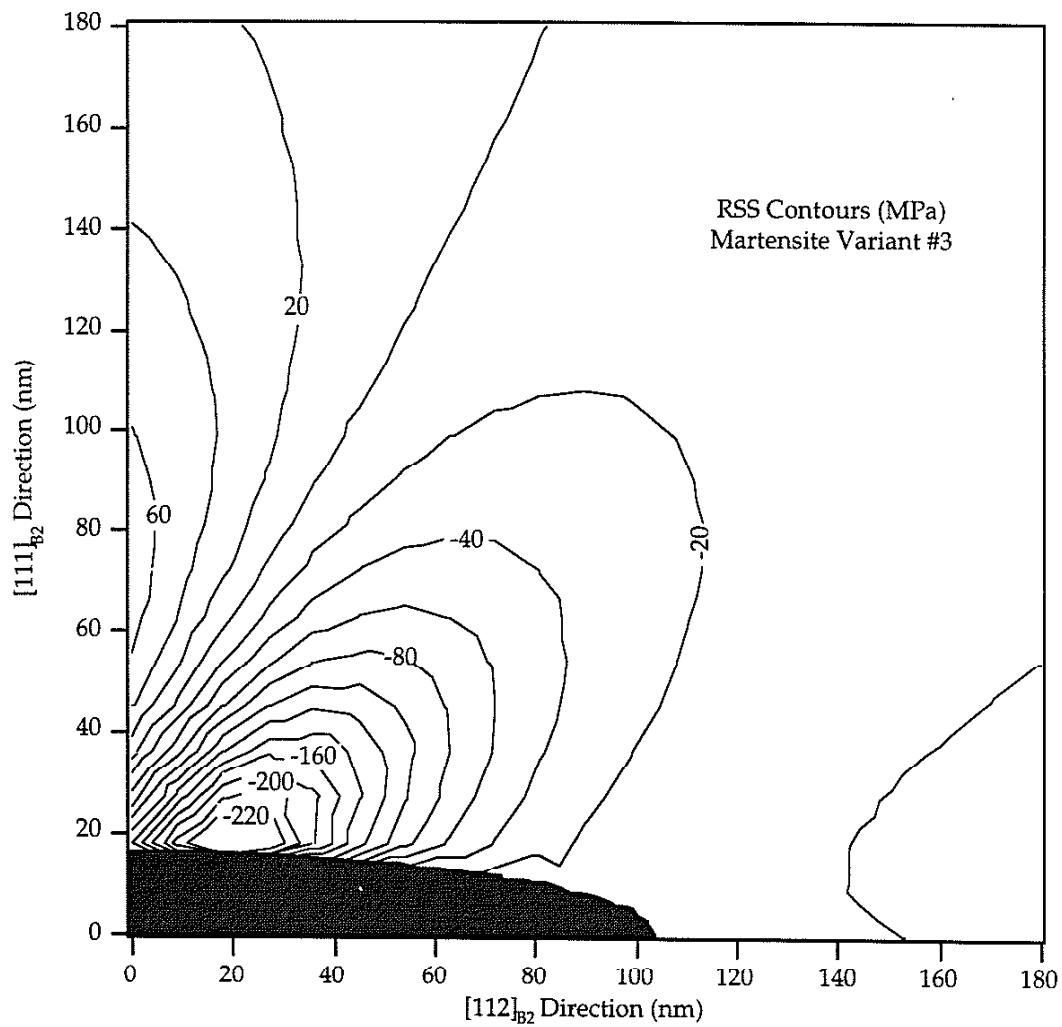


Figure B.3: Resolved shear stress contours due to lattice mismatch strains around a $Ti_{11}Ni_{14}$ precipitate in a NiTi matrix. The resolved shear stresses are calculated on martensite variant #3. The plot is axessymmetric around the $[111]$ axes and posses mirror symmetry about the $\{111\}$ plane.

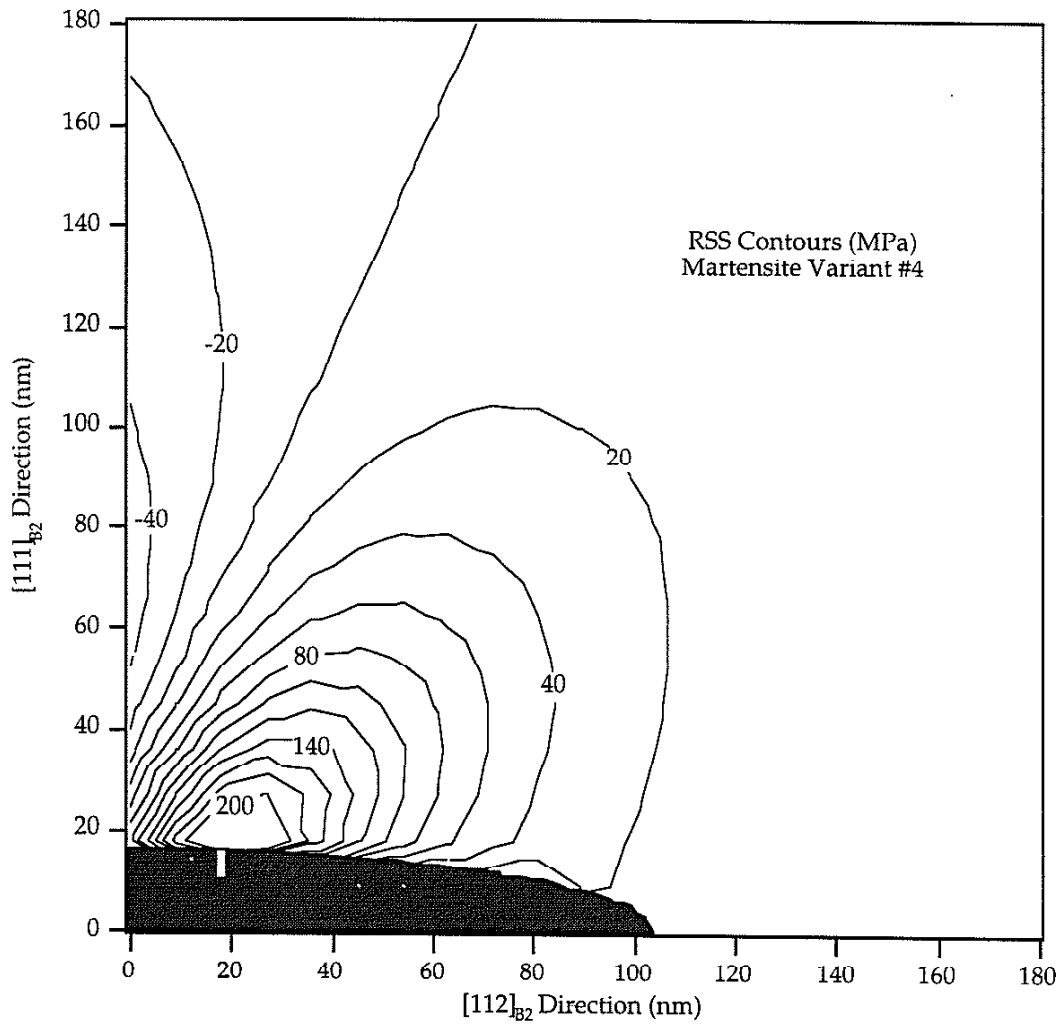


Figure B.4: Resolved shear stress contours due to lattice mismatch strains around a $\text{Ti}_{11}\text{Ni}_{14}$ precipitate in a NiTi matrix. The resolved shear stresses are calculated on martensite variant #4. The plot is axessymmetric around the $[111]$ axes and posses mirror symmetry about the $\{111\}$ plane.

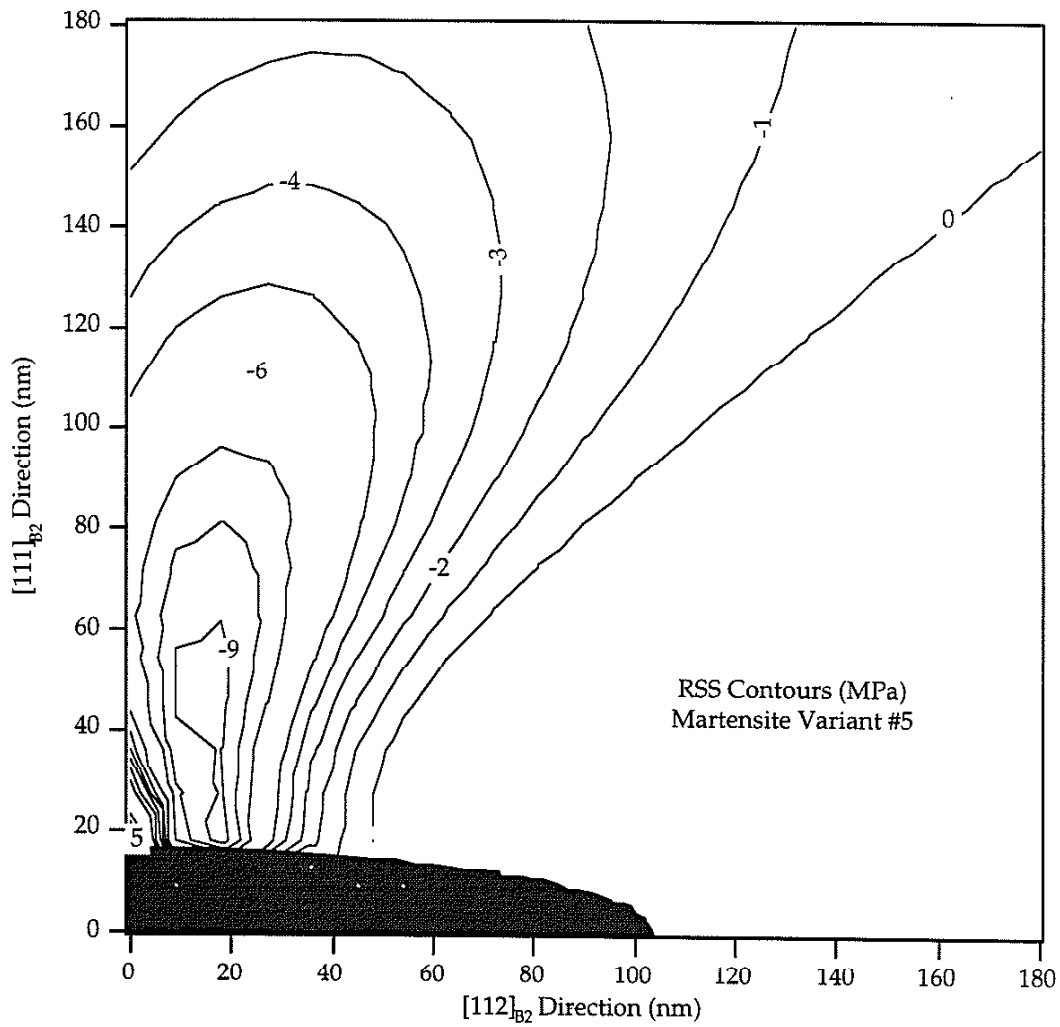


Figure B.5: Resolved shear stress contours due to lattice mismatch strains around a $Ti_{11}Ni_{14}$ precipitate in a NiTi matrix. The resolved shear stresses are calculated on martensite variant #5. The plot is axessymmetric around the $[111]$ axes and posses mirror symmetry about the $\{111\}$ plane.

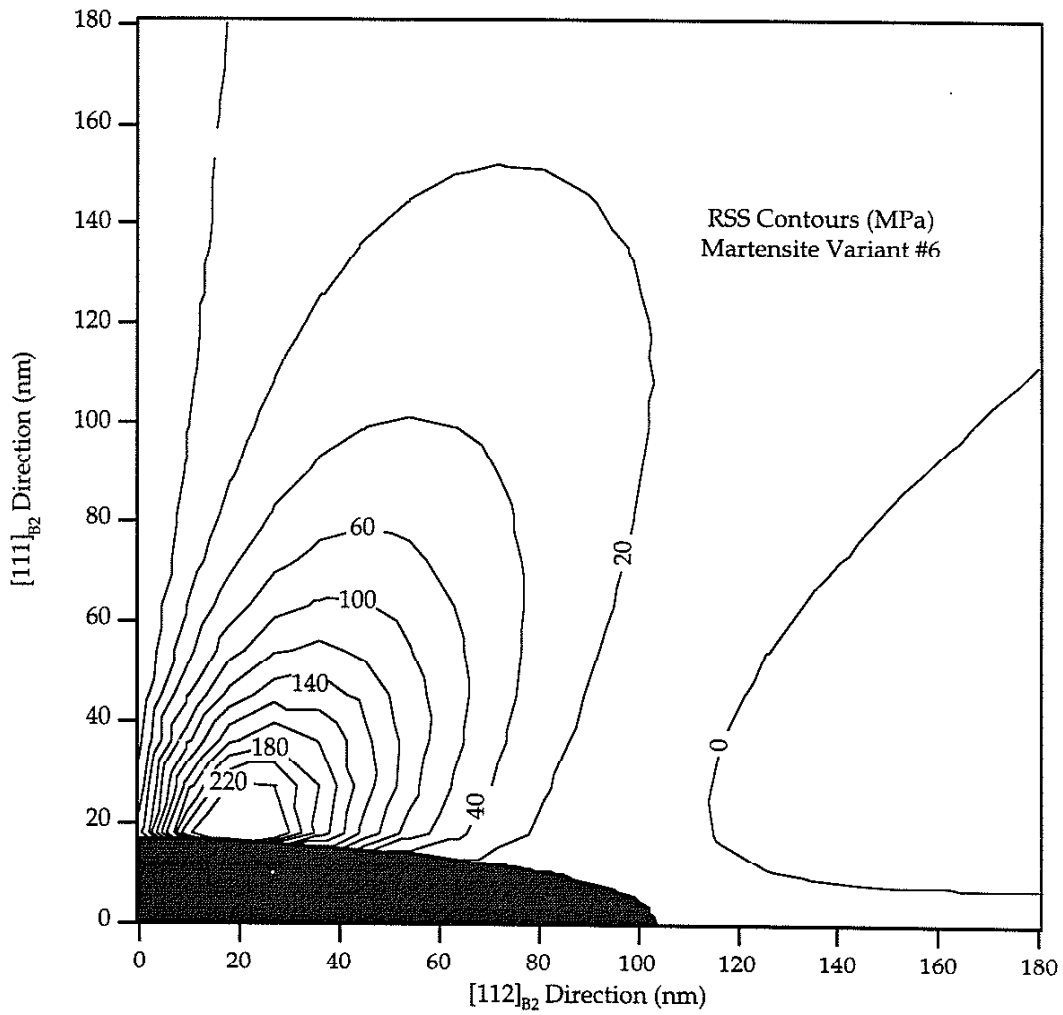


Figure B.6: Resolved shear stress contours due to lattice mismatch strains around a $Ti_{11}Ni_{14}$ precipitate in a NiTi matrix. The resolved shear stresses are calculated on martensite variant #6. The plot is axissymmetric around the $[111]$ axes and posses mirror symmetry about the $[111]$ plane.

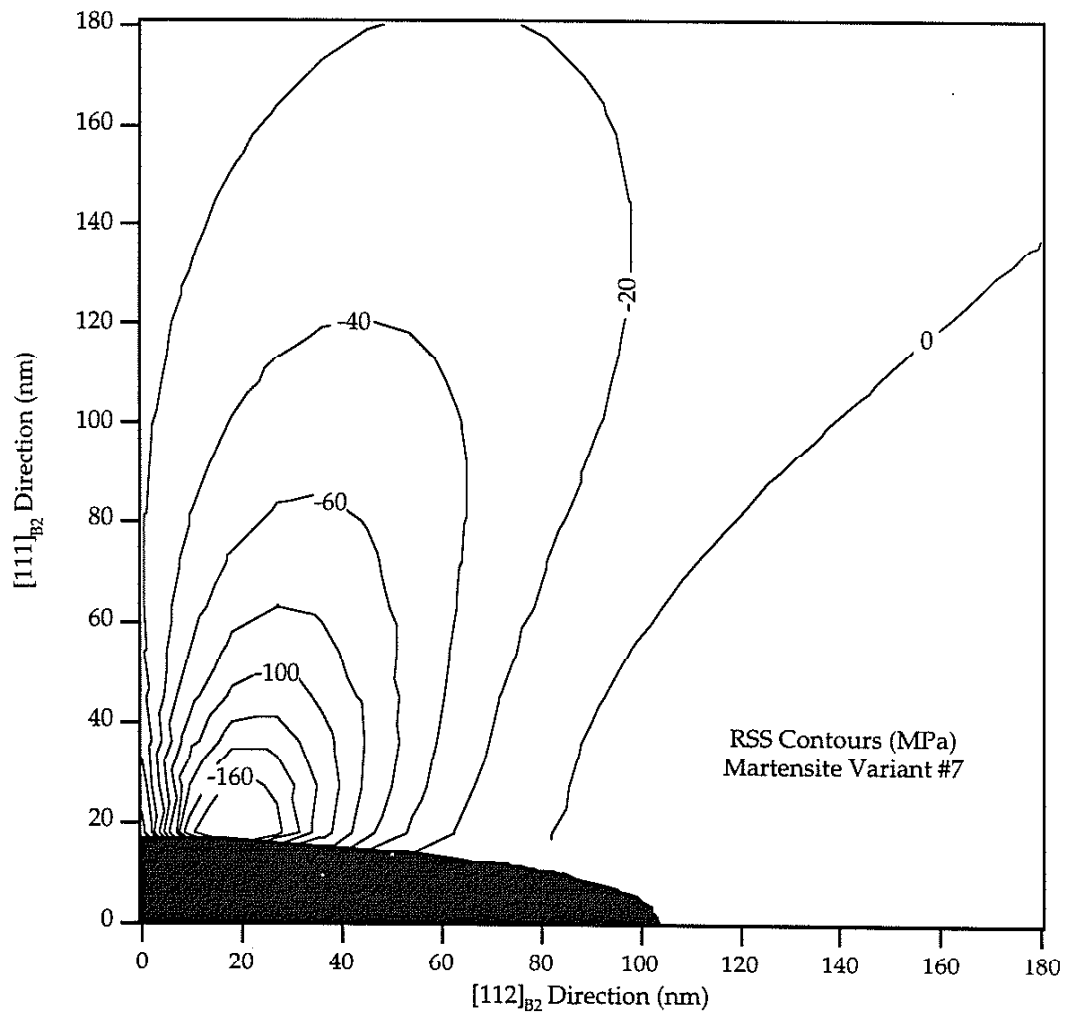


Figure B.7: Resolved shear stress contours due to lattice mismatch strains around a $Ti_{11}Ni_{14}$ precipitate in a NiTi matrix. The resolved shear stresses are calculated on martensite variant #7. The plot is axessymmetric around the $[111]$ axes and posses mirror symmetry about the $[111]$ plane.

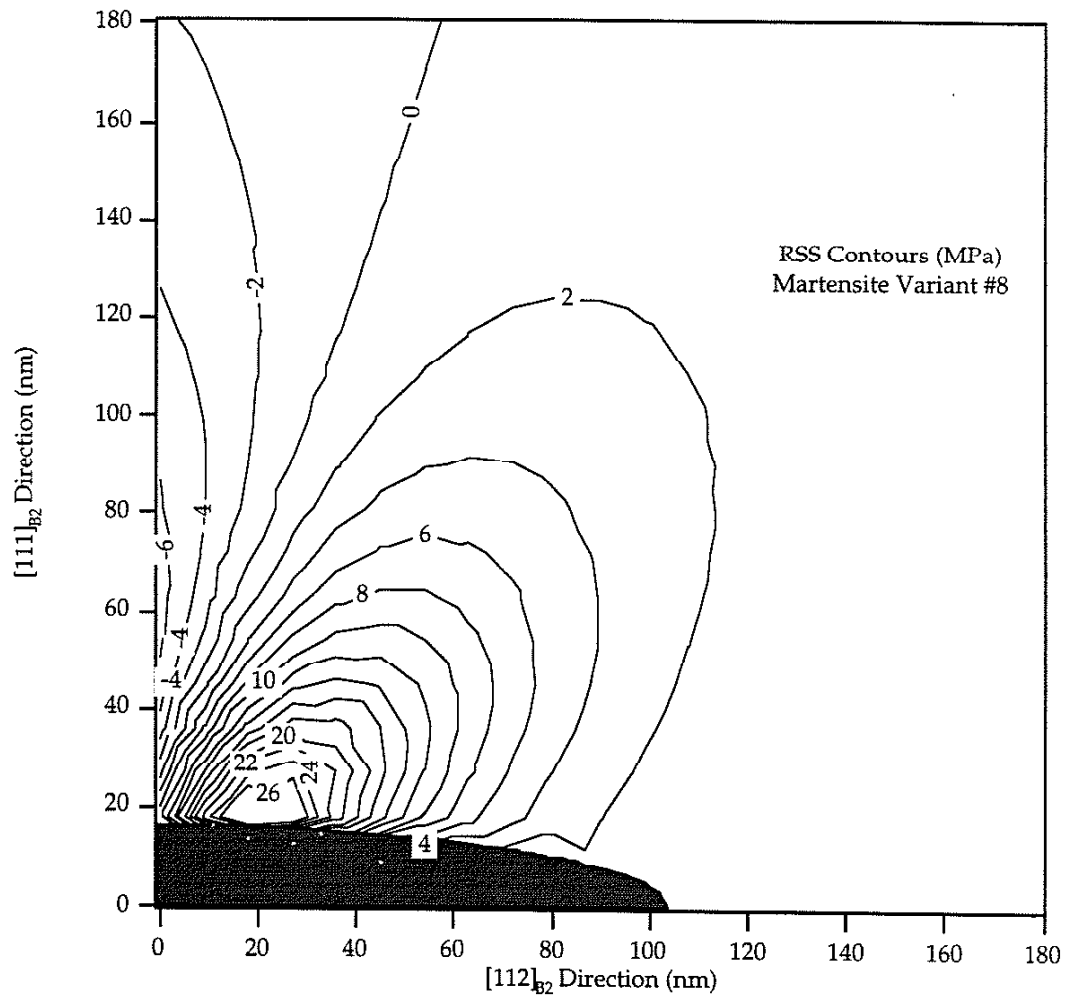


Figure B.8: Resolved shear stress contours due to lattice mismatch strains around a $\text{Ti}_{11}\text{Ni}_{14}$ precipitate in a NiTi matrix. The resolved shear stresses are calculated on martensite variant #8. The plot is axessymmetric around the $[111]$ axes and posses mirror symmetry about the $\{111\}$ plane.

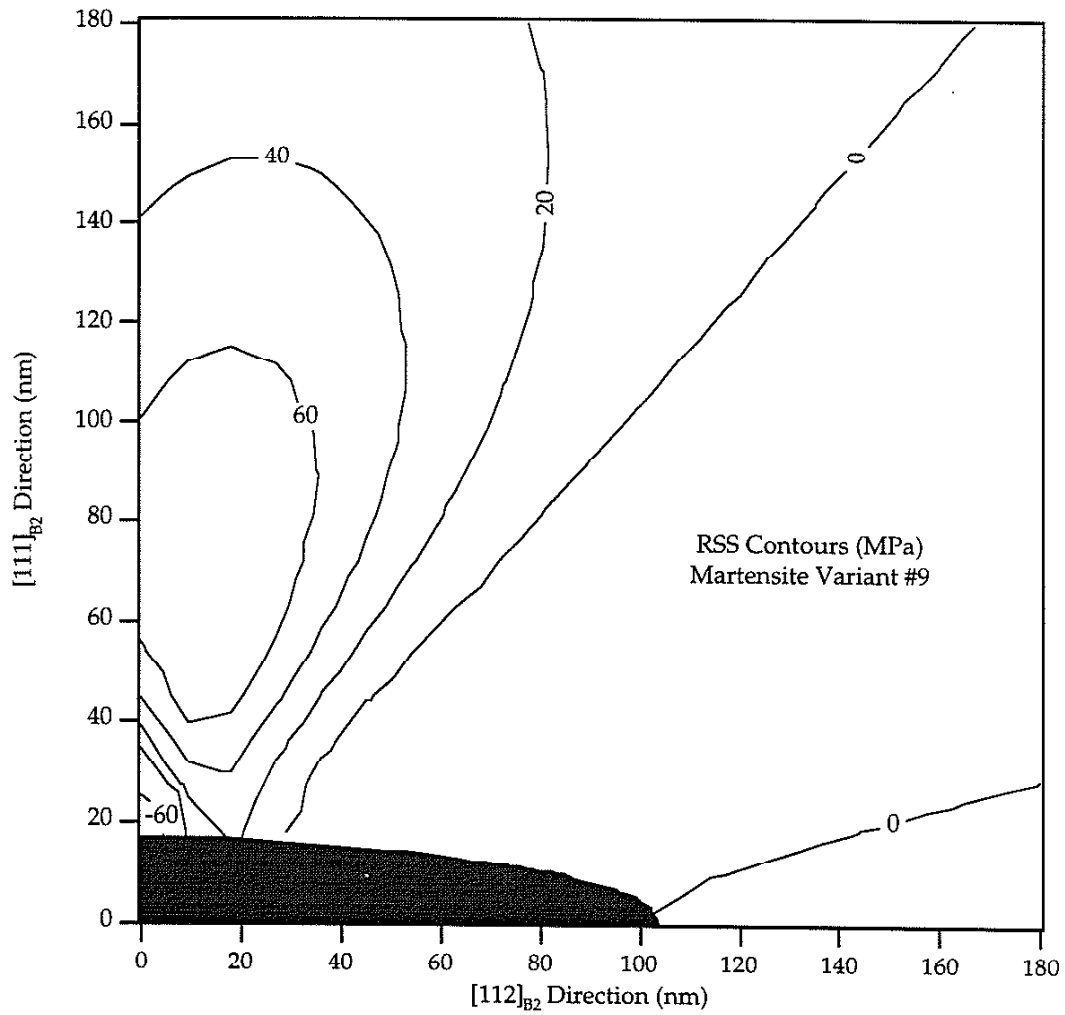


Figure B.9: Resolved shear stress contours due to lattice mismatch strains around a $Ti_{11}Ni_{11}$ precipitate in a NiTi matrix. The resolved shear stresses are calculated on martensite variant #9. The plot is axessymmetric around the [111] axes and posses mirror symmetry about the {111} plane.

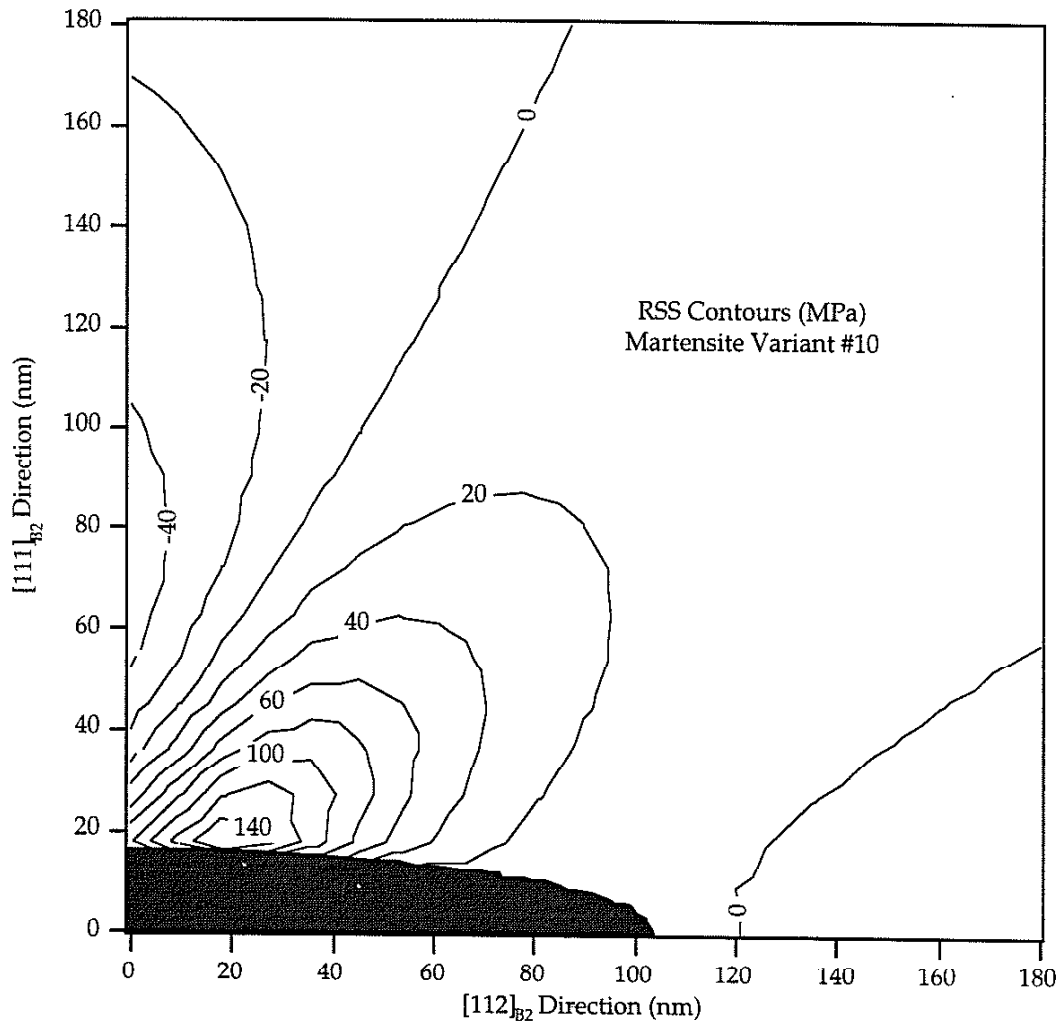


Figure B.10: Resolved shear stress contours due to lattice mismatch strains around a $\text{Ti}_{11}\text{Ni}_{14}$ precipitate in a NiTi matrix. The resolved shear stresses are calculated on martensite variant #10. The plot is axessymmetric around the $\{111\}$ axes and posses mirror symmetry about the $\{111\}$ plane.

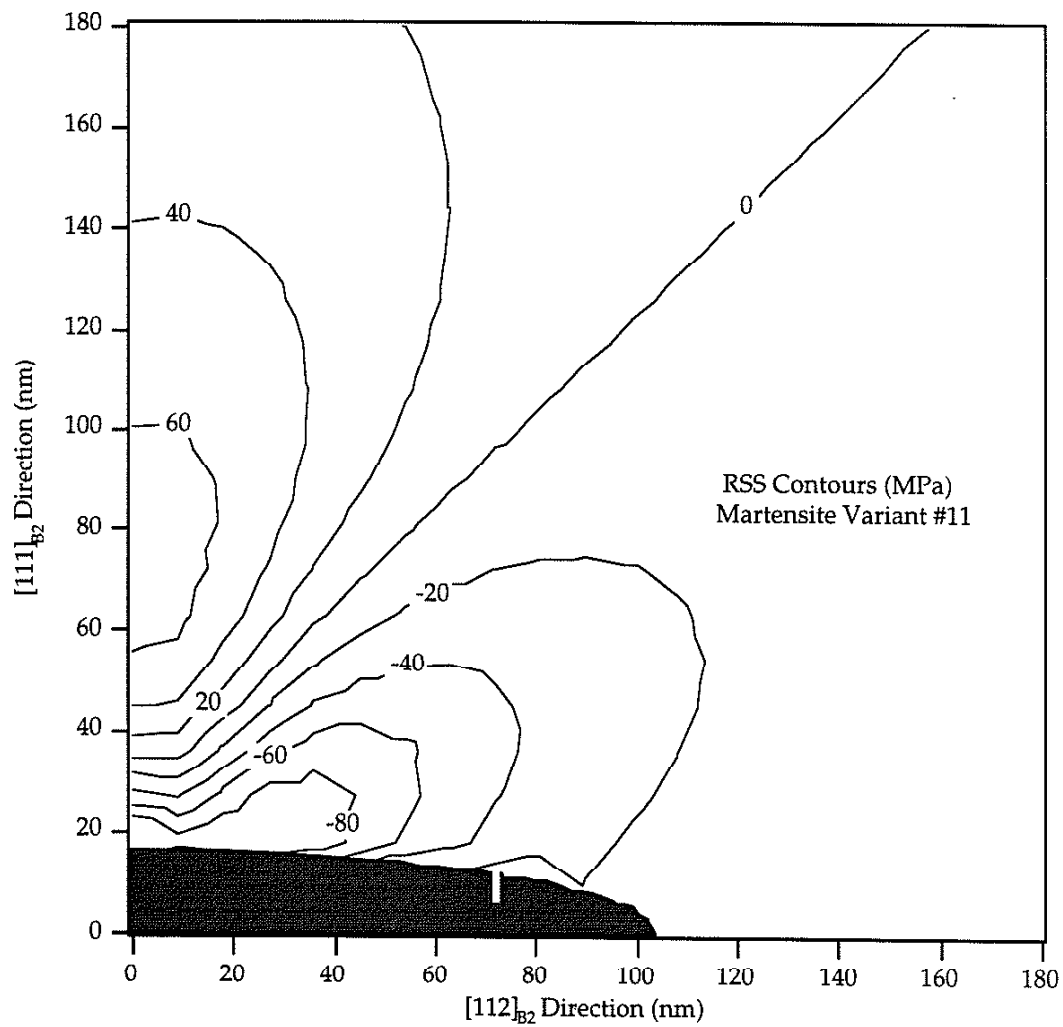


Figure B.11: Resolved shear stress contours due to lattice mismatch strains around a $\text{Ti}_{11}\text{Ni}_{14}$ precipitate in a NiTi matrix. The resolved shear stresses are calculated on martensite variant #11. The plot is axissymmetric around the [111] axes and posses mirror symmetry about the {111} plane.

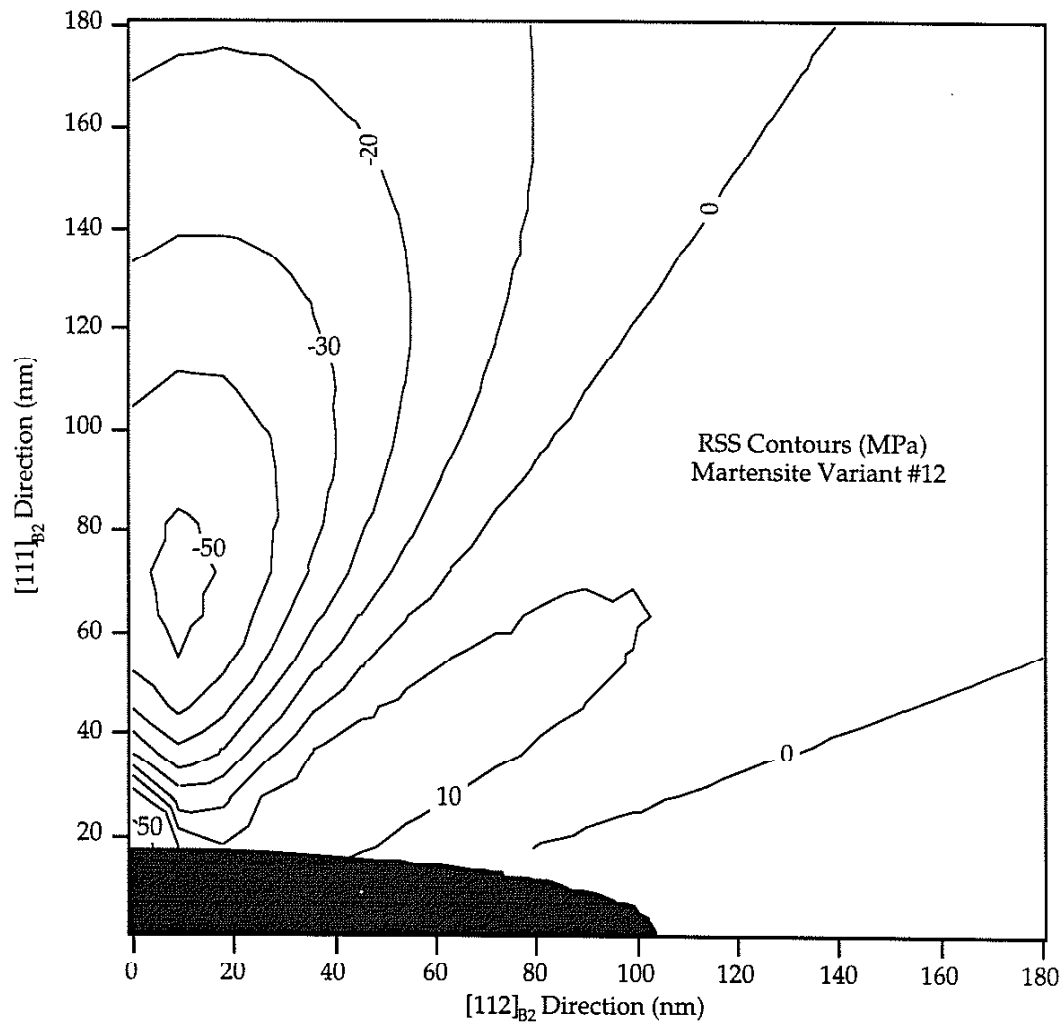


Figure B.12: Resolved shear stress contours due to lattice mismatch strains around a $\text{Ti}_{11}\text{Ni}_{14}$ precipitate in a NiTi matrix. The resolved shear stresses are calculated on martensite variant #12. The plot is axissymmetric around the $\{111\}$ axes and posses mirror symmetry about the $\{111\}$ plane.

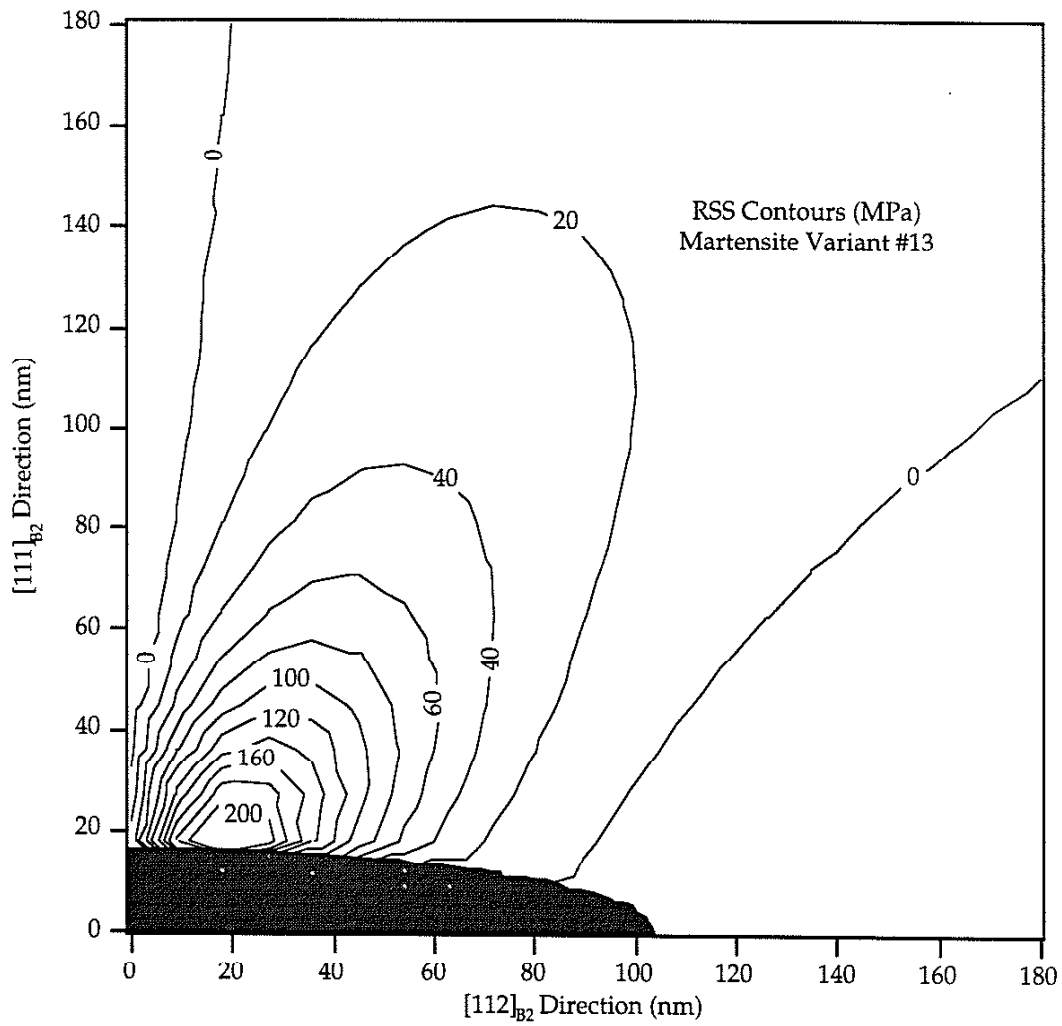


Figure B.13: Resolved shear stress contours due to lattice mismatch strains around a $Ti_{11}Ni_{14}$ precipitate in a NiTi matrix. The resolved shear stresses are calculated on martensite variant #13. The plot is axissymmetric around the $[111]$ axes and posses mirror symmetry about the $\{111\}$ plane.

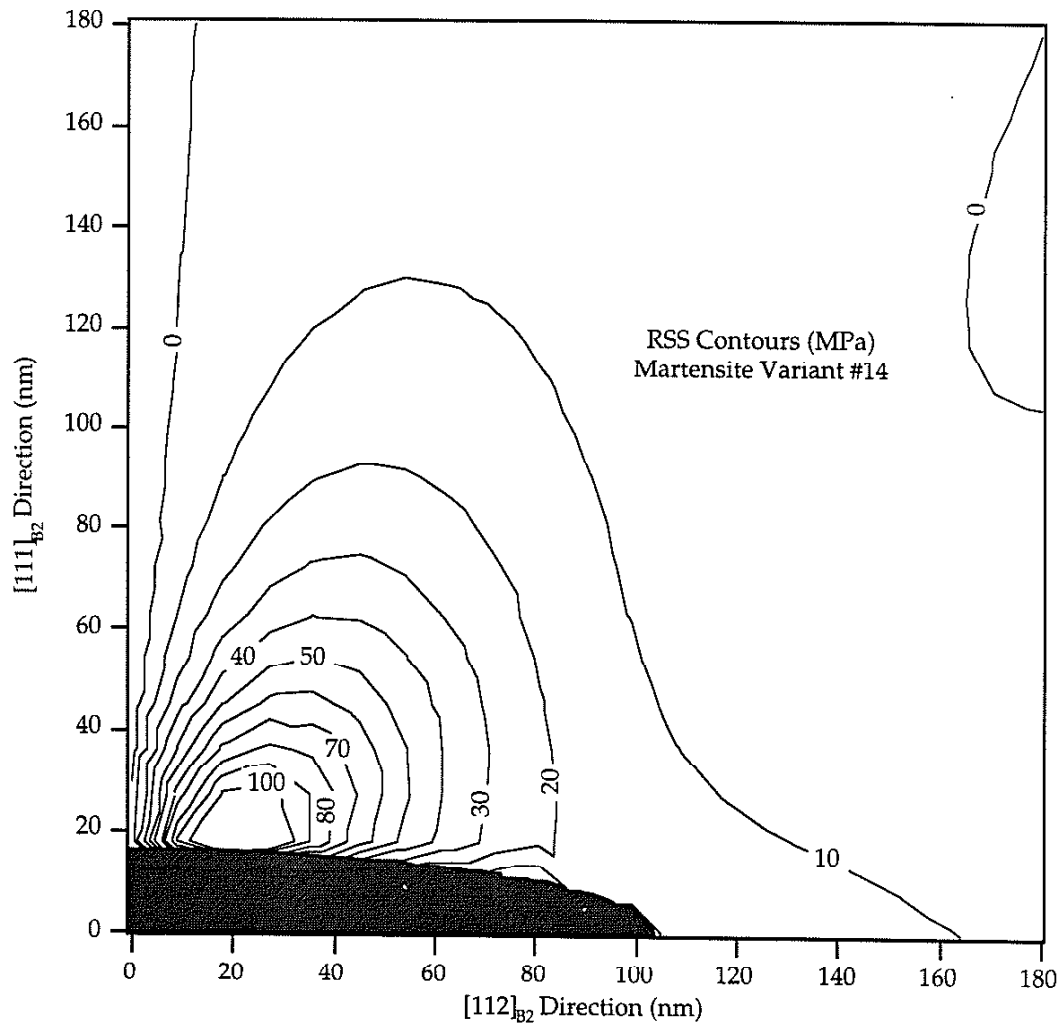


Figure B.14: Resolved shear stress contours due to lattice mismatch strains around a $\text{Ti}_{11}\text{Ni}_{14}$ precipitate in a NiTi matrix. The resolved shear stresses are calculated on martensite variant #14. The plot is axessymmetric around the $\{111\}$ axes and posses mirror symmetry about the $\{111\}$ plane.

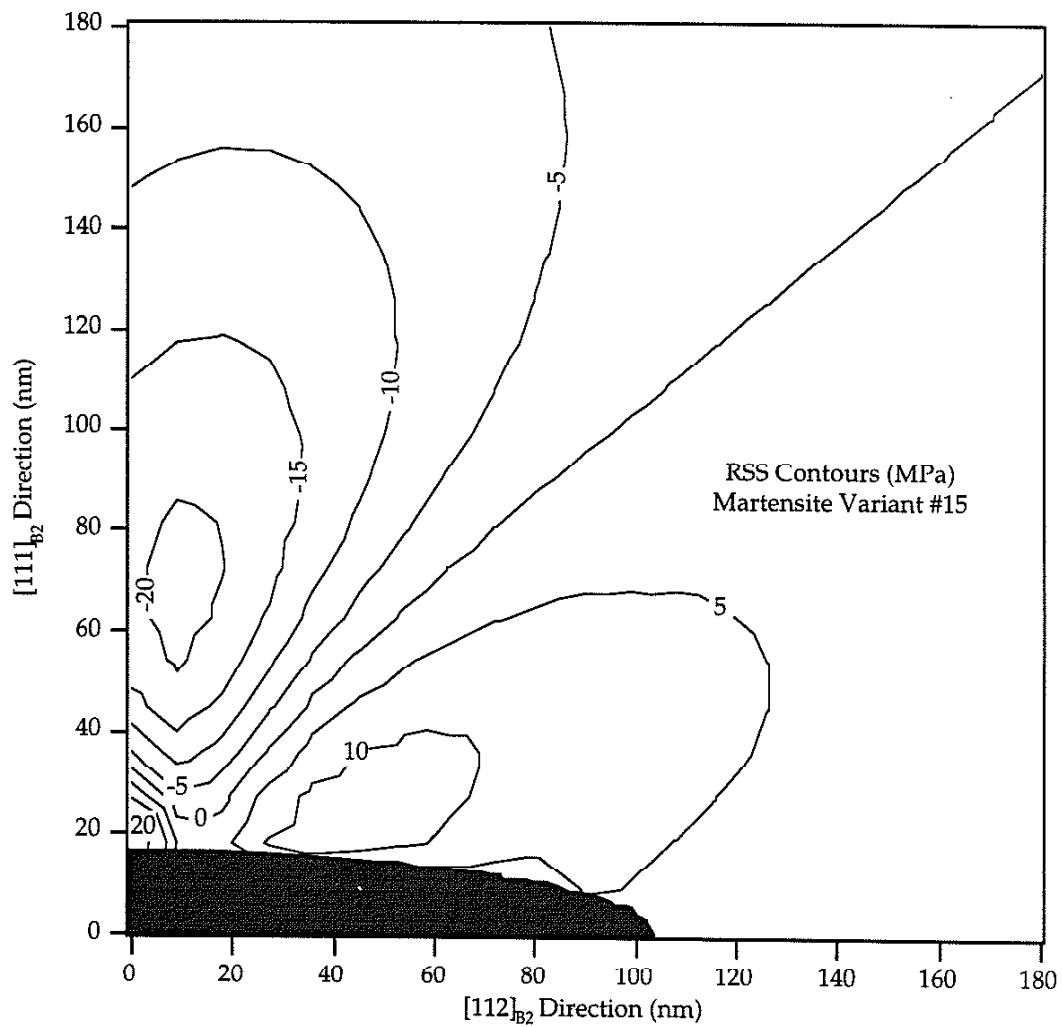


Figure B.15: Resolved shear stress contours due to lattice mismatch strains around a $Ti_{11}Ni_{14}$ precipitate in a NiTi matrix. The resolved shear stresses are calculated on martensite variant #15. The plot is axisymmetric around the $\{111\}$ axes and possesses mirror symmetry about the $\{111\}$ plane.

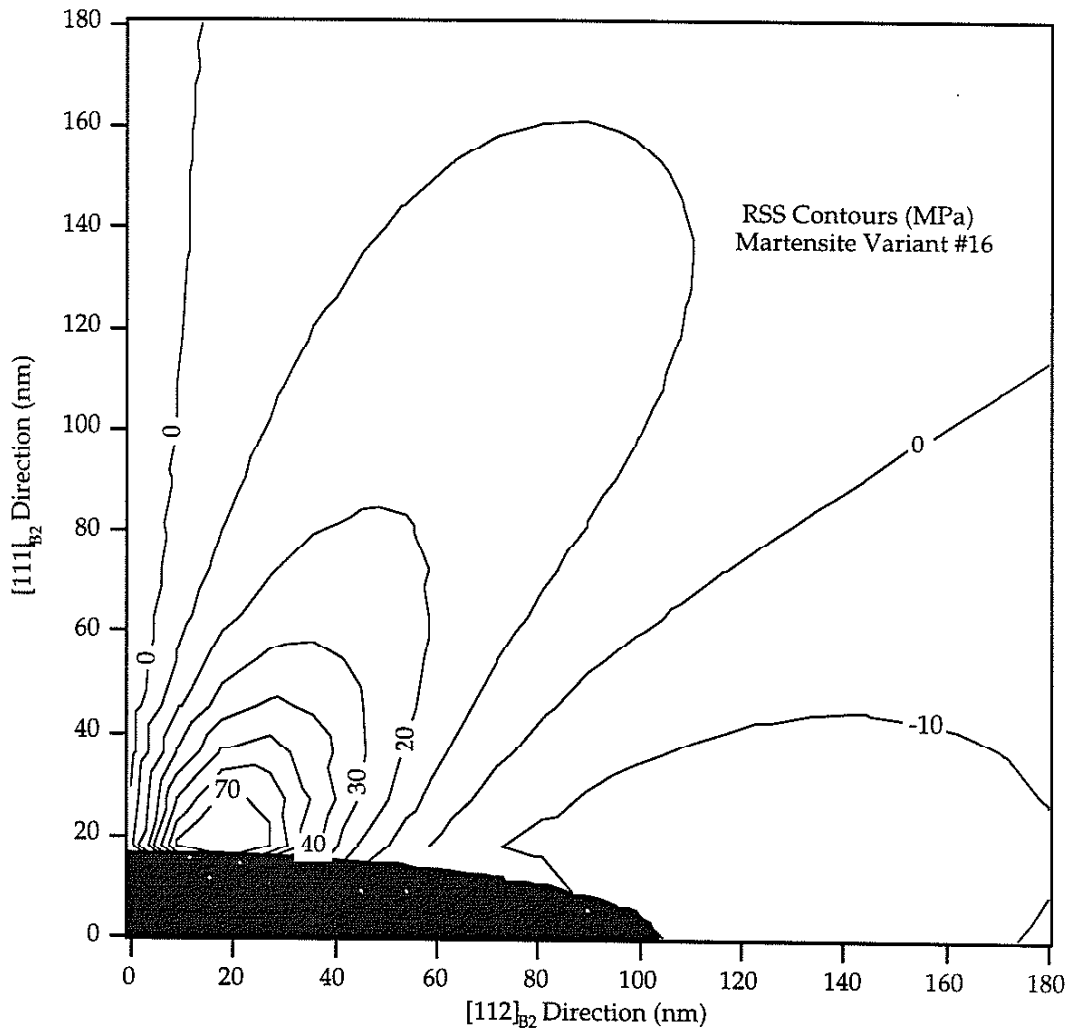


Figure B.16: Resolved shear stress contours due to lattice mismatch strains around a $Ti_{11}Ni_{14}$ precipitate in a NiTi matrix. The resolved shear stresses are calculated on martensite variant #16. The plot is axessymmetric around the $\{111\}$ axes and posses mirror symmetry about the $\{111\}$ plane.

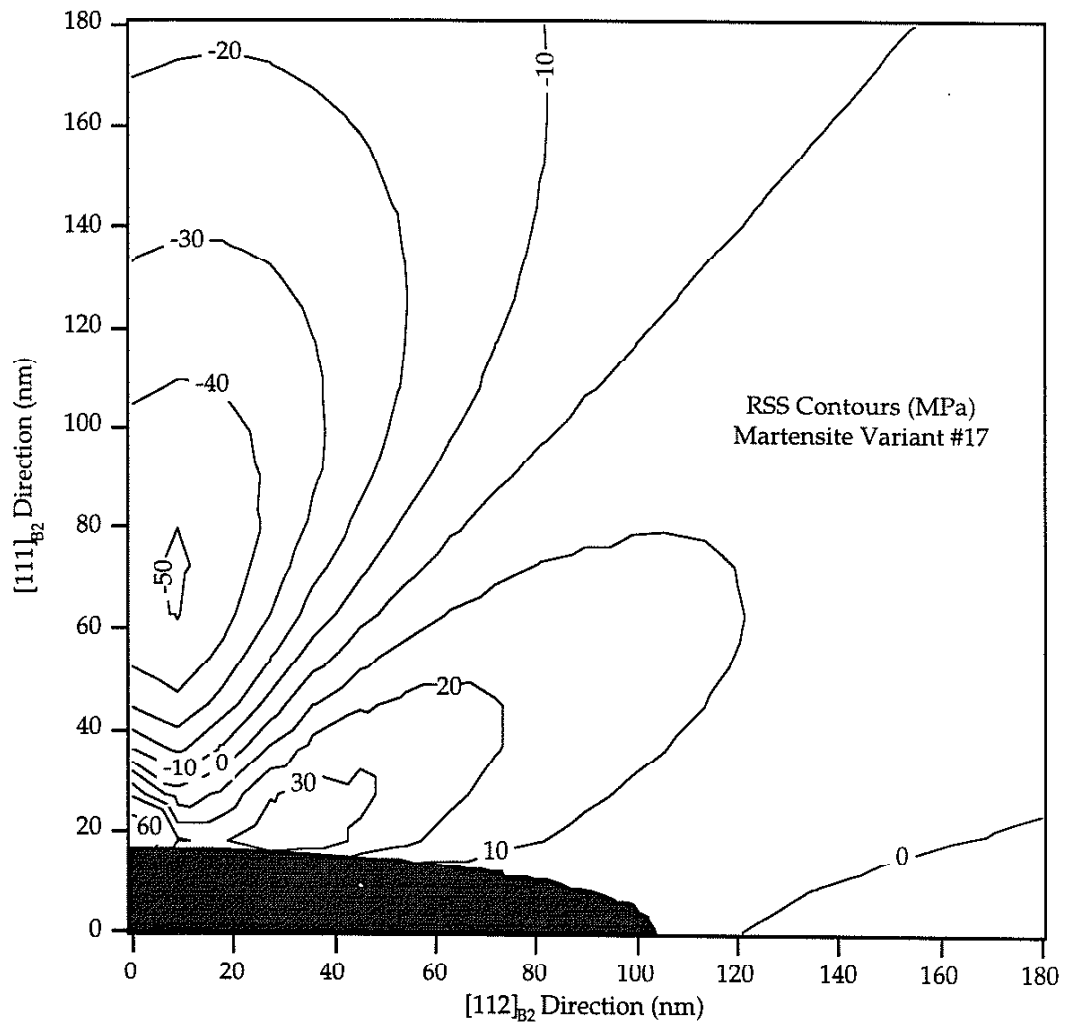


Figure B.17: Resolved shear stress contours due to lattice mismatch strains around a $\text{Ti}_{11}\text{Ni}_{14}$ precipitate in a NiTi matrix. The resolved shear stresses are calculated on martensite variant #17. The plot is axessymmetric around the $\{111\}$ axes and posses mirror symmetry about the $\{111\}$ plane.

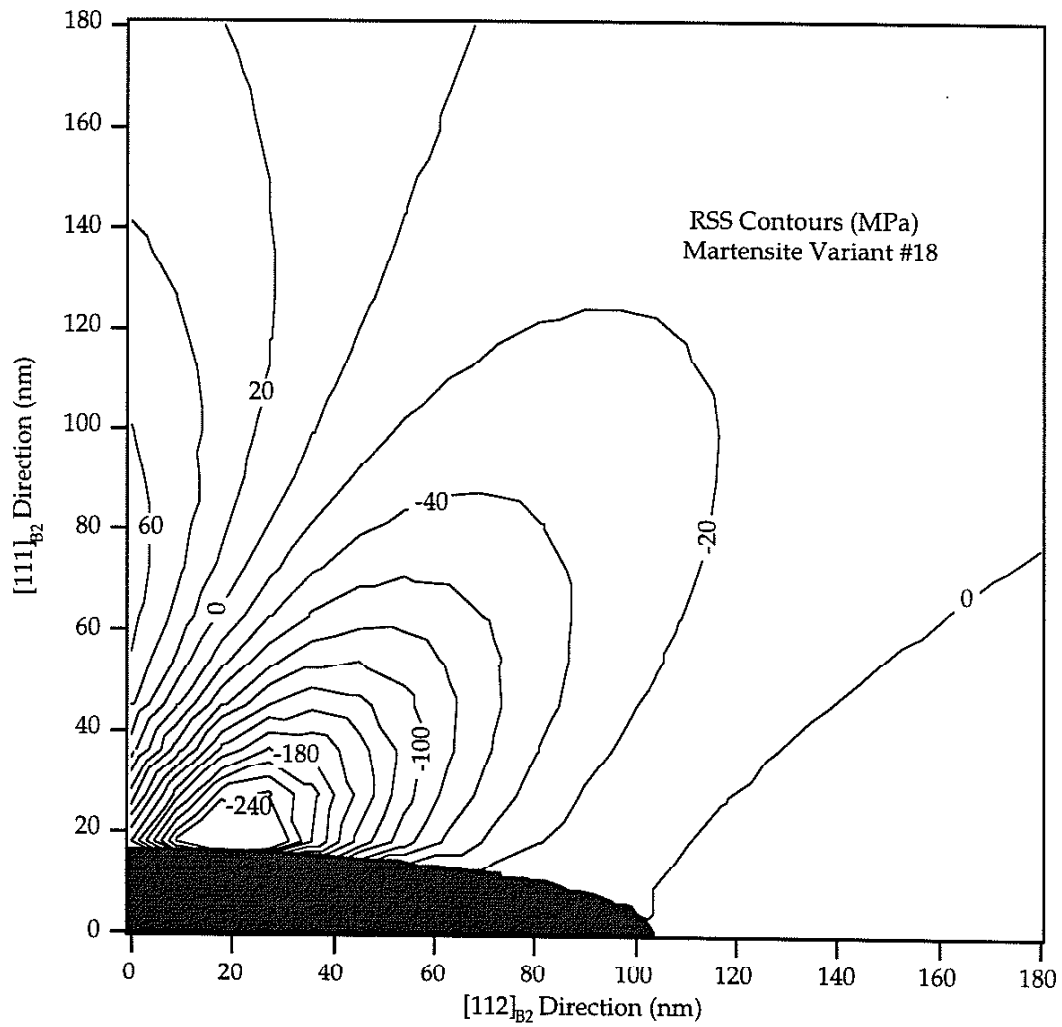


Figure B.18: Resolved shear stress contours due to lattice mismatch strains around a $Ti_{11}Ni_{14}$ precipitate in a NiTi matrix. The resolved shear stresses are calculated on martensite variant #18. The plot is axessymmetric around the $[111]$ axes and posses mirror symmetry about the $\{111\}$ plane.

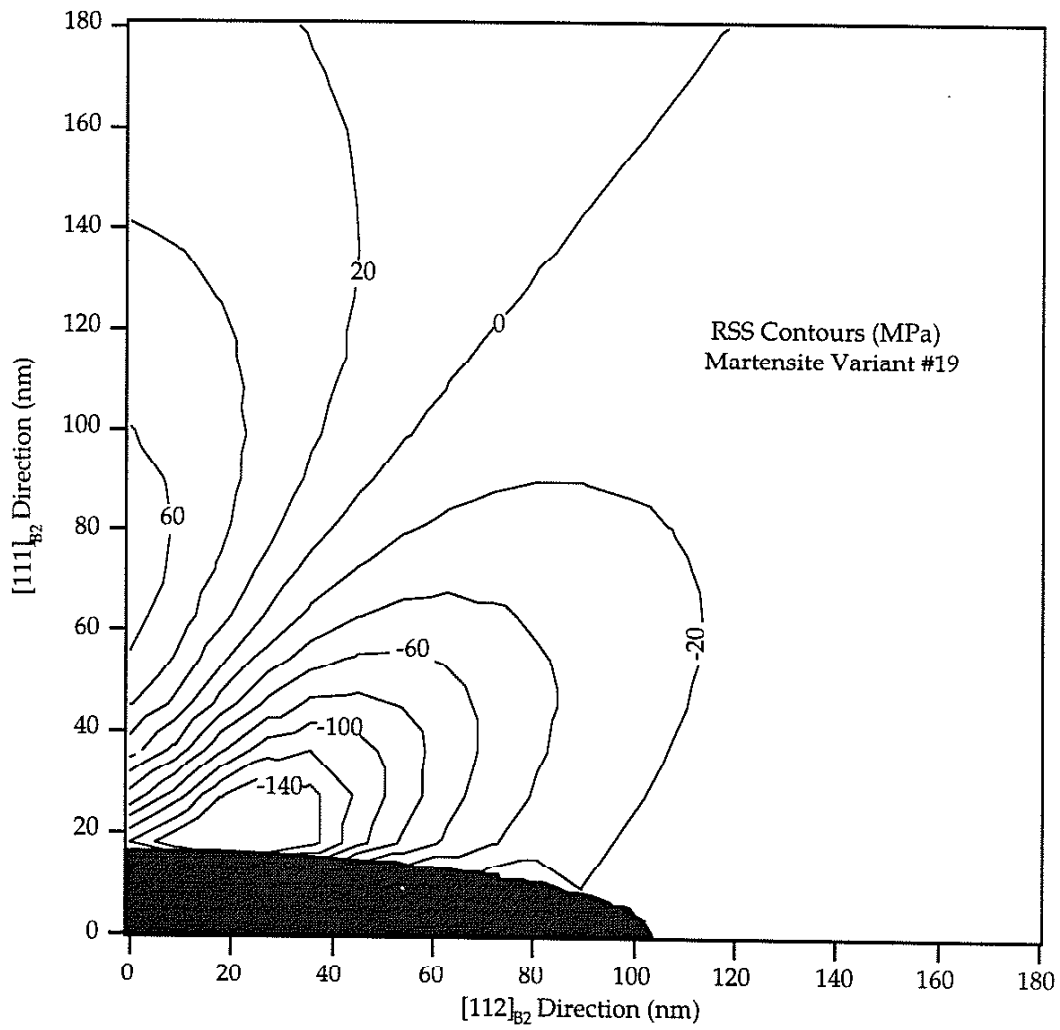


Figure B.19: Resolved shear stress contours due to lattice mismatch strains around a $\text{Ti}_{11}\text{Ni}_{14}$ precipitate in a NiTi matrix. The resolved shear stresses are calculated on martensite variant #19. The plot is axessymmetric around the $[111]$ axes and posses mirror symmetry about the $\{111\}$ plane.

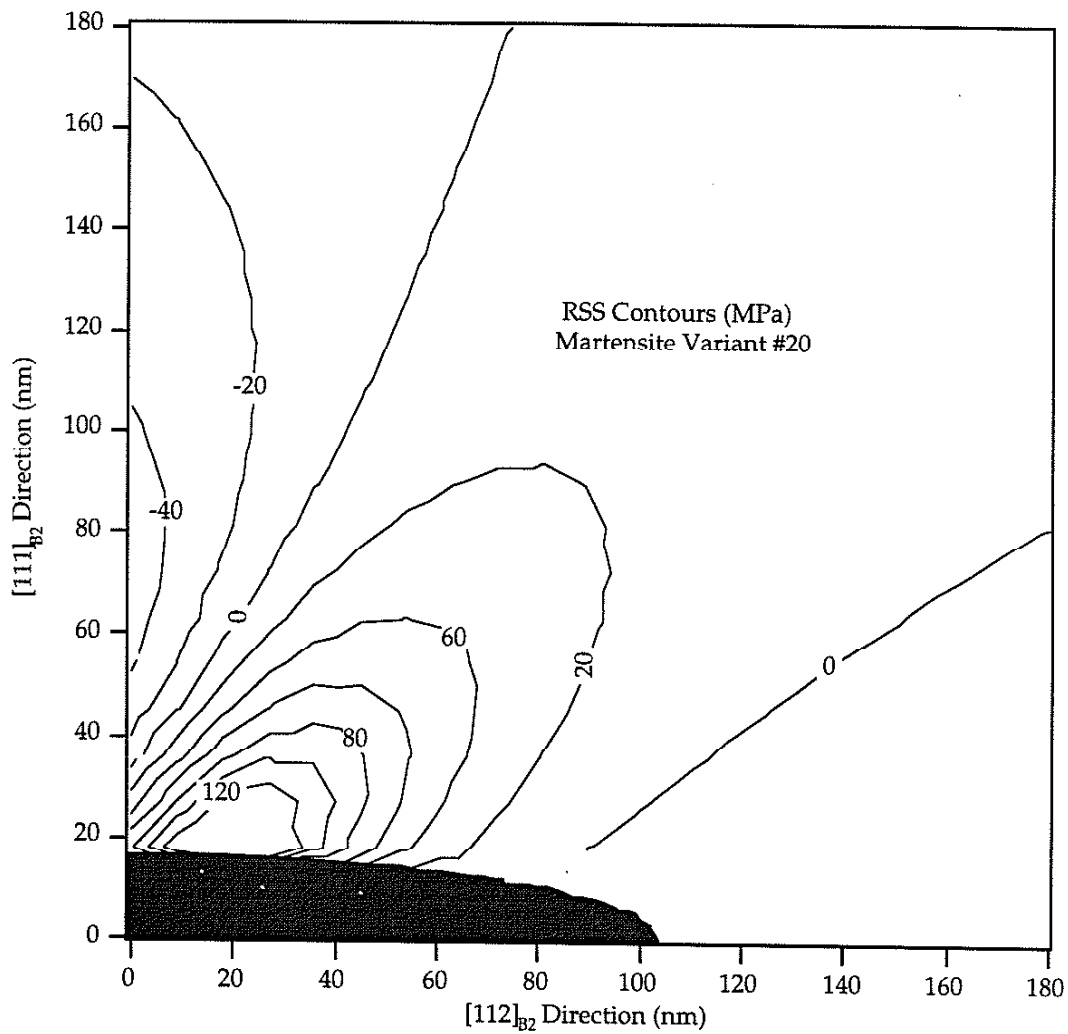


Figure B.20: Resolved shear stress contours due to lattice mismatch strains around a $Ti_{11}Ni_{14}$ precipitate in a NiTi matrix. The resolved shear stresses are calculated on martensite variant #20. The plot is axessymmetric around the $\{111\}$ axes and posses mirror symmetry about the $\{111\}$ plane.

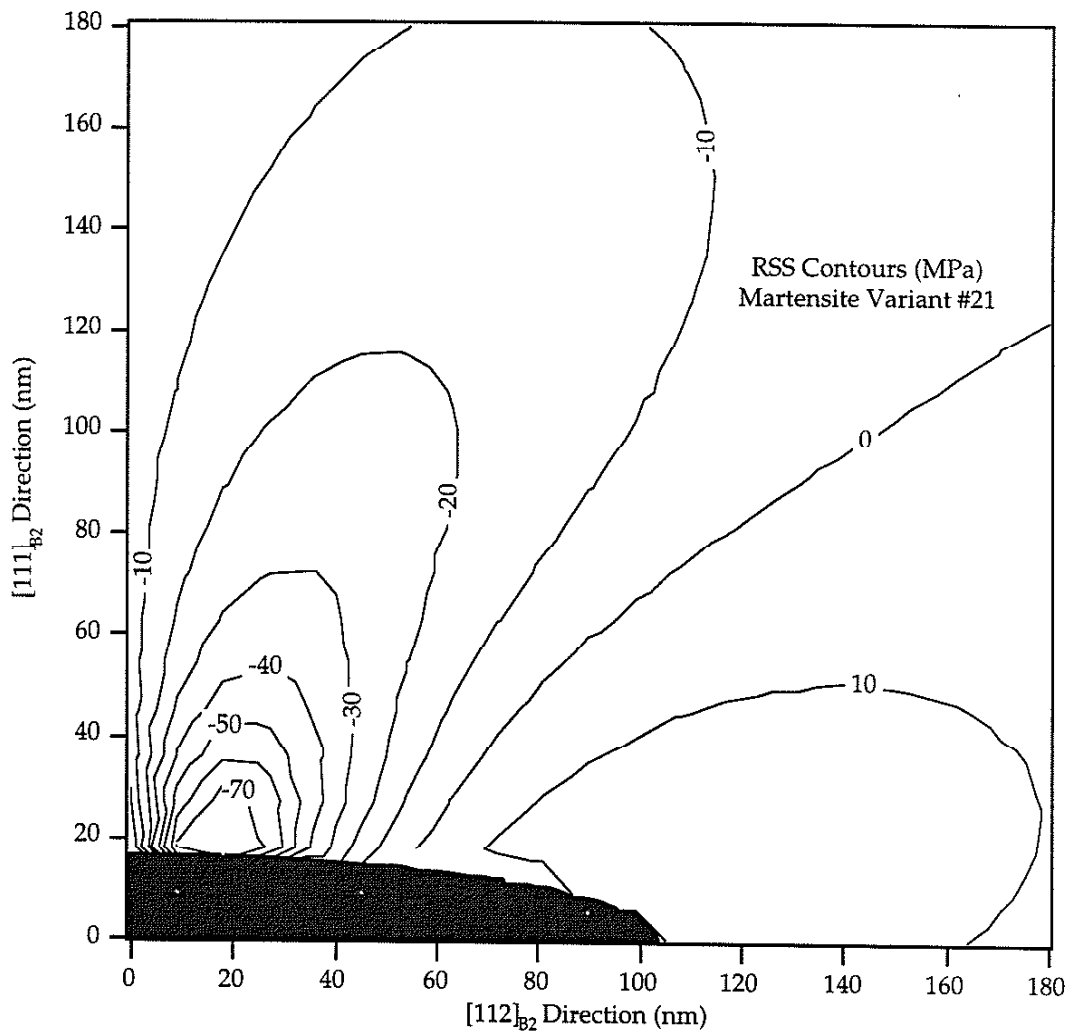


Figure B.21: Resolved shear stress contours due to lattice mismatch strains around a $Ti_{11}Ni_{14}$ precipitate in a NiTi matrix. The resolved shear stresses are calculated on martensite variant #21. The plot is axessymmetric around the $[111]$ axes and posses mirror symmetry about the $\{111\}$ plane.

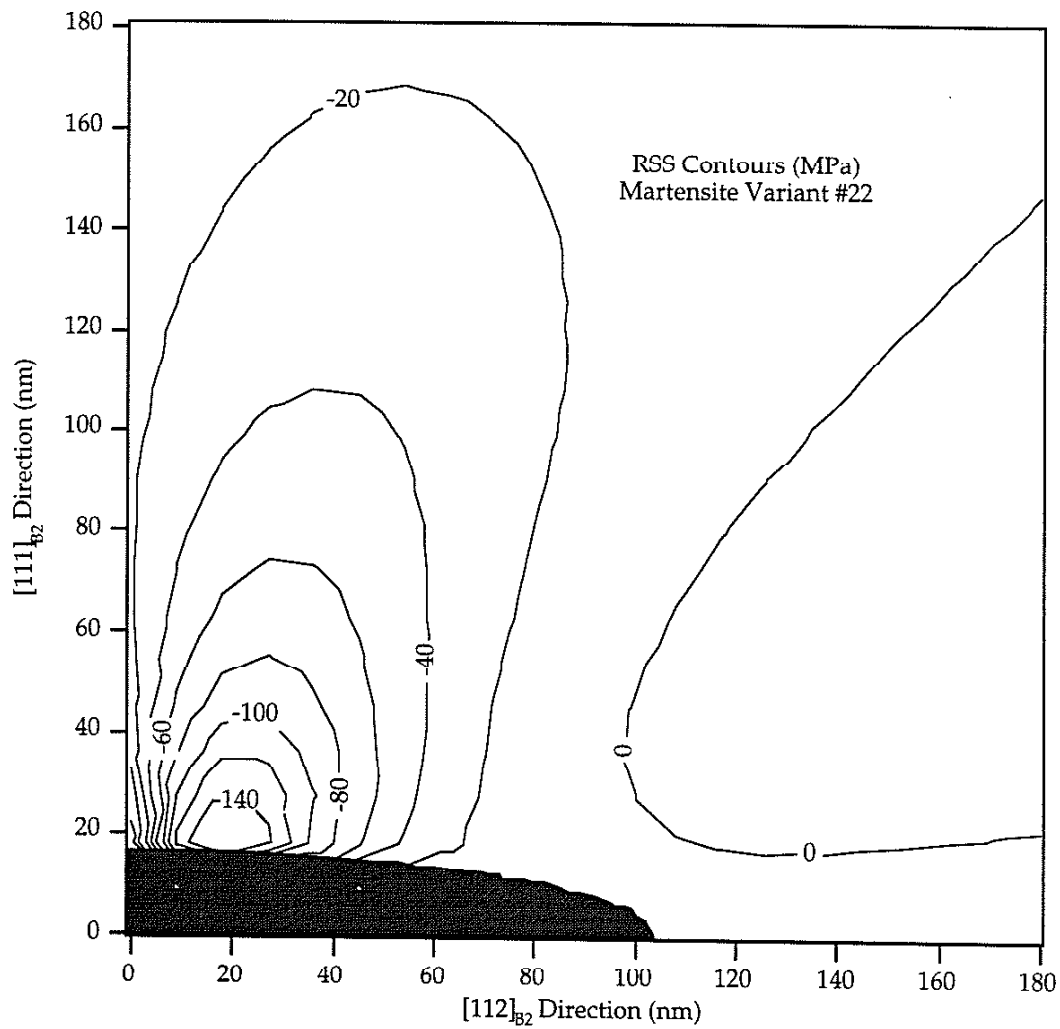


Figure B.22: Resolved shear stress contours due to lattice mismatch strains around a $\text{Ti}_{11}\text{Ni}_{14}$ precipitate in a NiTi matrix. The resolved shear stresses are calculated on martensite variant #22. The plot is axissymmetric around the $[111]$ axes and posses mirror symmetry about the $\{111\}$ plane.

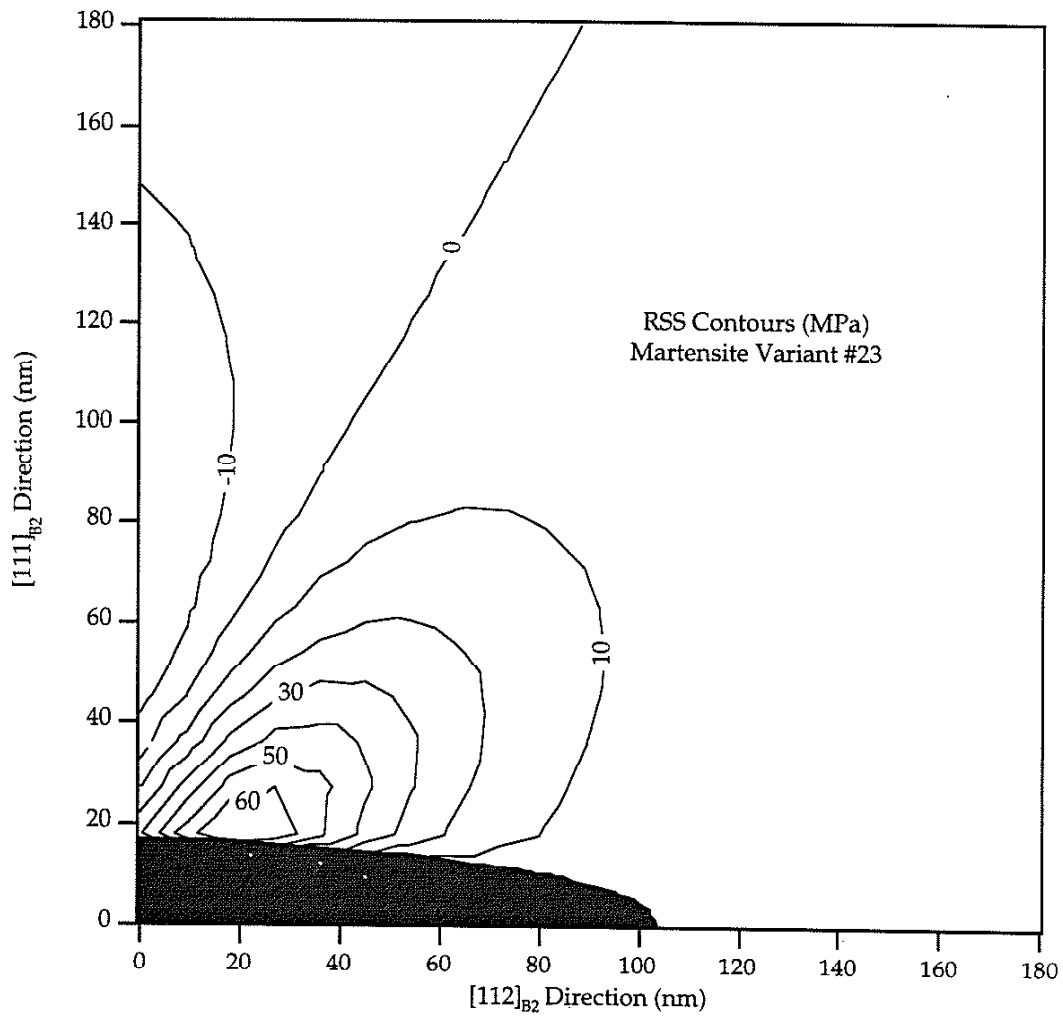


Figure B.23: Resolved shear stress contours due to lattice mismatch strains around a $\text{Ti}_{17}\text{Ni}_{11}$ precipitate in a NiTi matrix. The resolved shear stresses are calculated on martensite variant #23. The plot is axessymmetric around the $\{111\}$ axes and posses mirror symmetry about the $\{111\}$ plane.

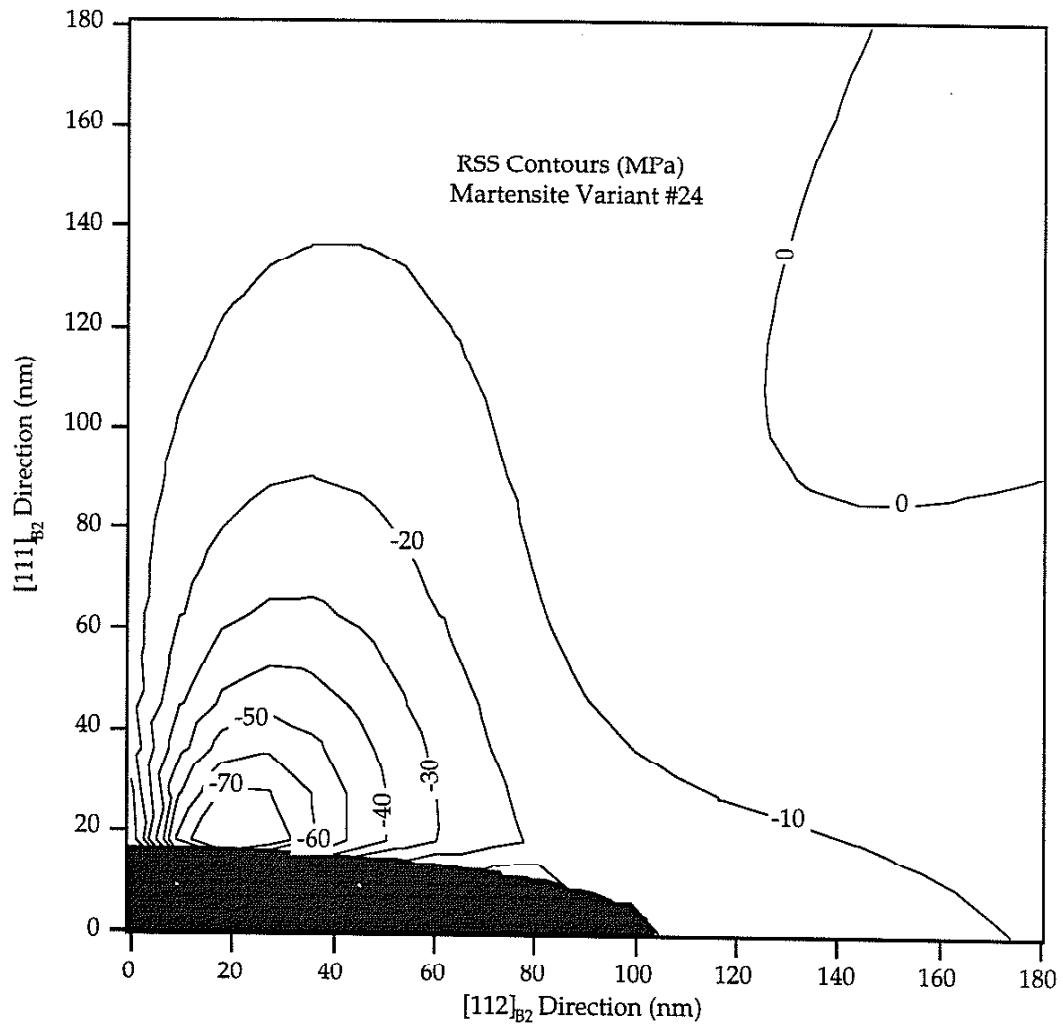


Figure B.24: Resolved shear stress contours due to lattice mismatch strains around a $\text{Ti}_{11}\text{Ni}_{14}$ precipitate in a NiTi matrix. The resolved shear stresses are calculated on martensite variant #24. The plot is axisymmetric around the $[111]$ axes and possesses mirror symmetry about the $\{111\}$ plane.

APPENDIX C: PRECIPITATE STRESS FIELD PROGRAM

THE FOLLOWING PROGRAM IS WRITTEN FOR MATHEMATICA 3.0 AND WILL CALCULATE THE RESOLVED SHEAR STRESS FIELDS OUTSIDE OF PERFECTLY COHERENT PRECIPITATES GIVEN LATTICE MISMATCH STRAINS . THE BOLDFACE IS INPUT AND THE LIGHT TEXT IS OUTPUT .

(* INPUT KNOWN PRECIPITATE DATA *)

a[1] = 104 (* nm *);
a[2] = 104 (* nm *);
a[3] = 16.25 (* nm *);
pi = N[Pi];
nu = .3;
Elas = 74000 (* MPa *)

74000

(* ESTABLISH A FIXED VALUE FOR LAMBDA *)

NumberForm[Solve [x[1]^2 / (a[1] + 1)
+ x[2]^2 / (a[2] + 1) + x[3]^2 / (a[3] + 1) == 1, 1], 4]

{ {1 -> 0.125 (-481. + 4. x[1]^2 + 4. x[2]^2 +
4. x[3]^2 - 1. $\sqrt{-16.00 (6760. - 65.00 x[1]^2 - 65.00 x[2]^2 - 416.0 x[3]^2) + (481.0 - 4.000 x[1]^2 - 4.000 x[2]^2 - 4.000 x[3]^2)^2}$)}},
{1 -> 0.125 (-481. + 4. x[1]^2 + 4. x[2]^2 +
4. x[3]^2 + $\sqrt{-16.00 (6760. - 65.00 x[1]^2 - 65.00 x[2]^2 - 416.0 x[3]^2) + (481.0 - 4.000 x[1]^2 - 4.000 x[2]^2 - 4.000 x[3]^2)^2}$)} } }

(* LAMBDA EQUALS THE LARGER, OR MAX VALUE *)

lam = 0.125 (-481. + 4. x[1]^2 + 4. x[2]^2 +
4. x[3]^2 + $\sqrt{-16.00 (6760. - 65.00 x[1]^2 - 65.00 x[2]^2 - 416.0 x[3]^2) + (481.0 - 4.000 x[1]^2 - 4.000 x[2]^2 - 4.000 x[3]^2)^2}$))
0.125 (-481. + 4. x[1]^2 + 4. x[2]^2 + 4. x[3]^2 +
 $\sqrt{-16. (6760. - 65. x[1]^2 - 65. x[2]^2 - 416. x[3]^2) + (481. - 4. x[1]^2 - 4. x[2]^2 - 4. x[3]^2)^2}$))

(* INPUT VALUE FOR DELTA *)

DELTA = ((a[1]^2 + s) * (a[2]^2 + s) * (a[3]^2 + s))^(1/2)

$\sqrt{(264.063 + s) (10816 + s)^2}$

(* CALCULATE EXPLICIT I-INTEGRALS *)

b = ((a[3]^2 + lam) / (a[1]^2 + lam))^(1/2);
d = ((a[1]^2 - a[3]^2) / (a[1]^2 + lam))^(1/2);

I1 = 4*pi*a[1]^2*a[3] / (a[1]^2 - a[3]^2)^(1/2) * ArcCos[b];

I1am[1] = 2*pi*a[1]^2*a[3] * (ArcCos[b] - b*d) / (a[1]^2 - a[3]^2)^(3/2);

I1am[2] = I1am[1];

I1am[3] = 4*pi*a[1]^2*a[3] * (d/b - ArcCos[b]) / (a[1]^2 - a[3]^2)^(3/2)

2.03766 (-ArcCos[
sqrt(((264.063 + 0.125 (-481. + 4. x[1]^2 + 4. x[2]^2 + 4. x[3]^2 + sqrt(-16. (6760. - 65. x[1]^2 -
65. x[2]^2 - 416. x[3]^2) + (481. - 4. x[1]^2 - 4. x[2]^2 - 4. x[3]^2)^2)))) /
(10816 + 0.125 (-481. + 4. x[1]^2 + 4. x[2]^2 +
4. x[3]^2 + sqrt(-16. (6760. - 65. x[1]^2 - 65. x[2]^2 - 416. x[3]^2) +
(481. - 4. x[1]^2 - 4. x[2]^2 - 4. x[3]^2)^2)))))) +
(102.723
sqrt(1 / (10816 + 0.125 (-481. + 4. x[1]^2 + 4. x[2]^2 + 4. x[3]^2 + sqrt(-16. (6760. - 65. x[1]^2
65. x[2]^2 - 416. x[3]^2) + (481. - 4. x[1]^2 - 4. x[2]^2 - 4. x[3]^2)^2)))))) /
(sqrt(((264.063 + 0.125 (-481. + 4. x[1]^2 + 4. x[2]^2 + 4. x[3]^2 + sqrt(-16. (6760. - 65. x[1]^2 -
65. x[2]^2 - 416. x[3]^2) + (481. - 4. x[1]^2 - 4. x[2]^2 - 4. x[3]^2)^2)))) /
(10816 + 0.125 (-481. + 4. x[1]^2 + 4. x[2]^2 +
4. x[3]^2 + sqrt(-16. (6760. - 65. x[1]^2 - 65. x[2]^2 - 416. x[3]^2) +
(481. - 4. x[1]^2 - 4. x[2]^2 - 4. x[3]^2)^2)))))))))

(* CALCULATE SECOND ORDER I-INTEGRALS *)

Do[Print[i];

I1a[i, j] = 2*pi*a[1]^2*a[3] *

Integrate[1 / ((a[i]^2 + s) * (a[j]^2 + s) * DELTA), {s, lam, Infinity}], {i, 1, 3},
{j, 1, 3}]

1

1

1

2

2

2

3

3

3

```

(* DEFINE THE IDENTITY TENSOR *)

{kd[1, 1] = 1;
kd[1, 2] = 0;
kd[1, 3] = 0;
kd[2, 1] = 0;
kd[2, 2] = 1;
kd[2, 3] = 0;
kd[3, 1] = 0;
kd[3, 2] = 0;
kd[3, 3] = 1}

{1}

(* CALCULATE ALL COMPONENTS OF THE DijkI MATRIX *)

Do[
Dmat[i, j, k, l] =

1/8/pi/(1-nu)* (

kd[i, j]*kd[k, l]*(2*nu*Ilam[i] - Ilam[k] + a[i]^2*Ila[k, i]) +
(kd[i, k]*kd[j, l] + kd[j, k]*kd[i, l])*
(a[i]^2*Ila[i, j] - Ilam[j] +
(1-nu)*(Ilam[k] + Ilam[l])) +

2*nu*kd[k, l]*x[i]*D[Ilam[i], x[j]] +

+(1-nu)*(kd[i, l]*x[k]*D[Ilam[k], x[j]] +
kd[j, l]*x[k]*D[Ilam[k], x[i]] +
kd[i, k]*x[l]*D[Ilam[l], x[j]] +
kd[j, k]*x[l]*D[Ilam[l], x[i]]) -

kd[i, j]*x[k]*D[Ilam[k] - a[i]^2*Ila[k, i], x[l]] -

(kd[i, k]*x[j] + kd[j, k]*x[i])*
D[Ilam[j] - a[i]^2*Ila[i, j], x[l]] -

(kd[i, l]*x[j] + kd[j, l]*x[i])*
D[Ilam[j] - a[i]^2*Ila[i, j], x[k]] -

x[i]*x[j]*
D[Ilam[j] - a[i]^2*Ila[i, j], x[l], x[k]]

),
{i, 1, 3}, {j, 1, 3}, {k, 1, 3}, {l, 1, 3}]

```

```

(* INPUT LATTICE MISMATCH EIGENSTRAINS *)

es[1, 1] = .014;
es[1, 2] = 0;
es[1, 3] = 0;
es[2, 1] = 0;
es[2, 2] = .014;
es[2, 3] = 0;
es[3, 1] = 0;
es[3, 2] = 0;
es[3, 3] = -.029

-0.029

(* CALCULATE STRAIN FIELD OUTSIDE THE PRECIPITATE *)

Do [
  eout[i, j] =
    Sum[Dmat[i, j, k, 1]*es[k, 1], {k, 1, 3}, {1, 1, 3}],
  {i, 1, 3}, {j, 1, 3}]

(* CALCULATE STRESS FIELD OUTSIDE THE PRECIPITATE *)

Do[
  Sig[i, j] = E1as / (1 + nu) * eout[i, j]
    + nu * E1as / ((1 + nu) * (1 - 2 * nu)) *
    (eout[1, 1] + eout[2, 2] + eout[3, 3]) * kd[i, j],
  {i, 1, 3}, {j, 1, 3}]

(* INPUT CRYSTALLOGRAPHIC DATA FOR NiTi *)

{n1 = .8684; n2 = 0.2688; n3 = -0.4138;
 m1 = -0.4580; m2 = 0.7706; m3 = -.4432;
 gee = 0.13}

{0.13}

(* CALCULATE DATA FOR 24 MARTENSITE CVP'S *)

{ nvec[1, 1] = -n1
  nvec[2, 1] = n3;
  nvec[3, 1] = n2;

  mvec[1, 1] = -m1;
  mvec[2, 1] = m3;
  mvec[3, 1] = m2;

  nvec[1, 2] = n3;
  nvec[2, 2] = -n1;
  nvec[3, 2] = -n2;

  mvec[1, 2] = m3;
  mvec[2, 2] = -m1;
  mvec[3, 2] = -m2;

```

nvec [1, 3] = **n1**;
nvec [2, 3] = **-n3**;
nvec [3, 3] = **n2**;

mvec [1, 3] = **m1**;
mvec [2, 3] = **-m3**;
mvec [3, 3] = **m2**;

nvec [1, 4] = **-n3**;
nvec [2, 4] = **n1**;
nvec [3, 4] = **-n2**;

mvec [1, 4] = **-m3**;
mvec [2, 4] = **m1**;
mvec [3, 4] = **-m2**;

nvec [1, 5] = **-n1**;
nvec [2, 5] = **-n3**;
nvec [3, 5] = **-n2**;

mvec [1, 5] = **-m1**;
mvec [2, 5] = **-m3**;
mvec [3, 5] = **-m2**;

nvec [1, 6] = **-n3**;
nvec [2, 6] = **-n1**;
nvec [3, 6] = **n2**;

mvec [1, 6] = **-m3**;
mvec [2, 6] = **-m1**;
mvec [3, 6] = **m2**;

nvec [1, 7] = **n1**;
nvec [2, 7] = **n3**;
nvec [3, 7] = **-n2**;

mvec [1, 7] = **m1**;
mvec [2, 7] = **m3**;
mvec [3, 7] = **-m2**;

nvec [1, 8] = **n3**;
nvec [2, 8] = **n1**;
nvec [3, 8] = **n2**;

mvec [1, 8] = **m3**;
mvec [2, 8] = **m1**;
mvec [3, 8] = **m2**;

nvec [1, 9] = **n2**;
nvec [2, 9] = **n1**;

nvec[3, 9] = -n3;

mvec[1, 9] = m2;
mvec[2, 9] = m1;
mvec[3, 9] = -m3;

nvec[1, 10] = n2;
nvec[2, 10] = -n1;
nvec[3, 10] = n3;

mvec[1, 10] = m2;
mvec[2, 10] = -m1;
mvec[3, 10] = m3;

nvec[1, 11] = -n2;
nvec[2, 11] = n3;
nvec[3, 11] = -n1;

mvec[1, 11] = -m2;
mvec[2, 11] = m3;
mvec[3, 11] = -m1;

nvec[1, 12] = -n2;
nvec[2, 12] = -n3;
nvec[3, 12] = n1;

mvec[1, 12] = -m2;
mvec[2, 12] = -m3;
mvec[3, 12] = m1;

nvec[1, 13] = -n2;
nvec[2, 13] = n1;
nvec[3, 13] = n3;

mvec[1, 13] = -m2;
mvec[2, 13] = m1;
mvec[3, 13] = m3;

nvec[1, 14] = -n2;
nvec[2, 14] = -n1;
nvec[3, 14] = -n3;

mvec[1, 14] = -m2;
mvec[2, 14] = -m1;
mvec[3, 14] = -m3;

nvec[1, 15] = n2;
nvec[2, 15] = -n3;
nvec[3, 15] = -n1;

mvec[1, 15] = m2;
mvec[2, 15] = -m3;
mvec[3, 15] = -m1;


```
nvec[1, 16] = n2;  
nvec[2, 16] = n3;  
nvec[3, 16] = n1;
```

```
mvec[1, 16] = m2;  
mvec[2, 16] = m3;  
mvec[3, 16] = m1;
```

```
nvec[1, 17] = n1;  
nvec[2, 17] = -n2;  
nvec[3, 17] = -n3;
```

```
mvec[1, 17] = m1;  
mvec[2, 17] = -m2;  
mvec[3, 17] = -m3;
```

```
nvec[1, 18] = -n1;  
nvec[2, 18] = -n2;  
nvec[3, 18] = n3;
```

```
mvec[1, 18] = -m1;  
mvec[2, 18] = -m2;  
mvec[3, 18] = m3;
```

```
nvec[1, 19] = -n3;  
nvec[2, 19] = n2;  
nvec[3, 19] = n1;
```

```
mvec[1, 19] = -m3;  
mvec[2, 19] = m2;  
mvec[3, 19] = m1;
```

```
nvec[1, 20] = n3;  
nvec[2, 20] = n2;  
nvec[3, 20] = -n1;
```

```
mvec[1, 20] = m3;  
mvec[2, 20] = m2;  
mvec[3, 20] = -m1;
```

```
nvec[1, 21] = n1;  
nvec[2, 21] = n2;  
nvec[3, 21] = n3;
```

```
mvec[1, 21] = m1;  
mvec[2, 21] = m2;  
mvec[3, 21] = m3;
```

```
nvec[1, 22] = -n1;  
nvec[2, 22] = n2;  
nvec[3, 22] = -n3;
```

```
mvec[1, 22] = -m1;  
mvec[2, 22] = m2;  
mvec[3, 22] = -m3;
```

```
nvec[1, 23] = n3;  
nvec[2, 23] = -n2;  
nvec[3, 23] = n1;
```

```
mvec[1, 23] = m3;  
mvec[2, 23] = -m2;  
mvec[3, 23] = m1;
```

```
nvec[1, 24] = -n3;  
nvec[2, 24] = -n2;  
nvec[3, 24] = -n1;
```

```
mvec[1, 24] = -m3;  
mvec[2, 24] = -m2;  
mvec[3, 24] = -m1;
```

```
{-0.397727}
```

```
(* ALPHA TENSOR FOR NITI *)
```

```
Do [ Do [ Do [  
  alij[i, j, k] = .5 * (nvec[i, k] * mvec[j, k] + nvec[j, k] * mvec[i, k]),  
  {i, 3}], {j, 3}], {k, 24}]
```

(* CREATE A ROTATION TENSOR *)

$$a001 = \{0, 0, 1\}$$

$$a010 = \{0, 1, 0\}$$

$$a100 = \{1, 0, 0\}$$

$$ap001 = 1/3^{(1/2)} * \{1, 1, 1\}$$

$$ap010 = 1/6^{(1/2)} * \{1, 1, -2\}$$

$$ap100 = 1/2^{(1/2)} * \{1, -1, 0\}$$

$$\{0, 0, 1\}$$

$$\{0, 1, 0\}$$

$$\{1, 0, 0\}$$

$$\left\{ \frac{1}{\sqrt{3}}, \frac{1}{\sqrt{3}}, \frac{1}{\sqrt{3}} \right\}$$

$$\left\{ \frac{1}{\sqrt{6}}, \frac{1}{\sqrt{6}}, -\sqrt{\frac{2}{3}} \right\}$$

$$\left\{ \frac{1}{\sqrt{2}}, -\frac{1}{\sqrt{2}}, 0 \right\}$$

```

RO[1, 1] = ap100 . a100
RO[1, 2] = ap100 . a010
RO[1, 3] = ap100 . a001

RO[2, 1] = ap010 . a100
RO[2, 2] = ap010 . a010
RO[2, 3] = ap010 . a001

RO[3, 1] = ap001 . a100
RO[3, 2] = ap001 . a010
RO[3, 3] = ap001 . a001

```

$$\frac{1}{\sqrt{2}}$$

$$-\frac{1}{\sqrt{2}}$$

0

$$\frac{1}{\sqrt{6}}$$

$$\frac{1}{\sqrt{6}}$$

$$-\sqrt{\frac{2}{3}}$$

$$\frac{1}{\sqrt{3}}$$

$$\frac{1}{\sqrt{3}}$$

$$\frac{1}{\sqrt{3}}$$

(* ROTATE THE HABIT PLANES INTO PRECIPITATE SYSTEM *)

Do [

```

ALP[i, j, m] = Sum[
  RO[i, k] * RO[j, l] * ali[j][k, l, m], {k, 1, 3}, {l, 1, 3}],
{i, 1, 3}, {j, 1, 3}, {m, 1, 24}]

```

(* PRINT OUT ALPHAij' s FOR DIFFERENT ORIENTATIONS *)

```

(*100*)
Do [
  Print[{alij[1, 1, m], alij[2, 2, m], alij[3, 3, m]},
    {m, 1, 24}]
{-0.397727, 0.183396, 0.207137}
{0.183396, -0.397727, 0.207137}
{-0.397727, 0.183396, 0.207137}
{0.183396, -0.397727, 0.207137}
{-0.397727, 0.183396, 0.207137}
{0.183396, -0.397727, 0.207137}
{-0.397727, 0.183396, 0.207137}
{0.183396, -0.397727, 0.207137}
{0.207137, -0.397727, 0.183396}
{0.207137, -0.397727, 0.183396}
{0.207137, 0.183396, -0.397727}
{0.207137, 0.183396, -0.397727}
{0.207137, -0.397727, 0.183396}
{0.207137, -0.397727, 0.183396}
{0.207137, 0.183396, -0.397727}
{0.207137, 0.183396, -0.397727}
{-0.397727, 0.207137, 0.183396}
{-0.397727, 0.207137, 0.183396}
{0.183396, 0.207137, -0.397727}
{0.183396, 0.207137, -0.397727}
{-0.397727, 0.207137, 0.183396}
{-0.397727, 0.207137, 0.183396}
{0.183396, 0.207137, -0.397727}
{0.183396, 0.207137, -0.397727}

```

```

(*110, 112, 111*)
Do [
  Print[{Alp[1, 1, m], Alp[2, 2, m], Alp[3, 3, m]}],
  {m, 1, 24}]

{-0.204843, 0.462957, -0.265308}
{-0.204843, -0.1931, 0.390749}
{-0.204843, -0.1931, 0.390749}
{-0.204843, 0.462957, -0.265308}
{-0.00948828, 0.0337865, -0.031492}
{-0.00948828, 0.105835, -0.10354}
{-0.00948828, 0.105835, -0.10354}
{-0.00948828, 0.0337865, -0.031492}
{-0.368334, -0.0296081, 0.390749}
{0.177744, 0.08037, -0.265308}
{-0.0237365, -0.374206, 0.390749}
{0.41427, -0.156156, -0.265308}
{0.177744, -0.081398, -0.10354}
{-0.368334, 0.392633, -0.031492}
{-0.0237365, 0.120083, -0.10354}
{0.41427, -0.389972, -0.031492}
{0.177744, 0.08037, -0.265308}
{-0.368334, -0.0296081, 0.390749}
{-0.0237365, -0.374206, 0.390749}
{0.41427, -0.156156, -0.265308}
{-0.368334, 0.392633, -0.031492}
{0.177744, -0.081398, -0.10354}
{-0.0237365, 0.120083, -0.10354}
{0.41427, -0.389972, -0.031492}

(* CALCULATE THE RESOLVED SHEAR STRESS FIELD *)
(* ON THE 24 CVP' S OUTSIDE THE PRECIPITATE *)

Do[
  rss[m] = Sum[
    Alp[i, j, m] * Sig[i, j], {i, 1, 3}, {j, 1, 3}],
  {m, 1, 24}]

```

```

(* The problem is axis-symmetric about x[3] *)
(* so set x[2] = 0 since information in x[2] *)
(* direction is same as information in x[1] *)
(* direction *)

x[2] = 0

0

(* CALCULATE THE STRESS FIELD POINWISE FOR *)
(* A 20 BY 20 MATRIX OF POSITIONS. THIS *)
(* MATRIX CAN BE USED TO MAKE CONTOUR PLOTS *)

Do[

  a = 180/20*i;
  b = 180/20*j;
  Ken[i, j] = If [ (a^2/104^2+b^2/16.25^2) < 1,
    0,
    rss[1] /. {x[1] -> 180/20*i, x[3] -> 180/20*j}];
  Print[Ken[i, j]],

{i, 0, 20}, {j, 0, 20}]

```

VITA

Kenneth Allen Gall was born on November 6, 1972 in Dupage County, Illinois to Kathy and Glenn Gall. He graduated from Glenbard North High School in May of 1990. After graduating high school he attended Elmhurst College for two years. At Elmhurst he majored in Atomic Physics and accumulated a perfect grade point average. In August of 1992 he transferred to the University of Illinois at Urbana-Champaign. He graduated from the University of Illinois in January of 1995 with honors from the Department of Mechanical and Industrial Engineering. As an undergraduate student he was the winner of the Fred Eggers engineering award. After graduation he entered directly into graduate school in the Department of Mechanical and Industrial Engineering at the University of Illinois at Urbana-Champaign. In January of 1996 he graduated with his masters of science. During his first year in graduate school he was an author on 5 journal and conference publications. In January of 1996 he switched research fields and began working on his Ph.D. thesis. In the two years that followed he has been an author on 9 additional journal and conference publications, and the winner of several awards such as the General Electric Teaching Incentive Grant. Upon leaving the University of Illinois he will work as a post-doc research assistant at Sandia National Laboratories for two years. After the post-doc at Sandia he will pursue a job in academia.